

The role of disorder in the electronic and transport properties of monolayer and bilayer graphene

THÈSE N° 6759 (2015)

PRÉSENTÉE LE 7 DÉCEMBRE 2015
À LA FACULTÉ DES SCIENCES DE BASE
GROUPE YAZYEV
PROGRAMME DOCTORAL EN PHYSIQUE

ÉCOLE POLYTECHNIQUE FÉDÉRALE DE LAUSANNE

POUR L'OBTENTION DU GRADE DE DOCTEUR ÈS SCIENCES

PAR

Fernando GARGIULO

acceptée sur proposition du jury:

Prof. R. Houdré, président du jury
Prof. O. Yazyev, directeur de thèse
Prof. T. Wehling, rapporteur
Prof. D. Abanin, rapporteur
Prof. A. Kis, rapporteur



ÉCOLE POLYTECHNIQUE
FÉDÉRALE DE LAUSANNE

Suisse
2015

To my family and especially to my father who, when I was eight, asked me:
“What about becoming a physicist?”

Acknowledgements

Above all, I am grateful to my supervisor, Professor Oleg Yazyev, for his support over the last four years. During the redaction of this thesis, I took time to wonder which aspect of his guidance I most benefited from. I arrived to the conclusion that by trusting me, even in those moment when I would not trusted myself, he pushed me to do more than I thought possible. Any PhD student could hardly ask more.

From the practical side, the development of my PhD would have been significantly delayed without the support of Gabriel Autès, who has represented an authentic school of pragmatism for me. I acknowledge many stimulating and intellectually intense discussions with Professor Vincenzo Savona, who accorded me the honor of being his teaching assistant. Past and present members of my research group deserve a mention for sharing their knowledge with me and also for bearing me during our group meetings, which - I admit - can be tough sometimes: Naunidh, Gabriel, Artem, Zhiyong, Hyungjun, Vamshi, Diego.

I thank my officemates in chronological order: Luca, who was a point of reference for me when I was a newcomer in Switzerland, Grégoire, Xiaoliang, and Diego. From all the students I met during the courses and the hours of "Travaux Pratiques" I learned at least as much as I taught them.

One does not understand the irreplaceable role of good secretaries until they are missing. Now, I can wittingly say thanks to Noemi, Tanya, and Anh. I should thank the EPFL institutions and facilities at many levels, in particular the Institut de Théorie des Phénomènes Physiques, the Scientific IT and Application Support, the EPFL library, the Doctoral School of Physics, as well as two other federal institutions: the Swiss National Supercomputing Centre and the Science National Foundation.

This thesis is dedicated to my family, namely, my parents Luigi and Antonella, my siblings Alessandra and Federico, my grandparents Anna, Ferdinando, and Maria. Regarding the latter, I hope that after ten years spent in Physics, I managed to convince her that being a physicist can be as rewarding as being a lawyer. I also acknowledge support from several further relatives: Nello, Laura, Peppe, Giacomo, Alessia, Ferdinando, and Anna. I thank my four Italian best friends Gaetano, Gennaro, Domenico, Salvatore, and all my friends in Switzerland, especially my comrades of GGAL (Gruppo Giovani Adulti Losanna) hosted by the Catholic Mission of Lausanne. My years in Lausanne would have been much poorer without the sweet presence of a fine soul called Gloria. I thank her and her family.

Finally, though very often overlooked, I acknowledge the instruction that I received from the Italian education system, built with wisdom over centuries, a common good that sometimes

Acknowledgements

the Italians do not appreciate as needed. I sometimes feel the burden of representing the world most ancient state-supported institution of higher education, the University of Naples “Federico II”. And, of course, I am indebted to Switzerland for having refined my education and broadened my horizons to an extent that I could not even imagine before. I hope that I have been able to give to this country as much as I received from it.

Lausanne, September 2015

F. G.

Abstract

This thesis is devoted to the computational study of the electronic and transport properties of monolayer and bilayer graphene in the presence of disorder arising from both topological and point defects. Among the former, we study grain boundaries in monolayer graphene and stacking domain boundaries in bilayer graphene, whereas among the latter we study hydrogen atoms covalently bound on the graphene crystal lattice. The electronic spectrum of disordered graphene has been studied within a tight-binding framework, which has been coupled to the Landauer-Büttiker theory and Green's function techniques in order to have access to the properties of coherent transport of graphene charge carriers. We assess the low-energy equilibrium structures of defective graphene by a combination of *ab initio* density functional theory, classical potentials, and Monte Carlo methods.

We study periodic grain boundaries in monolayer graphene and individuate two classes of defects with opposite effects in terms of scattering of low-energy charge carriers. One class, unexpectedly, is highly reflecting in the limit of low defect density, whereas another is highly transparent. Subsequently, we study disordered grain boundaries in order to predict the intrinsic conductance of realistic polycrystalline graphene samples. In two related works, conducted in collaboration with experimentalists, we identify the atomic structure of periodic grain boundaries imaged by scanning tunneling microscopy, and discuss the valley-filtering capabilities of a line defect of graphene that can be grown in a controllable manner.

Next, we investigate the electronic transport of graphene with realistic hydrogen adsorbates, whose equilibrium configurations are obtained by means of Monte Carlo simulations. We find that the conductance of graphene dramatically increases upon formation of cluster adatoms, which we predict to happen spontaneously at room temperature. This is due to the non-resonant nature of a large fraction of hydrogen clusters in the room-temperature distribution, which we further elucidate by means of an analytical solvable model.

Finally, we study the behavior, in terms of structural and electronic properties, of twisted bilayer graphene in the limit of zero twist angle. We find a critical angle below which the system arranges in a triangular superlattice of Bernal-stacking domains, separated by a hexagonal network of stacking domain boundaries. The presence of stacking domain boundaries is at the base of our interpretation of an experiment reporting oscillations in the electrical conductance of bilayer graphene subjected to mechanical indentation.

Keywords: graphene, bilayer graphene, disorder, topological defects, grain boundaries, hydrogenated graphene, stacking domain boundaries, electronic transport, Landauer-Büttiker, Green's function, Monte Carlo

Sommario

Questa tesi è dedicata allo studio, condotto attraverso tecniche computazionali, delle proprietà elettroniche e di trasporto di carica del grafene a singolo e doppio strato in presenza di disordine. Abbiamo considerato disordine originato da difetti sia topologici che puntuali. All'interno della prima categoria, abbiamo studiato i bordi di grano del grafene a singolo strato e le interfacce tra regioni del grafene a doppio strato con diversa traslazione relativa dei due strati ("stacking domain boundaries"). Tra i difetti puntuali, ci siamo interessati agli adatomi di idrogeno che formano legami covalenti con gli atomi di carbonio del grafene a singolo strato.

Lo spettro elettronico del grafene disordinato è stato studiato attraverso il metodo del "legame stretto" (Tight Binding). Tale teoria è stata associata a quella di Landauer e Büttiker e ai metodi basati sulla funzione di Green per estrarre le proprietà di trasporto di carica del grafene. Le configurazioni strutturali di equilibrio del grafene disordinato sono state ottenute combinando metodi *ab initio*, potenziali classici e metodi Monte Carlo. Tra i bordi di grano periodici del grafene a singolo strato abbiamo individuato due classi caratterizzate da opposte proprietà di scattering nei confronti dei portatori di carica di bassa energia. Mentre i bordi di grano appartenenti alla prima classe prevalentemente riflettono i portatori di carica, quelli della seconda classe sono praticamente trasparenti. Dopodiché, abbiamo studiato bordi di grano disordinati per calcolare le conduttanza intrinseca di esemplari realistici di grafene policristallino. La parte dedicata ai bordi di grano si chiude con due lavori realizzati in collaborazione con gruppi sperimentali. Nel primo abbiamo identificato la struttura atomica di alcuni bordi di grano periodici le cui immagini sono state ottenute attraverso la microscopia a effetto tunnel, mentre nel secondo abbiamo discusso le proprietà di selezione di valle di un difetto lineare che può essere introdotto nel grafene in maniera controllata.

In seguito, abbiamo studiato il trasporto elettronico nel grafene contenente adsorbati di idrogeno. Abbiamo trovato che la conduttanza del grafene aumenta in maniera considerevole contestualmente alla formazione di piccoli aggregati di adatomi di idrogeno, che abbiamo previsto formarsi spontaneamente a temperatura ambiente. Questo effetto è dovuto alla natura non risonante di una larga frazione degli aggregati di idrogeno, che abbiamo delucidato anche attraverso un modello analitico.

Successivamente, abbiamo studiato dal punto di vista strutturale ed elettronico il grafene a doppio strato in presenza di un angolo di rotazione relativo tra i due strati, specialmente nel limite di piccolo angolo. Abbiamo trovato un angolo critico al di sotto del quale gli atomi del sistema si dispongono formando un reticolo di regioni triangolari nelle quali i due strati

Acknowledgements

esibiscono l'allineamento relativo di minore energia ("Bernal stacking"). Le interfacce tra tali regioni formano una maglia esagonale precedentemente documentata negli esperimenti. Per finire, la presenza spontanea di simili interfacce è alla base della nostra interpretazione di un esperimento nel quale sono state misurate oscillazioni della conduttanza elettrica nel grafene a doppio strato sottoposto a deformazione meccanica.

Parole chiave: grafene, grafene a doppio strato, disordine, difetti topologici, bordi di grano, grafene idrogenato, trasporto elettronico, Landauer-Büttiker, funzione di Green, Monte Carlo

Résumé

Cette thèse est dédiée à l'étude computationnelle des propriétés électroniques et de transport du graphène à une et deux couches, en présence de défauts ponctuels et topologiques. Parmi ces derniers, on étudie les joints de grains dans le graphène monocouche ainsi que les interfaces entre les régions du graphène à deux couches avec différentes translations relatives des deux couches ("stacking domain boundaries"). Parmi les défauts ponctuels, on s'intéresse à l'effet d'atomes d'hydrogènes liés de façon covalente au réseau cristallin. Ces études ont été réalisées dans l'approximation des liaisons fortes, couplée à la théorie de Landauer-Büttiker et à des techniques de fonctions de Green, afin d'avoir accès aux propriétés de transport cohérent des porteurs de charge. On évalue la structure d'équilibre du graphène avec des défauts à l'aide d'une combinaison de la théorie de la fonctionnelle de la densité, de potentiels classiques ainsi que de méthodes de Monte Carlo.

On étudie les joints de grains périodiques dans le graphène monocouche et on identifie deux classes de défauts, avec des effets opposés en termes de diffusion des porteurs de charge. Une classe correspond aux défauts qui, de façon surprenante, sont fortement réfléchissants dans la limite de faible densité de défauts, alors que la deuxième correspond à des défauts fortement transparents. Par la suite, on étudie les joints de grains désordonnés afin de prédire la conductance intrinsèque d'échantillons réalistes de graphène polycristallin. Dans deux études conduites en collaboration avec des expérimentateurs, on identifie la structure atomique de joints de grains périodiques visualisée par microscopie à effet tunnel et on discute des capacités de filtrage de vallée d'un défaut linéaire dans le graphène qui peut être introduit dans le graphène de manière contrôlée.

Ensuite, on examine le transport dans le graphène avec des adsorbats d'hydrogène réalistes, dont les configurations d'équilibre sont obtenues à l'aide de simulations de Monte Carlo. On trouve que la conductance du graphène augmente de manière significative lors de la formation de clusters d'adatoms d'hydrogène, formation dont on prédit l'occurrence spontanée à température ambiante. Cela est dû à la nature non-résonante d'une large fraction des clusters d'hydrogène dans la distribution à température ambiante, que l'on explique avec un modèle soluble analytiquement.

Finalement, on étudie le comportement, en termes de propriétés structurales et électroniques, du graphène à deux couches qui présentent un angle de pivotage entre eux, notamment, dans la limite où cet angle tend vers zéro. On trouve un angle critique en-dessous duquel le système s'ordonne dans un super réseau triangulaire de domaines avec empilement graphitique séparés par un réseau hexagonal de joints entre domaines avec empilement inéquivalent. La

Acknowledgements

présence de ces derniers est à la base de notre interprétation d'une expérience reportant des oscillations de la conductance électrique de graphène à deux couches sujet à indentation mécanique

Mots clés : graphène, graphène à deux couches, désordre, défauts topologiques, joints de grains, graphène hydrogéné, stacking domain boundaries, transport électronique, Landauer-Büttiker, fonctions de Green, Monte Carlo

Contents

Acknowledgements	i
Abstract	iii
Sommario	v
Résumé	vii
Introduction	1
1 The electronic structure of graphene	7
1.1 Electronic configuration of carbon atoms in graphene	7
1.2 The lattice	7
1.3 The tight-binding model for graphene	9
1.4 Dirac fermions	13
1.5 The tight-binding model for bilayer graphene	15
2 Electronic transport in graphene	21
2.1 Ballistic transport	21
2.1.1 Klein tunnelling	22
2.1.2 Universal minimal conductivity	25
2.2 Diffusive transport at high charge concentration	28
2.2.1 Phonon scattering	32
2.3 Anomalous Quantum Hall Effect	34
2.4 Anderson Localization	37
3 Defects in graphene	39
3.1 Introduction	39
3.2 Local defects	40
3.3 Topological defects	43
3.3.1 The topological defect hierarchy in graphene	44
3.3.2 Experimental studies of topological defects	46
3.3.3 Electronic transport in polycrystalline GBs	49
3.3.4 Stacking domain boundaries in bilayer graphene	52

4	Methods	55
4.1	Density functional theory	55
4.2	Minimization methods	59
4.2.1	Conjugate gradient	60
4.2.2	Fast Inertia Relaxation Engine (FIRE) method	63
4.3	LCBOP	64
4.4	Electronic transport	68
4.4.1	Drude theory of diffusive transport	68
4.5	Coherent vs. non-coherent transport	70
4.5.1	Landauer-Büttiker theory of coherent transport	71
4.5.2	Green's function method for the calculation of transmission	77
4.6	Monte Carlo method for thermodynamical averages	83
5	Electronic transport across grain boundaries in graphene	89
5.1	Electronic conductance across periodic grain boundaries	90
5.1.1	Introduction	90
5.1.2	Methods and models	91
5.1.3	Results and discussion	93
5.1.4	Conclusions	97
5.1.5	Additional calculations	98
5.2	Electronic transport across disordered grain boundaries	99
5.2.1	Introduction	99
5.2.2	Description of the work	99
5.2.3	Results and discussion	102
5.2.4	Conclusions	107
5.3	Controlled growth of a line defect in graphene with valley filtering properties .	110
5.4	Periodic grain boundaries in graphene on SiC substrate	113
6	Electronic Transport in Graphene with Hydrogen Adatoms	117
6.1	Electronic transport in graphene with aggregated hydrogen adatoms	118
6.1.1	Introduction	118
6.1.2	DFT study of effective hydrogen interaction	119
6.1.3	Equilibrium configuration of adsorbed hydrogen	120
6.1.4	Electronic spectrum	122
6.1.5	Electronic transport	123
6.1.6	Conclusions	126
6.1.7	Methodological details and additional calculations	126
6.1.7.a	First-principles calculations of the energies of hydrogen adatom clusters	126
6.1.7.b	Landauer-Büttiker electronic transport calculations and scaling analysis of conductivity	127
6.2	Resonant and non-resonant nature of cluster of vacancies in the honeycomb lattice	131

6.2.1 Preliminary theory	131
6.2.2 Single impurity	134
6.2.3 Impurity dimer	136
7 Stacking domain boundaries in bilayer graphene	139
7.1 Stacking domain boundaries in twisted bilayer graphene	140
7.1.1 Introduction	140
7.1.2 Simulation of low-angle Twisted Bilayer Graphene	141
7.1.3 Electronic structure	146
7.1.4 Conclusions	149
7.1.5 Methodological details and additional calculations	150
7.1.5.a DFT study of interlayer interaction in bilayer graphene	150
7.1.5.b Determination of the classical carbon-carbon potential	150
7.1.5.c Structural relaxations	152
7.1.5.d Electronic structure calculations	153
7.2 Electromechanical Oscillations in Bilayer Graphene	154
Outlook	161
Bibliography	180
Curriculum Vitae	181

Introduction

Graphene is the first truly two-dimensional material ever synthesized. It is one of the several allotropic forms of carbon, namely, a single layer of atoms arranged in a honeycomb lattice. The aim of this introduction is to retrace the fundamental steps that have led to the isolation of graphene, and to sketch briefly the state of the art of the research on graphene and its applications. Finally, I will summarize what has been my (humble) contribution to this immense scientific field.

One question should be addressed before diving into the Physics of graphene. What is the unfulfilled curiosity that has stimulated researchers to look for graphene over the years? My personal answer is that physicists like to play with dimensionality, namely, the number of space (or space-time) dimensions needed to describe a physical system. A common procedure taught in freshmen courses to approach a physical problem is to reduce its dimensionality by discarding non-relevant dimensions. We know, for example, that the orbit of a planet around the sun is planar because of angular momentum conservation, so that two spatial degrees of freedom are enough to describe it. In the 20th century, the first theories where dimensionality was enlarged rather than reduced entered the stage. One of the early attempts to unify Quantum Field Theory and General Relativity was made by Kaluza and Klein in the 20's, who conjectured the existence of a fourth unobservable spatial dimension. This prompted a multitude of modern unification theories based on a large number of rolled-up dimensions of the space-time (early Bosonic String Theory developed in the late 60's and early 70's had 25 spatial dimensions!). Perhaps, the acme of the "game of dimensions" was reached by 't Hooft and Veltman, who proposed to treat dimensionality in Quantum Field Theory as a continuous parameter in order to eliminate the divergences of certain Feynman integrals ("dimensional regularization"). Despite its audacity, this is an important technique of Quantum Field Theory and has been worth a Nobel Prize in 1999. Dimensionality has a fundamental role in universally accepted Physics theories. Although Newton's mechanics does not radically change with the dimensionality of the system under study, the same cannot be said about Classical Field Theories and is even less true for Quantum Mechanics, which offers a long list of dimensionality-dependent phenomena. Think of Bose-Einstein Condensation, Anderson Localization or the quantization of energy in presence of magnetic fields (Quantum Hall Effect), just to mention a few but outstanding examples.

This overview of the role of dimensionality in Physics serves to justify the efforts that have been

put in the realization of physical systems with non-trivial dimensionality. Of course, as it is unlikely that we will ever be able to realize a system with more than three spatial dimensions, research focused on systems with less than three dimensions. This challenge already started in the late 60s, as the improving techniques in semiconducting manufacturing allowed highly controlled fabrication of heterostructures. Devices such as quantum wells (based, for example, on AlAs/GaAs/AlAs heterostructures) and field-effect transistors (FET) operated in inversion mode confine electrons in a thin region of space with a thickness of the order of 10 nm, giving rise to what is called a two-dimensional electron gas (2DEG). Besides the strong technological implications that these devices have nowadays, especially for optical applications (diode lasers, infrared photodetectors, etc.), the study of the 2DEG has revealed rich and, sometimes, unexpected fundamental phenomena. Two examples are the Quantum Hall Effect and the ballistic propagation of charge carriers with ultra high mobilities.

And now we come to graphene. Clearly, the lower limit for the thickness of a condensed matter system is represented by a one-atom thick layer. In this respect, it has seemed natural to start from a well-known layered material such as graphite to isolate an individual layer of atoms, that is, graphene. Ironically, it seems that the isolation of graphene was achieved in 1969 [May, 1969], three years before the realization of the first heterostructure quantum well. Even more ironically, this was done by a theoretician, namely, John May. He analyzed low-energy diffraction data obtained by exposing a metal surface to hydrocarbons at high temperature (chemical vapor deposition) that had been published few years before [Hagstrom *et al.*, 1965; Lyon and Somorjai, 1967; Morgan and Somorjai, 1968]. These data remained unassigned until May suggested they had been originated by “monolayer graphite” deposited on a substrate. This had little notice until the 90’s, when several groups started wondering how to exfoliate graphite or to use other bottom-up approaches to produce graphene. One proof of this wide interest is the 1995 decision of the International Union of Pure Applied Chemistry to register the term “graphene” to define monolayer graphite. Two years later, Oshima and Nagashima reported on epitaxial growth of few-layer graphite samples, among which, probably, also monolayers [Oshima and Nagashima, 1997]. Anyway, the first unambiguous report of graphene isolation was published in 2004 by Novoselov and Geim [Novoselov *et al.*, 2004], who have received the Nobel Prize in 2010 for this discovery. The “Scotch taping” method they used to isolate graphene is at the same time simple and ingenious. By peeling the surface of a block of graphite with a piece of Scotch tape, they managed to obtain graphene flakes of micrometer size. Moreover, they built field-effect transistor devices based on graphene in order to provide a first characterization of the electronic transport properties of such a new material. The isolation of graphene proved that two-dimensional crystals actually exist, thus fostering an intense search for similar materials. This search has turned out to be very fruitful and at the time I am writing, several dozens of two-dimensional compounds have been already isolated spanning a large range of different physical properties (see Ref[Geim and Grigorieva, 2013] for a perspective about this field).

The scientific discoveries that have rapidly come out during the first years of the “graphene era” have been spectacular (see Ref. [Novoselov, 2011] for a review). First of all, it was confirmed the

theoretical prediction that the low-energy excitations of graphene are massless Dirac fermions with linear dispersion and zero-dimensional Fermi surface. A remarkable signature of such an unconventional nature is the Anomalous Quantum Hall Effect, found in experiments only one year after the discovery of graphene. Moreover, the charge carriers of graphene are endowed with the property of chirality, which protect them from backscattering and is responsible for their insensitiveness to electrostatic potential variations (Klein tunneling). This is one of the reasons for ballistic conduction of electrons in graphene over distances up to tens of micrometers. A related phenomenon is the Universal Minimal Conductivity, namely, graphene exhibits finite conductivity even at vanishing charge-carrier concentration. Here is a (perhaps non-exhaustive) list of the graphene records: besides being the material with the highest intrinsic mobility at room temperature reaching up to $10^6 \text{ cm}^2/(\text{V} \cdot \text{s})$ at low temperature, graphene has the highest known Young modulus (1 TPa), tensile strength for a crystal (130 GPa, stretching up to 25% of its length), thermal conductivity (5300 W/(m * K)), and it is one of the most impermeable material, as only protons pass across graphene's lattice.

Such a variety of amazing properties has made graphene very promising for applications (see Ref. [Novoselov *et al.*, 2012] for a review). Since its discovery there has been a large interest in field-effect transistors made of graphene, taking advantage of its high charge-carrier mobility. Analog transistors based on graphene in few years have reached a cut-off frequency about 300 GHz comparable to those based on inorganic III-V semiconductors, thus raising interest in radio-frequency applications. Unfortunately, the absence of bandgap makes intrinsic graphene not an ideal choice for digital transistors, since the on-off ratio in the best case is 3 orders of magnitude lower than what achieved with silicon. In this respect, the large effort spent to induce a bandgap in graphene has not given the expected results. Conceiving graphene as a conductor rather than a semiconductor is bringing to more promising applications, at least in the short term. For example, touch screen displays and LEDs might take big advantage of the simultaneous transparency and high charge-carrier mobility of graphene. These two properties, combined with an exceptional flexibility, are expected to enable the realization of rollable e-paper, flexible solar cells, etc. Yet, in digital electronics, graphene might be successfully employed for interconnects, or thermal dissipation. Prototypes of simple logic circuits where graphene is integrated with other two-dimensional layered materials have been already realized [Yu *et al.*, 2014]. Definitely, combining different two-dimensional materials in heterostructures will lead to unpredictable technological developments. Among the other innumerable applications of graphene that are being studied let us mention graphene ink, obtained from liquid exfoliation, for realizing conductive or anti-corrosion coating, combinations of graphene and carbon fibers to be used as reinforcement in constructions, chemical sensors that take advantage of graphene impermeability, etc. At the same time, we are assisting to a rapid evolution of graphene production techniques, whose scalability is crucial to turn graphene devices into commercial reality. At present, we count about a dozen different production techniques, though the scalable ones are many less. It is hard to say if and when graphene will replace another material in available technologies. The disruption and cost of changing established industrial processes will be justified only if the use of graphene will offer

Contents

significant improvements in terms of costs and technological performance. Most probably, graphene will realize its full potential in novel applications, such as flexible electronic devices, where no established competing material exists at the moment.

The main subject of this thesis is the theoretical study of electronic transport properties of graphene. As I hope to have efficiently conveyed, the investigation of electronic transport in graphene is motivated by both fundamental Physics and practical applications. Specifically, I have studied with computational techniques the effect of several types of defects on coherent transport of charge carriers in graphene.

The thesis is structured as follows: The first chapter is meant to provide the reader with the basic knowledge of the electronic structure of monolayer and bilayer graphene. The next two chapters have been conceived to motivate my almost four years of work in this field. The second chapter is a review of the phenomenology of electronic transport in graphene, in which I try to give equal relevance to the theoretical and experimental aspects. The main aim of this chapter is to discuss the scattering mechanisms that limit the electronic mobility of graphene charge carriers. The third chapter is an *excursus* on the various kinds of defects that are found in graphene, with a special focus on the experiments that imaged and systematically studied the defects. Moreover, I briefly review the early experimental and theoretical studies that have addressed the electronic transport properties of graphene in presence of grain boundaries. The fourth chapter is a review of the computational methods that I have employed to obtain the results presented in further chapters. This presentation is unavoidably limited to the fundamental concepts of all the methods (Density Functional Theory, Monte Carlo, classical potentials, minimization techniques, Landauer-Büttiker formalism). Differently, an extensive treatment would have required a thesis itself. Nevertheless, I hope to be able to convey at least the underlying physical ideas so that the reader can understand how I have employed these methods in my work. Chapters from five to seven present my original contribution to the field, whose authorship I share entirely with Prof. Oleg Yazyev and partially with Dr. Gabriel Autès. The fifth chapter is a collection of our studies about grain boundaries in graphene. First, I present an investigation of the coherent electronic transport across periodic grain boundaries based on Landauer-Büttiker theory. Second, I expose a study where I have employed a Monte Carlo technique to explore the configurational space of graphene grain boundaries in order to address the problem of electronic transport across disordered grain boundaries. In the last sections, I report on two projects carried out in collaboration with experimentalists. The first consists in the identification, based on *ab initio* simulations, of the atomic structure of periodic grain boundaries imaged by Scanning Tunneling Microscopy, whereas the second is an investigation of the valley-filtering capabilities of a line defect that can be controllably grown in graphene. In the sixth chapter, I present a study of the electronic transport in graphene with realistic hydrogen adsorbates, conducted by lifting the usual assumption of adatom diluteness. Importantly, the equilibrium distribution of hydrogen atoms are obtained by means of Monte Carlo simulations. The main results of the chapter, obtained employing computational techniques, are complemented by an analytic study of the resonant or non-resonant nature of cluster of hydrogen atoms adsorbed on graphene.

The works presented in the seventh and last chapter regards topological defects in bilayer graphene. I expose an investigation of the behavior of twisted bilayer graphene in the limit of zero twist angle, performed by means of large-scale simulations, and I link this system to a particular arrangement of stacking domain boundaries found in experiments. Finally, I review briefly an unexpected experimental finding of oscillations in the electrical conductance of bilayer graphene subjected to mechanical indentation. Supported by numerical calculations, we have provided an interpretation of this phenomenon that relies on the presence of stacking domain boundaries in the inspected samples.

1 The electronic structure of graphene

1.1 Electronic configuration of carbon atoms in graphene

The atomic number of carbon is $Z=6$ and its electronic configuration is $1s^2 2s^2 2p^2$. However, the four valence orbitals $2s$ and $2p_x, 2p_y, 2p_z$ often combine to form so-called hybrid orbitals. The hybridization found in layered carbon structures, such as graphene, is sp^2 that means that one $2s$ orbital and two $2p$ orbitals mix to form three hybrid sp^2 orbitals whose axes are contained into one plane (the xy plane, conventionally) and form three angles of 120° , see fig. 1.1(a). In layered crystals, the sp^2 orbitals of the carbon atoms couple to each other to form the σ (bonding) band and the σ^* (antibonding) band. The states of the σ band are responsible for the strong planar covalent bond between carbon atoms in graphene. The fourth p electron of each carbon atom (p_z , conventionally) is oriented orthogonally to the crystal plane and forms the π and π^* bands due to the weaker coupling with its neighbor p_z orbitals.

Both in graphene and graphite, the π and π^* bands touch each other at the Fermi level, whereas the σ and σ^* bands are separated by a gap of $\simeq 6$ eV, see fig. 1.1(b). The stacking of several graphene layers is enabled by the weak van der Waals interaction arising from dynamical correlations of π electrons in neighbor layers, thus making xy planes natural cleavage planes. This property of graphite can be experienced whenever a pencil is rubbed over a sheet of paper, where it leaves a stroke made of graphitic layers cleaved from the lead. Importantly, the cleavability of graphite is also the reason why individual graphene layers can be singled out of a graphitic surface by scotch taping [Novoselov *et al.*, 2004].

1.2 The lattice

sp^2 carbon atoms in graphene are arranged in a two-dimensional honeycomb lattice, see Fig. 1.2(a). This consists in an equilateral triangular lattice with two atoms per cell. The vectors which define the periodicity of the lattice are $\mathbf{a}_1 = a/2(3, \sqrt{3})$ and $\mathbf{a}_2 = a/2(3, -\sqrt{3})$ where $a = 1.42\text{\AA}$ is the carbon-carbon bondlength. \mathbf{a}_1 and \mathbf{a}_2 form a 60° angle, whence the equilateral triangular lattice. The area of the unit cell is $A_s = |\mathbf{a}_1| |\mathbf{a}_2| \sqrt{3}/2 = 3\sqrt{3}a/2$. The two atoms in the

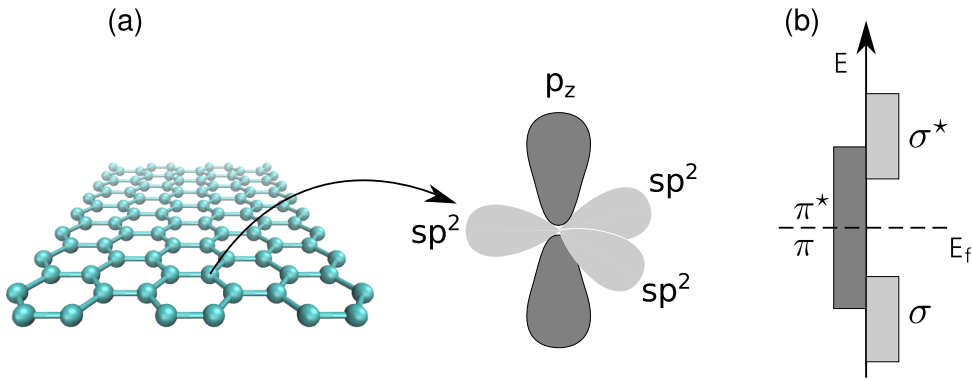


Figure 1.1 – sp^2 hybridization of carbon atoms. (a) The three sp^2 states are contained in the layer plane, whereas the p_z atomic orbital is perpendicular to the crystal plane. (b) Sketch of the σ and π bands. Bonding and antibonding bands π and π^* cover a continuous energy range which crosses the Fermi energy E_f . Differently, bonding and antibonding bands σ and σ^* are separated by an energy gap and are far from the Fermi energy.

unit cell (often labeled A and B) are identical and define two equivalent triangular sublattices. This equivalency is at the basis of what is called the “bipartite lattice symmetry”.

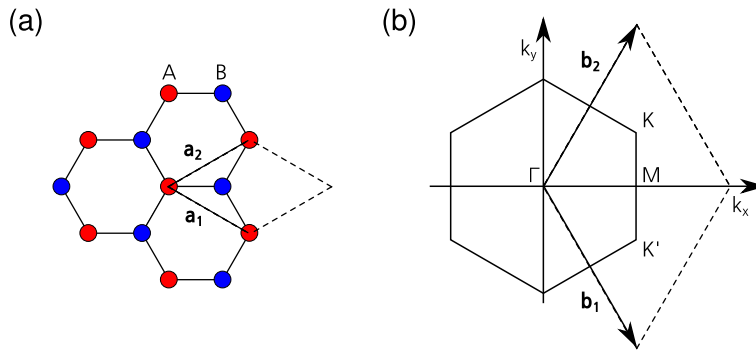


Figure 1.2 – (a) Graphene 2D honeycomb lattice. Atoms owing to different sublattices are shown in different colors. The lattice vectors \mathbf{a}_1 and \mathbf{a}_2 and the unit cell (dashed line) are shown. (b) First Brillouin zone of the 2D honeycomb lattice. The reciprocal vectors \mathbf{b}_1 and \mathbf{b}_2 and the primitive cell (dashed line) are shown. The high symmetry points Γ , M, K and K' are indicated.

The primitive vectors of the reciprocal space \mathbf{b}_1 and \mathbf{b}_2 are found according to the rule $\mathbf{a}_i \cdot \mathbf{b}_j = 2\pi\delta_{ij}$, giving $\mathbf{b}_1 = 2\pi/3a(1, -\sqrt{3})$ and $\mathbf{b}_2 = 2\pi/3a(1, \sqrt{3})$. The Brillouin zone (BZ), defined as the set of those points which are closest to the center the reciprocal space than to any other vector $m\mathbf{b}_1 + n\mathbf{b}_2$ with $(m, n) \neq (0, 0)$, is an hexagon, as shown in Fig. 1.2(b). The area of the BZ is derived from that of the unit cell of the direct lattice as $A_{BZ} = (2\pi)^2 / A_S$. Although the BZ contains six vertices, only two are inequivalent, $K = 2\pi/3a(1, \sqrt{3})$ and $K' = 2\pi/3a(1, -\sqrt{3})$, since each vertex is shared among the BZ and two of its periodic replicas. As will be shown in Section 1.3, the low-energy Physics of graphene takes place at points K and K' .

1.3. The tight-binding model for graphene

The addition of a second layer gives rise to the system called “bilayer graphene”, see Fig. 1.3(a-b). Both the direct and the reciprocal lattice stay unaltered, but an additional degree of freedom is needed to exhaustively define its geometry: the stacking vector $\Delta\mathbf{u}$. This is defined as the in-plane component of the rigid shift of one layer with respect to another. In the stable configuration called AB stacking, one layer is in-plane shifted with respect to the opposite layer by one bond-length, as shown in Fig. 1.3(a). As a consequence, two atoms of the unit cell lying in opposite layers are on top of each other, whereas the other two atoms are misaligned. On the contrary, in the AA stacking there is no in-plane shift and all atoms of one layer are aligned to their equivalent in the opposite layer, see Fig. 1.3(b). The interlayer distance for AB bilayer graphene is $\Delta z_{AB} = 3.4 \text{ \AA}$, whereas for AA stacking is $\Delta z_{AA} = 3.6 \text{ \AA}$. Graphite is a periodic stacking of graphene layers, which in the low-energy structural configuration follow the pattern *ABABAB...*, see Fig. 1.3(c) (Ref. [Bernal, 1924; Dresselhaus and Dresselhaus, 2002]). The additional crystal axis in the stacking direction, denoted as c , has a length 6.7 \AA , approximately twice as long as Δz_{AB} .

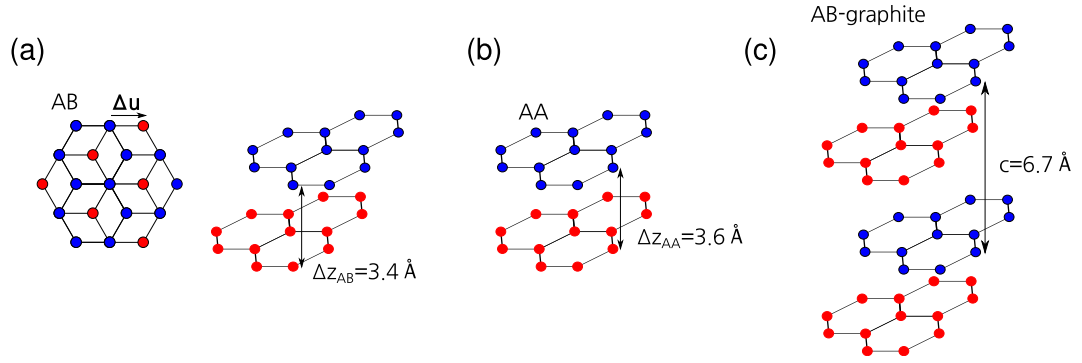


Figure 1.3 – Structure of bilayer graphene and graphite. (a) Planar and three-dimensional ball-and-stick representation of AB bilayer graphene. (b) Three-dimensional representation of AA bilayer graphene. (c) Three-dimensional representation of AB graphite.

The stacking order has a strong effect on the electronic structure of bilayer graphene and, in general, on multilayer graphene.

1.3 The tight-binding model for graphene

The tight-binding (TB) model of graphene was introduced for the first time in 1947 in the context of a description of the low-energy band structure of graphite [Wallace, 1947]. Later, several refinements to the original model have been introduced, ending up into the Slonczewski-Weiss-McClure model [Slonczewski and Weiss, 1958; McClure, 1957, 1960].

As seen in the previous section, σ and σ^* bands are further in energy than π and π^* bands. Moreover, since p_z orbitals are odd with respect to a planar mirror symmetry, their coupling with sp^2 -orbitals, which are even, is zero. For this reasons, the description of the low-energy excitations in graphene can be limited to p_z orbitals. The minimal TB Hamiltonian only

Chapter 1. The electronic structure of graphene

considers first-neighbor coupling between p_z orbitals [Wallace, 1947; Slonczewski and Weiss, 1958; Pisanty, 1991]:

$$H = -t \sum_{\langle i,j \rangle} a_i^\dagger b_j + b_i^\dagger a_j \quad (1.1)$$

where the operators $a_i^\dagger (b_i^\dagger)$ and $a_i (b_i)$, respectively, create or annihilate a p_z -electron at the i -th site in the A(B) sublattice. The only non-zero matrix element t couples first-neighbor atoms in opposite sublattices and is invariant due to translational and sublattice symmetry. The estimates for t vary in the range [2.5, 3.2] eV [Castro Neto *et al.*, 2009; Dresselhaus and Dresselhaus, 2002; Das Sarma *et al.*, 2011; Foa Torres *et al.*, 2014; Slonczewski and Weiss, 1958]. Throughout the present thesis, we assume $t = 2.7$ eV, unless explicitly stated otherwise. We further assume that p_z -orbitals form an orthogonal set, that is, we neglect the overlap $\langle p_i | p_j \rangle$ between distinct atoms.

Since the system is periodic, we can define creation and annihilation operators in reciprocal space:

$$a_{\mathbf{k}} = \frac{1}{\sqrt{N_{\text{cell}}}} \sum_i e^{-i\mathbf{R}_i \mathbf{k}} a_i \quad b_{\mathbf{k}} = \frac{1}{\sqrt{N_{\text{cell}}}} \sum_i e^{-i\mathbf{R}_i \mathbf{k}} b_i \quad (1.2a)$$

$$a_{\mathbf{k}}^\dagger = \frac{1}{\sqrt{N_{\text{cell}}}} \sum_i e^{i\mathbf{R}_i \mathbf{k}} a_i^\dagger \quad b_{\mathbf{k}}^\dagger = \frac{1}{\sqrt{N_{\text{cell}}}} \sum_i e^{i\mathbf{R}_i \mathbf{k}} b_i^\dagger, \quad (1.2b)$$

where \mathbf{k} varies in the BZ and N_{cell} is the total number of unit cells composing the system. Eventually, the limit $N_{\text{cell}} \rightarrow \infty$ will be taken. Eqs. 1.2a and 1.2b can be inverted, giving

$$a_i = \frac{1}{\sqrt{N_{\text{cell}}}} \sum_{\mathbf{k}} e^{i\mathbf{R}_i \mathbf{k}} a_{\mathbf{k}} \quad b_i = \frac{1}{\sqrt{N_{\text{cell}}}} \sum_{\mathbf{k}} e^{i\mathbf{R}_i \mathbf{k}} b_{\mathbf{k}} \quad (1.3a)$$

$$a_i^\dagger = \frac{1}{\sqrt{N_{\text{cell}}}} \sum_{\mathbf{k}} e^{-i\mathbf{R}_i \mathbf{k}} a_{\mathbf{k}}^\dagger \quad b_i^\dagger = \frac{1}{\sqrt{N_{\text{cell}}}} \sum_{\mathbf{k}} e^{-i\mathbf{R}_i \mathbf{k}} b_{\mathbf{k}}^\dagger. \quad (1.3b)$$

By substituting eqs. 1.3a into eq. 1.1, H can be expressed as

$$H = -\frac{t}{N_{\text{cell}}} \sum_{\mathbf{k}} \sum_{\mathbf{k}'} \sum_{\langle i,j \rangle} \left(e^{-i\mathbf{k}\mathbf{R}_i} e^{i\mathbf{k}'\mathbf{R}_j} a_{\mathbf{k}}^\dagger b_{\mathbf{k}'} + e^{-i\mathbf{k}\mathbf{R}_i} e^{i\mathbf{k}'\mathbf{R}_j} b_{\mathbf{k}}^\dagger a_{\mathbf{k}'} \right) = \\ -\frac{t}{N_{\text{cell}}} \sum_{\mathbf{k}} \sum_{\mathbf{k}'} \sum_{\langle i,j \rangle} \left(e^{-i(\mathbf{k}-\mathbf{k}')\mathbf{R}_i} e^{i\mathbf{k}(\mathbf{R}_j-\mathbf{R}_i)} a_{\mathbf{k}}^\dagger b_{\mathbf{k}'} + e^{-i(\mathbf{k}-\mathbf{k}')\mathbf{R}_i} e^{i\mathbf{k}(\mathbf{R}_j-\mathbf{R}_i)} b_{\mathbf{k}}^\dagger a_{\mathbf{k}'} \right). \quad (1.4)$$

At this point we exploit the identity $e^{-i(\mathbf{k}-\mathbf{k}')\mathbf{R}_i} = N_{\text{cell}} \delta_{\mathbf{k}\mathbf{k}'}$ and notice from Fig. 1.2(a) that the vectors $\mathbf{R}_j - \mathbf{R}_i$ connecting the cell of one atom in A(B) sublattice to those of its neighbors are 0 , $-\mathbf{a}_1$ (\mathbf{a}_1) and $-\mathbf{a}_2$ (\mathbf{a}_2). Hence, we have

$$H = \begin{pmatrix} a_{\mathbf{k}}^\dagger \\ b_{\mathbf{k}'}^\dagger \end{pmatrix} \mathcal{H}(\mathbf{k}) \begin{pmatrix} a_{\mathbf{k}} & b_{\mathbf{k}} \end{pmatrix} \quad (1.5a)$$

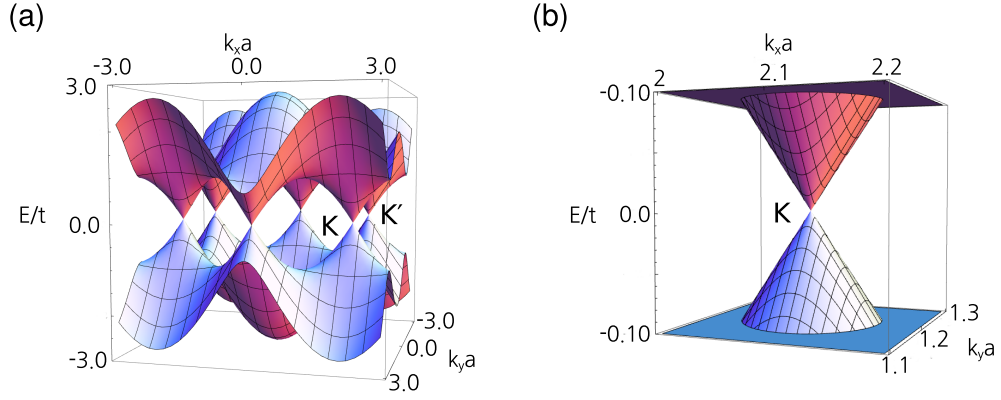


Figure 1.4 – Energy spectrum of the first-neighbor TB model graphene. In panel (b) the spectrum is zoomed around the K point.

$$\mathcal{H}(\mathbf{k}) = -t \begin{pmatrix} 0 & f^*(\mathbf{k}) \\ f(\mathbf{k}) & 0 \end{pmatrix}, \quad (1.5b)$$

where the function $f(\mathbf{k})$ is defined as

$$f(\mathbf{k}) = 1 + e^{ika_1} + e^{ika_2}. \quad (1.6)$$

The peculiar form of Hamiltonian 1.5b is a consequence of the so-called “bipartite symmetry” of the graphene lattice, which express the fact that electrons of one sublattice only couple with electrons of the opposite sublattice. The eigenvalues of $\mathcal{H}(\mathbf{k})$ are given by

$$E_{\pm}(\mathbf{k}) = \pm t |f(\mathbf{k})| = \pm t \sqrt{3 + 2 \cos(\sqrt{3}k_y a) + 4 \cos\left(\frac{\sqrt{3}}{2}k_y a\right) \cos\left(\frac{3}{2}k_y a\right)}. \quad (1.7)$$

The existence of two bands symmetric with respect to $E = 0$ is a direct consequence of the bipartite symmetry and goes under the name of electron-hole symmetry. Given the spin degeneracy of each band, the Fermi energy E_f for an undoped system lies exactly at zero.

It can be verified that the two bands touch at K and K' (and only at these points) where the energy $E_{\pm}(\mathbf{k} = \mathbf{K}) = E_{\pm}(\mathbf{k} = \mathbf{K}') = E_f = 0$, see Fig. 1.4. As a consequence, no gap separates the valence and conductance band, although the Fermi surface, rather than being a one-dimensional object, reduces to a set of two inequivalent points. For this peculiarity graphene is identified as a semi-metal or a zero-gap semiconductor.

To first order approximation, the dispersion of low-energy states is linear. For low momentum $\mathbf{q} = \mathbf{k} - \mathbf{K}$ with $|\mathbf{q}| \ll |\mathbf{K}|$ eq. 1.7 can be Taylor expanded as

$$E_{\pm}(\mathbf{q}) = E_{\pm}(\mathbf{K}) + \left. \frac{\partial E_{\pm}}{\partial \mathbf{k}} \right|_{\mathbf{k}=\mathbf{K}} \cdot \mathbf{q} + \mathcal{O}\left(\left(\frac{q}{K}\right)^2\right) \simeq \pm \hbar v_f |\mathbf{q}| + \mathcal{O}\left(\left(\frac{q}{K}\right)^2\right), \quad (1.8)$$

Chapter 1. The electronic structure of graphene

with the Fermi velocity $v_f = 3ta/2\hbar \simeq 10^6$ m/s. Eq. 1.8 means that the low-energy excitations of graphene are described by massless quasiparticles with linear dispersion and constant Fermi velocity. This represents one of the most striking differences between graphene and ordinary semiconductors. Though not immediately recognized with graphene's discovery, the peculiar nature of low-energy excitation has been demonstrated in 2005 [Novoselov *et al.*, 2005; Zhang *et al.*, 2005] (remarkably, graphene was initially proposed to have a tiny overlap between valence and conduction bands [Novoselov *et al.*, 2004]).

An expansion up to quadratic terms of eq. 1.7 leads to an angle dependent distortion of the dispersion cone called "trigonal warping" (from the angular periodicity of $2\pi/3$) [Ando *et al.*, 1998; Dresselhaus and Dresselhaus, 2002; Castro Neto *et al.*, 2009]:

$$E_{\pm}(\mathbf{q}) = \pm \hbar v_f |\mathbf{q}| \pm \frac{3ta^2}{8} \sin(3\theta_{\mathbf{q}}) |\mathbf{q}|^2 + \mathcal{O}((q/K)^3) \quad (1.9)$$

where $\theta_{\mathbf{q}} = \arctan(q_y/q_x)$.

The density of states (DOS) $\rho(E) = \int_{\text{BZ}} \sum_n \delta(E - E_{\mathbf{k}}^n) d\mathbf{k}$, where the index $n = 1, 2$ runs over the two bands of the present model, is shown in Fig. 1.5(a,c). Due to electron-hole symmetry $\rho(E)$ is an even function of the energy. As a consequence of the low-energy linear dispersion eq. 1.8, $\rho(E)$ can be approximated around $E = 0$ as

$$\rho(E) \simeq \frac{4A_S}{2\pi} \frac{|E|}{(\hbar v_f)^2}. \quad (1.10)$$

The exact analytic expression of $\rho(E)$ can be found in Ref. [Castro Neto *et al.*, 2009]

The inclusion of coupling terms beyond first neighbors leads to a breakdown of the bipartite symmetry since diagonal terms appear in $\mathcal{H}(\mathbf{k})$. The inclusion of second-neighbor terms defines the Hamiltonian

$$H = -t \sum_{\langle i,j \rangle} a_i^\dagger b_j + b_i^\dagger a_j - t' \sum_{\langle\langle i,j \rangle\rangle} a_i^\dagger a_j + b_i^\dagger b_j. \quad (1.11)$$

As there is no established consensus about the value of t' , we just state the most likely range $0.02t < t' < 0.25t$ [Reich *et al.*, 2002; Grüneis *et al.*, 2008; Dresselhaus and Dresselhaus, 2002]. By applying Fourier transform, eq. 1.11 becomes

$$\mathcal{H}(\mathbf{k}) = -t \begin{pmatrix} \frac{t'}{t} g(\mathbf{k}) & f^*(\mathbf{k}) \\ f(\mathbf{k}) & \frac{t'}{t} g(\mathbf{k}) \end{pmatrix}, \quad (1.12)$$

where $g(\mathbf{k}) = \sum_{\langle\langle i,j \rangle\rangle} e^{i\mathbf{k}(\mathbf{R}_j - \mathbf{R}_i)}$. Therefore, the spectrum contains a momentum-dependent correction proportional to t'/t :

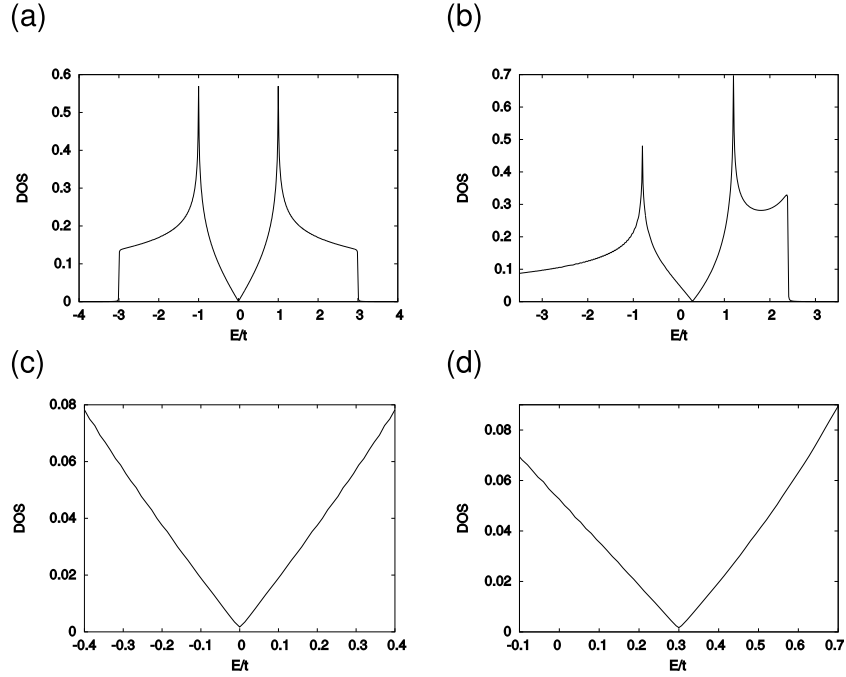


Figure 1.5 – Density of states of graphene as a function of energy calculated within the TB model. Panel (a) refers to the first-neighbor Hamiltonian defined in eq. 1.1. Panel (b) refers to the Hamiltonian defined in eq. 1.11, including up to second neighbor interaction ($t'/t = 0.1$). Panels (c-d) show the same as panels (a-b) zooming in the energy range $[-0.4, 0.4] t$. Energies are expressed in units of t .

$$E(\mathbf{k}) = \pm t \left[\sqrt{3 + 2 \cos(\sqrt{3}k_y a) + 4 \cos\left(\frac{\sqrt{3}}{2}k_y a\right) \cos\left(\frac{3}{2}k_y a\right)} - \frac{t'}{t} \left(2 \cos(\sqrt{3}k_y a) + 4 \cos\left(\frac{\sqrt{3}}{2}k_y a\right) \cos\left(\frac{3}{2}k_y a\right) \right) \right]. \quad (1.13)$$

As shown in Fig. 1.5(b,d), for a finite ratio t'/t the density of states $\rho(E)$ is no longer electron-hole symmetric and the Fermi energy is shifted to $E_f = 3t'/t$. Nevertheless, the low-energy linear dispersion (eq. 1.8) stays unaltered as the first non-vanishing momentum-dependent correction is proportional to $|\mathbf{q}|^2$.

1.4 Dirac fermions

The fact that low-energy excitation in graphene are akin to massless Dirac particles was found in 1984 [Semenoff, 1984]. The Hamiltonian defined in eq. 1.5b is an operator acting in the 2×2 sublattice space containing momentum \mathbf{k} as a parameter. Given that the three Pauli matrices

$\{\sigma_i\}_{i=x,y,z}$ complemented by the identity σ_0 :

$$\sigma_x = \begin{Bmatrix} 0 & 1 \\ 1 & 0 \end{Bmatrix}, \quad \sigma_y = \begin{Bmatrix} 0 & -i \\ i & 0 \end{Bmatrix}, \quad \sigma_z = \begin{Bmatrix} 1 & 0 \\ 0 & -1 \end{Bmatrix}, \quad \sigma_0 = \begin{Bmatrix} 1 & 0 \\ 0 & 1 \end{Bmatrix} \quad (1.14)$$

represent a basis for the 2×2 matrix space, eq. 1.5b can be expressed as

$$\mathcal{H}(\mathbf{k}) = \text{Re}f(\mathbf{k})\sigma_1 + \text{Im}f(\mathbf{k})\sigma_2. \quad (1.15)$$

The function $f(\mathbf{k} = \mathbf{K} + \mathbf{q})$ can be expanded for $|\mathbf{q}| \ll |\mathbf{K}|$ as

$$f(\mathbf{K} + \mathbf{q}) = -\frac{3}{2}a(iq_x + q_y) + \mathcal{O}\left((q/K)^2\right), \quad (1.16)$$

whence

$$\mathcal{H}(\mathbf{k} = \mathbf{K} + \mathbf{q}) = \hbar v_f (-q_y \sigma_x + q_x \sigma_y). \quad (1.17)$$

Performing a unitary transformation in sublattice space, the Hamiltonian can be rewritten as

$$\mathcal{H}(\mathbf{k} = \mathbf{K} + \mathbf{q}) = \hbar v_f (q_x \sigma_x + q_y \sigma_y) = \hbar v_f \mathbf{q} \cdot \boldsymbol{\sigma} \quad \boldsymbol{\sigma} = (\sigma_x, \sigma_y), \quad (1.18)$$

where the linear dispersion is evident. To express the last equation in real space, it suffices to replace momentum \mathbf{q} by the operator $\hat{\mathbf{p}} = -i\vec{\nabla}$:

$$H_K = \hbar v_f \hat{\mathbf{p}} \cdot \boldsymbol{\sigma} = -i\hbar v_f \vec{\nabla} \cdot \boldsymbol{\sigma}. \quad (1.19)$$

As the Hamiltonian defined in eq. 1.18 is valid for small momenta \mathbf{q} or, equivalently, long wavelength, the real space Hamiltonian 1.19 describes electrons over lengths larger than the lattice spacing, disregarding features at the atomic level. In other words, the Dirac equation only allows for a continuous description of graphene low-energy excitations. In the vicinity of \mathbf{K}' the low-energy Hamiltonian is obtained by the substitution $q_y \rightarrow -q_y$ in eq. 1.18, thus obtaining

$$\mathcal{H}(\mathbf{k} = \mathbf{K}' + \mathbf{q}) = \hbar v_f (q_x \sigma_x - q_y \sigma_y) = \hbar v_f \mathbf{q} \cdot \boldsymbol{\sigma}^* \quad \boldsymbol{\sigma}^* = (\sigma_x, -\sigma_y) \quad (1.20)$$

and the corresponding real-space Hamiltonian

$$H_K = \hbar v_f \hat{\mathbf{p}} \cdot \boldsymbol{\sigma}^* = -i\hbar v_f \vec{\nabla} \cdot \boldsymbol{\sigma}^*. \quad (1.21)$$

Equations 1.18 and 1.20 are two realizations of the Dirac equation for massless relativistic particles in two dimensions. It is worth stressing that the role of spin in the original Dirac equation is played here by the sublattice degree of freedom, called ‘‘pseudospin’’ for this reason.

1.5. The tight-binding model for bilayer graphene

In fact, the wavefunction in momentum space in proximity of K is a two-component spinor:

$$\Psi_{\pm, \mathbf{k}}(\mathbf{q}) = \frac{1}{\sqrt{2}} \begin{pmatrix} e^{i\theta_{\mathbf{q}}/2} \\ \pm e^{-i\theta_{\mathbf{q}}/2} \end{pmatrix}, \quad (1.22)$$

where the \pm sign refers, respectively, to the conduction and the valence band and $\theta_{\mathbf{q}}$ is the same angle appearing in 1.9. In proximity of K' the wavefunction is $\Psi_{\pm, K'}(\mathbf{q}) = \Psi_{\pm, K}^*(\mathbf{q})$, as K and K' are connected by time-reversal symmetry. Finally, as a spinor, the wavefunction 1.22 acquires a phase of π (that is, changes sign) upon a rotation of 2π in the sublattice space.

The Dirac Hamiltonian (eq. 1.15) is proportional to the chirality operator, that is, the projection of pseudospin along the momentum direction

$$\hat{h} = \frac{\hat{\mathbf{p}}}{|\mathbf{p}|} \cdot \boldsymbol{\sigma}. \quad (1.23)$$

Therefore, chirality is a good quantum number and the wavefunction 1.22 is an eigenstate of the operator \hat{h} with eigenvalue $+1$ (-1) for conduction (valence) band, meaning that its momentum is parallel (antiparallel) to its pseudospin. At K' the eigenvalues of the chirality for valence and conduction band are inverted. Although the nature of pseudospin hardly allows a geometrical representation, chirality has a profound consequence on many of the electronic properties of graphene such as the *absence of backscattering* in pristine graphene, a phenomenon previously discussed in the context of carbon nanotubes [Ando *et al.*, 1998]. In order to reverse its momentum (i.e. changing $\mathbf{p} \rightarrow -\mathbf{p}$), a chiral charge carrier needs to flip its pseudospin, otherwise chirality would not be conserved. This means that backscattering is forbidden, unless a term capable of inducing a pseudospin flip is added to the Hamiltonian.

The two valley K and K' can be treated independently in all those situations where intervalley scattering can be neglected. In this case, the full Hamiltonian is the tensor product of the two single-valley Hamiltonians:

$$H = H_K \otimes H_{K'} \quad (1.24)$$

and the full wavefunction is the four-component object $(\Psi_K, \Psi_{K'})^t$ (bispinor). The valley degree of freedom $\xi = \pm 1$, respectively, for K and K' , can be treated similarly to pseudospin. Given three Pauli-like matrices $\{\tau_i\}_{i=x,y,z}$ and the identity τ_0 acting in the 2×2 space of valley, H can be expressed as [Mesaros *et al.*, 2009]

$$H = \hbar v_f (\hat{p}_x \cdot \boldsymbol{\sigma}_x \otimes \tau_0 + \hat{p}_y \cdot \boldsymbol{\sigma}_y \otimes \tau_z). \quad (1.25)$$

1.5 The tight-binding model for bilayer graphene

The minimal coupling between two graphene layers in the TB description takes into account a single interlayer hopping parameter γ_1 between two atoms that have the same in-plane

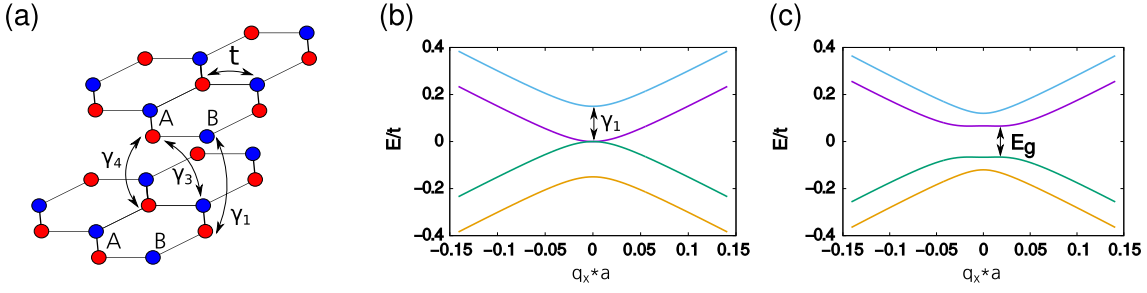


Figure 1.6 – TB model for bilayer graphene. (a) Schematic representation of the hopping terms defining the TB model of bilayer graphene with AB stacking. Atoms in different colors belong to opposite sublattices. (b-c) Band structure obtained with the minimal coupling model ($\gamma_1 = 0.15t$, $\gamma_3 = \gamma_4 = 0$) for (b) intrinsic bilayer graphene and (c) bilayer graphene in presence of a layer symmetry breaking term $V = 0.1t$.

coordinates (also said to form a “dimer”), as shown in fig. 1.6(a) [McCann and Fal’ko, 2006; McCann and Koshino, 2013; Castro Neto *et al.*, 2009; Das Sarma *et al.*, 2011]. A commonly accepted value of γ_1 is $\approx 0.15t$ [Dresselhaus and Dresselhaus, 2002; Grüneis *et al.*, 2008]. The additional hopping terms illustrated in fig. 1.6(a) have typical values $\gamma_3 \approx 0.12t$ and $\gamma_4 \approx 0.015t$. However, their effect on the electronic structure is relatively less important than that of γ_1 . In particular, the effect of γ_4 is very small and will not be discussed in the present section [McCann and Koshino, 2013; Castro Neto *et al.*, 2009].

Because of the misalignment between the layers, γ_1 couples two atoms of the same unit cell but in opposite sublattices, thus preserving electron-hole symmetry. The wavefunction in reciprocal space is the four-component spinor $\psi = (\psi_{A1}, \psi_{A2}, \psi_{B1}, \psi_{B2})$ where subscripts 1, 2 identify each layer. Once introduced the operator $\Psi_{\mathbf{k}} = (a_{1\mathbf{k}}, b_{1\mathbf{k}}, a_{2\mathbf{k}}, b_{2\mathbf{k}})$, the TB Hamiltonian is [McCann and Koshino, 2013; Castro Neto *et al.*, 2009]

$$H = \hat{\Psi}_{\mathbf{k}}^\dagger \begin{pmatrix} 0 & -tf^*(\mathbf{k}) & 0 & 0 \\ -tf(\mathbf{k}) & 0 & -\gamma_1 & 0 \\ 0 & -\gamma_1 & 0 & -tf^*(\mathbf{k}) \\ 0 & 0 & -tf(\mathbf{k}) & 0 \end{pmatrix} \hat{\Psi}_{\mathbf{k}}, \quad (1.26)$$

where the interlayer coupling is momentum independent because it couples atoms in the same unit cell. The resulting four bands follow the dispersion relations

$$E^2(\mathbf{k}) = t^2 |f(\mathbf{k})|^2 + \frac{\gamma_1^2}{2} \pm \sqrt{\left(\frac{\gamma_1^2}{2}\right)^2 + \gamma_1^2 t^2 |f(\mathbf{k})|^2}, \quad (1.27)$$

which are plotted in Fig. 1.6(b). The two lower-energy bands obtained from eq. 1.27 touch at $\mathbf{k} = \mathbf{K}, \mathbf{K}'$ where $E(\mathbf{k} = \mathbf{K}/\mathbf{K}') = 0$, meaning that intrinsic bilayer graphene is a gapless system as its monolayer counterpart. For the two higher-energy bands $E(\mathbf{k} = \mathbf{K}/\mathbf{K}') = \pm\gamma_1$. In the region

1.5. The tight-binding model for bilayer graphene

of reciprocal space where $|\mathbf{q}| = |K|$, we have $|f(\mathbf{k})| \simeq \hbar v_f q$ and, therefore,

$$E^2(\mathbf{q}) \simeq (\hbar v_f q)^2 + \frac{\gamma_1^2}{2} \pm \sqrt{\left(\frac{\gamma_1^2}{2}\right)^2 + \gamma_1^2 (\hbar v_f q)^2} \quad (1.28)$$

which can be further approximated for the two lowest bands by the quadratic dispersion $E(\mathbf{q}) = \pm v_f^2 q^2 / \gamma_1$ in the regime $q \ll \gamma_1 / \hbar v_f$. For larger q such that $\gamma_1 / \hbar v_f \ll |q| \ll |K|$ the dispersion approaches the linear function $E(\mathbf{q}) = \sqrt{1 - \gamma_1 / t} \hbar v_f q$. In this regime, the effect of the finite interlayer coupling γ_1 reduces to a renormalization of the monolayer graphene Fermi velocity.

If the two layers are kept at a different chemical potential - for example, as a consequence of an applied constant electric field orthogonal to the layers - without loss of generality we can assume that the layers have opposite chemical potentials $\mu_1 = V$ and $\mu_2 = -V$. This can be achieved by conveniently setting the origin of the energy scale. If the imbalance is due to a constant transverse electric field of intensity ϵ , we would have $\mu_1 - \mu_2 = 2V = \epsilon \Delta z$. Therefore, non-zero diagonal elements must be included in the Hamiltonian [McCann, 2006]:

$$H = \hat{\Psi}_{\mathbf{k}}^\dagger \begin{pmatrix} V & -t f^*(\mathbf{k}) & 0 & 0 \\ -t f(\mathbf{k}) & V & -\gamma_1 & 0 \\ 0 & -\gamma_1 & -V & -t f^*(\mathbf{k}) \\ 0 & 0 & -t f(\mathbf{k}) & -V \end{pmatrix} \hat{\Psi}_{\mathbf{k}} \quad (1.29)$$

In this situation, the dispersion law is

$$E^2(\mathbf{k}) = V^2 + |f(\mathbf{k})|^2 + \frac{\gamma_1^2}{2} \pm \sqrt{\left(\frac{\gamma_1^2}{2}\right)^2 + \gamma_1^2 |f(\mathbf{k})|^2 + 4V^2 |f(\mathbf{k})|^2} \quad (1.30)$$

which is still electron-hole symmetric but has a gap at K and K' , see Fig. 1.6(b). For small momenta \mathbf{q} and $V \ll \gamma_1$ eq. 1.30 can be expanded as

$$E(\mathbf{k}) = \pm \left(V - \frac{2V}{\gamma_1^2} (\hbar v_f q)^2 + \frac{(\hbar v_f q)^4}{2\gamma_1^2 V} \right), \quad (1.31)$$

which has an energy gap $E_g = 2V(1 - 2V^2/\gamma_1^2)$ at momentum \mathbf{q}_g such that $q_g^2 = 2V^2 / (\hbar v_f)^2$. Experiments have demonstrated the possibility to induce a tunable band gap in double-gate bilayer graphene field effect transistors, where the potential of the two layers can be changed independently [Castro *et al.*, 2007]. Previous experiments on epitaxial bilayer graphene samples grown on SiC exploited the dipole field generated in the depletion layers of the SiC surface to break the sublattice symmetry and induce a gap [Ohta *et al.*, 2006].

The inclusion of finite hopping γ_3 between “non-dimer” atoms couples different unit cells, see Fig. 1.6, and modifies the bilayer graphene Hamiltonian as follows [McCann and Fal’ko,

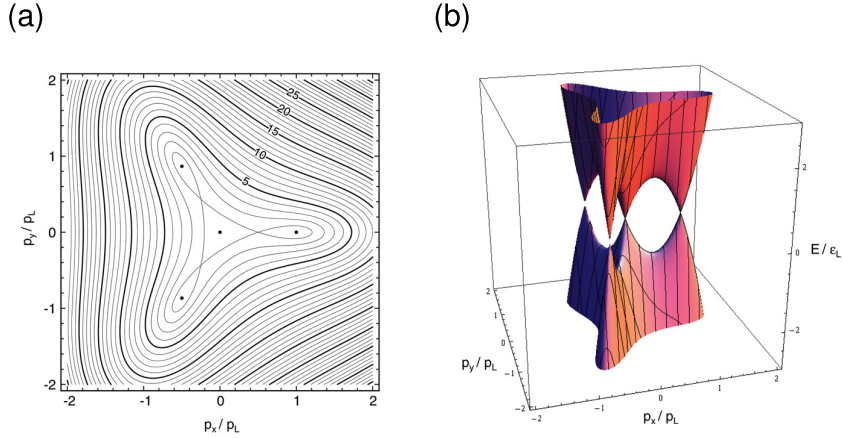


Figure 1.7 – Low-energy bands obtained by solving Hamiltonian 1.32 including a finite γ_3 . (a) Isoenergetic lines drawn in proximity of the K point, with energy (momenta) expressed in units of ϵ_L (p_L). (b) Three-dimensional representation of the low-energy dispersion. Reproduced with permission from Ref. [McCann and Koshino, 2013], ©2013 IOP Publishing.

2006; Castro Neto *et al.*, 2009]:

$$H = \Psi_{\mathbf{k}}^\dagger \begin{pmatrix} 0 & -tf^*(\mathbf{k}) & 0 & -\gamma_3 f(\mathbf{k}) \\ -tf(\mathbf{k}) & 0 & -\gamma_1 & 0 \\ 0 & -\gamma_1 & 0 & -t^* f(\mathbf{k}) \\ -\gamma_3 f^*(\mathbf{k}) & 0 & -tf(\mathbf{k}) & 0 \end{pmatrix} \Psi_{\mathbf{k}} \quad (1.32)$$

The main effect of the inclusion of a finite γ_3 is a low-energy trigonal warping characterized by the emergence of 4 linear-dispersion Dirac points in proximity of K and K' point. This so-called “Lifshitz transition” takes place below the critical energy $\epsilon_L = \gamma_1/4 (\gamma_3/t)^2 \simeq 1.5 \text{ meV}$ [Lifshitz, I. M., 1960]. In this regime, the isoenergetic lines break into one circular “central” pocket and three elliptical “leg” pockets at momenta such that $q \simeq p_L = \gamma_1 \gamma_3 / (3at^2/2)$ and $\theta_{\mathbf{q}} = 0, \pm 2\pi/3$, see Fig. 1.7. Because of its small characteristic energy scale, the four-pocket splitting has been detected only recently [Varlet *et al.*, 2014].

The low-energy electronic structure of bilayer graphene can be efficiently described by a two-bands Hamiltonian acting on the space spanned by the non-dimer components of the wavefunction $\chi = (\psi_{A1}, \psi_{B2})$ that are predominant at low energy. Once introduced the operator $\pi = p_x + ip_y$, the low-energy Hamiltonian in valley K is [McCann and Fal’ko, 2006; McCann and Koshino, 2013]

$$H_K = \begin{pmatrix} V & \frac{(\hbar v_f)^2}{\gamma_1} (\pi^\dagger)^2 + 3\gamma_3 a \pi \\ \frac{(\hbar v_f)^2}{\gamma_1} \pi^2 + 3\gamma_3 a \pi^\dagger & -V \end{pmatrix}, \quad (1.33)$$

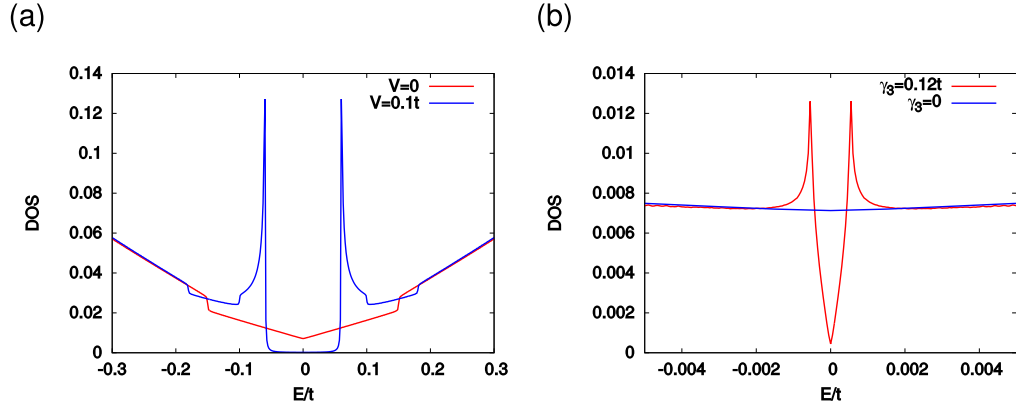


Figure 1.8 – Density of states for bilayer graphene calculated within the TB model. (a) Comparison between the DOS obtained within the minimal coupling model ($\gamma_1 = 0.15t$, $\gamma_3 = \gamma_4 = 0$) for intrinsic bilayer graphene (red curve) and including a chemical potential imbalance between the two layers $2V = 0.2t$ (blue curve). (b) Effect of an additional coupling term $\gamma_3 = 0.12t$ on the DOS of intrinsic bilayer graphene.

which for $\gamma_3 = V = 0$ reduces to

$$H_K = \begin{pmatrix} 0 & \frac{(\hbar v_f)^2}{\gamma_1} (\pi^\dagger)^2 \\ \frac{(\hbar v_f)^2}{\gamma_1} \pi^2 & 0 \end{pmatrix} = \frac{(\hbar q)^2}{2m} \mathbf{n}_2 \cdot \boldsymbol{\sigma}. \quad (1.34)$$

In the last equation, we have introduced the effective mass $m = \gamma_1 / v_f^2$ and the axis $\mathbf{n}_2 = -(\cos(2\theta_{\mathbf{q}}), \xi \sin(2\theta_{\mathbf{q}}))$. This Hamiltonian has the advantage of making evident that the low-energy charge carriers of bilayer graphene are eigenstates of the chirality operator $\mathbf{n}_2 \cdot \boldsymbol{\sigma}$. However, upon rotation of momentum \mathbf{q} , chirality of bilayer-graphene charge carriers turns twice as quick as in monolayer graphene.

We conclude this section on bilayer graphene discussing the low-energy density of states within the different models that have been treated. In the simplest situation where $V = \gamma_3 = 0$ the density of states has a constant finite value in a narrow central energy region, then becomes linear, as a consequence of the quadratic-to-linear crossover of the bands, see Fig. 1.8(a). At energy $E = \pm\gamma_1$, a finite discontinuity appears because of the onset of the second pair of bands. When a potential $V \neq 0$ breaks the layer symmetry a gap in the DOS appears surrounded by two van Hove singularities resulting from the fourth-power term of eq. 1.31. Finally, as shown in Fig. 1.8(b), accounting for a non-zero value of γ_3 produces van Hove singularities at $E = \pm\epsilon_L$ because of flat bands interpolating between the four Dirac cones.

2 Electronic transport in graphene

2.1 Ballistic transport

Ballistic transport is the regime of electrical conduction where charge carriers flow in a medium with negligible scattering. This requires that all sources of scattering, namely, impurities and imperfections of the crystal lattice, interaction with phonons and other electrons are largely eliminated. Indeed, ballistic transport is achieved at low temperature and density of charge carriers, in order to limit, respectively, electron-phonon and electron-electron interactions. In this regime, electrical resistance is mostly due to scattering off the contacts. Therefore, the mean free path is limited by the channel length of the device used to probe transport. Ballistic transport was initially reported in two-dimensional electron gas embedded in semiconductor heterostructures. Nowadays, continuous advances in synthesis methods and in the engineering of electronic devices have allowed to realize ballistic transport also in graphene, see Fig. 2.1. When the number of phase breaking events (prevalently due to electron-phonon scattering) is very low, the time evolution of charge carriers is essentially coherent, so that phenomena connected to the conservation of the phase emerge, such as interference effects. In graphene, such phenomena are very important and deserve to be briefly revised.

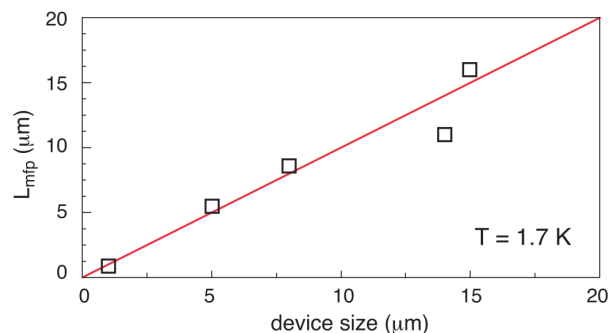


Figure 2.1 – Experimental mean free path of graphene charge carriers L_{mfp} as a function of device size. Adapted with permission from [Wang *et al.*, 2013] © 2013 American Association for the Advancement of Science

2.1.1 Klein tunnelling

One of the, perhaps unexpected, consequences of graphene's discovery has been to transform what was considered just a "gedanken" experiment into a real implementable one. The Klein paradox - mostly known as Klein tunneling after its verification - was conceived in 1929 in the context of relativistic fermions described by the Dirac equation [Klein, 1929].

Consider the situation of a free particle impinging on a sharp potential barrier that is higher than the particle's energy. Contrarily to classical particles which would just be reflected, non-relativistic quantum particles have a finite probability to tunnel through the barrier because the incident and transmitted waves are connected by an evanescent wave within the barrier. Transmission probability decays exponentially as a function of the barrier's width, but is, strictly speaking, never zero. Differently from both cases, Dirac particles can either have positive energy (electrons) or negative energy (positrons, holes). Upon crossing a barrier's edge an electron state can transform into a hole state still maintaining its propagating character. However, one constraint applies to massive Dirac particles: the height of the barrier must be at least twice larger than the rest energy $m_e c^2 = 0.51 \text{ MeV}$ in order to connect electron and positron states. The insurmountable difficulty to produce such an intense potential, which must set in over a distance of the order of the Compton length ($\hbar/m_e c \approx 2 * 10^{-12} \text{ m}$), has made an experimental verification of Klein tunneling unlikely, whence the common opinion of "gedanken" experiment. However, in graphene, the absence of an energy gap separating electron and hole states does not impose such a condition. In other words, independently of the height of the barrier, incident electrons can turn to holes and get back to their original nature once the barrier is overcome.

We expose now a theoretical treatment of Klein tunneling following Ref. [Katsnelson *et al.*, 2006]. A very similar derivation can be found in Refs. [Tworzydło *et al.*, 2006a,b]. Consider a massless Dirac particle with energy E described by the Hamiltonian 1.19 impinging on a square potential barrier of height V and width D . With reference to fig. 2.2(a), we assume that the particle comes from region *I* and is partially reflected into region *I* and partially transmitted to region *III*. The first step is to write down the wavefunction in the three regions *I*, *II*, *III*. Since the whole system is assumed to be periodic along y , the corresponding momentum component q_y is conserved, that is, $q_y^I = q_y^{II} = q_y^{III} = q_y$. In contrast, the momentum components along x inside and outside the barrier must differ: $q_x^I = q_x^{III} = q_x \neq q_x^{II}$. The momentum of the incident particle (q_x, q_y) is an independent parameter of the problem and determines the incidence angle $\theta = \arctan(q_y/q_x)$ as well as the energy $E = \hbar v_f (q_x^2 + q_y^2)^{0.5}$. The refraction angle inside the barrier is $\phi = \arctan(q_y/q_x^{II})$. The wavefunction of the incoming particle is obtained by eq. 1.22 including the Bloch phase:

$$\Psi(x, y) = \frac{1}{\sqrt{2L}} \begin{pmatrix} 1 \\ s e^{-i\theta_{\mathbf{q}}} \end{pmatrix} e^{i(q_x x + q_y y)}, \quad (2.1)$$

where the index $s = \text{sign}(E)$ denotes electron or hole states and L is a normalization factor taking into account the geometry of the system. In region *II* the wavefunction is a solution of

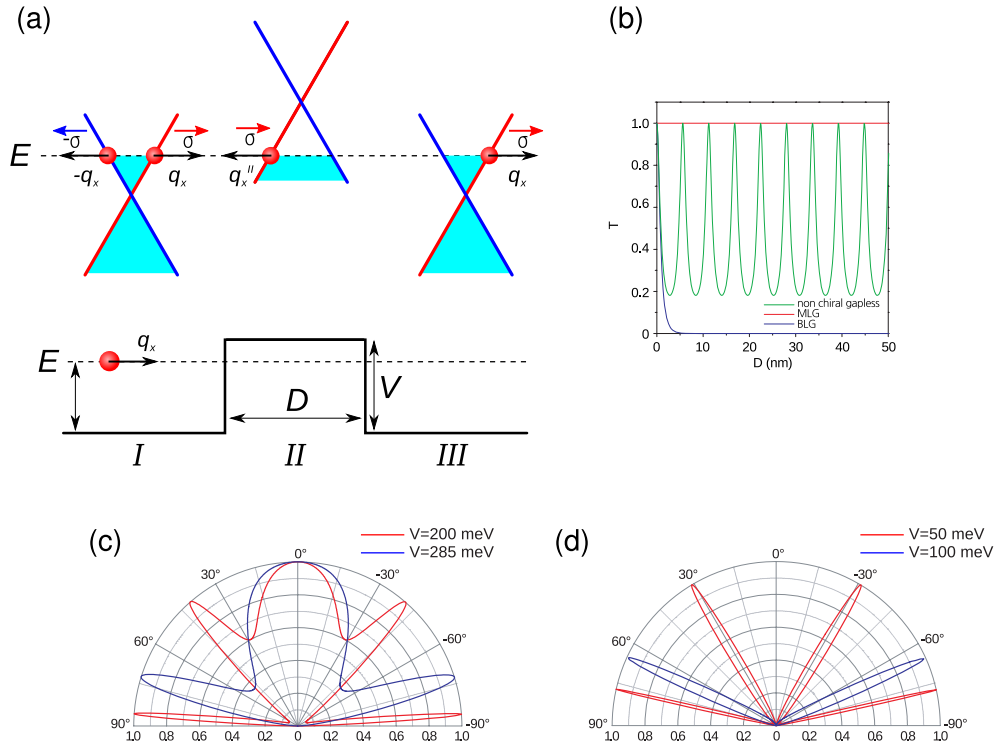


Figure 2.2 – Klein tunneling in monolayer and bilayer graphene. (a) Energy levels in regions *I*, *II*, and *III* corresponding to *n*, *p*, and *n* doping, respectively. In each region momentum and pseudospin (σ) of the charge carriers are shown. (b) Transmission at normal incidence as a function of the barrier's width D for monolayer graphene, bilayer graphene and a gapless non-chiral semiconductor. The barrier height is 450 meV for monolayer graphene and 240 meV for the other two materials. (c-d) Polar plots of the transmission as a function of the incidence angle θ for (c) monolayer graphene and (d) bilayer graphene. In both cases the width of the barrier is 100 nm. Panels (b-d) adapted with permission from [Katsnelson *et al.*, 2006] © 2006 *McMillan publisher Ltd.*

the Dirac equation

$$\begin{pmatrix} 0 & \hbar v_f (q_x^{II} - i q_y) \\ \hbar v_f (q_x^{II} + i q_y) & 0 \end{pmatrix} \begin{pmatrix} \Psi_A^{II} \\ \Psi_B^{II} \end{pmatrix} = (E - V_0) \begin{pmatrix} \Psi_A^{II} \\ \Psi_B^{II} \end{pmatrix} \quad (2.2)$$

and, correspondingly, one has

$$q_x^{II} = \sqrt{\left(\frac{E - V_0}{\hbar v_f}\right)^2 - q_y^2}, \quad (2.3a)$$

$$\tan(\phi) = \frac{q_y}{\sqrt{\left(\frac{E - V_0}{\hbar v_f}\right)^2 - q_y^2}}. \quad (2.3b)$$

The complete wavefunction can be written in terms of incident and reflected waves:

$$\Psi^I(x, y) = \frac{1}{\sqrt{2L}} \left[\begin{pmatrix} 1 \\ se^{-i\theta} \end{pmatrix} e^{i(q_x x + q_y y)} + r \begin{pmatrix} 1 \\ se^{-i(\pi-\theta)} \end{pmatrix} e^{i(-q_x x + q_y y)} \right], \quad (2.4a)$$

$$\Psi^{II}(x, y) = \frac{1}{\sqrt{2L}} \left[a \begin{pmatrix} 1 \\ s'e^{-i\phi} \end{pmatrix} e^{i(q_x^{II} x + q_y y)} + b \begin{pmatrix} 1 \\ s'e^{-i(\pi-\phi)} \end{pmatrix} e^{i(-q_x^{II} x + q_y y)} \right], \quad (2.4b)$$

$$\Psi^{III}(x, y) = \frac{t}{\sqrt{2L}} \left[\begin{pmatrix} 1 \\ se^{-i\theta} \end{pmatrix} e^{i(q_x x + q_y y)} \right], \quad (2.4c)$$

where $s' = \text{sign}(E - V_0)$. The overall spatial continuity of the wavefunction requires

$$\Psi^I(0, y) = \Psi^{II}(0, y), \quad (2.5a)$$

$$\Psi^{II}(D, y) = \Psi^{III}(D, y) \quad (2.5b)$$

from which we find that

$$r = \frac{ie^{i\theta} \sin(q_x D) (\sin\theta - ss' \sin(\phi))}{\sin(q_x D) + -s' [\sin(\theta) \sin(\phi) \sin(q_x D) - i \cos(\theta) \cos(\phi) \cos(q_x D)]}. \quad (2.6)$$

Transmission probability is obtained from the last equation imposing probability conservation:

$$T(\theta) = tt^* = 1 - rr^* = \frac{\cos^2(\phi) \cos^2(\theta)}{\cos^2(q_x D) \cos^2(\phi) \cos^2(\theta) + \sin^2(q_x D) (1 - ss' \sin(\theta) \sin(\phi))^2}. \quad (2.7)$$

In the limit of very high barrier $|V| \gg |E|$ one has $\phi \rightarrow 0$ and eq. 2.7 simplifies to

$$T(\theta) = \frac{\cos^2(\theta)}{\cos^2(q_x D) \cos^2(\theta) + \sin^2(q_x D)} = \frac{\cos^2(\theta)}{1 - \cos^2(q_x D) \sin^2(\theta)}, \quad (2.8)$$

which means perfect transparency ($T = 1$) at normal incidence ($\theta = 0$) or at whatever angle if the resonance condition $q_x D / \pi = 0, \pm 1, \pm 2, \dots$ is met. The result of eq. 2.8 must be compared to the transmission probability of non-relativistic particles in ordinary gapless semiconductors. For the latter the transmission amplitude at $\theta = 0$ is

$$t = \frac{4q_x q_x^{II}}{(q_x^{II} + q_x)^2 e^{-iq_x^{II} D} - (q_x^{II} - q_x)^2 e^{iq_x^{II} D}}, \quad (2.9)$$

meaning that $T = 1$ is achieved only if $q_x D / \pi = 0, \pm 1, \pm 2, \dots$, in contrast to massless chiral fermions for which at normal incidence a barrier of whatever width would be transparent. Transmission probability in the two cases is shown in Fig. 2.2(b).

Klein tunneling can be understood as a consequence of chirality conservation of massless Dirac particles. As previously discussed in Section ??, backscattering is suppressed in absence of a mechanism that induces a net pseudo-spin flip. The case of a potential step of height

$V > E$ (p-n junction) bears some similarities to Klein tunneling, such as full transmission at normal incidence and has been discussed in details in Ref. [Cheianov and Fal'ko, 2006]. Notice that the assumption of square barrier requires the Fermi wavelength λ_f to be much larger than the smearing width of the barrier edges, but the latter must be larger than the lattice constant in order not to introduce high-momentum scattering between the two valleys that would flip pseudo-spin.

Experimental confirmations of Klein tunneling came few years after its prediction, first using p-n junction devices [Williams *et al.*, 2007], and later in n-p-n junctions [Stander *et al.*, 2009; Young and Kim, 2009].

In bilayer graphene tunneling through a potential barrier has radically different features with respect to monolayer graphene. Consider the Hamiltonian

$$H = \frac{(\hbar v_f)^2}{\gamma_1} \begin{pmatrix} 0 & (\pi^\dagger)^2 \\ \pi^2 & 0 \end{pmatrix} \quad (2.10)$$

corresponding to eq. 1.33 where $\gamma_3 = 0$. This Hamiltonian describes particles with energy $\epsilon_L \ll |E| \ll t$. Similar steps as those followed for monolayer graphene lead to the following expression for transmission at $q_y = 0$

$$T = \frac{4(q_x q_x^{II})^2}{(q_x^2 + (q_x^{II})^2) \sinh^2(q_x^{II} D) + 4(q_x q_x^{II})^2}, \quad (2.11)$$

where

$$q_x = \sqrt{\frac{\gamma_1}{(\hbar v_f)^2} |E|}, \quad q_x^{II} = \sqrt{\frac{\gamma_1}{(\hbar v_f)^2} |E - V_0|}. \quad (2.12)$$

The expression of eq. 2.11 decays exponentially upon an increase of either the width or the height of the barrier. Notably, for a potential step ($D \rightarrow \infty$) T is exactly 0. Once more the argument of chirality conservation gives some insight into the physics behind this ‘‘anti-Klein-tunneling’’ behavior. As shown in Section 1.5, upon turning momentum of a particle in bilayer graphene by an angle π , the chirality stays unchanged, differently from monolayer graphene. This means that no selection rule applies to prevent backscattering. Moreover, the wavefunction of a particle propagating with momentum q_x in region I is coupled to the wavefunction of a hole in region II having imaginary momentum $i q_x^{II}$, that is, an evanescent wave, whence the exponential decay of T [Katsnelson *et al.*, 2006].

2.1.2 Universal minimal conductivity

In the presentation of the tunneling through a potential barrier of mass-less chiral particle we have surreptitiously assumed that momentum q_x^{II} inside the barrier is a well defined real quantity. This is true when $|E - V| > \hbar v_f q_y$, which is always fulfilled when the barrier is

sufficiently high. If the last condition is not satisfied, q_x^{II} is a pure imaginary quantity and the wavefunction is an evanescent wave $\Psi \propto \exp(\pm q_x^{II} x)$. These are not physical states in infinite space because of exponential divergence, but they became well-defined in confined regions such as inside a potential barrier. In the previous section, the wavefunction for monolayer graphene's particles has been constructed disregarding evanescent states as they give a negligible contribution to transmission compared to propagating states. On the other hand, for bilayer graphene their inclusion is essential to obtain a finite transmission since propagating states inside and outside the barrier are not coupled.

However, also for monolayer graphene there exists a situation where the contribution to transmission originating from evanescent states largely overtakes that originating from propagating states. This is the case of a two-probe conductivity measurement performed on an intrinsic graphene sample attached to two metallic contacts with high density of states. Since at the charge neutrality point the density of states of graphene vanishes, the charge carriers coming from the leads do not couple to any propagating state of the sample, thus one would simply expect zero conductivity. However, this is too naive and, indeed, in 2006 the universal minimal conductivity $\sigma_{\min} \simeq 4e^2/h\pi$ for undoped graphene was predicted. This finite conductivity is a consequence of evanescent waves present in a finite-length sample [Tworzydło *et al.*, 2006b; Katsnelson, 2006; Tworzydło *et al.*, 2006a].

The present derivation follows Ref. [Katsnelson, 2006]. With reference to Fig. 2.3 consider a graphene sheet of finite length L_x that is attached along x to two leads made of n -doped graphene where the Dirac energy lies at $V < 0$. The whole system (leads *plus* sample) is periodic along y with periodicity L_y and, consequently, the wavefunctions have quantized allowed moment $k_y = 2\pi/L_y(0, \pm 1, \pm 3 \dots)$. This assumption simplifies the derivation but is, strictly speaking, unphysical and its effects must be minimized by taking $L_y \gg L_x$.

The two-dimensional Dirac equations in real space 1.18 at $E = 0$ have the form

$$\left(\frac{\partial}{\partial x} - i \frac{\partial}{\partial y} \right) \Psi_A = 0 \quad (2.13a)$$

$$\left(\frac{\partial}{\partial x} + i \frac{\partial}{\partial y} \right) \Psi_B = 0 \quad (2.13b)$$

and its solutions are analytic functions of the conjugate variables $z = x + iy$ and $u = x - iy$:

$$\Psi_A(x, y) = \Psi_A(x + iy) \quad (2.14a)$$

$$\Psi_B(x, y) = \Psi_B(x - iy). \quad (2.14b)$$

Since the dependence on y is enclosed in the Bloch phase $\exp(iq_y y)$, the wavefunction in region *II* must be $\Psi_{A/B} \propto \exp(\pm q_y x) \exp(iq_y y)$. Proceeding in the same way as in the

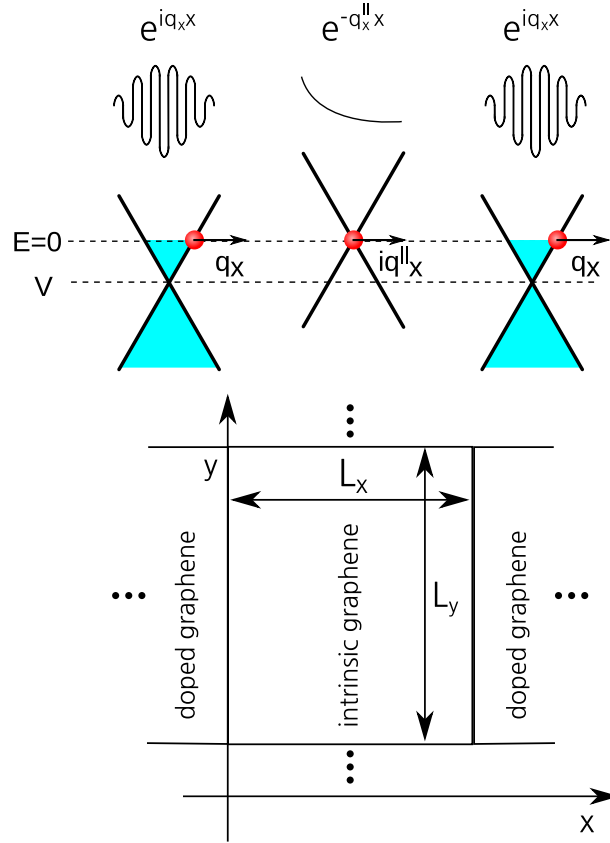


Figure 2.3 – Sketch of the ideal two-probe transport setup for the measurement of graphene minimal conductivity. A rectangular sample of undoped graphene of size $L_x \times L_y$ is attached to two semi-infinite contacts of n-doped graphene. The overall system is periodic along y . Incoming electrons have energy E and momentum $q_f = \sqrt{(q_x^2 + q_y^2)}$. The energy diagram and the wavefunction shape of each region is illustrated in the panel above.

derivation of Klein tunneling, the complete wavefunction is

$$\Psi^I(x, y) = \begin{pmatrix} \Psi_A^I(x, y) \\ \Psi_B^I(x, y) \end{pmatrix} = \frac{1}{\sqrt{2L}} \left[e^{iq_x x} \begin{pmatrix} 1 \\ e^{i\theta} \end{pmatrix} + r e^{-iq_x x} \begin{pmatrix} 1 \\ e^{i(\pi-\theta)} \end{pmatrix} \right] e^{iq_y y} \quad (2.15a)$$

$$\Psi^{II}(x, y) = \begin{pmatrix} \Psi_A^{II}(x, y) \\ \Psi_B^{II}(x, y) \end{pmatrix} = \frac{1}{\sqrt{2L}} \begin{bmatrix} a e^{q_y x} \\ b e^{-q_y x} \end{bmatrix} e^{iq_y y} \quad (2.15b)$$

$$\Psi^{III}(x, y) = \begin{pmatrix} \Psi_A^{III}(x, y) \\ \Psi_B^{III}(x, y) \end{pmatrix} = \frac{1}{\sqrt{2L}} \left[t e^{iq_x x} \begin{pmatrix} 1 \\ e^{i\theta} \end{pmatrix} \right] e^{iq_y y} \quad (2.15c)$$

where $\tan \theta = q_y / q_x$, $q_x = \sqrt{q_f^2 - q_y^2}$, $k_f = q_f / \hbar = V / \hbar v_f$ is the Fermi wave vector of the incoming particles and we have assumed that the leads are n-doped, that is, electron-type wavefunction have been used (see eq. 1.22). By imposing continuity conditions, the transmis-

sion probability is obtained:

$$T(q_y) = tt^* = \frac{\cos^2(\phi)}{\cosh^2(q_y L_x) - \sin^2 \phi} \quad (2.16)$$

which can be further simplified as

$$T(q_y) = \frac{1}{\cosh^2(q_y L_x)} \quad (2.17)$$

assuming $\phi \simeq 0$ which is justified for high doping of the leads V_0 . The total transmission is obtained by summing over the k_y modes:

$$T = \sum_{i=-\infty}^{i=+\infty} T\left(\frac{2\pi i}{L_y}\right) \simeq \frac{L_y}{2\pi} \int dq_y \frac{1}{\cosh^2(q_y L_x)} = \frac{L_y}{\pi L_x}. \quad (2.18)$$

Anticipating the main result of the Landauer-Büttiker theory which is treated in Section 4.5.1, the conductance is $G = (4e^2/h)T$, including the spin and valley degeneracy factor $g_s g_v = 4$. Hence, the conductivity is $\sigma = GL_y/L_x = 4e^2/h\pi$. A similar derivation accounting for closed boundary conditions leads to the same result in the limit $L_y \gg L_x$ [Tworzydło *et al.*, 2006b]. Numerical calculations based on tight-binding model have confirmed the result of the analytical derivation [Cresti *et al.*, 2007]. Although the existence of some universal minimal conductivity has never been questioned, early experiments measured values clustering around $4e^2/h$, roughly three times larger than the theoretical value [Novoselov *et al.*, 2005; Geim and Novoselov, 2007]. This so-called “mystery of the missing pie” motivated the graphene community to propose alternative mechanisms responsible for the minimal conductivity. Indeed, a quasi-universal conductivity of $4e^2/h$ in “dirty” samples was predicted [Stauber *et al.*, 2007]. The disputation ended in 2007, when an experiment on very clean graphene samples confirmed the minimal conductivity $4e^2/\pi h$, pointing out that a large aspect ratio ($L_y/L_x \simeq 8$ in the experiment) is crucial to measure such a value [Miao *et al.*, 2007; Danneau *et al.*, 2008].

2.2 Diffusive transport at high charge concentration

Diffusive transport takes place in graphene samples having a length L larger than the mean free path l_{mfp} . Typical values of l_{mfp} in graphene range from 50 – 200 nm for graphene deposited on a substrate [Berger *et al.*, 2006] up to 1 – 5 μm for suspended or encapsulated samples [Bolotin *et al.*, 2008; Wang *et al.*, 2013]. It must be stressed that mean free path and conductivity strongly depend on temperature and charge-carrier concentration. The main scattering mechanism for electronic transport in graphene has been debated since the very first days of the graphene era. The experimental starting point is that conductivity σ depends linearly on the gate voltage $|V_g|$ in field-effect devices built on graphene samples, as shown in Fig. 2.4(a,c). For $V_g \gtrsim 1$ eV,

2.2. Diffusive transport at high charge concentration

the charge concentration grows linearly with the gate voltage:

$$n(V_g) = C_g (V_g - V_D) / e, \quad (2.19)$$

where C_g is the graphene-substrate capacitance, e is the fundamental charge and V_D is the voltage corresponding to the minimum of resistivity.

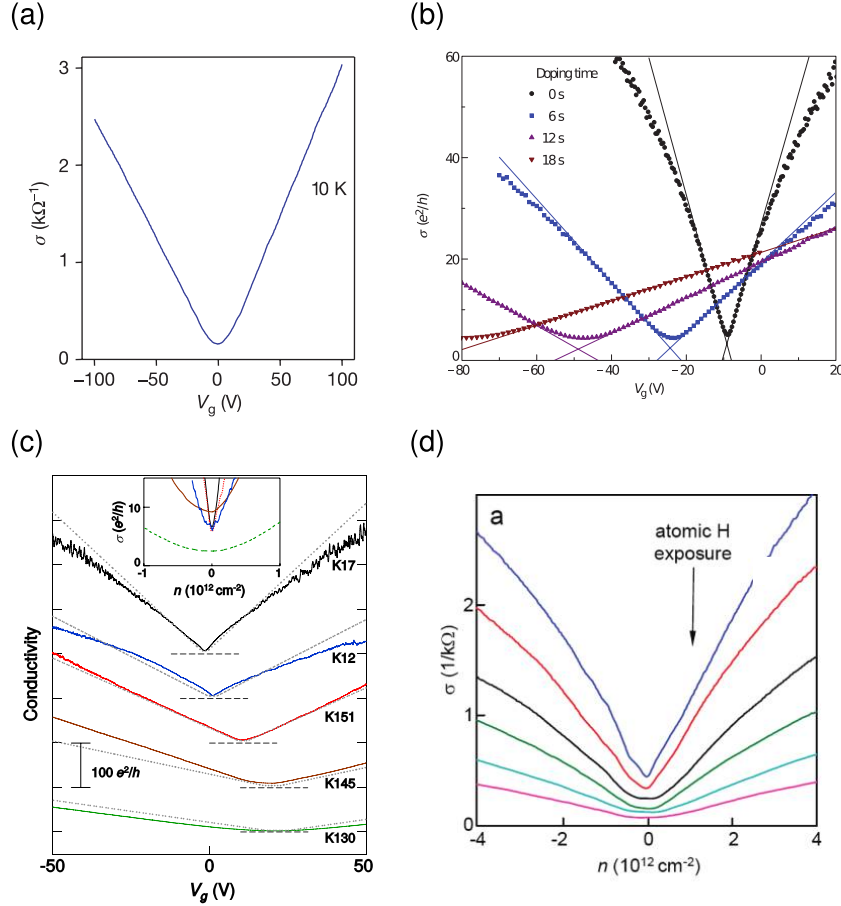


Figure 2.4 – Experimental dependence of graphene conductivity σ as a function of charge carrier concentration n or, equivalently, gate voltage V_g . In all plots the zero of the gate voltage axis corresponds to the charge neutrality point. (a) $\sigma(V_g)$ for a graphene sample obtained by mechanical cleavage. (b) $\sigma(V_g)$ for graphene exposed to potassium at different exposure times. (c) $\sigma(V_g)$ for five graphene samples with different amount of impurities. (d) $\sigma(n)$ for graphene samples exposed to atomic hydrogen. In panels (c-d) the amount of impurities increases going downward in the data series. Concentration n is measured with respect to the charge neutrality point. Reprinted with permission from (a) [Novoselov *et al.*, 2005] © 2005 *McMillan publisher Ltd*, (b) [Chen *et al.*, 2008], © 2008 *McMillan publisher Ltd*, (c) [Tan *et al.*, 2007] © 2007 *American Physical Society*, (d) [Ni *et al.*, 2010] © 2010 *American Chemical Society*.

Therefore, it can be deduced that $\sigma \propto n$ or, equivalently in the framework of Drude theory, one has $\mu = \sigma / en = \text{const}$. Notice that graphene's capacitance bears a significant quantum contribution $C_q \propto V_g$ at low V_g [Xia *et al.*, 2009]. Remarkably, graphene exhibits an almost

perfect ambipolar behavior due to its gapless and approximately electron-hole symmetric nature, see Fig. 2.4(a-d). This scenario is quite different from 2D electron gas found in thin layers of standard semiconductors (e.g. Si, Ge, GaAs) where the conductivity shows a rather complicated evolution from low to high charge-carrier concentration regime. The most prominent difference is, of course, that the presence of a band gap in a 2DEG prevents from immediate switching from an electron metal to a hole metal. For sufficiently large value of V_g that allow to overcome the band gap, conductivity shows first a superlinear trend upon an increase of the carrier density $\sigma \propto n^\alpha$ with $1 < \alpha < 2$ until mobility μ reaches a maximum, then it increases sublinearly such that μ progressively drops [Das Sarma *et al.*, 2011].

Moreover, differently from standard semiconductors, it was found for graphene deposited on a SiO_2 substrate that μ weakly depends on the temperature - no more than a few percents change from $T = 0\text{K}$ to $T = 300\text{K}$ [Morozov *et al.*, 2008] - so that electron-phonon interaction cannot be the main source of scattering. Three main scattering mechanisms involving impurity disorder have been proposed to explain the properties of diffusive transport of graphene: i) Scattering from long-range charged impurities located either in the substrate or on the exposed graphene surface, ii) Short-range neutral point defects, and iii) Resonant scattering from low-energy localized states due to realistic impurities such as adsorbates.

The total conductivity can be calculated in the semiclassical Boltzmann-Drude framework as

$$\sigma = \frac{e^2}{2} \int d\epsilon \rho(\epsilon) \mathbf{v}_{\mathbf{k}}^2 \tau(\epsilon) \left(-\frac{\partial f}{\partial \epsilon} \right), \quad (2.20)$$

where $\tau(\epsilon)$ is the relaxation time at energy ϵ , $\mathbf{v}_{\mathbf{k}} = d\epsilon_{\mathbf{k}}/d\mathbf{k}$, and f is the Fermi-Dirac distribution [Economou, 2006; Das Sarma *et al.*, 2011]. In the limit $T \rightarrow 0$, the last equation becomes the Drude formula

$$\sigma = \frac{e^2 v_f^2}{2} \rho(E_f) \tau(E_f). \quad (2.21)$$

The relaxation time can be calculated by means of the Fermi's golden rule:

$$\frac{1}{\tau(\epsilon_{\mathbf{k}})} = \frac{2\pi}{\hbar} n_i \int \frac{d^2\mathbf{k}'}{(2\pi)^2}, |\langle V_{\mathbf{k},\mathbf{k}'} \rangle|^2 (1 - \cos\theta_{\mathbf{k},\mathbf{k}'}) \delta(\epsilon_{\mathbf{k}'} - \epsilon_{\mathbf{k}}), \quad (2.22)$$

where n_i is the concentration of scattering centers, $\epsilon_{\mathbf{k}}$ is the dispersion law, $\theta_{\mathbf{k},\mathbf{k}'}$ is the angle formed by the incoming and outgoing momenta \mathbf{k} and \mathbf{k}' , and $V_{\mathbf{k},\mathbf{k}'}$ is the scattering potential in Fourier space. The potential $V_{\mathbf{k},\mathbf{k}'}$ in Eq. 2.22 is, actually, the first term of the Born series that defines the T matrix, see Section 4.5.2. A more accurate estimate of the scattering time is obtained by including the full knowledge of the T matrix [Economou, 2006]:

$$\frac{1}{\tau(\epsilon_{\mathbf{k}})} = \frac{2\pi}{\hbar} n_i \int \frac{d^2\mathbf{k}'}{(2\pi)^2}, |\langle T_{\mathbf{k},\mathbf{k}'}(\epsilon_{\mathbf{k}}) \rangle|^2 (1 - \cos\theta_{\mathbf{k},\mathbf{k}'}) \delta(\epsilon - \epsilon_{\mathbf{k}}). \quad (2.23)$$

2.2. Diffusive transport at high charge concentration

The scattering time depends on the type of defect considered. The potential of charged impurities can be described by a Thomas-Fermi screened Coulomb potential generated at position \mathbf{r}_i by N_{imp} identical impurities at position \mathbf{r}_j

$$U(\mathbf{r}) = U_{\text{TF}} \sum_{j=1}^{N_{\text{imp}}} \frac{e^{-\xi_{\text{TF}}|\mathbf{r}_i - \mathbf{r}_j|}}{|\mathbf{r}_i - \mathbf{r}_j|}, \quad (2.24)$$

where U_{TF} and ξ_{TF} are parameters describing the strength and the decay length of the scattering centers [Foa Torres *et al.*, 2014]. Adam *et al.* employed a self-consistent method in the random phase approximation (RPA) and found to the leading order [Adam *et al.*, 2007]

$$\sigma_{\text{LR}} = C \frac{4e^2}{\hbar} \frac{n}{n_i}, \quad (2.25)$$

where $C \simeq 5$ if the dielectric constant of a SiO_2 substrate is considered [Das Sarma *et al.*, 2011]. Eq. 2.25 is consistent with the experimental findings and would lead to identify Coulomb scatterers as the one responsible for diffusive transport in graphene. Moreover, Chen *et al.* showed that under a controlled addition of potassium adsorbates, graphene's conductivity conserves the behavior $\sigma \propto n$ and μ is roughly inversely proportional to the amount of adsorbates [Chen *et al.*, 2008], see Fig. 2.4(b). Such adatoms can be considered charged impurities, due to the weak electronegativity of potassium. Indeed, the Dirac point shifts to lower energies as a result of the charge donated to the system by potassium adatoms. It was found that the product of mobility and impurity concentration roughly equals a constant $C = \mu n_i = 5 \times 10^{15} (\text{Vs})^{-1}$. However, if a substrate with a high dielectric constant (e.g. SrTiO_2) is used instead of SiO_2 , the change in mobility is very weak [Couto *et al.*, 2011; Ponomarenko *et al.*, 2009]. This evidence has weakened the arguments in favour of Coulomb scattering as the mechanism that governs electronic transport at high charge-carrier concentration.

For point defects at position \mathbf{r}_i described by the potential

$$U(\mathbf{r}) = \sum_{j=1}^{N_{\text{imp}}} U_j \delta(\mathbf{r} - \mathbf{r}_j) \quad (2.26)$$

the Boltzmann conductivity is found to be independent of charge concentration [Foa Torres *et al.*, 2014]:

$$\sigma_{\text{SR}} = \frac{4e^2}{h} \frac{2(\hbar v_f)^2}{n_i \langle U_j^2 \rangle}. \quad (2.27)$$

This result rules out generic short-range defects as the main scattering source at high density. However, the sublinear behavior of μ observed at low concentration of charge-carrier in very high-mobility samples, that are affected by a low concentration of charged impurities, has been attributed to a relative stronger role of short range disorder [Tan *et al.*, 2007], see Fig. 2.4(c).

Finally, we discuss the role of resonant scattering, that is, scattering from quasi-localized states in the vicinity of the Dirac point (also called “midgap states” in analogy with ordinary semiconductors). The signature of such states is a peak in the density of states - a resonance, indeed - in correspondence of their energy. Such states naturally arise in case of unreconstructed vacancies [Pereira *et al.*, 2006] but, on the other hand, it is very unlikely that vacancies are naturally present in graphene if not created intentionally [Chen *et al.*, 2009]. However, it has been predicted that adsorbed hydrogen or small organic radicals such as CH₃, C₂H₅ and OH groups produce resonances within 30 meV away from the Dirac point [Wehling *et al.*, 2010, 2009a]. A T -matrix approach based on a TB model for graphene with adsorbates leads to the following expression for conductivity

$$\sigma = \frac{e^2}{h\pi} \frac{n}{n_i} \ln^2(n_e), \quad (2.28)$$

where $n_e = 2nA_s$ is the number of carriers per carbon atom [Wehling *et al.*, 2010; Stauber *et al.*, 2007]. This equation mimics the linear dependence on n at sufficiently high concentrations that has been also found for charged impurities. Moreover, it naturally contains the sublinear behavior for low n which is found in experiments on clean graphene samples. The conductivity measured in graphene samples where vacancies are intentionally created by ion bombardment is well fitted by eq. 2.28 [Chen *et al.*, 2009]. A similar trend of $\sigma(n)$ has been found in graphene samples exposed to atomic hydrogen, see Fig. 2.4 [Ni *et al.*, 2010]. It has been argued that a non-negligible concentration of resonant scatterers is present in graphene deposited on a substrate, as revealed by a weak D peak in Raman spectra, which is a signature of intervalley scattering induced by atomic-scale defects. For this reason, resonant scatterers have been proposed to be the main factor limiting carrier mobility in graphene [Ni *et al.*, 2010]. In particular, a small concentration of such scatterers $n_e < 10^{-4}$ would be sufficient to limit mobility down to $2 * 10^4 \text{cm}^2/\text{Vs}$, somewhat more efficiently than charge impurities.

2.2.1 Phonon scattering

The role of extrinsic disorder is particularly important when graphene is deposited on a substrate. Generally, electron-phonon scattering, that is the main factor limiting mobility in standard semiconductors at room temperature, is expected to be negligible in graphene because of the high frequency of its optical phonons [Mounet and Marzari, 2005]. However, in suspended graphene the contribution of low-energy acoustic phonons cannot be neglected as it generally dominates with respect to the contribution of extrinsic scatterers. For such samples, similarly to graphene on substrate, experiments have shown that conductivity is proportional to the charge-carrier density $\sigma = e\mu n$ and that the dependence of mobility on temperature is described by the law

$$\mu^{-1}(T) = \mu^{-1}(T=0) + \gamma T^2, \quad (2.29)$$

2.2. Diffusive transport at high charge concentration

as shown in Fig. 2.5(c) [Castro *et al.*, 2010]. In the last equation, the constant $\mu^{-1}(T=0)$ is due to intrinsic defects and the coefficient γ depends on the measured sample.

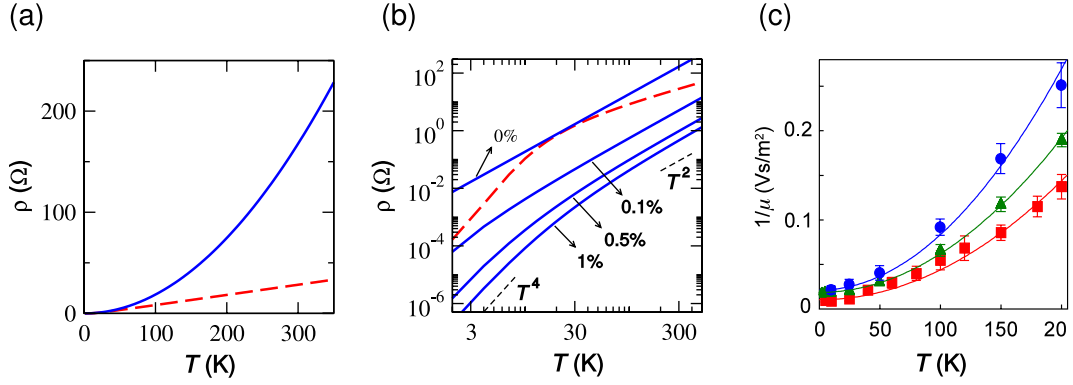


Figure 2.5 – Temperature dependence of resistivity in graphene $\rho(T)$. (a) Theoretical contribution to resistivity of flexural (continuous blue line) and in-plane (dashed red line) acoustic phonons for an unstrained sample. (b) Same as panel (a) for different amount of strain as indicated by percentages. The crossover from a low-temperature $\rho \propto T^4$ to a high-temperature $\rho \propto T^2$ behavior appears in the curves with larger strain. In both panels the charge-carrier concentration is $n = 10^{12} \text{cm}^{-2}$. (c) Experimental resistivity for varying temperature measured on three different samples. Lines have been drawn by fitting eq. 2.29 on the experimental data. Reprinted with permission from Ref. [Castro *et al.*, 2010], © 2010 American Physical Society.

Theoretical studies have found that scattering due to flexural phonons leads to $\sigma \propto n$ consistently with experiments, whereas in-plane phonon scattering leads to a conductivity independent of n [Castro *et al.*, 2010]. For unstrained systems above the cross-over temperature $T_c \simeq 57\text{K} * n/10^{12} \text{cm}^{-2}$, the dominant scattering process is due to flexural phonons. The relaxation time of the latter depends on the temperature as

$$\frac{1}{\tau} \propto T^2 \ln\left(\frac{T}{T^*}\right). \quad (2.30)$$

In eq. 2.30, T^* is a free parameter arising from the infrared cut-off below which anharmonic effects become important. An estimate based on Ginzburg's criterion gives $T^* \simeq 70\text{K}$ [Zakharchenko *et al.*, 2010]. The complete expression for the relaxation time can be found in Ref. [Castro *et al.*, 2010]. Notice that at sufficiently high temperature the functional dependence expressed in eq. 2.30 becomes indistinguishable from that of eq. 2.29. Figure 2.5(a) shows that at $T = 300\text{K}$ the relative contribution to resistivity due to flexural phonons largely overtakes that of in-plane phonons. However, in the low temperature regime $T < T_c$ the in-plane phonon scattering becomes dominant and the scattering time rather behaves as $1/\tau \propto T$. Strain can have a beneficial effect on mobility since an expansion of the sample suppresses flexural phonons. It has been shown that even a small strain below 1% can increase the room-temperature mobility by up to an order of magnitude, see Fig. 2.5(b) [Castro *et al.*, 2010]. To the best of our knowledge the record value of mobility achieved in suspended graphene is $2.3 * 10^5 \text{cm}^2/\text{Vs}$ at $T = 5\text{K}$ and $n = 2 * 10^{12} \text{cm}^{-2}$ corresponding to a mean free

path $l_{\text{mfp}} \simeq 1.2\mu\text{m}$ [Bolotin *et al.*, 2008]. For completeness, we report that higher mobilities have been achieved in ultra-clean graphene samples encapsulated in boron nitride and with one-dimensional metallic contacts to the graphene edges [Mayorov *et al.*, 2011; Wang *et al.*, 2013]. Encapsulation suppresses out-of-plane flexural modes and mobility is limited by in-plane longitudinal phonons, thus scaling as $\mu \propto 1/Tn$, while one-dimensional contacts reduce the contact resistance (as low as $100\Omega\mu\text{m}$) [Wang *et al.*, 2013]. At room temperature a mobility of $1.4 * 10^5\text{cm}^2/\text{Vs}$ has been measured for low carrier concentration $n \simeq 10^{11}\text{cm}^{-2}$, whereas at low temperature the record mobility of $10^6\text{cm}^2/\text{Vs}$ at concentration $n \simeq 3 * 10^{12}$ has been achieved. For samples whose width is comparable to the mean free path $l_{\text{mfp}} \simeq \mu\text{m}$, the conductivity is limited by scattering at the sample boundaries rather than in graphene bulk. We conclude pointing out that flexural phonon scattering in bilayer graphene leads to a behavior analogous to monolayer graphene both in the temperature dependence of mobility and in the concentration dependence of conductivity [Ochoa *et al.*, 2011].

2.3 Anomalous Quantum Hall Effect

The massless Dirac fermion nature of graphene charge carriers has peculiar signature in the quantum Hall effect. Consider a uniform magnetic field $\mathbf{B} = B\mathbf{e}_z$ applied perpendicularly to the graphene plane xy and described by the vector potential $\mathbf{A} = -yB\mathbf{e}_x$. The Dirac Hamiltonian in presence of magnetic field is obtained by replacing the operator $\hat{\mathbf{p}} = (\hbar/i)\vec{\nabla}$ by $\hat{\mathbf{p}} + (e/c)\mathbf{A} = (\hbar/i)\vec{\nabla} + (e/c)\mathbf{A}$. In proximity of K, the Hamiltonian reads

$$\hbar v_f \begin{bmatrix} 0 & -i\frac{\partial}{\partial x} + \frac{\partial}{\partial y} - \frac{eB}{\hbar c}y \\ -i\frac{\partial}{\partial x} - \frac{\partial}{\partial y} - \frac{eB}{\hbar c}y & 0 \end{bmatrix} \Psi = E\Psi. \quad (2.31)$$

Because of the gauge choice, the wavefunction has the form $\Psi = \exp(ikx)\phi(y)$, which, substituted in the Hamiltonian, leads to

$$\hbar v_f \begin{bmatrix} 0 & k + \frac{\partial}{\partial y} - \frac{1}{l_B^2}y \\ k - \frac{\partial}{\partial y} - \frac{1}{l_B^2}y & 0 \end{bmatrix} \phi(y) = E\phi(y), \quad (2.32)$$

where we have introduced the magnetic length $l_B = \sqrt{\hbar c/eB}$. We remind that ϕ represents the two-component spinor (ϕ_A, ϕ_B) . Once introduced the adimensional variable $\xi = l_B k - \frac{1}{l_B}y$, let us define the operators \hat{a} and \hat{a}^\dagger , akin to 1D harmonic-oscillator creation and annihilation operators,

$$\hat{a} = \frac{1}{\sqrt{2}} \left(\frac{\partial}{\partial \xi} + \xi \right) \quad (2.33)$$

and

$$\hat{a}^\dagger = \frac{1}{\sqrt{2}} \left(-\frac{\partial}{\partial \xi} + \xi \right), \quad (2.34)$$

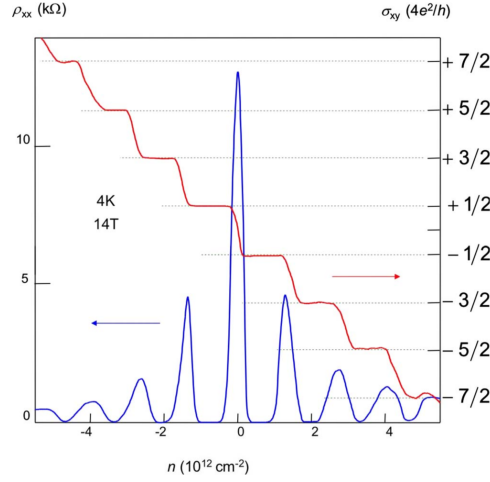


Figure 2.6 – Quantum Hall effect in graphene. Shubnikov-de Haas oscillations in longitudinal conductivity σ_{xx} and plateaus in transverse conductivity σ_{xy} measured as a function of charge carrier concentration n . Reprinted with permission from [Novoselov *et al.*, 2005], © 2005 *McMillan publisher Ltd.*

which satisfy the commutation relation $[\hat{a}, \hat{a}^\dagger] = 1$. Thus, eq. 2.32 becomes

$$\hbar\omega_c \begin{bmatrix} 0 & \hat{a} \\ \hat{a}^\dagger & 0 \end{bmatrix} \begin{pmatrix} \phi^A \\ \phi^B \end{pmatrix} = E \begin{pmatrix} \phi^A \\ \phi^B \end{pmatrix}, \quad (2.35)$$

where the cyclotron frequency ω_c is given by $\sqrt{2}v_f/l_B = \sqrt{2ev_f^2B/\hbar c}$. From the first row of eq. 2.35 we get $\phi_A = E/\hbar\omega_c \hat{a}\phi_B$, which, substituted into the second row, leads to

$$\hat{a}^\dagger \hat{a}\phi_B = \left(\frac{E}{\hbar\omega_c} \right)^2 \phi_B. \quad (2.36)$$

From the commutation properties of \hat{a} and \hat{a}^\dagger , we know that the energy spectrum is found from $(E/\hbar\omega_c)^2 = N$, with $N = 0, 1, 2, \dots$, whence the Landau levels are given by [McClure, 1956]

$$E_\pm(N) = \pm\hbar\omega_c\sqrt{N} = \pm v_f\sqrt{2e\hbar B}\sqrt{N}. \quad (2.37)$$

The corresponding eigenfunctions are found by solving eq. 2.35

$$\begin{pmatrix} \phi_N^A \\ \phi_N^B \end{pmatrix} = \begin{pmatrix} \pm\psi_{N-1} \\ \psi_N \end{pmatrix}, \quad (2.38)$$

where $\psi_N(\xi) = 1/\sqrt{2^N N!} \exp(-\xi^2/2) H_N(\xi)$, with H_N being a Hermite polynomial, is the eigenfunction corresponding to the N -th eigenvalue of the 1D harmonic oscillator. The sublattice asymmetry of the wavefunctions (eq. 2.38) depends on the particular gauge chosen. For the opposite point K' , the energy spectrum is exactly the same, so that considering spin degeneracy, each energy level has degeneracy $g_L = 4$. The spectrum given by eq. 2.37 differs from

Chapter 2. Electronic transport in graphene

the classical Landau level spectrum in two aspects: i) the presence of an $N = 0$ state, and ii) the unequal spacing between the levels $E_{N+1} - E_N \propto \sqrt{N+1} - \sqrt{N}$. These peculiarities are responsible for the anomalous quantum Hall effect in graphene.

In presence of disorder, Landau levels develop a finite broadening and mobility edges appears, namely, the states close to the original Landau states are delocalized and those in the gap between two states are localized at the edges of the sample. When the chemical potential lies inside a region of localized states, the longitudinal conductivity $\sigma_{xx} = 0$ and the Hall conductivity σ_{xy} assumes quantized values. Differently, when the chemical potential lies close to the center of a Landau level, σ_{xx} assume a finite value and σ_{xy} varies continuously between two quantized values. As shown by Laughlin, the quantized values of σ_{xy} for 2D free electrons in a perpendicular magnetic field are an integer multiple of the conductance quantum $\sigma_{xy} = \pm (e^2/h) M$, where plus (minus) sign applies when charge-carriers are electrons (holes) [Laughlin, 1981]. Ultimately, M corresponds to the number of Landau levels, occupied or unoccupied, with respect to the charge neutrality point of the system. From a naive extension of this argument to massless Dirac fermions one would expect $\sigma_{xy} = \pm g_L (e^2/h) N$, where N is the index of the highest occupied Landau level. However, the charge neutrality point of undoped graphene lies at $E = 0$, namely, in correspondence of the $N = 0$ Landau level. We assume that, upon disorder-induced broadening, this level hosts an equal number of electron and hole states. Therefore, the conductivity of the undoped system at $E_f = 0$ must lie in the middle of two Hall plateaus $\sigma_{xy} = \pm g_L/2 (e^2/h)$ so that, by symmetry, $\sigma_{xy}(E_f = 0) = 0$. In general, Hall conductivity in graphene assumes shifted (but still integer) values

$$\sigma_{xy} = \pm g_L \frac{e^2}{h} \left(N + \frac{1}{2} \right), \quad (2.39)$$

as shown in Fig. 2.6. This anomalous quantum Hall effect in graphene has been confirmed in experiments by two independent - and almost simultaneous - experiments [Zhang *et al.*, 2005; Novoselov *et al.*, 2005]. As a consequence of the Landau level spectrum 2.37, the energy spacing between Landau levels $\Delta_n = E_n - E_{n-1} = \hbar\omega_c (\sqrt{n+1} - \sqrt{n})$ can be rather large for low n . For example, assuming a field $B = 10\text{T}$, one has $\Delta_1 \simeq 114\text{meV}$ and $\Delta_2 = 47\text{meV}$, well above the room-temperature $k_b T$, which is the ultimate requirement for the observation of Landau levels. To the best of our knowledge, graphene is the only material that exhibits QHE at room temperature [Novoselov *et al.*, 2007]. Finally, the spectrum of Landau levels in bilayer graphene can be derived starting from the Hamiltonian (eq. 1.34) by implementing the substitution $\hat{\mathbf{p}} \leftarrow \hat{\mathbf{p}} + (e/c)\mathbf{A}$. The spectrum contains two degenerate levels with energy $E_0 = E_1 = 0$ and, defining the cyclotron frequency $\omega_c = eB/mc$ with $m = v_f^2/\gamma_1$, the energy of the other states is given by

$$E_{\pm}(N) = \pm \hbar\omega_c \sqrt{N(N-1)} \quad N \geq 2, \quad (2.40)$$

for B and N low enough to fulfill $|E_{\pm}(N)| \ll \gamma_1$. The degeneracy of the $E = 0$ Landau level is $2g_L = 8$, whereas the degeneracy of the other states is simply g_L . Thus, the Hall conductivity

must exhibit plateaus at quantized values

$$\sigma_{xy} = \pm g_L \frac{e^2}{h} N, \quad (2.41)$$

which was confirmed experimentally [Novoselov *et al.*, 2006]. Differently from monolayer graphene, where the plateau spacing is constantly $g_L e^2/h$, the spacing between the first electron and hole plateaus of bilayer graphene is $2g_L e^2/h$, twice larger than the spacing between all other levels.

2.4 Anderson Localization

Anderson localization is a phenomenon taking place in disordered systems described by single-particle Hamiltonians. Traditionally, Anderson localization has been studied by employing tight-binding Hamiltonians with the inclusion of random diagonal terms ϵ_m distributed in the interval $[-W, W]$

$$H = \sum_{m \neq n} t_{m,n} |m\rangle \langle n| + \sum_m \epsilon_m |m\rangle \langle m|. \quad (2.42)$$

As demonstrated by Anderson [Anderson, 1958], a finite amount of disorder $W \neq 0$ is responsible for the appearance of regions of localized states in the spectrum of Hamiltonian 2.42. Such regions are separated from those of delocalized states (scattered Bloch states) by so-called “mobility edges”. For increasing disorder, the localized regions grow at the expense of delocalized ones, which may eventually disappear if the disorder strength exceeds a threshold W^* characteristic of the system. In absence of extended states, electrons cannot diffuse into an originally metallic system, which turns into an insulator. In other words, disorder may induce a metal-insulator transition (Anderson MIT).

The classical scaling theory of Anderson localization [Abrahams *et al.*, 1979] predicts that, while for systems with dimensionality $d > 2$ the threshold strength of disorder is $W^* > 0$, for systems with $d \leq 2$ one has $W^* = 0$. This means that, in systems with reduced dimensionality, whatever non-vanishing amount of disorder triggers the localization of the whole spectrum. Moreover, these results were claimed to hold universally, regardless the nature of the disorder potential. However, it was soon realized that several universality classes of Anderson localization exist, prevalently identified by the symmetry of the disordered Hamiltonian. In this scenario, the universality class described by the classical scaling theory, nowadays referred to as Wigner-Dyson orthogonal class, is only one possibility. Importantly, none of the other universality classes shows full localization for 2D systems.

The classification of disordered Hamiltonians by means of random-matrix theory has been accomplished in the 90’s (see Ref. [Evers and Mirlin, 2008] for a historical perspective of the field), leading to the discovery of ten different symmetry classes. However, the connection between symmetry class of random Hamiltonian and universality class of Anderson localization

is not strictly one-to-one and, within the same symmetry class, Anderson localization may manifest in different forms [Evers and Mirlin, 2008]. This is, indeed, the case for graphene. The low-energy states of graphene in presence of long-range random scatterers are described by two decoupled Dirac Hamiltonian (one for each valley) with the addition of a random diagonal potential $U(\mathbf{r})$. An example is correlated Gaussian disorder [Bardarson *et al.*, 2007]

$$\langle U(\mathbf{r}) U(\mathbf{r}') \rangle = K_0 \frac{(\hbar v_f)^2}{2\pi\xi^2} \exp\left(-\frac{|\mathbf{r}-\mathbf{r}'|^2}{2\xi^2}\right). \quad (2.43)$$

The resulting Hamiltonian

$$H = \hbar v_f \sigma \cdot \hat{\mathbf{p}} + U(\mathbf{r}) \quad (2.44)$$

is invariant under the transformation $\sigma_y H \sigma_y = H^*$ and belongs to the symplectic Wigner-Dyson class, similarly to the disordered electron gas with spin-orbit coupling [Das Sarma *et al.*, 2011]. For the latter, numerical studies have shown that Anderson metal-insulator transition takes place also in 2 dimensions [Markoš and Schweitzer, 2006]. By contrast, several studies of Hamiltonian 2.44 have shown that Dirac fermions do not undergo Anderson localization at all, so that graphene remains metallic [Bardarson *et al.*, 2007; Nomura and MacDonald, 2007; Tworzydło *et al.*, 2008].

However, as was pointed out in Ref. [Suzuura and Ando, 2002], the presence of atomically sharp potentials, such as those induced by a vacancy or a hydrogen adatom, introduce intervalley scattering and drive the system into the Wigner-Dyson orthogonal class. This means that intervalley scattering induces full localization of the spectrum and graphene with atomically sharp defects becomes an insulator. From the experimental point of view, Anderson localization is difficult to identify with electronic transport measurement for several reasons: i) phase-coherency over long distances is required to unveil Anderson localization, ii) localization length ξ must be shorter than the size of the sample L , and iii) experimental conditions such as the presence of a substrate, the non-planarity of graphene etc. may play an important role in defining the localization behavior of Dirac fermions [Adam *et al.*, 2008; Bostwick *et al.*, 2009; Song *et al.*, 2011; Jayasingha *et al.*, 2013].

3 Defects in graphene

3.1 Introduction

Defects in crystalline solids play a major role in determining electronic, transport, optical and mechanical properties just to mention few. In systems with reduced dimensionality, such as graphene, carbon nanotubes etc. defects have even a stronger effect on electronic transport properties with respect to three-dimensional solids. This can be understood with the following qualitative argument. If a vacancy is introduced in a linear chain of atoms, the conductance through the chain is strongly suppressed, namely vanishing if the only relevant hopping takes place between neighboring atoms. This would not be the case if the current flow had more available dimensions to find alternative paths, for example in two or three-dimensional systems. Of course, the case of a linear atomic chain with a vacancy is very special. However, given a d -dimensional system in presence of a d' -dimensional defects ($d' < d$), the effect of the latter on the electronic transport properties of the system can be assessed on the basis on the difference $\Delta d = d - d'$. At a very qualitative level, it can be stated that the smaller Δd , the stronger the role that defects have on the charge-carrier flow.

Graphene has a large variety of possible defects which depend on the method and the conditions of its production. Nevertheless, a general property of graphene is that it is relative inert and has a small amount of point defects due to their high formation energy. Moreover, contrarily to three-dimensional crystals where impurities are often buried inside the bulk, graphene's contaminants are exposed and can be efficiently eliminated by means of techniques such as temperature annealing, current-induced cleaning, oxygen plasma cleaning [Moser *et al.*, 2007; Avouris and Dimitrakopoulos, 2012]. This is one of the reason why graphene has very high performances in terms of charge-carrier mobility. Before reviewing the most common defects of graphene, it is important to give a brief classification of the type of defects.

A first distinction is between intrinsic and extrinsic defects. The former break the lattice order without involving atomic species that are not naturally present in the material, e.g. vacancies, structural defects. Conversely, extrinsic defects contain at least one species that is not present in the material, e.g. substitutional impurities, adsorbed atoms or molecules.

The second distinction is between local and topological defects. In the former, the perfect crystalline order can be restored by local modifications of the atomic structure. For example, a vacancy or a substitutional impurity can be eliminated by adding or replacing one single atom, respectively. On the other hand, a grain boundary, that is, the interface between two misoriented crystalline domains would stay unavoidably there if one would try to rearrange the atoms that compose the grain boundary. The only way to get rid of such a defect would be to detach the two domains, re-orient and stitch them together. This procedure is inherently non-local. Topological defects are associated to topological invariants, that is, observables which do not change upon local atomic modifications.

3.2 Local defects

Throughout this section, all the information for which no explicit reference is given, is taken from from Ref. [Banhart *et al.*, 2011].

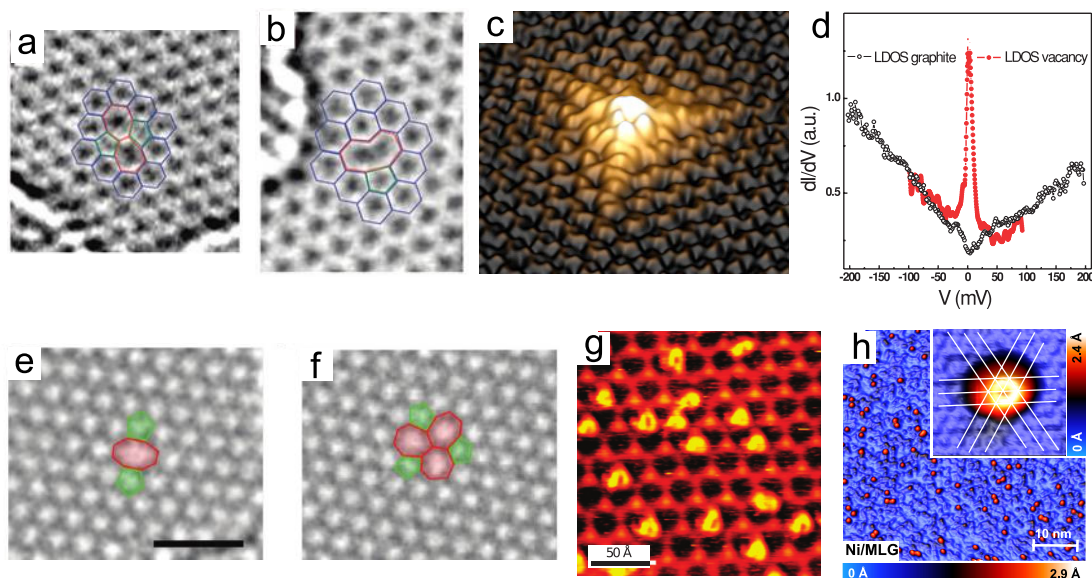


Figure 3.1 – Experimental images of point defects in graphene. (a) TEM image of a Stone-Wales defect formed by two pentagons and two heptagons contoured in red and green, respectively. (b) TEM image of a vacancy. After reconstruction a pentagon (green contour) and a nine-membered ring (red contour) are present. (c) STM image of a vacancy in graphite surface and (d) STS measurement of LDOS on top of a single vacancy in graphite surface (red dots) and on pristine graphite (black dots). (e-f) TEM image of two possible reconstruction of divacancy in graphene. The reconstruction shown in (f) has lower energy. (g) STM image of hydrogen adatoms on graphene. (h) STM image of Ni adatom on graphene. Reprinted with permission from (a-b) Ref. [Meyer *et al.*, 2008], © 2008 American Chemical Society, (c-d) Ref. [Ugeda *et al.*, 2010], © 2010 American Physical Society, (e-f) Ref. [Kotakoski *et al.*, 2012], © 2012 American Chemical Society, (g) Ref. [Balog *et al.*, 2010], © 2010 Mcmillan Ltd., (h) Ref. [Eelbo *et al.*, 2013], © 2013 American Physical Society

Structural defects One of the simplest defects is a vacancy, that is, a single atom missing from a lattice site. The knock-on energy for a carbon atom in sp^2 carbon nanostructures is about 18 – 20 eV, as found in early transmission electron microscopy experiments (TEM) of carbon nanotubes under irradiation [Banhart, 1999] and from theoretical calculations on graphene [Yazyev *et al.*, 2007]. Once created in non-equilibrium conditions, vacancies reconstruct forming a structural defect composed by one pentagon and one nine-membered ring containing one undercoordinated atom, see Fig. 3.1(b) [Meyer *et al.*, 2008]. The formation energy of a vacancy calculated in DFT is about $E_v = 7.5$ eV, mostly due to the presence of one unsaturated bond. This value is larger than in other materials such as silicon for which $E_v = 4.0$ eV. This makes unlikely the spontaneous presence of vacancies in graphene in equilibrium conditions. However, multiple vacancies can have a lower energy per missing atom. Indeed, divacancies can reconstruct forming two pentagons and one octagon ($V_2(5-8-5)$) getting rid of undercoordinated atoms, see Fig. 3.1(e) [Kotakoski *et al.*, 2012]. The calculated energy per missing atom is $E_{2v} = 4.0$ eV. Another possible reconstruction for a divacancy consists in a defect formed by three pentagon-heptagon pairs arranged in the flower shape shown in Fig. 3.1(f) (V_2 555-777 defect) [Kotakoski *et al.*, 2012]. The formation energy of this defect is about 3 eV per missing atom. As a general trend, vacancies with an even number of missing atoms are energetically favorable as they fully reconstruct leaving no dangling bonds, whereas vacancies with an odd number of missing atoms are always left with at least one unsaturated bond. However, dangling bonds are in general very reactive and tend to be saturated with foreign atoms or small groups which lower the energy of the defect.

As seen in the case of vacancies, the honeycomb lattice can accommodate non six-membered rings such as pentagons or heptagons. This allows the existence of structural defects which do not require any missing atom. One example is the Stone-Wales (SW) defect where four hexagons are transformed into two pentagons-heptagons pairs by the rotation of a C-C bond by 90° , see Fig. 3.1(a) [Stone and Wales, 1986]. The formation energy of such a defect is $E_{SW} = 5.0$ eV and the barrier for rigidly rotating a bond by 90° is about 10 eV [Banhart *et al.*, 2011]. Similarly to vacancies, the spontaneous creation of Stone-Wales defects at equilibrium conditions for typical experimental temperature below 1000°C has a negligible probability and, indeed, SW defects have been imaged and studied in non-equilibrium conditions (e.g. under electron irradiation in TEM instruments). Importantly, it has been found in simulations that SW defects start appearing around $T = 3800$ K and are the precursors of the structural modifications that lead to the melting of graphene at $T = 4900$ K [Zakharchenko *et al.*, 2011].

Adsorbates Extra carbon atoms attached on the graphene lattice represent the simplest form of adsorbates for graphene. We point out that interstitial carbon atoms do not exist in graphene, due to the extremely high energy required to place an additional carbon atom in any in-plane position. Indeed, an extra carbon atom would preferentially bind in a bridge configuration forming covalent bonds with two atoms of the graphene lattice. The binding energy of such a defect is of the order of 1.5-2.0 eV. Carbon adatoms have a migration barrier of about 0.4 eV - one of the lowest among graphene defects - which makes them very mobile

at room temperature. For this reason, though carbon adatoms are predicted to be one of the most common defects in synthesized graphene, they are not visible in experimental images. Another consequence of the mobility of carbon adatoms is that they can recombine with vacancies, thus further lowering the equilibrium vacancy concentration at room temperature.

Extrinsic (non-carbon) adsorbates are mainly a result of the decomposition of the organic molecules used as precursors in CVD growth of graphene. Among those we mention H and O atoms, OH groups and small organic groups such as CH₃ and C₂H₅. Other species such as metal adatoms are rarely found in standard samples and, in order to be studied are intentionally deposited on graphene. The properties of adsorbates of graphene strongly depend on their bonding. Depending on the strength of the interaction, the character of the bonding can vary from prevalently van der Waals (weak interaction) to prevalently covalent (strong interaction). Hydrogen atoms form covalent bonds placing on top of a carbon atom as predicted by theory and found in experiments, see Fig. 3.1(g), and represent the prototypical monovalent adsorbate. In order to form an extra σ -bonding with an hydrogen adatom, the carbon partner changes its hybridization from sp^2 to sp^3 , thus breaking the π -bonds with its nearest carbon neighbors [Yazyev and Helm, 2007; Boukhvalov *et al.*, 2008]. The situation is very similar for other monovalent impurities (e.g. CH₃, C₂H₅, F), whereas divalent impurities such as O atoms preferentially bind in bridge configuration between two carbon atoms whose hybridization is intermediate between sp^2 and sp^3 . Besides the qualitative similarities, the calculated binding energy of monovalent impurities vary in a wide range, going from 0.27 eV for CH₃ to 1.99 eV for F [Wehling *et al.*, 2009b].

Alkali metal atoms such as Li, Na, K bind ionically to graphene sitting in the center of the hexagons, with binding energies in the range 0.48-1.08 eV [Wehling *et al.*, 2009b]. Remarkably, as strong charge transfer is responsible for ionic bonding, this class of adatoms induce doping and act as Coulomb scatterers for the charge carriers of graphene [Chen *et al.*, 2008]. Halogen atoms (Cl, I, Br) with the exception of F, form ionic bonding too, but bind preferentially in top or bridge positions [Wehling *et al.*, 2009b]. Moreover, they induce opposite doping with respect to alkali atoms.

Transition metal adatoms have on average weaker interaction with the graphene substrate, which leads to low binding energies (in a calculated range of 0.14-0.8 eV [Wehling *et al.*, 2009b]) and low migration barriers (the measured diffusion barrier of Au is about 0.26 eV). Typical configurations are on top of a carbon atom (e.g. Co) or at the center of an hexagon (e.g. Ni) [Eelbo *et al.*, 2013]. The experimental STM picture of Ni and Co atoms absorbed on graphene are shown in Fig. 3.1(h).

Substitutional impurities Boron and nitrogen, the neighbor elements of carbon in the periodic table, are natural dopants for graphene. Besides inducing a shift of the Fermi energy, such dopants can significantly alter the electronic structure of graphene. Experiments have also shown the possibility to introduce transition metal atoms in graphene vacancies, thus

effectively creating a substitutional impurity. Finally, all the mentioned dopants have been predicted to have a high formation energy 2-8 eV due to the formation of strong covalent bonding.

Properties of point defects As a general trend, adatoms bind more strongly in proximity of structural defects as the latter increase the local reactivity of the π -electron system. This is due to an effective attractive interaction between the adatoms and the strain field induced by structural defects. This suggests that a controlled introduction of structural defects in graphene could be used as a way to facilitate its chemical functionalization or even to use graphene as a catalytic substrate.

From the point of view of the electronic properties, impurities and structural defects may lead to localized states, as a consequence of breaking the crystal order. This is the case of monovalent impurities, which induce localized states close to the charge neutrality point of the undoped system, leading to a zero-energy peak in the density of states (resonant states) [Pereira *et al.*, 2006; Wehling *et al.*, 2007; Adam *et al.*, 2007; Yazyev and Helm, 2007; Wehling *et al.*, 2009b]. These states are very similar to those induced by vacancies in graphitic surfaces which, differently from vacancies in graphene, do not reconstruct. Figs. 3.1(c-d) show the STM image of such a localized state and the corresponding zero-energy peak of the local density of state measured in proximity of the vacancy. As already mentioned in Section 2.2, scattering off resonant states strongly decreases the mobility of charge carriers in graphene and has been proposed as the main scattering mechanism that determines the electronic transport properties [Wehling *et al.*, 2010]. Point defects, especially covalently bound adatoms and structural defects, give rise to a localized potential with high momentum components which is responsible for intervalley scattering. This is revealed by the characteristic D peak of Raman spectra [Ferrari *et al.*, 2006; Ni *et al.*, 2010].

Although pristine graphene is a diamagnetic system, carbon atoms with an unpaired number of electrons can give rise to a net magnetic moment. This is the case of undercoordinated atoms in proximity of defects such as single vacancies, or binding partners of monovalent adatoms [Yazyev and Helm, 2007; Yazyev, 2010; Nair *et al.*, 2013]. Alternatively, paramagnetism can be induced by magnetic adsorbates such as Fe and Co atoms [Eelbo *et al.*, 2013].

Finally, point defects, especially vacancies are expected to degrade the mechanical properties of graphene, reducing the Young modulus and the mechanical strength. Nevertheless, the efficient reconstruction of vacancies in graphene should minimize these effects.

3.3 Topological defects

Two classes of topological defects are found in monolayer graphene, namely grain boundaries and dislocations. The former are inherent to polycrystalline materials since they accommodate the mismatches of the lattice orientation. Early-day samples of graphene obtained with

mechanical exfoliation had a typical size of the order of few μm and were prevalently single-crystalline. Technological applications require a large-scale industrial production of graphene, which makes mechanical exfoliation of graphene unsuitable. In this respect, chemical vapor deposition has become the standard method for producing graphene. In this technique carbon atoms originating from the high temperature decomposition of hydrocarbon gas, usually CH_4 , assemble on a metal surface, most commonly a Cu substrate, into what will eventually become the graphene layer. Graphene single-crystalline grains with random orientation grow starting from multiple nucleation centers and eventually coalesce, thus forming a continuous layer of polycrystalline graphene. CVD gives rise to large graphene samples with small amount of disorder (except for the presence of GBs) and is a low-cost and scalable technique (we refer to Ref. [Yan *et al.*, 2014] for review of the advances of CVD production of graphene). For these reasons, the study of GBs and how they affect nearly all properties of graphene has become of paramount importance.

We will first go through the theoretical construction of grain-boundary models, introducing the concept of topological invariant. Then, we will revise the first experiments which demonstrated polycrystallinity in graphene and studied the characteristics of GBs. Finally, we will end this chapter with a brief survey on how GBs affect the properties of graphene, with a special focus on electronic transport.

Throughout this section, all the information for which no explicit references are given, are taken from Ref. [Yazyev and Chen, 2014].

3.3.1 The topological defect hierarchy in graphene

Following the Read-Shockley approach [Read and Shockley, 1950], grain boundaries can be described in terms of array of dislocations that, in turn, are formed by pairs of disclinations. Disclinations are obtained by the addition, or removal, of a semi-infinite wedge of material in an ideal 2D lattice. The corresponding topological invariant is the wedge angle s , taken positive (negative) if the wedge is added (removed). As illustrated in Fig. 3.2(a), in graphene's honeycomb lattice, positive $s = 60^\circ$ and negative $s = -60^\circ$ disclination are realized by replacing one hexagon by, respectively, a heptagon or a pentagon.

Unlike 3D materials, where several type of dislocations exist, in graphene only edge dislocations are allowed. This class of dislocations consists in the insertion of an extra semi-infinite line of atoms in the crystal. An edge dislocation is equivalent to a pair of disclinations with $s = +60^\circ$ and $s = -60^\circ$ and, therefore, the core of a dislocation in graphene consists of a pentagon-heptagon pair. The topological invariant of a dislocation is the Burgers vector, which is a proper translational vector of the lattice and describes the width of the embedded strip of material. The example of dislocation illustrated in the upper panel of Fig. 3.2(b) is realized by the closest possible arrangement of the two disclinations and corresponds to the smallest Burgers vector $\mathbf{b} = (1, 0)$. Larger distances between disclinations correspond to longer Burgers vectors, as shown in the lower panel of Fig. 3.2(b). It can be proved that the

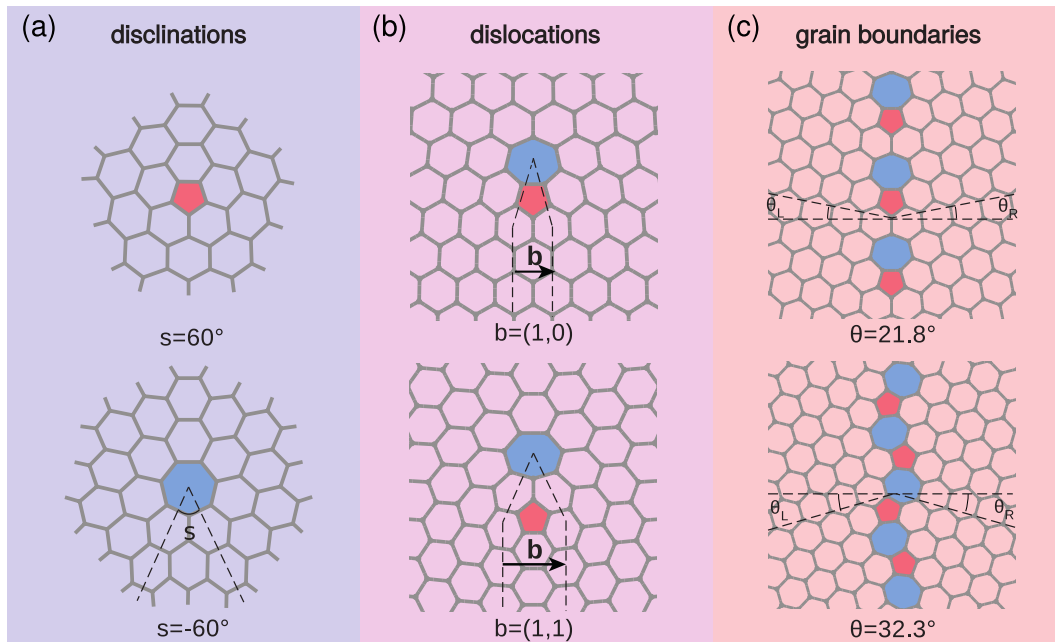


Figure 3.2 – Models of topological defects in graphene crystal lattice (disclinations, dislocations, GBs) and illustration of the corresponding topological invariants (wedge angle, Burgers vector, misorientation angle). Non six-membered rings are highlighted in blue (heptagons) and red (pentagons). (a) Positive (upper model) and negative (lower model) disclinations with wedge angle $s = \mp 60^\circ$ (b) Dislocations in graphene with Burgers vector $\mathbf{b} = (1, 0)$ (upper model) and $\mathbf{b} = (1, 1)$ (lower model). (c) Large-angle GBs formed by periodic arrays of the dislocations shown in (b). The misorientation angle is $\theta = \theta_L + \theta_R = 21.8^\circ (32.3^\circ)$ for the upper (lower) model. Reprinted with permission from (a-c) Ref [Yazyev and Chen, 2014], © 2014 *McMillan Ltd.*

distance between the two disclinations strictly corresponds to the modulus of the Burgers vector [Yazyev and Louie, 2010b].

As pointed out by Read and Shockley, GBs are equivalent to an array of dislocations [Read and Shockley, 1950]. The topological invariant for GBs is the misorientation angle $\theta = \theta_L + \theta_R$ ($0^\circ < \theta < 60^\circ$), as shown in Fig. 3.2(c). When a GB is formed by a periodic arrangement of identical dislocations, θ can be directly determined by the Frank's equations which involve the Burgers vector \mathbf{b} and the periodicity d . For $\mathbf{b} = (1, 0)$ dislocation, the Frank's equation reads:

$$\theta = 2 \arcsin \left(\frac{|\mathbf{b}|}{2d} \right), \quad (3.1)$$

whereas for $\mathbf{b} = (1, 1)$ one has

$$\theta = 60^\circ - 2 \arcsin \left(\frac{|\mathbf{b}|}{2d} \right). \quad (3.2)$$

The GB model shown in the upper panel of Fig. 3.2(c) is formed by an array of $\mathbf{b} = (1, 0)$ dislocations, whereas the building block of the model shown in the lower panel is a pair of

rotated $\mathbf{b} = (1, 0)$ dislocations. Both are examples of large-angle grain boundaries, respectively, with $\theta = 21.8^\circ$ and $\theta = 32.2^\circ$. We stress that these hierarchical rules allow to build atomic structures of dislocations and GBs containing only three-fold coordinated atoms.

The formation energies of periodic grain boundaries has been investigated by means of density functional theory and empirical classical potentials [Yazyev and Louie, 2010b; Carlsson *et al.*, 2011]. These estimates are of fundamental importance to determine the configurations of GBs at thermodynamic equilibrium. Graphene models can be either constrained to be flat, mimicking the situation where graphene strongly adhere on a substrate, or can be free to displace in the out-of-plane direction, an assumption which is suitable for modeling free-standing graphene. DFT calculated formation energies γ of periodic GBs as a function of misorientation angle θ are reported in Fig. 3.3(a). The different series of data refer to two classes of GBs built by aligning $\mathbf{b} = (1, 0)$ or a pair of rotated $\mathbf{b} = (1, 0)$ and $\mathbf{b} = (0, 1)$ dislocations. A general trend is that buckled configurations have lower γ with respect to GBs which are constrained to be in-plane, with the relevant exceptions of the two large-angle GBs with $\theta = 21.8^\circ$ and $\theta = 32.2^\circ$, for which no buckled stable configuration exist. In particular, these configurations have particularly low γ of, respectively, 0.34 eV/\AA and 0.29 eV/\AA . The latter, in particular, represents a local minimum of $\gamma(\theta)$. Out-of-plane deformations efficiently 'screen' the in-plane strain field produced by individual dislocations, thus lowering the formation energy. A different effect takes place when dislocations are densely packed, as in large-angle GBs, where the strain fields induced by individual dislocations mutually cancel each other, thus leading to flat GBs. This transition from flat large-angle GBs to buckled low-angle GBs has recently received experimental confirmation from STM studies of polycrystalline graphene epitaxially grown on SiC [Tison *et al.*, 2014]. As can be seen from eqs. 3.1,3.2, the low-angle regimes $\theta \rightarrow 0^\circ$ and $\theta \rightarrow 60^\circ$ correspond to large periodicity d that is equivalent to a low density of dislocations. This explains the decrease of γ in the low-angle regime. Notably, the behavior of γ for flat GBs in the low-angle regime can be described by the Read-Shockley equation $\gamma = A(\theta - \ln\theta)$, represented by the continuous line in Fig. 3.3(a), where the constant A depends on the elasticity constants of graphene and the radius of the dislocation core [Read and Shockley, 1950]. In this regime, out-of-plane displacement lead to a strong corrugation of the region around the defects. For instance, $\mathbf{b} = (1, 0)$ dislocations assume the shape of a prolate hillock, shown in Fig. 3.3(b). In fact, corrugation leads to finite formation energy for isolated dislocations (e.g. $\gamma = 7.5 \text{ eV}$, for $\mathbf{b} = (1, 0)$), which would otherwise diverge, as in three-dimensional bulk materials.

3.3.2 Experimental studies of topological defects

The first experimental investigations of dislocations in sp^2 -carbon materials trace back to TEM studies of dislocations in graphitic surfaces in the early 1960s [Amelinckx and Delavignette, 1960]. An atomic model of tilt GBs in graphite based on pentagon-heptagon pairs was proposed in 1966 [Roscoe and Thomas, 1966]. Few years after the observation of a single dislocation [Hashimoto *et al.*, 2004], the first atomic-scale investigation of GBs in graphene

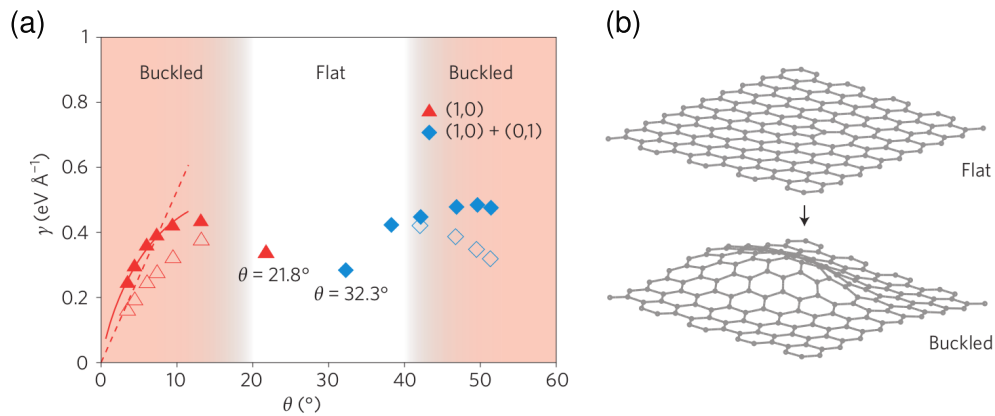


Figure 3.3 – (a) Formation energy γ of symmetric periodic GBs as a function of misorientation angle θ . The color of the markers represents the basic dislocation which constitute the GBs. The configurations corresponding to filled symbols are constrained to be planar, whereas those corresponding to open symbols are buckled. In the ranges of misorientation angle corresponding to shaded areas, buckled configurations are energetically favorable over planar ones. The solid curve represents the formation energies calculated by means of the Read-Shockley equation assuming a dislocation core radius $r_0 = 1.2 \text{ \AA}$. The dashed curve represents the formation energy calculated assuming a finite energy per dislocation of 7.5 eV. (b) Buckling of the graphene lattice induced by the introduction of an individual $\mathbf{b} = (1, 0)$ dislocation. Reprinted with permission from (a-b) Ref [Yazyev and Chen, 2014], © 2014 *McMillan Ltd.* (c) Ref. [Coraux *et al.*, 2008], © 2008 *American Chemical Society*.

appeared [Huang *et al.*, 2011]. By filtering the TEM diffraction pattern originating from a polycrystalline graphene sample, Huang *et al.* obtained a false-color image which reveals the location, the size and the orientation of the individual grains composing the sample, see Fig. 3.4(a-b). In their work, the grain distribution is approximately an exponentially decaying function of the size with a negligible number of grains larger than $1 \mu\text{m}$. On the other hand, misorientation angles between adjacent grains shows a rather complex multimodal distribution. As reported by other works, both the size and the misorientation angle distribution depend on the specific methodology employed to produce graphene. From the morphological point of view, the large-angle GBs investigated by Huang *et al.* consist in chains of alternating pentagons and heptagons containing only three-coordinated atoms, see Fig. 3.4(c), thus confirming the theoretical predictions. Differently, other works found the presence of undercoordinated atoms, whose dangling bonds are expected to be saturated by extrinsic adsorbates. Although most large-angle GBs imaged at the atomic scale reveal a meandering non-periodic shape, an example of periodic large-angle GB in epitaxial graphene has been recently reported [Ma *et al.*, 2014; Yang *et al.*, 2014; Tison *et al.*, 2014]. Low-angle grain boundaries constituted of disperse $\mathbf{b} = (1, 0)$ dislocations were imaged using STM, see Fig. 3.4(d) [Coraux *et al.*, 2008]. Although the dislocations found in this experiment did not form a periodic aligned sequence, the angle of the grain boundary was well reproduced by eq. 3.1 taking for d the average inter-dislocation distance. Moreover, the local height measured by STM confirmed the predicted corrugation of disperse dislocations.

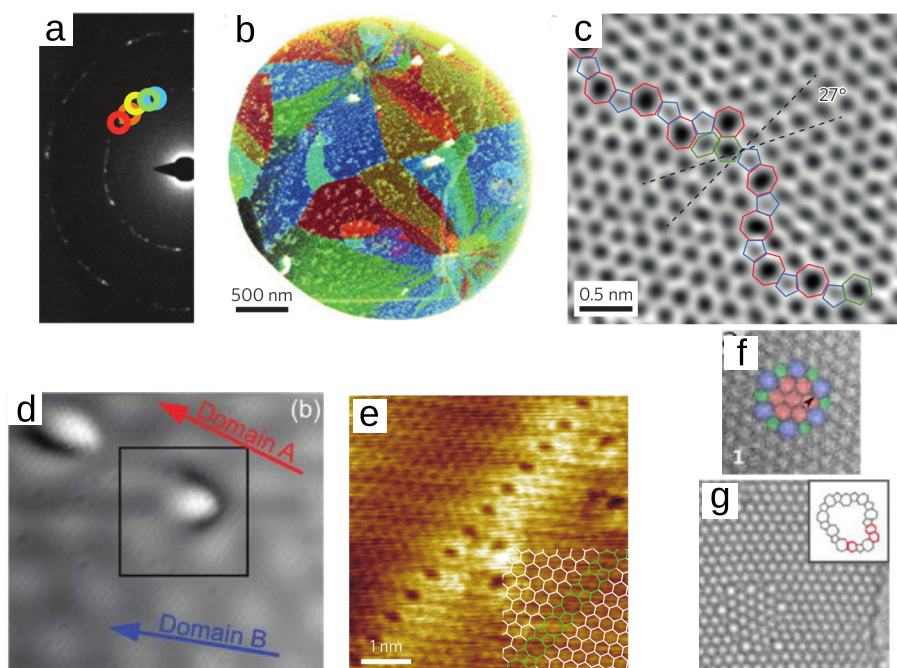


Figure 3.4 – Experimental studies of polycrystalline graphene. (a) TEM diffraction pattern originated by a polycrystalline graphene sample. Several sets of six-fold-symmetric Bragg peaks appear indicating the presence of various misoriented crystalline domains. (b) False-colored dark-field TEM image revealing individual crystalline domains. Grains are colored according to the corresponding set of Bragg peaks appearing in the diffraction pattern shown in (a). (c) Annular dark-field scanning transmission electron microscopy (ADF-STEM) image with atomic resolution showing two graphene grains with a relative rotation of 27° stitched by a grain boundary. (c) Experimental STM image showing two dislocations in a graphene sample grown on Iridium substrate. The square outlines a $\mathbf{b} = (1, 0)$ dislocation appearing as a bright protrusion. Domains A and B are misoriented by $\theta = 2.1^\circ$ which corresponds, applying eq. 3.1 and assuming that the GB contains only $\mathbf{b} = (1, 0)$ dislocations, to an average interdislocation distance of $r = 6.8$ nm, in agreement with the distance measured in the image (6.2 ± 1.3 nm). (e) STM image of a periodic line-defect in graphene grown on Ni, with the corresponding structural model overlaid. (f) TEM image of a grain-boundary forming a “flower-shaped” closed path. (g) TEM image of a grain-boundary with irregular shape. Reprinted with permission from (a-c) Ref. [Huang *et al.*, 2011], © 2011 *Mcmillan Ltd.*, (d) Ref. [Coraux *et al.*, 2008], © 2012 *American Chemical Society.*, (e) Ref. [Lahiri *et al.*, 2010], © 2010 *Mcmillan Ltd.*, (f-g) Ref. [Kurasch *et al.*, 2012], © 2012 *American Chemical Society.*

Several cases of degenerate GB, that is, line defects interfacing two grains with the same orientation, have been reported. In particular, Lahiri *et al.* observed an extended line defect made by a regular alternation of an octagon and a pair of pentagons in graphene grown on Ni(111) substrate, see Fig. 3.4(e) [Lahiri *et al.*, 2010]. More recently, Chen *et al.* managed to engineer such a degenerate GB in a controlled way [Chen *et al.*, 2014]. When GBs form closed loops they lose their topological nature, being equivalent to point defects. Such loops show a large variety going from small ordered examples, see Fig. 3.4(f), to larger disordered ones, see

Fig. 3.4(g).

Due to their increased reactivity, the atoms owing to dislocations and GBs are thought to be preferential sites for the absorption of external atoms. It was proposed that GBs can serve as pathways for spatially controlled functionalization with hydrogen or other dopants (B and N) [Brito *et al.*, 2011, 2012].

Similarly to non-topological structural defects, the motion of individual dislocations and grain boundaries has been imaged using TEM in non-equilibrium conditions. The two basic steps of dislocation motion, a glide and a climb, are realized, respectively, by means of a C-C bond rotation and removal of two carbon atoms. These two mechanisms imply high energy barriers of, respectively, 5 and 20 eV [Lehtinen *et al.*, 2013]. Similar high energy barriers have been calculated for the motion of grain boundaries with closely packed non-hexagonal rings [Kurasch *et al.*, 2012]. Therefore, the typical topological defects of graphene can be considered immobile for systems at room temperature and close to equilibrium.

Besides TEM and STM imaging techniques, Raman spectroscopy must be mentioned as a cheap and relatively simple tool to recognize GBs due to increased intensity of the D peak activated by the intervalley scattering induced by GBs [Yu *et al.*, 2011; Duong *et al.*, 2012].

3.3.3 Electronic transport in polycrystalline GBs

There is, nowadays, a large amount of studies concerning that effect of GBs on virtually all the properties of graphene. We focus here on how GBs affect electronic transport properties, as graphene is a very promising material for electronics due to the outstanding mobility of its charge carriers. In this section we define the experimental and theoretical contest which will serve as the basis for much of the work of the next chapters.

Polycrystallinity does not alter the nature of low-energy charge carrier of graphene which still show half-integer quantum Hall effect typical of massless Dirac fermions (see Section 2.3). However, the strong intervalley scattering induced by GBs changes the magnetotransport regime from weak anti-localization typical for ultra-pure single-crystal samples to weak localization (see Section 2.4).

On the other hand, there is experimental evidence that graphene GBs scatter back charge carriers, thus degrading the electronic conductivity of graphene. STM studies of the electronic states in proximity of GBs have imaged the standing wave pattern originating from the interference of the incident and the reflected wavefunctions [Koepke *et al.*, 2013]. GBs also reflect collective charge oscillations due to plasmonic excitations induced by infrared laser, as shown by means of near-field optical microscopy [Fei *et al.*, 2013]. Consequently, the electron mobilities measured on polycrystalline samples of graphene are lower than those measured on single-crystal samples, although samples with larger grain sizes have higher electron mobilities. Two-probe transport measurements in CVD samples obtained by the controlled coalescence of two grains, have shown that both the transport within each grain and across

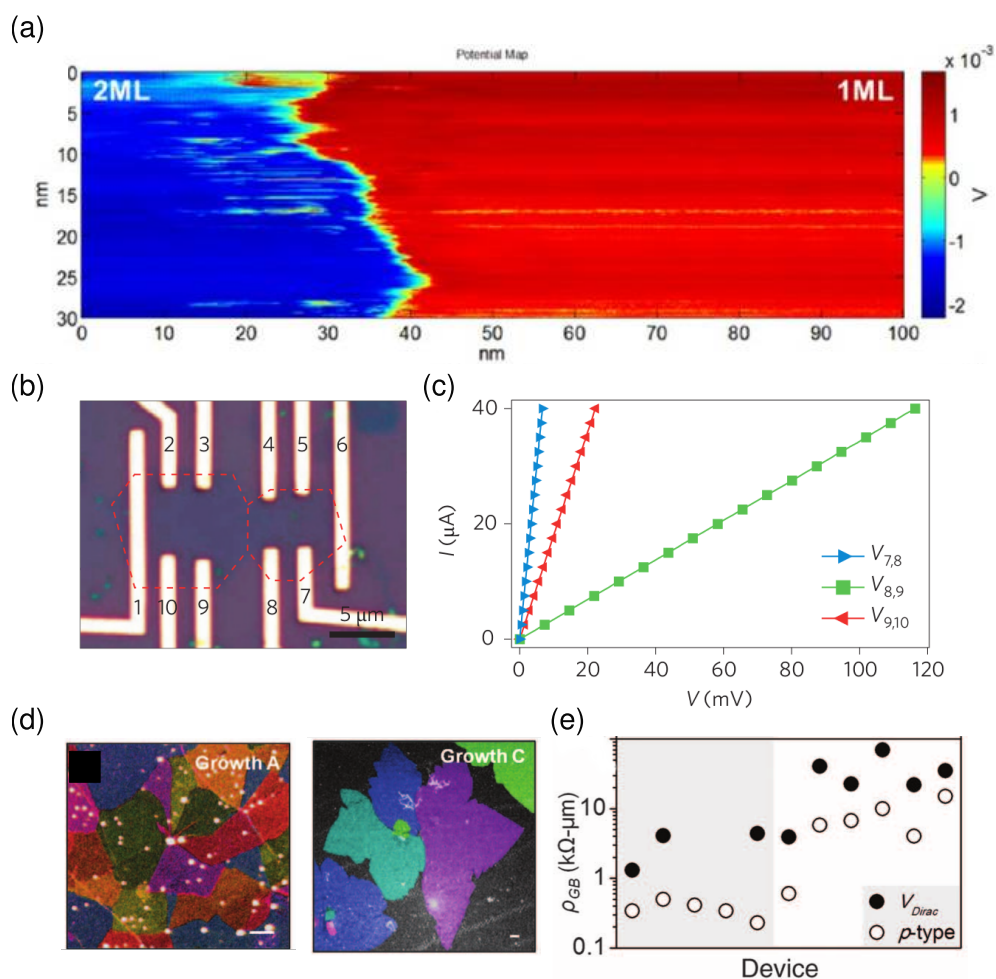


Figure 3.5 – Electronic transport across individual GBs of graphene. (a) Chemical potential map of a sample where a voltage $V = 4$ mV is established between the two boundaries. The latter are inside two distinct crystalline domains separated by a GB crossing the sample. The potential drop is largely concentrated around the GB due to its large resistivity. (b) Multi-electrode device for electronic transport measurements built on a CVD-grown sample composed by two coalesced grains. (c) Characteristic I - V curves measured for different choice of the two electrodes among those shown in (b). When the two electrodes are such that the charge carrier flow crosses the GB the resistance is larger. (d) False-color TEM images of CVD polycrystalline graphene grown under two different set of conditions denominated “Growth A” and “Growth C” (see Ref. [Tsen *et al.*, 2012] for details). (e) Resistivity (measured in $k\Omega\mu m$) of individual GBs found in samples of the same study as those shown in (d). Reprinted with permission from (a) Ref. [Clark *et al.*, 2013], © 2013 American Chemical Society, (b-c) Ref. [Yu *et al.*, 2011], © 2011 Mcmillan Ltd., (d-e) Ref [Tsen *et al.*, 2012], © 2012 American Association for the Advancement of Science.

the GB have ohmic character [Yu *et al.*, 2011]. However, the measured inter-grain resistivity $\rho_{GB} = 5000\Omega/\square$ was much larger than the intra-grain resistivity ($\rho_G = 400 - 2000\Omega/\square$), see Fig. 3.5(b-c). Chemical potential maps measured by scanning tunneling potentiometry (STP)

when a DC current is driven orthogonally to an individual GB shows that the majority of the potential drop takes place in the vicinity of the GB, see Fig. 3.5(a) [Clark *et al.*, 2013]. In these experiments the resistivity measured for different individual grain-boundaries varies can vary by up to a factor 3, very much depending on the width of the disordered region around the GBs. Tsen *et al.* investigated simultaneously the morphology (though not at the atomic level) of CVD-grown polycrystalline graphene by means of TEM and its transport properties, showing that the growth protocol used to produce graphene is essential to determine the resistivity of individual GBs [Tsen *et al.*, 2012]. With reference to Fig. 3.5(e), the method called “A” by the authors gives rise to well-stitched polygonal grains with an average size of $1\ \mu\text{m}$, whereas method “C” produces larger flower-shaped grains with average size of $50\ \mu\text{m}$. The overall lower density of GBs in “C” samples is counterbalanced by the higher resistivity of individual GBs which is, on average, one order of magnitude larger than that of “A” samples, see Fig. 3.5(e). Interestingly, in the same study the inter-grain resistivity measured in some samples was lower than the intra-grain one. This effect was explained assuming a finite overlapping between the layers of the two adjacent grains, as also suggested by the TEM images. The temperature dependence of mobility in polycrystalline graphene samples is, practically, negligible as the amount of scattering due to GBs largely overtakes that due to phonons. Finally, we remark that the interpretation of experimental data is complicated by the fact that GBs, similarly to other structural disorder, can contain various species of contaminants that further degrade conductivity and mask the intrinsic effect of GBs.

One of the first theoretical studies of electronic transport across periodic GBs derived a momentum-based selection rule which allow to sort periodic GBs in the two classes, as illustrated in Fig. 3.6 [Yazyev and Louie, 2010a]. The transmission probability for low-energy charge carriers to come across GBs owing to the first class is typically high ($T \simeq 1$), whereas the members of the second class completely reflect the charge carrier in an energy range determined by the periodicity d of the GB. The width of such a transport gap - not to be confused with a band gap - is obtained by the simple relation $E_{\text{TG}} = 1.38\ \text{eV}/d$.

Based on the experimental evidence that GBs are prevalently n -doped, whereas the bulk of the grains are rather p -doped, it was proposed that the potential barrier occurring at the GBs acts as an additional source of scattering [Song *et al.*, 2012]. Importantly, simulations performed on large-scale models of polycrystalline graphene demonstrated that conductivity scales linearly with the size of the grains, that is, inversely proportional to the density of GBs [Van Tuan *et al.*, 2013]. This indicates that coherence effects due to scattering off multiple GBs are not significant and the transport regime is diffusive. Finally, it has been proposed that the grain-boundary shown in Fig. 3.4(c) can filter charge-carriers owing to a specific valley according to their incidence angle, leading to strong valley polarization [Gunlycke and White, 2011].

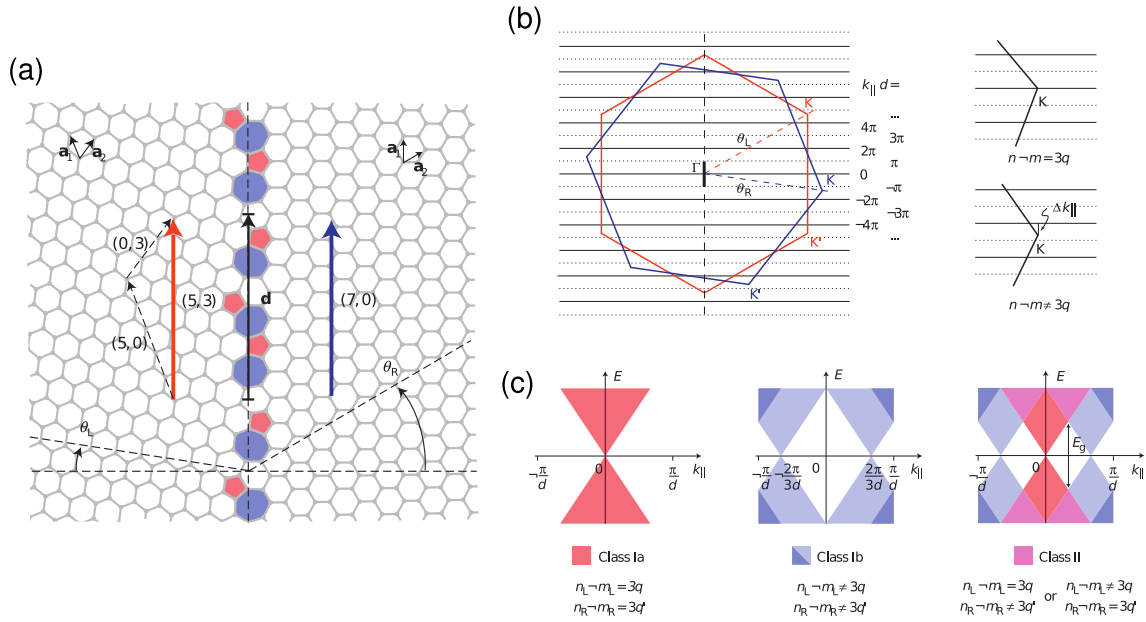


Figure 3.6 – Transmission across periodic GB. (a) Model of periodic GB interfacial two graphene domains with misorientation angle $\theta = \theta_L + \theta_R$. The chirality of each domain is defined as the components of the periodicity vector \mathbf{d} in the reference system of each lattice. (b) The Brillouin zones (BZs) of the left and right domains are rotated with respect to each other by θ . The K points of the left and right BZ are projected on either Γ or K of the 1D mini-Brillouin zone of the periodic GB, according to their chirality (n, m) . (c) If the K points of both domains are projected in the same point of the 1D-BZ, states in the left and right domains overlap and there exist transmission channels in the whole energy range (Class I GBs). Conversely, if the K points of the two domains are projected onto different points of the 1D-BZ, a transport gap appears in the energy range where the projected states do not overlap (Class II GBs). Figures reprinted with permission from Ref. [Yazyev and Louie, 2010a], © 2010 *McMillan. Ltd.*

3.3.4 Stacking domain boundaries in bilayer graphene

In bilayer graphene, the relative interlayer shift represents an additional degree of freedom with respect to monolayer graphene. As said in Chapter 1, the so-called Bernal stacking represents the configuration that minimizes the interlayer energy. However, Bernal stacking comes in two inequivalent realizations that conventionally go under the name of AB and BA (sometimes referred to as AC), and are connected by a rotation of 60° of the whole system, see Fig. 3.7(a). Of course, these two stacking orders have the same interlayer energy per atom, so that in one sample of bilayer graphene regions with inequivalent Bernal stacking can coexist. This situation has turned out to be very common in micro-meter scale bilayer graphene samples where the whole surface is tiled by domains with inequivalent stacking, see Figs. 3.7(b-c) [Brown *et al.*, 2012; Lin *et al.*, 2013; Alden *et al.*, 2013]. Regions with definite Bernal stacking have a size varying from few tens to hundreds of nanometers and the transition between two adjacent AB and BA stacking domains is confined in regions with a typical width

of ≈ 10 nm, called stacking domain boundaries. Such defects have a topological nature and their topological invariant is the difference of the vectors representing the interlayer shift of the two interfacing domains. At a closer inspection, stacking domain boundaries appear as strain solitons with shear or tensile character, as shown in Figs. 3.7(d-e). Solitons with hybrid tensile-shear character have also been found in experiments [Alden *et al.*, 2013]. Equivalently, stacking domain boundaries can be described as partial dislocations, that is, dislocations with a Burgers vector which is a fraction of a translational vector of the bilayer graphene lattice [Butz *et al.*, 2014]. Finally, stacking domains can arrange in a relatively regular hexagonal pattern, as shown in Fig. 3.7(c) [Alden *et al.*, 2013]. In Chapter 7, this pattern will be shown to be the relaxed configuration of bilayer graphene samples with a small rotation angle between the two layers.

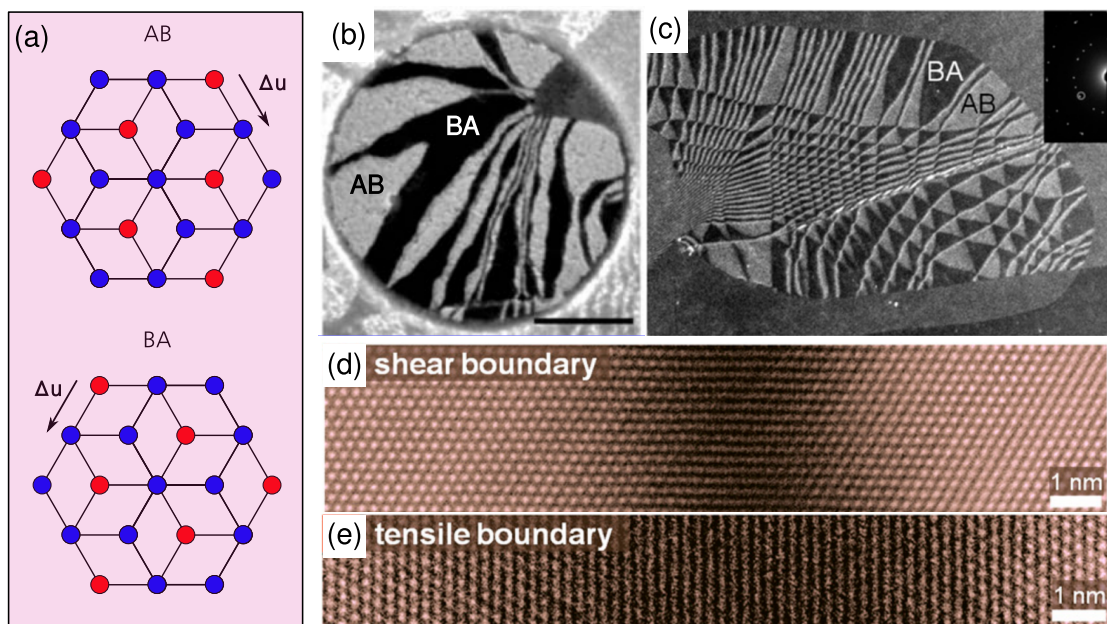


Figure 3.7 – Experimental images of stacking domain boundaries in bilayer graphene. (a) False-color dark field-TEM image of bilayer graphene. Bright and dark areas correspond to inequivalent AB or BA stacking. (b) False-color dark field-TEM image of bilayer graphene. In large part of the sample stacking domains arrange in a hexagonal network. (c-d) Scanning TEM images of stacking domain boundaries. In particular, the defect in (c) is a shear soliton, whereas the defects in (d) is a tensile soliton. Reprinted with permission from (b) Ref. [Lin *et al.*, 2013], © 2013 American Chemical Society, (c-e) Ref. [Alden *et al.*, 2013], © 2013 National Academy of Science.

4 Methods

4.1 Density functional theory

Density Functional Theory (DFT) is a mean field theory for the ground state of a system of interacting particles. Very often the system under study is represented by the electrons of a molecule or a solid, once the electronic degrees of freedom have been separated from the nuclear ones by means of the Born-Oppenheimer approximation. The key object of DFT is the density $n(\mathbf{r})$ of a system of N particles, defined such that

$$\int n(\mathbf{r}) \, d\mathbf{r} = N. \quad (4.1)$$

The two fundamental theorems of DFT are due to Hohenberg and Kohn (Nobel Prize in 1998) [Hohenberg and Kohn, 1964]. We state them omitting the proof:

1. The ground state density $n_0(\mathbf{r})$ of a system of interacting particles uniquely determines the external potential $v_{ext}(\mathbf{r})$ acting on the particles except for a constant shift. An immediate corollary is that the ground state density fixes the Hamiltonian of the system, which, in turn, determines the many-body wavefunction for all states and, ultimately, all the properties of the system. In most practical cases, v_{ext} is the potential generated by the nuclei in a certain spatial configuration.
2. The total energy E is given by a *universal functional* $E(n)$ of the ground state density. For a specific system, defined by a particular potential $v_{ext}(\mathbf{r})$, the exact ground state density n_0 minimizes the value of the functional $E(n)$. So the search for the ground state density is reduced to a variational problem.

A more clear expression of $E(n)$ is obtained by writing its contributions explicitly:

$$E[n(\mathbf{r})] = T[n(\mathbf{r})] + V_{ee}[n(\mathbf{r})] + \int d\mathbf{r} v_{ext}(\mathbf{r}) n(\mathbf{r}), \quad (4.2)$$

where T is the kinetic energy, V_{ee} the energy of the mutual interaction between the particles, and $\int d\mathbf{r} v_{ext}(\mathbf{r}) n(\mathbf{r})$ is the contribution due to the interaction with the external potential. The exact knowledge of $E[n(\mathbf{r})]$ would allow to determine the ground state energy and density. Unfortunately, there are two main limitations to DFT: i) the functional $E[n]$ is not known and ii) DFT's basic formulation tells little about the excited states which, on the other hand, can be of great interest. As an example, the optical properties of a system are inherently excited-state properties. Besides its limitations, DFT leads to an enormous simplification of quantum mechanics: it allows to treat a many-body system by handling a real field with 3 degrees of freedom (the density) instead of a complex field with $3N$ degrees of freedom (the many-body wavefunction). The *ansatz* proposed by Kohn and Sham represented a further important step for practical applications of DFT [Kohn and Sham, 1965]. This consists in introducing an auxiliary system of N independent particles described by an orthonormal set of wavefunctions $\{\phi_i(\mathbf{r})\}_{i=1}^N$, having the same ground-state density as that of the interacting system under study:

$$n(\mathbf{r}) = n(\mathbf{r})_{\text{KS}} = \sum_i |\phi_i(\mathbf{r})|^2. \quad (4.3)$$

More specifically, the energy functional can be written as

$$E_{\text{KS}}[n(\mathbf{r})] = T_s[n(\mathbf{r})] + \int d\mathbf{r} v_{ext}(\mathbf{r}) n(\mathbf{r}) + E_{\text{Hartree}}[n(\mathbf{r})] + E_{\text{xc}}[n(\mathbf{r})]. \quad (4.4)$$

Due to the Kohn-Sham *ansatz*, the kinetic energy is

$$T_s[n(\mathbf{r})] = -\frac{1}{2} \sum_{i_{\text{occ}}} d\mathbf{r} \phi_i^*(\mathbf{r}) \nabla^2 \phi_i(\mathbf{r}). \quad (4.5)$$

Moreover, in eq. 4.4, the energy due to the mutual interaction of the particles has been broken in two terms: the classical Coulomb contribution

$$E_{\text{Hartree}}[n(\mathbf{r})] = \frac{1}{2} \int \frac{n(\mathbf{r}) n(\mathbf{r}')}{|\mathbf{r} - \mathbf{r}'|} d\mathbf{r} d\mathbf{r}' = \frac{1}{2} \int n(\mathbf{r}) \hat{v}_{\text{H}}(\mathbf{r}) d\mathbf{r}, \quad (4.6)$$

with

$$\hat{v}_{\text{H}} = \int \frac{n(\mathbf{r}')}{|\mathbf{r} - \mathbf{r}'|} d\mathbf{r}', \quad (4.7)$$

and the exchange-correlation energy $E_{\text{xc}}[n(\mathbf{r})]$ that contains purely quantum many-body contributions to the total energy and is defined by eq. 4.4 itself.

By applying the variational principle to eq. 4.4, together with the orthonormality conditions

$$\int d\mathbf{r} \phi_i(\mathbf{r}) \phi_j(\mathbf{r}) = \delta_{ij}, \quad (4.8)$$

a set of Schrödinger-like equations, the so-called Kohn-Sham equations can be derived:

$$\begin{aligned} H_{\text{KS}}\phi_i &= \left(-\frac{1}{2}\nabla^2 + \hat{v}_s \right) \phi_i = \epsilon_i \phi_i, \\ \hat{v}_s &= \hat{v}_{\text{ext}} + \hat{v}_{\text{H}} + \hat{v}_{\text{xc}}. \end{aligned} \quad (4.9)$$

It is important to stress that both the ϕ_i s and the eigenvalues ϵ_i have no physical meaning, as the former are the wavefunctions of a fictitious system of non-interacting particles and the latter are Lagrange multipliers used to implement the constraint 4.8.

Over the years, a large theoretical effort has been devoted to the search of reliable approximations to the functional $E_{\text{xc}}[n]$. The two most common classes of approximations are the local density approximation (LDA), and the generalized gradient approximation (GGA). In the LDA, the exchange-correlation density is a local functional of the density :

$$E_{\text{xc}}^{\text{LDA}}[n] = \int d\mathbf{r} n(\mathbf{r}) \epsilon_{\text{xc}}(n(\mathbf{r})), \quad (4.10)$$

where ϵ_{xc} is often a function parametrized in order to reproduce the exchange-correlation energy of a homogeneous electron gas, calculated to great accuracy by Monte Carlo methods [Ceperley and Alder, 1980]. GGA denotes a large variety of functionals devised to account for non-smooth variations of the density. For this reason, the gradient ∇n explicitly enters the definition of the functional:

$$E_{\text{xc}}^{\text{GGA}}[n] = \int d\mathbf{r} n(\mathbf{r}) \epsilon_{\text{xc}}(n(\mathbf{r}), |\nabla n|). \quad (4.11)$$

GGA functionals represent a wide range of functionals due to the freedom in the definition of $\epsilon_{\text{xc}}(n(\mathbf{r}), |\nabla n|)$. One of the most (if not the most) popular GGA functional is due to Perdew, Burke and Enzerhof (PBE) [Perdew *et al.*, 1996]. In this thesis, we have used the PBE functional for all the calculations concerning monolayer graphene.

More recently, fully non-local corrections to the exchange-correlation functional have been proposed. The main purpose of such corrections is to describe long-range interactions such as van der Waals forces that have an intrinsic non-local nature. The general form of a non-local functional is:

$$E_c^{\text{nl}} = \iint d\mathbf{r} d\mathbf{r}' n(\mathbf{r}) \Phi(n(\mathbf{r}), n(\mathbf{r}'), |\nabla n(\mathbf{r})|, |\nabla n(\mathbf{r}')|, \mathbf{r}, \mathbf{r}') n'(\mathbf{r}). \quad (4.12)$$

Once more, the arbitrariness of the kernel Φ leaves a large freedom in the definition of the non-local correction E_c^{nl} . Among all the functionals taking advantage of non-local corrections, we mention the revised version of the functional proposed by Vydrov and van Voorhis (revised VV10, or rVV10) [Vydrov and Voorhis, 2010; Sabatini *et al.*, 2013]. In this thesis, we have used the rVV10 functional for all calculations concerning bilayer graphene, due to its capability of describing accurately the van der Waals interaction between graphene layers.

To conclude this simplified presentation of DFT, we give some details about actual calculations based on the solution of the Kohn-Sham equations 4.9. The variational search of the ground-state Kohn-Sham wavefunction is performed in a restricted Hilbert space. This is typically the space generated by a basis set of wavefunctions. The choice of the basis set is between plane waves or some set of localized wave functions. Plane waves are endowed with many convenient properties: they form an orthonormal and complete basis (or at least arbitrarily completable), and they can naturally form Bloch states for periodic systems. On the other hand, a large number of wavefunctions may be needed to correctly reproduce the atomic-like density in proximity of the nuclei. Localized basis sets of atomic-like orbitals have the advantage of describing rather accurately the density close to the nuclei. Moreover, codes based on localized basis sets need generally a smaller amount of computational resources. On the other hand, atomic-like orbitals do not form a complete basis and are less efficient than plane waves in reproducing the density in the interatomic region.

A simplification of Kohn-Sham equations comes from the pseudopotential approach, first introduced in 1934 by Hellmann in a more general context of many-body problems [Hellmann, 1935]. The introduction of a pseudopotential has a double aim: first, to limit the complexity of the problem by treating explicitly only valence electrons. For this reason, the combined effect of the nucleus and the core electrons on the valence electrons of an atom is described by introducing an effective potential, a pseudopotential indeed. When doing this, the “frozen-core” approximation is assumed, which implies that the core-electron distribution does not change upon physical or chemical stimuli. The validity of this assumption is crucial to ensure pseudopotential transferability, that is, the capability to describe the effect of the core electrons for different states of the valence electrons. Transferability allows to use the same pseudopotentials for different purposes, such as describing atoms in gas phase, ionized, forming chemical bonds, etc. The second aim is to replace the wavefunctions of the valence electrons by smoother pseudo-wavefunctions, especially in the regions close to the nuclei. This is achieved by taking advantage of the intrinsic arbitrariness in the definition of pseudopotentials.

The pseudopotentials used in this thesis own to two classes: norm-conservative [Hamann *et al.*, 1979] and ultrasoft [Vanderbilt, 1990]. The former ensure that the norm of the pseudo-wavefunctions ψ_i coincides with the all-electron wavefunctions ϕ_i , beyond a cut-off ratio r_c . Norm-conserving pseudopotentials have the advantage of preserving the form of the Kohn-Sham equations 4.9. However, in the Hamiltonian H_{KS} , the external potential \hat{v}_{ext} is replaced by the pseudopotential:

$$H_{\text{KS}} = \hat{v}_{\text{pseudo}} + \hat{v}_{\text{H}} + \hat{v}_{\text{xc}} \quad (4.13)$$

In ultrasoft pseudopotentials, the rigid constraint on the norm of the pseudo wave-functions is lifted at the expense of transforming the Kohn-Sham problem, eq. 4.9, in a generalized

eigenvalue problem:

$$H_{\text{KS}}\Psi_i = \epsilon_i S\Psi_i, \quad (4.14)$$

where the overlap operator S is defined such that $\langle \Psi_i | S | \Psi_j \rangle = \delta_{ij}$. A thorough treatment of the pseudopotential theory can be found in the textbook of R. Martin [Richard M. Martin, 2013].

For the DFT calculations reported in this thesis, we have employed two established open-source codes, both based on pseudopotentials: QUANTUM ESPRESSO [Giannozzi *et al.*, 2009] and SIESTA [Soler *et al.*, 2002]. The two codes differ mainly, but not exclusively, in the basis set used to expand wavefunctions: QUANTUM ESPRESSO employs plane waves, whereas SIESTA employs localized atomic-like orbitals. Moreover, SIESTA can only take advantage of norm-conserving pseudopotentials, whereas QUANTUM ESPRESSO allows to choose between several classes of pseudopotentials, among which norm-conserving and ultrasoft.

4.2 Minimization methods

One problem that will occur several times during the following chapters is the search of the equilibrium configuration of a system of interacting atoms. This problem is also called a geometry optimization or a structural relaxation. As long as the mutual interactions between particles are described by classical forces, an equilibrium state is defined as a state where the total force acting on each atom is zero. In case of conservative force, this problem reduces to the search of the minimum of the potential energy $E(\mathbf{x})$ with respect to the positions of N particles, collected in the $3N$ -dimensional vector \mathbf{x} .

A large set of numerical methods has been developed to tackle the problem of minimizing a function, though it must be stressed that none of them guarantees to find an absolute minimum. These methods are rather conceived to find a local minimum, often the closest minimum to the starting configuration \mathbf{x}_0 . For this reason, an educated guess of \mathbf{x}_0 , based on physical arguments, remains the key for a successful and efficient structural relaxation.

Minimization methods can be also applied to structural relaxations of quantum systems. However, instead of the potential energy, one should rather minimize the total energy of the system, which contains also contributions of kinetic and exchange nature. Therefore, those methods which intrinsically rely on total energy calculations, such as DFT, are very suitable for structural relaxation.

We now give a short introduction of the two methods that we have mostly employed in this thesis: conjugate gradient (CG) and fast inertia relaxation engine (FIRE). These are the two methods that we have employed for all structural relaxations of graphene structures based on classical potentials, performed by using the code LAMMPS [Plimpton, 1995; LAMMPS]. Concerning relaxations based on *ab initio* calculation of total energies, we have used the default

methods implemented in SIESTA and QUANTUM ESPRESSO that are, respectively, conjugate gradient and the Broyden-Fletcher-Goldfarb-Shanno (BFGS) method. A presentation of the latter method can be found in Ref. [Fletcher, 2013].

4.2.1 Conjugate gradient

The original conjugate gradient method is an algorithm to find the numerical solution \mathbf{x} of a linear system defined by a real, symmetric, and positive definite $N \times N$ matrix \mathbf{A} , and a N -dimensional real vector \mathbf{b} [Hestenes and Stiefel, 1952]:

$$\mathbf{Ax} = \mathbf{b}. \quad (4.15)$$

However, its importance resides in its extension to the minimization of nonlinear functions [Fletcher and Reeves, 1964]. Due to the positive-definiteness of \mathbf{A} , solving eq. 4.15 is equivalent to search for the minimum of the quadratic form

$$f(\mathbf{x}) = \frac{1}{2} \mathbf{x}^T \mathbf{Ax} - \mathbf{b}^T \mathbf{x} + c, \quad (4.16)$$

where c is a real constant. Suppose we know a complete set of independent vectors $\{\mathbf{p}_i\}_{i=1}^N$, with the property of being conjugated, that is, mutually orthogonal with respect to the scalar product defined by \mathbf{A} :

$$\mathbf{p}_i^T \mathbf{A} \mathbf{p}_j = 0 \quad i \neq j. \quad (4.17)$$

The solution \mathbf{x} of the system 4.15 can be expanded in the basis $\{\mathbf{p}_i\}_{i=1}^N$ as

$$\mathbf{x} = \sum_{i=1}^N \alpha_i \mathbf{p}_i. \quad (4.18)$$

The problem is solved if the coefficients α_i are known, but this can be achieved by left-multiplying eq. 4.18 by \mathbf{A} :

$$\mathbf{Ax} = \sum_{i=1}^N \alpha_i \mathbf{A} \mathbf{p}_i = \mathbf{b} \quad (4.19)$$

and left-multiplying, again, by the vectors \mathbf{p}_k :

$$\mathbf{p}_k^T \mathbf{Ax} = \sum_{i=1}^N \alpha_i \mathbf{p}_k^T \mathbf{A} \mathbf{p}_i = \mathbf{p}_k^T \mathbf{b} \iff \alpha_k = \frac{\mathbf{p}_k^T \mathbf{b}}{\mathbf{p}_k^T \mathbf{A} \mathbf{p}_k}. \quad (4.20)$$

So the problem is recast in the construction of the conjugate basis $\{\mathbf{p}_i\}_{i=1}^N$. If one starts from a set of linearly independent vectors $\{\mathbf{u}_i\}_{i=1}^N$, a conjugate basis can be obtained by a procedure

similar to the Gram-Schmidt orthogonalization algorithm, that gives

$$\mathbf{p}_k = \mathbf{u}_k - \sum_{i < k} \frac{\mathbf{p}_i^T \mathbf{A} \mathbf{u}_k}{\mathbf{p}_i^T \mathbf{A} \mathbf{p}_i} \mathbf{p}_i. \quad (4.21)$$

The main drawback of this procedure is that the number of operation required to generate the basis $\{\mathbf{p}_i\}_{i=1}^N$ has complexity $\mathcal{O}(N^4)$. However, it turns out that a particular choice of the vectors \mathbf{u}_k reduces the time complexity to $\mathcal{O}(N^3)$. Once defined $\mathbf{x}_k = \sum_{i=1}^k \alpha_k \mathbf{p}_k$, \mathbf{u}_k is taken as the residual $\mathbf{r}_k = \mathbf{b} - \mathbf{A} \mathbf{x}_{k-1}$. It can be shown that the residual \mathbf{r}_k has the property to be conjugate to all vectors \mathbf{p}_i for $i < k-1$. This property enormously simplifies the Gram-Schmidt orthogonalization formula that becomes

$$\mathbf{p}_{k+1} = \mathbf{r}_{k+1} - \frac{\mathbf{p}_k^T \mathbf{A} \mathbf{r}_{k+1}}{\mathbf{p}_k^T \mathbf{A} \mathbf{p}_k} \mathbf{p}_k = \mathbf{r}_{k+1} + \frac{\mathbf{r}_{k+1}^T \mathbf{r}_{k+1}}{\mathbf{r}_k^T \mathbf{r}_k} \mathbf{p}_k, \quad (4.22)$$

where the last equality is another consequence, though not evident, of the conjugacy of the residuals. The coefficients α_k are calculated from eq. 4.20:

$$\alpha_k = \frac{\mathbf{p}_k^T \mathbf{b}}{\mathbf{p}_k^T \mathbf{A} \mathbf{p}_k} = \frac{\mathbf{r}_k^T \mathbf{r}_k}{\mathbf{p}_k^T \mathbf{A} \mathbf{p}_k}. \quad (4.23)$$

The last equality in eq. 4.23 is, again, a consequence of residuals' conjugacy.

We have now all the ingredients to extract an algorithm out of the mathematics. We only need to set the starting point of the search. Let us assume that the starting guess for the solution is $\mathbf{x}_0 = \mathbf{0}$, which can always be assumed if the original system is replaced by $\mathbf{A} \bar{\mathbf{x}} = \mathbf{b} - \mathbf{A} \mathbf{x}_0$. Thus, the initialization of the algorithm is:

$$\mathbf{r}_1 = \mathbf{b} - \mathbf{A} \mathbf{x}_0 = \mathbf{b}, \quad \mathbf{p}_1 = \mathbf{r}_1. \quad (4.24)$$

Then, the iterative block is formed by the instructions:

1. Calculation of the Fourier coefficient α_k , by using eq. 4.23,
2. Update of the solution $\mathbf{x}_k = \mathbf{x}_{k-1} + \alpha_k \mathbf{p}_k$,
3. Update of the residual $\mathbf{r}_{k+1} = \mathbf{r}_k - \alpha_k \mathbf{A} \mathbf{p}_k$,
4. Construction of the next conjugate direction \mathbf{p}_{k+1} , by using eq. 4.22.

The conjugate gradient method assures that the exact solution of a linear system is found within N iterations, in absence of round-off errors. Indeed, the latter makes that at each iteration k , the new direction \mathbf{p}_{k+1} is not exactly conjugate to all the previous ones. This implies that the N -dimensional space of the problem is not fully spanned after N iterations.

Chapter 4. Methods

Therefore, reaching the exact solution within a fixed numerical precision often requires more than N steps.

An important property of coefficients $\alpha_1, \alpha_2, \dots, \alpha_n$ calculated by means of eq. 4.23 is that $\forall n < N$, they minimize the function $f(\mathbf{x})$ in the subspace generated by the vectors $\{\mathbf{p}_k\}_{k=1}^n$:

$$f\left(\mathbf{x} = \sum_{k=1}^n \alpha_k \mathbf{p}_k\right) = \min_{(\bar{\alpha}_1, \bar{\alpha}_2, \dots, \bar{\alpha}_n) \in \mathbb{R}^n} f\left(\mathbf{x} = \sum_{k=1}^n \bar{\alpha}_k \mathbf{p}_k\right). \quad (4.25)$$

Therefore, each coefficient α_k minimizes $f(\mathbf{x})$ along the conjugate direction defined by \mathbf{p}_k :

$$f(\mathbf{x}_k = \mathbf{x}_{k-1} + \alpha_k \mathbf{p}_k) = \min_{\bar{\alpha}} f(\mathbf{x}_k = \mathbf{x}_{k-1} + \bar{\alpha} \mathbf{p}_k), \quad (4.26)$$

whence

$$\frac{\partial f(\mathbf{x}_{k+1} = \mathbf{x}_k + \bar{\alpha} \mathbf{p}_{k+1})}{\partial \bar{\alpha}} = 0 \quad \forall k < N. \quad (4.27)$$

Obviously, the minimization problems which typically arise during the structural relaxation of an atomic system are far from being linear. However, in proximity of a minimum $\bar{\mathbf{x}}$, the potential energy surface $E(\mathbf{x})$ can be approximated by the quadratic form

$$E(\mathbf{x}) \simeq E(\bar{\mathbf{x}}) + \frac{1}{2} (\mathbf{x} - \bar{\mathbf{x}})^T \mathbf{H} (\mathbf{x} - \bar{\mathbf{x}}) + o(|\mathbf{x} - \bar{\mathbf{x}}|^3), \quad (4.28)$$

where \mathbf{H} is the Hessian matrix calculated at $\bar{\mathbf{x}}$. For the quadratic form, eq. 4.16, the following two identities hold:

$$\nabla f(\mathbf{x}) = \mathbf{A}\mathbf{x} - \mathbf{b} = -\mathbf{r}, \quad (4.29)$$

and

$$\mathbf{H}_{ij} = \frac{\partial^2 f}{\partial x_i \partial x_j} = \mathbf{A}_{ij}. \quad (4.30)$$

These suggest that the conjugate gradient method can be extended to non-quadratic functions by implementing the following two substitutions:

$$\mathbf{r}_k \leftarrow -\nabla E(\mathbf{x}_k), \quad (4.31)$$

and

$$\mathbf{A}_k \leftarrow \mathbf{H}(\mathbf{x}_k). \quad (4.32)$$

However, conjugacy of the search direction partially loses its power because the Hessian matrix changes at any update of the position \mathbf{x} . As the calculation of the Hessian matrix $\mathbf{H}(\mathbf{x}_k)$ is an expensive operation, eq. 4.23 is not the choice of preference to calculate the optimal

coefficients α_k . From eq. 4.27, it follows that the coefficients α_k can be found by minimizing f along the direction $\mathbf{x}_{k-1} + \alpha_k \mathbf{p}_k$. The advantage is that many of the available methods used to minimize one-variable functions only require first derivative (see Ref. [Dennis and Schnabel, 1996] for a detailed discussion).

For the update of the conjugate direction, eq. 4.22 is often replaced by

$$\mathbf{p}_{k+1} = \mathbf{r}_{k+1} + \beta_{k+1} \mathbf{p}_k \quad \beta_{k+1} = \max \left\{ 0, \frac{\mathbf{r}_{k+1}^T (\mathbf{r}_{k+1} - \mathbf{r}_k)}{\mathbf{r}_k^T \mathbf{r}_k} \right\} \quad (4.33)$$

which is equivalent to eq. 4.22 for quadratic forms. This variant, due to Polak and Ribière, is thought to be the most effective CG choice for the majority of nonlinear problems [Polak and Ribière, 1969]. The nonlinear conjugate gradient method is constituted by two nested loop: i) an external loop where the “pseudo-conjugate” search direction is updated and ii) an internal loop where coefficients α are calculated by means of a line-search method, which is inherently iterative. Unlike the linear case, there is no guarantee for the number of steps required to converge to the solution, even in absence of round-off errors. We refer to the manual page of LAMMPS, <http://lammps.sandia.gov/>, for details of the implementation of conjugate gradient as well as line-search methods.

4.2.2 Fast Inertia Relaxation Engine (FIRE) method

Minimization methods based on molecular dynamics (MD methods) use some modified form of Newton’s equations for the atomic coordinates \mathbf{x} , conceived to drive the system toward a minimum of the potential energy surface $E(\mathbf{x})$. Given an initial position in the configuration space $\mathbf{x}_0 = \mathbf{x}(t = 0)$, the trajectory $\mathbf{x}(t)$, solution of the Newton-like equations, approaches asymptotically the position $\bar{\mathbf{x}}$ of a minimum of $E(\mathbf{x})$:

$$\lim_{t \rightarrow \infty} \mathbf{x}(t) = \bar{\mathbf{x}}. \quad (4.34)$$

The trajectory $\mathbf{x}(t)$ may be calculated numerically by employing one of the well-established integrators used in molecular dynamics (see Ref. [Frenkel and Smit, 2001], for example).

One of the best performing MD methods is the so-called “fast inertia relaxation engine” (FIRE) [Bitzek *et al.*, 2006]. This method is defined by the equation of motion:

$$\dot{\mathbf{v}}(t) = \frac{\mathbf{F}(t)}{m} - \gamma(t) |\mathbf{v}(t)| (\hat{\mathbf{v}}(t) - \hat{\mathbf{F}}(t)), \quad (4.35)$$

where $\mathbf{v}(t)$ is the velocity, $\mathbf{F} = -\nabla E(\mathbf{x})$ is a conservative force, the hat indicate a unit vectors and $\gamma(t)$ is a free positive parameter of the method. With respect to Newton’s equation, eq. 4.35 contains an additional term which is maximum in modulus when \mathbf{v} and \mathbf{F} have opposite directions and is strictly zero when \mathbf{v} and \mathbf{F} are aligned. In other words, when the system moves in the direction of \mathbf{F} , it is governed by standard Newtonian dynamics. In the most

undesired situation where the system is moving uphill, the additional force acts as a viscous damper. In the more common case when \mathbf{v} and \mathbf{F} are neither parallel nor antiparallel, the additional force helps in realigning the velocity to the acceleration. The logic behind this method is traditionally explained by analogy to a “blind skier” who is skiing on a mountain profile which is unknown to him and wants to reach the bottom of the valley. He only feels whether the total force acting on him is parallel to the direction of his motion and, if this is not the case, he can steer, that is, generates an additional force in order to redirect his motion toward the steepest descent, or can even slow down, if he is going uphill.

In our experience, the FIRE method turned out to be very useful to refine a first estimate of the energy minimum obtained by the conjugate-gradient method. This fine search was useful in those situations where conjugate gradient stopped because the line-search step of the algorithm returned a value of α comparable with the precision of the machine.

4.3 Long-range Carbon Bond-Order Potential (LCBOP)

Classical potentials are a common tool to treat the interactions of the atoms that compose a system. It must be clear that classical potentials represent a computational tool, as the nature of atomic interactions is inherently quantum. The problem is that treating atomic systems in a fully quantum way, that is, solving the many-body Schrodinger equation is an impossible task, except for extremely simple systems. Even after the breakthrough represented by DFT, the search for the ground state properties of an atomic system is a realistic purpose only as long as the number of atoms is kept within the order of magnitude of a thousand. On the other hand, the advantages of a classical rather than quantum representation of the atomic interactions are evident. First, the dynamics of the system is governed by Newton’s law, and the equilibrium configurations of the system correspond to minima of the total potential energy E_p . The latter simply becomes the sum of the contributions V_{ij} due to the interaction of each pair of atoms (i, j) :

$$E_p = \frac{1}{2} \sum_i \sum_{j \neq i} V_{ij} \quad (4.36)$$

The computational effort to calculate those observables that can be consistently defined in a classical picture (for example, the lattice constant of a crystal, but not the band gap), is considerably smaller than a quantum treatment, even when this latter contains severe approximations.

There is no established functional form for a classical potential. Once an analytic expression is proposed, the parameters that define the potential are fitted to a selected database of observables (formation energy, bondlengths, elastic coefficients, etc.). This database may be derived from experiments or from *ab initio* theoretical methods, that is, with no adjustable parameters. In this sense, classical potentials are also called empirical potentials. The entries of a good fitting database contain multiple observables for a relatively wide range of structures. A

good database for carbon should contain observables for systems with different hybridizations and dimensionality, such as diamond, graphite, graphene, nanotubes, etc. As a general requirement, classical potentials must have the two following features:

- **Transferability:** once the potential has been optimized in its parameters, it should be able to reproduce data for observables and systems beyond the fitting database. For example, in this thesis, classical potentials have been used to study topological defects in graphene.
- **Computational efficiency:** The potential must perform better than any quantum method in calculating a specific observable, from the point of view of computational resources.

Given the absence of a recipe for defining a potential, it should not surprise that many different potentials exist for carbon. In this section, we describe the Long-Range Carbon Bond-Order Potential (LCBOP) [Los and Fasolino, 2003], mostly following the presentation of Ref. [Ghiringhelli, 2006]. The LCBOP belongs to the more general class of bond order potentials (BOP). The general form for the bond-order potential energy of two atoms, labeled by i and j , at the distance r_{ij} , is

$$V_{ij} = V^R(r_{ij}) - b_{ij}V^A(r_{ij}), \quad (4.37)$$

where $V^R(r_{ij})$ and $V^A(r_{ij})$ are pair-additive positive terms representing, respectively, the repulsion of core electrons and the attractive contribution of valence electrons. In most BOPs, $V^R(r_{ij})$ and $V^A(r_{ij})$ are exponentially decaying functions of r_{ij} . The bond order coefficients b_{ij} are a function of the local environment of atoms i and j . In chemistry language, the bond order represents the multiplicity of the bond between two atoms. A non-integer value of b_{ij} also accounts for partial bonds. The choice of the bond-order function is not unique and represents one of the main ingredients that define a specific BOP potential.

The LCBOP is built by adding a short-range (anisotropic) $V^{\text{SR}}(r_{ij})$ term, describing interaction between bonded atoms, and a long-range (isotropic) $V^{\text{LR}}(r_{ij})$ term, describing interactions between non-bonded atoms. The total potential energy of a system reads as follows:

$$E_b = \frac{1}{2} \sum_i \sum_{j \neq i} (V^{\text{SR}}(r_{ij}) + V^{\text{LR}}(r_{ij})). \quad (4.38)$$

The short-range term is defined by eq. 4.37 where

$$V^R(r_{ij}) = f_{ij}^c A e^{-\alpha r_{ij}}, \quad (4.39)$$

$$V^A(r_{ij}) = \left(B_1 e^{-\beta_1 r_{ij}} + B_2 e^{-\beta_2 r_{ij}} \right), \quad (4.40)$$

$$b_{ij} = \frac{1}{2} \left[\bar{b}_{ij} + \bar{b}_{ji} + f_{ij}^c F_{ij}^{\text{conj}} \right]. \quad (4.41)$$

f_{ij}^c is a cut-off function of the form

$$f_{ij}^c = \theta(-x) + \theta(x)\theta(1-x)e^{\frac{\gamma x}{x^3-1}}, \quad (4.42)$$

where $x=(r_{ij}-r_1)/(r_2-r_1)$ and $\gamma > 0$. f_{ij}^c is worth 1 for $r < r_1$, 0 for $r > r_2$ and some intermediate value for $r_1 < r < r_2$. The underlying idea is to choose r_1 close to the average radius of the first coordination sphere in carbon systems and r_2 slightly shorter than the average radius of the second coordination sphere. This way, a pair of bonded atoms will have $f_{ij}^c = 1$ and strictly non-bonded atoms will have $f_{ij}^c = 0$. Moreover, ‘‘fractional neighbors’’ with $0 < f_{ij}^c < 1$ are allowed. The non-symmetric bond-order coefficients \bar{b}_{ij} are defined as

$$\bar{b}_{ij} = \frac{f_{ij}^c}{\sqrt{1 + \sum_{k \neq i,j} f_{ik}^c G(\cos \theta_{j,ik}) H(\delta r_{j,ik})}}. \quad (4.43)$$

As shown in Fig. 4.1(a-b), the functions G and H are positive, so that $\bar{b}_{ij} \leq 1$. Notably, for two covalently bonded atoms with no other neighbors, the bond order would be $\bar{b} = 1$, that is, a carbon dimer is assigned one perfect σ -bond ($\bar{b} = 1$). Consider, now, atoms with higher coordination. If two atoms, j and k , are both neighbors of atom i , they compete to form bonds with the latter, with the result that both bonds are weakened with respect to the dimer case.

In addition, we expect that if one atom, say j , is further from atom i than atom k , it induces a weakening of the bond which is lower than the case where the two neighbors have the same distance. This justifies the introduction of the factor $H(\delta r_{j,ik})$ which depends on the difference $\delta r_{j,ik} = r_{ij} - r_{kj}$. The function $H(\delta r)$ is plotted in Fig. 4.1(b) and the explicit functional form of $H(\delta r)$ can be found in Ref. [Los and Fasolino, 2003]. The angular factor $G(\theta)$ is needed to introduce an energy penalization for structures that are far from the ideal angular configuration in a perfect lattice. This allows, for example, to differentiate the energy of two lattices with the same coordination such as the diamond lattice and the planar square lattice. $G(\theta)$ results from a cubic spline connecting five fixed points $G(\{\theta\}_{i=1}^5)$ based on reference data. In practice, once chosen a value θ_i (e.g. the bond angle in graphite or diamond), $G(\theta_i)$ is fixed in order to optimize observables such as binding energy and elasticity constants. The final interpolated function $G(\theta)$ is shown in Fig. 4.1(a).

The term F_{ij}^{conj} accounts for the degree of conjugation between atoms i and j . Conjugation is defined as the coupling between free p -orbitals of unsaturated neighbor carbon atoms, namely atoms having less than four neighbors. This coupling is responsible for the formation of π bonds which, though weaker than σ -bonds, are particularly strong in carbon compared to other IV group elements (Si, Ge, ...) since carbon has the smallest radius in the group. Due to the very complicated and non-fully analytic form of F_{ij}^{conj} , we will omit its definition. However, just to give an idea of how it behaves for different carbon structures, in diamond $F_{ij}^{\text{conj}} = 0$ due to the absence of unsaturated atoms. In graphite, where each atom form π -bonds with its three neighbors, $F_{ij}^{\text{conj}} = 4/3$, that is, each π -bond contributes 4/9 of a σ -bond in the bond-order

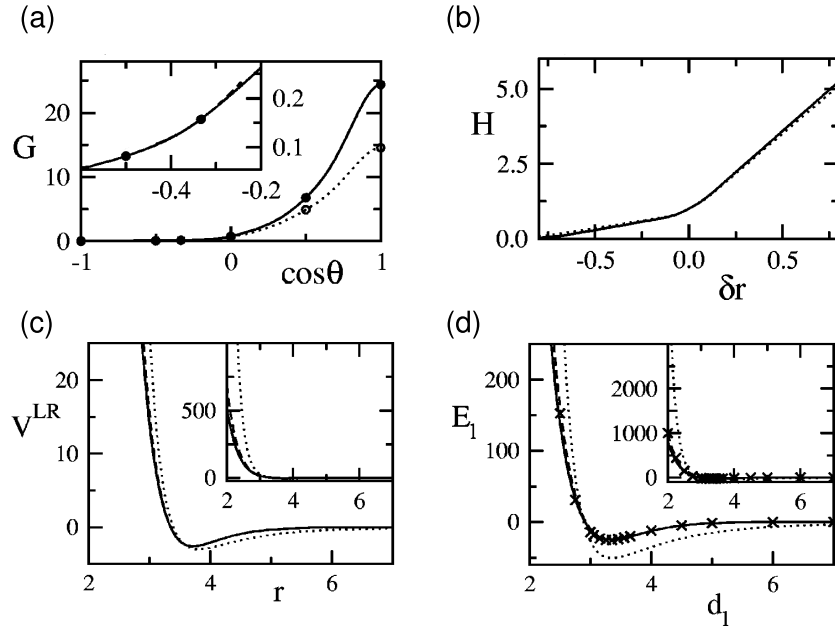


Figure 4.1 – (a-b) Bond order functions (a) $G(\cos\theta)$ and (b) $H(\delta r)$, appearing in the short-range term of the LCBOP potential. Solid lines (dashed lines) are obtained including (disregarding) the long-range contribution V^{LR} in the definition 4.38. Circles in panel (a) are the fixed points for the interpolation of $G(\theta)$. (c) (solid line) Long-range potential defined in eq. 4.44 and (dotted line) Lennard-Jones potential as a function of interatomic distance r . (d) Interlayer interaction energy in graphite E_l as a function of interlayer distance d_l calculated by means of (solid line) eq. 4.44 and (dotted line) Lennard-Jones potential. The crosses represent $E_l(d_l)$ calculated within DFT/LDA. Figure adapted with permission from Ref. , © 2003 *American Physical Society*.

coefficient defined by eq. 4.41.

The long-range potential $V^{\text{LR}}(r)$ has the form of a double Morse potential:

$$V^{\text{LR}}(r) = \left(1 - f_{ij}^c\right) f_{ij}^{c,\text{LR}} \left[\theta (r_0 - r) V_1^M + \theta (r - r_0) V_2^M(r) \right], \quad (4.44)$$

where

$$V_i^M = \epsilon_i \left(e^{-2\lambda_i(r-r_0)} - 2e^{-\lambda_i(r-r_0)} \right) + v_i, \quad (4.45)$$

$f_{ij}^{c,\text{LR}}$ represents a long-range cutoff:

$$f_{ij}^{c,\text{LR}} = \left[1 + \cos \left(\pi \frac{r - r_1^{\text{LR}}}{r_2^{\text{LR}} - r_1^{\text{LR}}} \right) \right] / 2, \quad (4.46)$$

and the factor $1 - f_{ij}^c$ switches off the long-range interaction between bonded atoms. The parameters ϵ_i and ν_i must be set in order to assure continuity of V_i^M up to the second derivative. The parameters defining V^{LR} are set by fitting DFT/LDA estimates of the interlayer binding energy of graphite E_l as a function of the distance d_l , defined as

$$E_l(d_l) = \frac{1}{2} \sum_i^l \sum_j V_{ij}^{\text{LR}}(r_{ij}). \quad (4.47)$$

In the last expression, the index i runs over the atoms of one unit cell of a layer and the index j runs over all atoms of all graphitic planes except that to which atom i belongs. The result of the fit is shown in Fig. 4.1(c-d). Once fixed the long-range potential, the parameters of the short range part are determined by fitting several observables such as bond distances, bond energies and stretching force constants calculated from *ab initio* for various carbon structures. The value of all parameters of the LCBOP potential can be found in Refs. [Los and Fasolino, 2003; Ghiringhelli, 2006]. After its first formulation LCBOP has been improved by adding a coordination-dependent middle-range attractive term for bond distances between 1.7 Å and 4.0 Å as well as other minor modifications (LCBOPII) [Los *et al.*, 2005]. Among other advantages, the introduction of the middle range term allows to reproduce the dissociation energy curves for single and multiple bonds, thus improving the description of the reactive properties of carbon. In this work we have always used the first formulation of the LCBOP, since we were not interested in the chemical reactions of carbon.

Unfortunately, the LCBOP fails in the correct description of the interlayer binding of multilayer graphene and graphite both in the magnitude of the binding energy and in its dependence on the stacking order, i.e. the relative shift of the layers. This has been ascertained by comparison with higher accuracy methods, such as DFT *plus* non local functionals and Quantum Monte Carlo [Spanu *et al.*, 2009; Reguzzoni *et al.*, 2012; Lebègue *et al.*, 2010]. As just mentioned, the long-range term V_{LR} is conceived to reproduce LDA binding energies, despite the fact that van der Waals interaction is poorly described by local functionals. To tackle this problem, Kolmogorov and Crespi proposed a long-range potential composed of a Lennard-Jones attractive contribution and an exponentially-decaying repulsive contribution with the crucial feature to be registry dependent, namely, to depend on the relative position of the atoms owing to different layers [Kolmogorov and Crespi, 2005]. We give the explicit definition as well as our reparametrization of the Kolmogorov-Crespi potential in Section 7.1.5.b, in the context of the study of stacking faults in bilayer graphene.

4.4 Electronic transport

4.4.1 Drude theory of diffusive transport

The problem of electronic transport deals with the description of the flow of electrons and, more generally, charged particles in materials. In a conductor, a portion of electrons is free to move across the material, and under non-equilibrium conditions it can give rise to a net

charge current. The classic case study used to illustrate electronic transport is represented by a conducting wire of length L and constant cross section S in presence of a longitudinal electric field \mathbf{E} or, equivalently, a potential difference V applied between the two ends. It is indeed the electric field \mathbf{E} that drives the system out of equilibrium and sets a current density \mathbf{J} across the conductor. In the classic Drude model, a linear relation between field and current is assumed:

$$\mathbf{J} = \sigma \mathbf{E}, \quad (4.48)$$

where the conductivity σ is constant everywhere in the conductor. More generally, it can be assumed that the current is related to the field in a non-local and history-dependent manner. Eq. 4.48 can be generalized as

$$j_\mu = \sum_\nu \int_{-\infty}^t d\tau \int d\mathbf{r}' \sigma_{\mu\nu}(\mathbf{r}, \mathbf{r}'; t - \tau) E_\nu(\mathbf{r}', \tau), \quad (4.49)$$

where the introduction of the conductivity tensor $\sigma_{\mu\nu}$ also takes into account situations where the induced current is not parallel to the direction of the field. Eqs. 4.48 and 4.49 are the local and geometry-independent version of the Ohm's laws:

$$V = RI, \quad (4.50)$$

and

$$R = \frac{1}{G} = \frac{\rho L}{S}, \quad (4.51)$$

where I is the total current flowing into the sample, R the resistance, and G the conductance.

What justifies the linear dependence between current and field, from the phenomenological point of view? The basic assumptions of Drude's theory are that electrons flowing in the conductors experience collisions that continually change the momentum of the electrons and make them flow with uniform average velocity \mathbf{v} . The nature of collisions, which may be due to impurities, other electrons, ionic vibrations, is of little importance. What matters is that collisions are independent, and that electrons lose memory of their own trajectory after each collision. This implies that the average velocity immediately after a collision is $\langle \mathbf{v}_0 \rangle = 0$. In the time interval τ , the momentum variation of the electrons is on average

$$\frac{d\mathbf{p}}{dt} = \frac{m\mathbf{v}}{\tau}. \quad (4.52)$$

Between two collisions, electrons are accelerated by the field and their momentum changes according to

$$\frac{d\mathbf{p}}{dt} = e\mathbf{E}, \quad (4.53)$$

where e is the electron charge. At a steady state, the momentum gained from the field and lost in collisions must be equal, so that

$$\frac{m\mathbf{v}}{\tau} = e\mathbf{E}, \quad (4.54)$$

whence, using the definition $\mathbf{j} = ne\mathbf{v}$,

$$\sigma = \frac{1}{\rho} = \frac{ne^2\tau}{m}. \quad (4.55)$$

The only unknown quantity at the right hand side of eq. 4.55 is the relaxation time τ . In fact, an experimental measurement of the conductivity σ , allows to determine τ . In typical metallic wires, relaxation times are of the order of 10^{-14} s, and are in large part dictated by inelastic scattering off ionic vibrations (phonons). A related concept is the mean free path $\lambda = |\mathbf{v}|\tau$, that is, the average distance traveled by electrons between two collisions. Assuming for $|\mathbf{v}|$ the typical values of the Fermi velocity for metals, v_F , of the order of 10^8 cm/s, one has λ of the order of 100 Å.

The validity condition of Drude's theory ultimately relies on a comparison of time scales, namely τ and the time needed for electrons to travel across the conductor T . If $T \gg \tau$, each electron undergoes many collisions, the average velocity \mathbf{v} is a well-defined quantity and the steady state condition 4.53 holds. Equivalently, in terms of length scales, the application of Drude's theory is justified if the distance traveled by electrons is much larger than the mean free path, that is, $L \gg \lambda$. In these conditions, the transport regime is said to be *diffusive*. For systems where $L \ll \lambda$, one rather says that electronic transport takes place in the *ballistic* regime. As will be shown in the next sections, the signature of ballistic transport is that the conductance is an integer multiple of the conductance quantum $G_0 = (25.8 \text{ k}\Omega)^{-1}$.

4.5 Coherent vs. non-coherent transport

In Drude's theory, collisions are events that change the momentum of the electrons flowing in a conductor. Collisions can be grouped in two classes:

- **Elastic:** collisions induce momentum change, but the total energy is conserved. This is the case of scattering off impurities and structural defects. In a many-body picture, also electron-electron scattering is an energy conserving process.
- **Inelastic:** both momentum and energy change after the collision. This is the case of scattering off thermal phonons.

An additional relaxation time τ_E can be introduced, defined as the average time interval between two successive collisions that change the single-particle energy. If $\tau_E \gg T$, the energy of the single electrons is to a good approximation conserved, and it is commonly assumed

that the phase of the corresponding time-dependent wavefunctions evolves with a constant frequency. The phase relaxation time τ_ϕ is defined as the average time between two collisions that change the phase of the electron wave-function. In reality, although one cannot have dephasing without energy change at all, τ_E and τ_ϕ are not strictly equal, and may even differ by several order of magnitudes. For example, dephasing induced by low-energy phonons in bulk systems may be orders of magnitude faster than energy relaxation [Massimiliano Di Ventra, 2008]. Electronic transport is said to be *coherent* (*incoherent*), if the phase of the electron is (not) conserved during their motion.

We end this brief discussion highlighting the relation between the different transport regimes, which is sometimes a source of confusion. Ballistic and coherent transport as well as diffusive and incoherent transport are not synonymous. As in ballistic transport the number of collisions, both elastic and inelastic, is very low, there is high chances that the transport regime is also coherent. Nevertheless, if processes are introduced in the system, which induce sizable dephasing but negligible change in energy and momentum, the transport regime is no longer coherent. Dephasing itself does not hinder the electronic transport and can even increase the conductance of a system, for example preventing quantum localization. On the other hand, diffusive transport may well take place in coherent regime, provided that the condition $\tau \ll T \ll \tau_E$ is fulfilled. This is the case of systems with high amount of structural disorder, such as amorphous solids, kept at sufficiently low temperature where phonons, which are the main source of inelastic scattering, are quenched.

4.5.1 Landauer-Büttiker theory of coherent transport

The present subsection briefly exposes the transport theory developed by Landauer and Büttiker and is based on Ref. [Massimiliano Di Ventra, 2008].

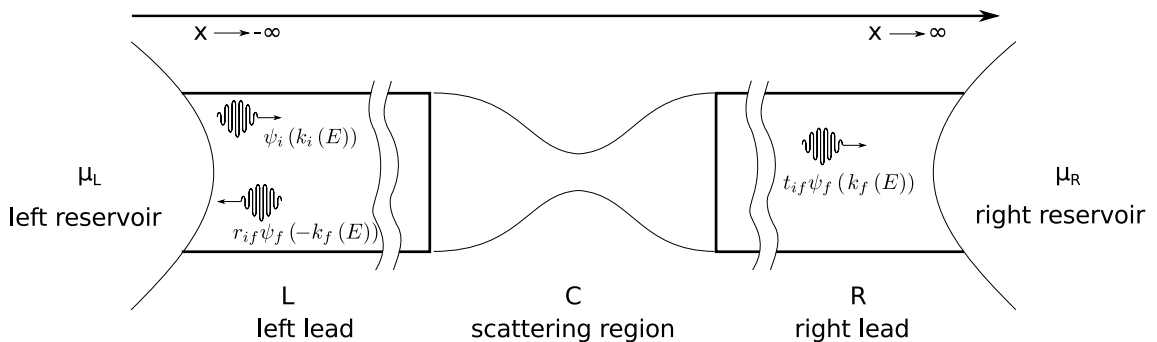


Figure 4.2 – Scheme of the system in Landauer-Büttiker theory.

The assumptions In Landauer-Büttiker theory, the calculation of the conductance of a system is achieved by solving a scattering problem [Landauer, 1957; Büttiker *et al.*, 1985]. Let us consider the system sketched in Fig. 4.2. We are interested in determining the transport properties of region C, called channel or scattering region, which is attached to regions L and

R, called leads or electrodes. Electronic transport takes place along the x axis. Although region C is sketched as a nanojunction, it represents whatever sample of which we are interested in calculating the resistance. The leads are attached to two reservoirs which provide the particles flowing across the system. The reservoirs are constantly at thermodynamic equilibrium, namely they have a well-defined chemical potential $\mu_{L/R}$ and temperature $T_{L/R}$, despite of the loss or gain of particles due to the electron flow. We assume that the distribution of the electrons in the reservoir over the energy states is given by Fermi-Dirac function

$$f(E - \mu_{L/R}, T_{L/R}) = \frac{1}{e^{(E - \mu_{L/R})/k_b T_{L/R}} + 1}, \quad (4.56)$$

where k_b is the Boltzmann constant. For simplicity we will assume $T_L = T_R = T$. The leads are conducting objects where electrons scatter negligibly compared to the central region and where the electron wavefunctions have propagating character, such as Bloch waves. In all the calculations based on Landauer-Büttiker theory reported in this thesis, the leads are constituted by semi-infinite regions of pristine graphene.

The situation that we have in mind is the following: electrons are prepared from reservoirs in the distant past and far from the central region into wave-packets that propagate through the leads, without being scattered. When electrons reach the central region, they are *elastically* scattered and move away toward the leads, such that in the distant future they are again described by propagating wave-packets, which do not scatter further. This assumption is referred to as “scattering boundary conditions”. In practice, the leads must be long enough such that electrons coming from the far past evolve without feeling the potential of the scattering region. Another assumption is that the bias, that is, the voltage ideally measured between the two reservoirs, is

$$V = (\mu_L - \mu_R) / e. \quad (4.57)$$

The Hamiltonian H_S of the system leads *plus* scattering region does not contain two-particle operators, namely the interaction between electrons is treated at a mean-field level (for example, within Tight Binding or Density Functional Theory). The eigenstates of H_S form an orthogonal set of scattering states $|E, \alpha\rangle$, identified by their energy E and by the label α , which includes all other quantum numbers. The states $|E, \alpha\rangle$ satisfy the equation

$$H_S |E, \alpha\rangle = E |E, \alpha\rangle. \quad (4.58)$$

Each of these states is called a channel. A fundamental assumption of Landauer-Büttiker theory is that the electrons injected by the reservoirs evolve immediately into a set of independent channels such that correlations between different states can be neglected. This means that electrons are described by a *diagonal* density matrix ρ_S . Electrons originating from the left reservoir populate the channels $|\Psi_L\rangle$, according to the equilibrium distribution $f(E - \mu_L)$, as well as electrons injected from the right reservoir populate the channels $|\Psi_R\rangle$ according to the equilibrium distribution $f(E - \mu_R)$. We conclude that the density matrix of the electrons

flowing through the system has the form

$$\rho_S = \sum_L |\Psi_L\rangle f(E - \mu_L) \langle \Psi_L| + \sum_R |\Psi_R\rangle f(E - \mu_R) \langle \Psi_R|. \quad (4.59)$$

With the last equation, we have implicitly assumed that the system reaches a steady state and ρ_S is time-independent. Thus, the stationary current I , defined as the mean value of the operator \hat{I} , is

$$I = e \text{Tr} \{ \rho_S \hat{I} \} = \text{const.} \quad (4.60)$$

However, the system is not at equilibrium, due to its openness, unless the two reservoirs have the same chemical potential, but in this case the net current would be zero.

The scattering problem Though not necessary, in order to simplify the discussion we assume that the leads are identical, translationally invariant in the x direction and confined in the plane yz by some potential $V_{L/R}(\mathbf{r}_\perp)$. This is, for example, the case of a carbon nanotube. However, the generalization to systems that are translationally invariant in the plane $y - z$ is straightforward. Deep into the leads, the asymptotic form of H_S is

$$\lim_{x \rightarrow -\infty} H_S = H_L = -\frac{\hbar^2}{2m^*} \nabla^2 + V_L(\mathbf{r}_\perp), \quad (4.61)$$

and

$$\lim_{x \rightarrow \infty} H_S = H_R = -\frac{\hbar^2}{2m^*} \nabla^2 + V_R(\mathbf{r}_\perp). \quad (4.62)$$

We have assumed that the effect of the periodic potential along x has been accounted for by introducing the effective mass m^* . The wavefunctions in the leads have the form

$$\psi_{ik} = \frac{1}{\sqrt{L_x}} e^{ikx} u_i(\mathbf{r}_\perp), \quad (4.63)$$

with energy

$$E_i(k) = \epsilon_i + \frac{(\hbar k)^2}{2m^*}. \quad (4.64)$$

In eq. 4.63, i is the subband index and the length L_x has been introduced for normalization convenience. Consider, now, a state injected from the left reservoir Ψ_L with energy E that at $x \rightarrow -\infty$ was in an eigenstate ψ_{ik_i} of H_L with the same energy E (actually, we could consider a combination of all the eigenstates of H_L having the same energy E , but this would not change the substance of the discussion). Deep into the right lead the state, Ψ_L evolves into a linear combination of eigenstates ψ_{fk_f} of H_R that have the same energy E and positive momentum

k_f :

$$\Psi_L \rightarrow \sum_{f=1}^{N_R} t_{if} \Psi_{fk_f} \quad x \rightarrow \infty, \quad (4.65)$$

where N_R is the number of states with energy E of H_R . Since the incoming electrons may be scattered back into the left lead, we expect that in stationary conditions the wavefunction deep into the left lead is a combination of the incoming wave and all states that have energy E and negative momentum $-k_f$:

$$\Psi_L \rightarrow \psi_i(k_i(E)) + \sum_{f=1}^{N_L} r_{if} \Psi_f(-k_f(E)) \quad x \rightarrow -\infty, \quad (4.66)$$

where N_L is the number of eigenstates of H_L with energy E . The current operator \hat{I} is defined as the integral over the transverse directions of the current density operator $\hat{\mathbf{J}}$:

$$\hat{I}(x) = \int_{-\infty}^{\infty} dy \int_{-\infty}^{\infty} dz \hat{\mathbf{J}}(\mathbf{r}) = \int_{-\infty}^{\infty} dy \int_{-\infty}^{\infty} dz \frac{1}{2m^*} \{ \delta(\mathbf{r} - \hat{\mathbf{r}}) \hat{\mathbf{p}} + \hat{\mathbf{p}} \delta(\mathbf{r} - \hat{\mathbf{r}}) \}. \quad (4.67)$$

For a state $\Psi_{fk_f} = \sqrt{1/L_x} e^{ik_f x} u_f(\mathbf{r})$, the current is independent of the position:

$$I_f = \langle \Psi_{fk_f} | \hat{I} | \Psi_{fk_f} \rangle = \frac{\hbar k_f}{m^* L_x} = \frac{v_f(k_f)}{L_x}, \quad (4.68)$$

where we have defined the velocity $v_f(k_f) = dE/dk_f = \hbar k_f / m^*$. The total current, deep into the left lead, is

$$I_L = I(x \rightarrow -\infty) = I_i - \sum_{f=1}^{N_L} |r_{if}|^2 |I_f| = I_i \left(1 - \sum_{f=1}^{N_L} R_{if} \right), \quad (4.69)$$

where we have defined the reflection probability

$$R_{if} = |r_{if}|^2 \frac{|I_f|}{|I_i|}. \quad (4.70)$$

The total current deep into the right lead is

$$I_R = I(x \rightarrow \infty) = \sum_{f=1}^{N_R} |t_{if}|^2 |I_f| = \sum_{f=1}^{N_R} T_{if} |I_i|. \quad (4.71)$$

Again, we have defined the transmission probability

$$T_{if}(E) = |t_{if}|^2 \frac{|I_f|}{|I_i|}. \quad (4.72)$$

Since in a steady state the currents I_L and I_R must be the same, the transmission and reflection probabilities, for a particle incident from the left lead, satisfy particle flux conservation

$$\sum_{f=1}^{N_R} T_{if} + \sum_{f=1}^{N_L} R_{if} = 1 \quad \psi_{ik_i} \in \text{left lead.} \quad (4.73)$$

The last relation holds also for a particle incident from the right lead:

$$\sum_{f=1}^{N_L} T_{if} + \sum_{f=1}^{N_R} R_{if} = 1 \quad \psi_{ik_i} \in \text{right lead.} \quad (4.74)$$

Let us calculate now the total current flowing into the right lead. In a steady-state situation the current would have two contributions: i) that due to the reflected wave of the electrons injected from the right, given by eq. 4.70, and ii) that due to the transmitted wave of the electrons injected from the left lead, given by eq. 4.72. We need to sum the contribution of all states with energy E , and to take into account the density matrix ρ_S given by eq. 4.59. The total current I_R^{Total} is given by:

$$I_R^{\text{Total}} = e \text{Tr} \{ \rho_S(x \rightarrow \infty) \hat{I} \} = \quad (4.75)$$

$$-e \int dE f(E - \mu_R) \sum_{i=1}^{N_R(E)} D_i(E) \left[I_i(E) - \sum_{f=1}^{N_R(E)} |r_{if}(E)|^2 I_f(E) \right] \quad (4.76)$$

$$+ e \int dE f(E - \mu_L) \sum_{i=1}^{N_L(E)} D_i(E) \left[\sum_{f=1}^{N_R(E)} |t_{if}(E)|^2 I_f(E) \right] = \quad (4.77)$$

$$-e \int dE f(E - \mu_R) \sum_{i=1}^{N_R(E)} D_i(E) I_i(E) \left[\sum_{f=1}^{N_L(E)} |t_{if}(E)|^2 \left| \frac{I_f(E)}{I_i(E)} \right| \right] \quad (4.78)$$

$$+ e \int dE f(E - \mu_L) \sum_{i=1}^{N_L(E)} D_i(E) I_i(E) \left[\sum_{f=1}^{N_R(E)} |t_{if}(E)|^2 \left| \frac{I_f(E)}{I_i(E)} \right| \right], \quad (4.79)$$

where $D_i(E) = (L_x/2\pi) dk_i/dE = L_x/(2\pi\hbar v(k_i)) = 1/(2\pi\hbar I_i(E))$ is the density of states of the i -th subband at energy E , and in the last equality we have used eq. 4.74. Notice that we have added an explicit dependence on E to all the quantities appearing in the right hand side of eq. 4.78, including the number of states in the leads which may vary as a function of energy. Eq. 4.78 can be rewritten as

$$I_R = e \frac{1}{2\pi\hbar} \int dE [f(E - \mu_L) \mathcal{T}_{LR}(E) - f(E - \mu_R) \mathcal{T}_{RL}(E)], \quad (4.80)$$

where the total transmission coefficients have been defined as

$$\mathcal{T}_{L \rightarrow R}(E) = \sum_{i=1}^{N_L(E)} \sum_{f=1}^{N_R(E)} |t_{if}(E)|^2 \frac{|I_f(E)|}{|I_i(E)|} \quad (4.81)$$

$$\mathcal{T}_{R \rightarrow L}(E) = \sum_{i=1}^{N_R(E)} \sum_{f=1}^{N_L(E)} |t_{if}(E)|^2 \frac{|I_f(E)|}{|I_i(E)|}. \quad (4.82)$$

Consider, now, the situation where the traveling states of the two leads are kept at the same chemical potential $\mu_L = \mu_R = \mu$. Eq. 4.80 becomes

$$I_R = e \frac{1}{2\pi\hbar} \int dE f(E - \mu) [\mathcal{T}_{LR}(E) - \mathcal{T}_{RL}(E)] = I_L = 0, \quad (4.83)$$

where the last equality holds because the system is at equilibrium. Due to the arbitrariness of μ , we deduce that the flux is conserved at any specific energy, so that

$$\mathcal{T}_{L \rightarrow R}(E) = \mathcal{T}_{R \rightarrow L}(E) = \mathcal{T}(E). \quad (4.84)$$

For non-zero bias, V , the two leads are populated differently, and a non-zero current flows into the system. The current is

$$I = \frac{e}{h} \int dE [f(E - \mu_L) - f(E - \mu_R)] \mathcal{T}(E). \quad (4.85)$$

In the limit of zero bias we can approximate the difference of the two lead populations as

$$f(E - \mu_L) - f(E - \mu_R) \simeq (\mu_L - \mu_R) \left. \frac{\partial f(E - \mu)}{\partial \mu} \right|_{\mu = (\mu_L + \mu_R)/2}. \quad (4.86)$$

In the limit of small bias, the quantity $(\mu_L + \mu_R)/2$ is very close to the Fermi energy E_f of the system in absence of bias. Hence, for the current, we have

$$I = \frac{e}{h} (\mu_L - \mu_R) \int dE \left. \frac{\partial f(E - \mu)}{\partial \mu} \right|_{\mu = E_f} = \frac{e^2}{h} V \int dE \left. \frac{\partial f(E - \mu)}{\partial \mu} \right|_{\mu = E_f}, \quad (4.87)$$

meaning that, for small bias, the current is proportional to the tension, namely, the statement of the first Ohm's law. In the limit $k_b T \ll V$, $f(E - \mu)$ becomes a step function ($f(E - \mu) = 1(0)$, for $E - \mu < 0(> 0)$), so that

$$I = \frac{e^2}{h} \mathcal{T}(E_f) V. \quad (4.88)$$

Despite its simplicity, eq. 4.88 states that the current, far from being an equilibrium property, can nevertheless be calculated from the quantum properties of the electrons at the Fermi level of a system at equilibrium. Eq. 4.88 is, ultimately, a fluctuation-dissipation relation.

From eqs. 4.73 and 4.74 one has that, $\sum_{f=1}^{N_L} T_{if} \leq 1$ and $\sum_{f=1}^{N_R} T_{if} \leq 1$, where the equal sign holds in absence of reflection. If the latter is the case, the total transmission coefficient is $\mathcal{T}_{LR}(E) = N_L(E)$ and $\mathcal{T}_{RL}(E) = N_R(E)$. Since we have assumed that the leads are identical, we have $N_L(E) = N_R(E) = N_C(E)$, consistently with $\mathcal{T}_{LR}(E) = \mathcal{T}_{RL}(E) = \mathcal{T}(E)$. This means that a

necessary condition for the system to be reflectionless, is that the leads have the same number of states at a given energy E . Consider, for example, a system lead-sample-lead represented by a perfect translationally invariant wire. Electrons are nowhere scattered and $\mathcal{T}(E)$ just counts the number of states at energy E , which is univocally defined all over the system.

Finally, we derive the expression of conductance within the Landauer-Büttiker theory. To evaluate the conductance of a system, the knowledge of the electrostatic potential drop between the two leads is required. In most cases, when the voltage probes are placed deep inside the leads, the potential drop is very close to the difference of chemical potential in the reservoirs. For small bias and very low temperature, the conductance is

$$G = \frac{I}{V} = \frac{e^2}{h} \mathcal{T}(E_f) = G_0 \mathcal{T}(E_f), \quad (4.89)$$

where the constant $G_0 = e^2/h = (25.8\text{k}\Omega)^{-1}$ is the quantum of conductance. In perfect reflection-less samples, the conductance is an integer multiple of G_0 .

In different conventions, the definition of G_0 may include a factor of 2, due to spin degeneracy. In the present derivation, spin degeneracy rather adds a factor of 2 to the transmission coefficient $\mathcal{T}(E)$. The quantization of conductance was found, for the first time, in the 2D electron gas obtained at the interface of GaAs-AlGaAs heterojunctions [van Wees *et al.*, 1988].

4.5.2 Green's function method for the calculation of transmission

A brief introduction on Green's functions Consider a physical system described by the single-particle Hamiltonian H , with a discrete spectrum formed by the states $|\Psi_\alpha\rangle$, satisfying the equation

$$H|\Psi_\alpha\rangle = E_\alpha|\Psi_\alpha\rangle, \quad (4.90)$$

and continuum spectrum formed by the states $|\lambda\rangle$, satisfying the equation

$$H|\lambda\rangle = \lambda|\lambda\rangle. \quad (4.91)$$

The discrete and continuum spectrum together form a complete single-particle Hilbert state. It holds

$$\mathbf{1} = \sum_\alpha |\Psi_\alpha\rangle \langle \Psi_\alpha| + \int d\lambda |\Psi_\lambda\rangle \langle \Psi_\lambda|. \quad (4.92)$$

The Green's function $G(z)$, associated to H , is an operator that depends on the complex variable z , defined by

$$G(z) = (z\mathbf{1} - H)^{-1} \quad z \in \mathbf{C}. \quad (4.93)$$

Chapter 4. Methods

$G(z)$ is, usually, defined in the complex plane as the analytic continuation of the Green's function defined on the real axis $G(E)$, with $E \in \mathbb{R}$. Indeed, the most interesting Green's function are the retarded one

$$G^+(E) = G(E + i\eta) \quad \eta \rightarrow 0^+, \quad (4.94)$$

and the advanced one

$$G^-(E) = G(E - i\eta) \quad \eta \rightarrow 0^+. \quad (4.95)$$

$G(z)$ can be represented in any basis, notably in the position basis:

$$G(z) = \int d\mathbf{r} d\mathbf{r}' |\mathbf{r}\rangle \langle \mathbf{r}| G(z) |\mathbf{r}'\rangle \langle \mathbf{r}'| = \int d\mathbf{r} d\mathbf{r}' |\mathbf{r}\rangle G(\mathbf{r}, \mathbf{r}'; z) \langle \mathbf{r}'|. \quad (4.96)$$

Alternatively, $G(z)$ can be expressed in terms of the eigenstates of the Hamiltonian H by means of the so-called Lehmann representation:

$$G(z) = \sum_{\alpha} \frac{|\Psi_{\alpha}\rangle \langle \Psi_{\alpha}|}{z - E_{\alpha}} + \int d\lambda \frac{|\Psi_{\lambda}\rangle \langle \Psi_{\lambda}|}{z - \lambda}. \quad (4.97)$$

The density of states $D(E)$, which counts the number of states at energy E , can be derived directly from the Green's function. Given the definition

$$D(E) = \sum_{\alpha} \delta(E - E_{\alpha}) + \int d\lambda \delta(E - \lambda), \quad (4.98)$$

it can be shown that $D(E)$ is related to the advanced or retarded Green's function as follows:

$$D(E) = \pm \frac{1}{\pi} \text{Tr} \text{Im} G^{\mp}(E). \quad (4.99)$$

The trace operation is basis-invariant, consistently with the fact that $D(E)$ is a scalar quantity. If the right hand side of eq. 4.99 is evaluated in the basis of the position, we have

$$D(E) = \pm \frac{1}{\pi} \int d\mathbf{r} \text{Im} G^{\mp}(\mathbf{r}, \mathbf{r}; E) = \int d\mathbf{r} D(\mathbf{r}, \mathbf{r}; E). \quad (4.100)$$

The quantity $D(\mathbf{r}, \mathbf{r}; E)$ counts the number of states with energy E at a given point \mathbf{r} , and is called local density of states (LDOS).

As an example, we write down the Green's function $G_0^+(\mathbf{r}, \mathbf{r}'; E)$ for the lead Hamiltonians $H_{L/R}$ defined in eqs. 4.61 and 4.62. By substituting the eigenstates given by 4.63 into eq. 4.97, and integrating over the continuous spectrum, we obtain:

$$G_0^+(\mathbf{r}, \mathbf{r}'; E) = \frac{m}{i\hbar} \sum_{\alpha} u_{\alpha}^*(\mathbf{r}_{\perp}) u_{\alpha}(\mathbf{r}'_{\perp}) \frac{e^{ik|x-x'|}}{k}, \quad (4.101)$$

where $E = E_{\alpha}(k) = \epsilon_{\alpha} + \hbar^2 k^2 / 2m$, and k is taken positive.

Consider now a system described by the Hamiltonian $H = H_0 + V$. For our purpose, it is convenient to think of H_0 as the Hamiltonian of the leads and V as an operator containing the Hamiltonian of the scattering region as well as the coupling between the leads and the scattering region. Next, we define the Green's functions $G_0 = (E - H_0)^{-1}$ and $G = (E - H)^{-1}$. We consider an incident state $|\Psi_{\text{in}}^0(E)\rangle$ that in the distant past was governed by H_0 , say a state injected into the left lead. $|\Psi_{\text{in}}^0(E)\rangle$ experiences the scattering potential V and evolves into the state $|\Psi^+(E)\rangle$. The incoming and final states are related by the so-called Lippmann-Schwinger equation

$$|\Psi^+(E)\rangle = |\Psi_{\text{in}}^0(E)\rangle + G^+(E) V |\Psi_{\text{in}}^0(E)\rangle. \quad (4.102)$$

Notice that we have employed the retarded Green's function $G^+(E)$, since we have considered a state which evolves from the distant past. If $G^-(E)$ were used, equation 4.102 would rather describe the evolution due to V of an outgoing state coming from the distant future.

Consider now the Hamiltonian H , which is the sum of two operators

$$H = H_0 + V. \quad (4.103)$$

The Green's functions $G_0(E) = (E - H_0)^{-1}$ and $G(E) = (E - H)^{-1}$ are related by the so-called Born series

$$G = G_0 + G_0 T G_0 \quad (4.104)$$

In the last equality we have introduced the T-matrix operator

$$T = V + V G_0(E) V + V G_0(E) V G_0(E) V + \dots = V + V G(E) V. \quad (4.105)$$

The Born series is of fundamental importance for scattering problems where H_0 is, usually, the Hamiltonian of free-propagating particles and V is a scattering potential.

Green's function and self-energy in the Landauer problem Let us consider the following partition of the Hamiltonian H_S that describes the system leads *plus* sample

$$H_S = H_C + H_L + H_R + V_{LC} + V_{LC}^\dagger + V_{CR} + V_{CR}^\dagger. \quad (4.106)$$

As illustrated in Fig. 4.3, H_L and H_R are the Hamiltonians of the isolated leads, and H_C is the Hamiltonian of the isolated scattering region. V_{LC} and V_{CR} are the coupling between the left lead and the central region, and between the central region and the right lead, respectively. We assume that there is no direct coupling between regions L and R. This is a condition always achievable by defining region C arbitrarily large. Finally, V_{LC} and V_{CR} are short-ranged and do not overlap in the scattering region. The Schrödinger equation can be written in matrix form

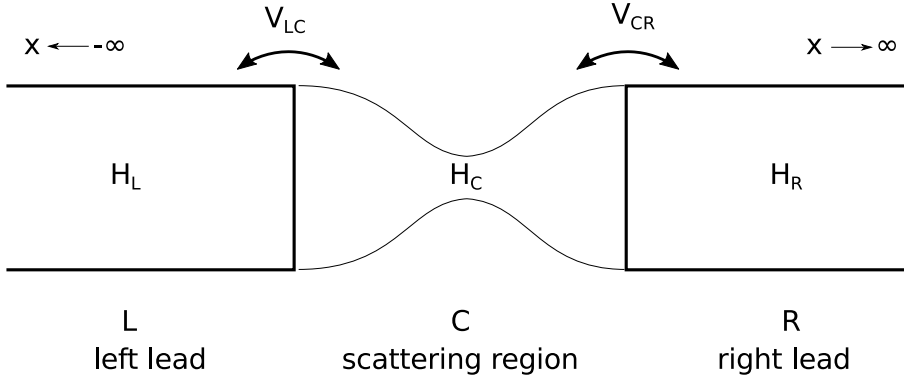


Figure 4.3 – Partitioning of the system. The meaning of building blocks of the Hamiltonian 4.107 is illustrated.

as

$$\begin{pmatrix} H_L & V_{LC} & \mathbf{0} \\ V_{LC}^\dagger & H_C & V_{CR} \\ \mathbf{0} & V_{CR}^\dagger & H_R \end{pmatrix} \begin{pmatrix} |\phi_L\rangle \\ |\phi_C\rangle \\ |\phi_R\rangle \end{pmatrix} = E \begin{pmatrix} |\phi_L\rangle \\ |\phi_C\rangle \\ |\phi_R\rangle \end{pmatrix}, \quad (4.107)$$

where the total wavefunction $|\phi\rangle$ has been spatially partitioned in $|\phi_L\rangle$, $|\phi_C\rangle$, and $|\phi_R\rangle$. This partition is very clear when H_S is built within a tight-binding model, so that $|\phi\rangle$ is a linear combinations of atomic orbitals. Thus, $|\phi_L\rangle$ contains all the components of $|\phi\rangle$ which come from atomic orbitals of the left lead, and similarly for $|\phi_C\rangle$ and $|\phi_R\rangle$. Moreover, in the tight-binding model, the orbitals of an atom are coupled to the orbitals of a finite number of neighbor atoms, so that V_{LC} and V_{CR} are intrinsically short-ranged. From the first and third rows of eq. 4.107 we obtain the following equations:

$$(E - H_L) |\phi_L\rangle = V_{LC} |\phi_C\rangle \quad (4.108)$$

$$(E - H_R) |\phi_R\rangle = V_{CR}^\dagger |\phi_C\rangle, \quad (4.109)$$

whence

$$|\phi_L\rangle = G_L(E) V_{LC} |\phi_C\rangle \quad (4.110)$$

$$|\phi_R\rangle = G_R(E) V_{CR}^\dagger |\phi_C\rangle, \quad (4.111)$$

where $G_{L/R}$ are the Green's function associated to $H_{L/R}$. The last two equations, substituted in the third row of eq. 4.107, give

$$(E - H_C - \Sigma_L(E) - \Sigma_R(E)) |\phi_C\rangle = 0, \quad (4.112)$$

where we have introduced the self-energy operators

$$\Sigma_L(E) = V_{LC}^\dagger G_L(E) V_{LC} \quad (4.113)$$

and

$$\Sigma_R(E) = V_{CR} G_R(E) V_{CR}^\dagger. \quad (4.114)$$

We have implicitly added a small imaginary part to E in eqs. 4.113 and 4.114, which define both the retarded self-energies $\Sigma_{L/R}^+(E) = \Sigma_{L/R}(E + i\eta)$ and the advanced self-energies $\Sigma_{L/R}^-(E) = \Sigma_{L/R}(E - i\eta)$. From eq. 4.112, we can derive the Green's function $G(E)$ for the scattering region in presence of a finite coupling to the leads:

$$G(E) = \frac{1}{E - H_C - \Sigma_L(E) - \Sigma_R(E)} = \frac{1}{E - H_C - \Sigma(E)}, \quad (4.115)$$

where we have defined the total self-energy

$$\Sigma(E) = \Sigma_L(E) + \Sigma_R(E). \quad (4.116)$$

The interpretation of $\Sigma(E)$ is the following: the eigenenergies ϵ_k of H_C are shifted by $Re\Sigma(\epsilon_k) = Re\Sigma_L(\epsilon_k) + Re\Sigma_R(\epsilon_k)$ and develop an imaginary part $Im\Sigma(\epsilon_k) = Im\Sigma_L(\epsilon_k) + Im\Sigma_R(\epsilon_k)$. The latter is associated to a finite lifetime of the original state with energy ϵ_k , which, strictly speaking, is no longer an eigenstate of the full Hamiltonian H_S . To first order approximation, the lifetime due to elastic tunneling into the leads is given by

$$\tau^{el}(\epsilon_k) = \frac{\hbar}{|Im[\Sigma_L^\pm(\epsilon_k) + \Sigma_R^\pm(\epsilon_k)]|}. \quad (4.117)$$

Finally, we introduce the coupling operators relative to the left and right lead $\Gamma_{L/R}(E)$:

$$\Gamma_{L/R}(E) = i(\Sigma_{L/R}^+(E) - \Sigma_{L/R}^-(E)) = \mp 2Im\Sigma_{L/R}^\pm(E). \quad (4.118)$$

The coupling operators are inversely proportional to τ^{el} , consistently with the intuitive picture that a larger coupling corresponds to a shorter lifetime of the electrons of the scattering region.

From the practical point of view, due to the infinite extension of the leads, the operators $H_{L/R}$ and $G_{L/R}$ are represented by matrices of infinite size. This represents a problem when self-energies are calculated by means of eqs. 4.113 and 4.114. However, since V_{LC} and V_{CR} are short-ranged, $G_{L/R}$ is needed only at the interface between the leads and the scattering region. This restriction of $G_{L/R}$ is called surface Green's function. Several recursive and semi-analytical techniques, taking advantage of the translational invariance of the leads, have been developed to calculate the surface Green's functions [Sancho *et al.*, 1984; Umerski, 1997; Autès, 2008].

Transmission from the Green's function We now explain very briefly the connection between the Green's function and the Landauer-Büttiker theory. The total Hamiltonian H_S can be partitioned as

$$H_S = H_0 + V, \quad (4.119)$$

where H_0 represents the leads and V contains everything is not included in the H_0 . Consider an incident state coming from the left lead $\psi_{i,k_i}(\mathbf{r})$ with energy $E_i(k_i)$ given by eq. 4.64. The final state $\Psi_L(\mathbf{r})$ can be obtained from the Lipmann-Schwinger equation 4.102. In the position representation we have

$$\Psi_L(\mathbf{r}) = \psi_{i,k_i}(\mathbf{r}) + \int d\mathbf{r}' G(\mathbf{r}, \mathbf{r}'; E_i(k_i)) V(\mathbf{r}') \psi_{i,k_i}(\mathbf{r}'). \quad (4.120)$$

The knowledge of $G(\mathbf{r}, \mathbf{r}')$ allows to derive $\Psi_L(\mathbf{r})$, and the asymptotic form of the latter gives the transmission and reflection coefficients. It turns out that the coefficients 4.65 and 4.66 are proportional to the elements T_{if} of the T-matrix defined in eq. 4.105. In particular, the reflection coefficients are given by

$$r_{if} = \frac{L_x}{i\hbar v(k_f)} T_{if}, \quad (4.121)$$

where f labels left-moving states with momentum $k_f < 0$. The transmission coefficients are given by

$$t_{if} = \delta_{if} + \frac{L_x}{i\hbar v(k_f)} T_{if}, \quad (4.122)$$

where f labels right-moving states with momentum $k_f > 0$. We can introduce the matrix

$$\tau_{if} = t_{if} \sqrt{\left| \frac{v_f}{v_i} \right|} = \left(\delta_{if} + \frac{L_x}{i\hbar \sqrt{v_f v_i}} T_{if} \right), \quad (4.123)$$

such that the asymptotic form of the wavefunction of a state coming from the left lead is

$$\lim_{x \rightarrow \infty} \Psi_{i,k_i}(\mathbf{r}) = \sum_{f=1}^{N_R} \tau_{if} \sqrt{\left| \frac{v_i}{v_f} \right|} \psi_{f,k_f}(\mathbf{r}) \quad (4.124)$$

and the total transmission probability is

$$\mathcal{T}_{L \rightarrow R} = \sum_{i=1}^{N_L} \sum_{f=1}^{N_R} t_{if} t_{if}^* \left| \frac{v_f}{v_i} \right| = \sum_{i=1}^{N_L} \sum_{f=1}^{N_R} \tau_{if} \tau_{if}^* = \text{Tr} \{ \tau \tau^\dagger \}. \quad (4.125)$$

4.6. Monte Carlo method for thermodynamical averages

Furthermore, if H_S can be partitioned as 4.106, $\mathcal{T}_{L \rightarrow R}$ can be evaluated by means of the formula [Fisher and Lee, 1981]

$$\mathcal{T}_{L \rightarrow R}(E) = \text{Tr} [\Gamma_R G^+ \Gamma_L G^-]. \quad (4.126)$$

Similarly, for $\mathcal{T}_{R \rightarrow L}(E)$ it holds

$$\mathcal{T}_{R \rightarrow L}(E) = \text{Tr} [\Gamma_L G^+ \Gamma_R G^-]. \quad (4.127)$$

As shown before, $\mathcal{T}_{L \rightarrow R}(E) = \mathcal{T}_{R \rightarrow L}(E) = \mathcal{T}(E)$, so that the current is given by

$$I = \frac{e}{h} \int dE (f_L - f_R) \text{Tr} [\Gamma_R G^+ \Gamma_L G^-] = \frac{e}{h} \int dE (f_L - f_R) \text{Tr} [\Gamma_L G^+ \Gamma_R G^-]. \quad (4.128)$$

4.6 Monte Carlo method for thermodynamical averages

Importance sampling Let us consider a system of N interacting particles at thermodynamic equilibrium with a bath at temperature T . We assume that the total energy is a function of the configuration specified by the collection of the positions of each particle $\{\mathbf{r}_i\}_{i=1}^N$. More generally, each vector \mathbf{r}_i can represent the whole set of degrees of freedom of the i -th particle. Suppose we want to calculate the thermodynamic average of an observable $A(\{\mathbf{r}_i\}_{i=1}^N)$, defined as

$$\langle A \rangle = \frac{\int A(\{\mathbf{r}_i\}_{i=1}^N) \exp(-\beta E(\{\mathbf{r}_i\}_{i=1}^N)) \Pi_{i=1}^N d\mathbf{r}_i}{\int \exp(-\beta E(\{\mathbf{r}_i\}_{i=1}^N)) \Pi_{i=1}^N d\mathbf{r}_i}, \quad (4.129)$$

where $E(\{\mathbf{r}_i\}_{i=1}^N)$ is the total energy corresponding to a specific configuration and we have introduced the Boltzmann factor $\beta = (k_B T)^{-1}$. The denominator of eq. 4.129 defines the partition function

$$\mathcal{Z} = \int \exp(-\beta E(\{\mathbf{r}_i\}_{i=1}^N)) \Pi_{i=1}^N d\mathbf{r}_i, \quad (4.130)$$

so that the average $\langle A \rangle$ can be written more clearly as a weighted average

$$\langle A \rangle = \int A(\{\mathbf{r}_i\}_{i=1}^N) W(\{\mathbf{r}_i\}_{i=1}^N) \Pi_{i=1}^N d\mathbf{r}_i, \quad (4.131)$$

where we have introduced the Boltzmann weight

$$W(\{\mathbf{r}_i\}_{i=1}^N) = \frac{\exp(-\beta E(\{\mathbf{r}_i\}_{i=1}^N))}{\mathcal{Z}}. \quad (4.132)$$

An evaluation of 4.131 by means of any discretization method is simply unfeasible even for systems composed of few tens of particles. As an example, consider a system of $N = 10$ particles and assume that the total energy depends only on the particles' positions. If the range of any

Chapter 4. Methods

degree of freedom is discretized by using 10 points, then the product $A(\{\mathbf{r}_i\}_{i=1}^N)W(\{\mathbf{r}_i\}_{i=1}^N)$ must be evaluated $10^{3N} \simeq 10^{30}$ times.

A valid alternative would come from the Monte Carlo method. To simplify the discussion, consider the one-dimensional integral

$$I = \int_a^b f(x) dx, \quad (4.133)$$

average $\langle f(x) \rangle$ as

$$I = (b-a) \langle f(x) \rangle. \quad (4.134)$$

$\langle f(x) \rangle$ can be approximated by evaluating $f(x)$ over a large number L of x values randomly distributed in the range $[a, b]$

$$\langle f(x) \rangle = \lim_{L \rightarrow \infty} \frac{1}{L} \sum_{i=1}^L f(x_i). \quad (4.135)$$

Due to the finiteness of L , the estimate of I has an intrinsic statistical error that can be quantified by the variance σ_I . This can be estimated by propagating the intrinsic variance of $f(x)$

$$\sigma_f^2 = (b-a)^{-1} \int_a^b \left(f^2(x) - \int_a^b f(x) dx / (b-a) \right) dx \quad (4.136)$$

through eqs. 4.135 and 4.134. We obtain

$$\sigma_I^2 = (b-a) \frac{1}{L} \left(\frac{1}{L} \sum_{i=1}^L \sigma_f^2 \right) = (b-a) \frac{1}{L^2} \sigma_f^2. \quad (4.137)$$

This means that the error on I is, obviously, reduced by increasing L , but also that it depends on how much $f(x)$ drifts from a constant function - the only case where $\sigma_f = 0$. Unweighted averages are also not suitable when the integrand is close to zero over a large portion of the whole space, since a large part of the random evaluations $f(x_i)$ would just negligibly contribute to the average. This is, indeed, the case of those integrals containing the Boltzmann factor, such as 4.129.

The efficiency of the Monte Carlo evaluation of I would be largely improved if the integral in eq. 4.133 could be replaced by an equivalent one containing a smoother integrand. Consider a function $u(x)$ with positive derivative $w(x) = u'(x) > 0$, $u(x=a) = 0$, and $u(x=b) = 1$. By substitution, we have

$$I = \int_a^b \frac{f(x)}{w(x)} w(x) dx = \int_a^b \frac{f(x)}{w(x)} u'(x) dx = \int_{u(x=a)=0}^{u(x=b)=1} \frac{f(x(u))}{w(x(u))} du \quad (4.138)$$

$$\simeq \frac{1}{L} \sum_{i=1}^L \left\langle \frac{f(x(u_i))}{w(x(u_i))} \right\rangle.$$

The problem of evaluating I is recast into the generation of random values for u uniformly distributed in the range $[0, 1]$ and successive evaluations of the function f/w . The variance of I is

$$\sigma_I^2 = \frac{1}{L} \sigma_{f/w}^2, \quad (4.139)$$

which can be drastically reduced if $w(x)$ is chosen in order to approximately reproduce the shape of $f(x)$, so that $f(x)/w(x)$ is as close as possible to 1. Anyway, we stress that the applicability of this method requires a function $w(x)$ that must be integrated analytically to obtain $u(x)$, which, in turn, must be invertible analytically.

Alternatively, if one would be able to generate random values x_i distributed according to $w(x)$ (for instance, this is easily done for Gaussian distributions), then the integral would be evaluated simply as

$$I \simeq (b-a) \sum_{i=1}^L \frac{f(x_i)}{w(x_i)}. \quad (4.140)$$

Sampling by a Markov chain and Metropolis algorithm As we wish to apply importance sampling to perform the thermodynamic average 4.129, the natural choice for $w(x)$ would be the Boltzmann weight $W(\{\mathbf{r}_i\}_{i=1}^N)$ defined in 4.132. Unfortunately, the Boltzmann weight itself is unknown, for its definition contains the partition function \mathcal{Z} , which is defined by an integral over the whole configuration space. However, as we will show in a moment, the *a priori* knowledge of the absolute probabilities W is not strictly necessary, as it can be reconstructed by the relative probabilities of any two configurations $\{\mathbf{r}_i\}_{i=1}^N$ and $\{\mathbf{r}'_i\}_{i=1}^N$, given by $W(\{\mathbf{r}_i\}_{i=1}^N) / W(\{\mathbf{r}'_i\}_{i=1}^N) = \exp\left[-\beta\left(E(\{\mathbf{r}_i\}_{i=1}^N) - E(\{\mathbf{r}'_i\}_{i=1}^N)\right)\right]$.

The goal is achieved by a Markov chain, that is, a sequence of configurations where each step depends exclusively on the previous one, in a probabilistic sense. To be more explicit, consider two neighbor configuration in the chain, which we label \mathcal{R}_o and \mathcal{R}_n , then the probability $P(\mathcal{R}_o \rightarrow \mathcal{R}_n)$ is exclusively a function of \mathcal{R}_o and \mathcal{R}_n . Now, suppose the Markov chain is initiated at a configuration $\mathcal{R}_{\text{start}}$, which we know to have a non-zero probability $W(\mathcal{R}_{\text{start}})$. It is convenient to think of a large number M of Markov chains run in parallel (Markov walkers), each one initiated at a different starting configuration. Provided that the Markov walkers will eventually reach the equilibrium configuration given by the Boltzmann weights W 's, the condition which allows to maintain it over further evolution of the system is

$$\sum_{\mathcal{R}_o} W(\mathcal{R}_o) P(\mathcal{R}_o \rightarrow \mathcal{R}_n) = \sum_{\mathcal{R}_n} W(\mathcal{R}_n) P(\mathcal{R}_n \rightarrow \mathcal{R}_o), \quad (4.141)$$

namely, the total number of walkers reaching the configuration \mathcal{R}_n equals the number of walkers departing from it. Usually, a more strict condition called “detailed balance” is required

$$W(\mathcal{R}_o)P(\mathcal{R}_o \rightarrow \mathcal{R}_n) = W(\mathcal{R}_n)P(\mathcal{R}_n \rightarrow \mathcal{R}_o). \quad (4.142)$$

This is the only set of constraints that applies to the, otherwise arbitrary, set of probabilities $P(\mathcal{R}_n \rightarrow \mathcal{R}_o)$. Enforcing a balance condition assure that the only distribution which can be maintained over the time is the Boltzmann one. In other words, if the Markov walkers reach an equilibrium distribution, it can only be the Boltzmann distribution.

A step in a Markov chain consists in two moves. First, a trial move is performed according to a probability distribution $\alpha(\mathcal{R}_o \rightarrow \mathcal{R}_n)$, which we assume to be a symmetric matrix: $\alpha(\mathcal{R}_o \rightarrow \mathcal{R}_n) = \alpha(\mathcal{R}_n \rightarrow \mathcal{R}_o)$. Second, the move is accepted or rejected according to the probability $\text{acc}(\mathcal{R}_o \rightarrow \mathcal{R}_n)$, in which the information on the equilibrium distribution is encoded. As the resulting probability is

$$P(\mathcal{R}_o \rightarrow \mathcal{R}_n) = \alpha(\mathcal{R}_o \rightarrow \mathcal{R}_n) \text{acc}(\mathcal{R}_o \rightarrow \mathcal{R}_n), \quad (4.143)$$

eq. 4.142 becomes

$$\frac{\text{acc}(\mathcal{R}_o \rightarrow \mathcal{R}_n)}{\text{acc}(\mathcal{R}_n \rightarrow \mathcal{R}_o)} = \frac{W(\mathcal{R}_n)}{W(\mathcal{R}_o)} = \exp\{-\beta[E(\mathcal{R}_n) - E(\mathcal{R}_o)]\}, \quad (4.144)$$

where we have used the symmetry of α . The choice suggested by Metropolis, Rosenbluth and Teller [Metropolis *et al.*, 1953] is the following:

$$\text{acc}(\mathcal{R}_o \rightarrow \mathcal{R}_n) = \begin{cases} W(\mathcal{R}_n) / W(\mathcal{R}_o) = \exp\{-\beta[E(\mathcal{R}_n) - E(\mathcal{R}_o)]\} & E(\mathcal{R}_n) > E(\mathcal{R}_o) \\ 1 & E(\mathcal{R}_n) < E(\mathcal{R}_o) \end{cases}. \quad (4.145)$$

It can be easily checked that this choice fulfills the detailed balance condition. Once equilibrium is reached, $\langle A \rangle$ is obtained as an unweighted average over the ensemble of configurations of the Markov walkers $\{\mathcal{R}_i\}_{i=1}^M$

$$\langle A \rangle = \frac{1}{M} \sum_{i=1}^M A(\mathcal{R}_i). \quad (4.146)$$

Although over the years other choices for $\text{acc}(\mathcal{R}_o \rightarrow \mathcal{R}_n)$ have been proposed, the original Metropolis scheme outperforms most of its alternatives in terms of sampling efficiency. The matrix α remains unspecified, except that it is symmetric. There is indeed an inherent freedom in the choice of α that can be exploited to accelerate the sampling. However, the set of probabilities $P(\mathcal{R}_o \rightarrow \mathcal{R}_n)$ must guarantee *ergodicity*, that is, each accessible point of the configuration space must be reachable in a finite number of Markov steps from any other point. Ergodicity allows to lift the requirement of having a large number of Markov walkers,

4.6. Monte Carlo method for thermodynamical averages

which can be replaced by a single longer sampling, with an enormous benefit in practical calculations. There is, however, a subtle conceptual difference: when dealing with a single walker, the configurations explored during the entire chain are distributed according to the Boltzmann function, whereas with a large number M of walkers we assume that the Boltzmann distribution is reproduced *at each step* by the ensemble of configurations of the walkers.

5 Electronic transport across grain boundaries in graphene

As discussed in Chapter 3, production of graphene for industrial applications requires manufacturing processes that can be robustly scaled up, for example, based on chemical vapor deposition. The output of such a technique is mostly polycrystalline samples and there is large evidence that the presence of grain boundaries strongly affects the electronic transport properties of graphene. However, a connection between polycrystals' morphology and electronic conductance posed on a quantitative basis is lacking. In the first two sections of this chapter, we study the problem of the electronic transport across grain boundaries in graphene by employing the Landauer-Büttiker theory.

In the first section, we systematically investigate the transmission of charge carriers across periodic grain boundaries. For GBs built from dislocations with the smallest Burger's vector $\mathbf{b} = (1, 0)$ (see Section 3.3.1), our calculations reveal an unexpected suppression of low-energy transmission upon decreasing the dislocation density. This counterintuitive behavior is a consequence of low-energy localized states of topological origin introduced by individual dislocations that backscatter the charge carriers.

In the second section we extend the scope of our investigation to include disordered grain boundaries. We perform a Monte Carlo sampling of the configurational space of GBs, thus generating ensembles of realistic models of disordered interfaces between misoriented domains of graphene. All along the simulations, transmission across GBs has been calculated, thus enabling us to establish a connection between average transmission and invariant misorientation angle.

In the last sections, we present two works performed in collaboration with experimental groups. In the third section, we describe a study demonstrating the controlled growth of a line defect in graphene formed by an array of 5-5-8 defects (two pentagons and one octagon), as revealed by transmission electron microscopy. This line defect can be thought as a GB with vanishing misori-

entation angle. By means of *ab initio* electronic transport calculations, we confirm earlier theoretical prediction suggesting that such defect acts as a valley filter. However, we find a strong energy dependence of the valley polarization of the charge carriers transmitted through the GB. Inspired by these findings, we propose an electrostatically operated “valley-valve” device based on two 5-5-8 defects. Such device would represent a fundamental building block for valleytronics logical circuits.

In the fourth section, we describe a study of grain boundaries in epitaxial graphene on SiC substrate performed using scanning tunneling microscopy/spectroscopy, which remarkably found periodic GBs, among the others. In particular, one highly ordered GB with misorientation angle $\theta = 33 \pm 2^\circ$ was recognized as the previously proposed model shown in the lower panel of Fig. 3.2(c). To achieve this identification, we performed *ab initio* simulations of STM images, finding strong qualitative resemblance to the experimental ones.

5.1 Electronic conductance across periodic grain boundaries

The work presented in this section has been published in *Nano Letters*, **14**, 250 (2014), whose manuscript was entirely written by Fernando Gargiulo. The reader will find a considerable overlap between the article and the present section.

5.1.1 Introduction

As discussed in Section 3.3.1, in the Read-Shockley model, grain boundaries in two-dimensional crystals are equivalent to one-dimensional arrays of dislocations [Read and Shockley, 1950]. In graphene, the low-energy configurations of the cores of dislocations are composed of pairs of pentagons and heptagons, and the resulting Burgers vector depends on their mutual positions [Carpio *et al.*, 2008; Liu and Yakobson, 2010; Yazyev and Louie, 2010b; Carlsson *et al.*, 2011]. In Section 3.3.3, we have reported a theoretical study predicting that, for a certain class of periodic GBs, the conservation of momentum results in a complete suppression of the transmission of low-energy charge carriers [Yazyev and Louie, 2010a]. However, it is important to understand the factors determining the charge-carrier transmission probability in a more general situation when no symmetry-related selection applies.

In this section, we report a systematic study of the charge-carrier transmission across grain boundaries in graphene by means of the Landauer-Büttiker approach. We find that the structural topological invariant of dislocations, the Burgers vector \mathbf{b} , plays a crucial role in determining the transport properties. In particular, in the case of grain boundaries formed by the minimal Burgers vector $\mathbf{b} = (1, 0)$ dislocations, we find an unexpected suppression of the transmission of low-energy charge carriers in the limit of small misorientation angles (or equivalently small dislocation densities). This counter-intuitive behavior is explained from

the point of view of resonant back-scattering involving localized states of topological origin, which arise due to the gauge field created by dislocations characterized by $\mathbf{b} = (n, m)$ with $n - m \neq 3q$ ($q \in \mathbb{Z}$). The $\mathbf{b} = (1, 1)$ dislocations are shown to behave as ordinary scattering centers with very weak effects on the electronic transport.

5.1.2 Methods and models

In our study, we employ the nearest-neighbor tight-binding model Hamiltonian

$$H = -t \sum_{\langle i, j \rangle} [c_i^\dagger c_j + \text{h.c.}], \quad (5.1)$$

where c_i (c_i^\dagger) annihilates (creates) an electron at site i and $\langle i, j \rangle$ stands for pairs of nearest-neighbor atoms. The hopping integral $t = 2.7$ eV is assumed to be constant. We verified by means of explicit calculations that including the dependence of the hopping integral on the variation of the interatomic distance due to the elastic strain field produced by the dislocations has only minor effect on the low-energy charge-carrier transmission. The tight-binding results also agree with the results of first-principles calculations, as shown previously [Yazyev and Louie, 2010a]. Coherent transport across grain boundaries in graphene is studied within the Landauer-Büttiker formalism, which relates conductance $G(E)$ at a given energy E to transmission $T(E)$ as $G(E) = G_0 T(E)$, with $G_0 = 2e^2/h$ being the conductance quantum [Büttiker *et al.*, 1985]. As a consequence of the periodicity of our models, transmission is also a function of the momentum component k_{\parallel} parallel to the GB. In the following, the explicit dependence of physical quantities on E and k_{\parallel} is omitted for the sake of compact notation, whenever clearness is preserved. Transmission is evaluated by means of the Green's function approach using two-terminal device configurations, with contacts represented by semi-infinite ideal graphene leads. Here, we briefly summarize the main formulas used in the calculations. For a detailed treatment of the Landauer-Büttiker theory we refer to Section 4.5.1. Transmission is calculated using the formula

$$T = \text{Tr}[\Gamma_L G_S^\dagger \Gamma_R G_S]. \quad (5.2)$$

The scattering region Green's function G_S is calculated as

$$G_S = [E^+ I - H_S - \Sigma_L - \Sigma_R]^{-1} \quad (5.3)$$

employing the coupling matrices $\Gamma_{L(R)}$ for the left (right) lead given by

$$\Gamma_{L(R)} = i[\Sigma_{L(R)} - \Sigma_{L(R)}^\dagger]. \quad (5.4)$$

In these expressions H_S is the Hamiltonian for the scattering region, $\Sigma_{L(R)}$ are the self-energies that couple the scattering region to the leads and $E^+ = E + i\eta I$ ($\eta \rightarrow 0^+$). The self-energies are calculated by means of the recursion technique described in Ref. [Sanvito *et al.*, 1999]. As the system under study is time-reversal symmetric, $T(k_{\parallel}, E) = T(-k_{\parallel}, E)$, allowing to consider only

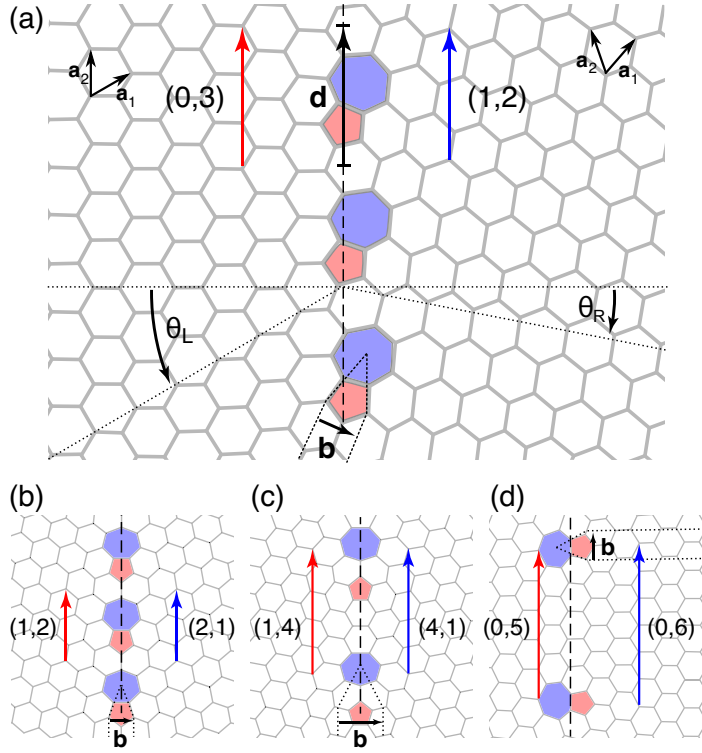


Figure 5.1 – (a) A generic example of asymmetric periodic grain boundary composed of $\mathbf{b} = (1, 0)$ dislocations. This grain-boundary structure is characterized by rotation angles $\theta_L = 30^\circ$ and $\theta_R = 10.9^\circ$, and the pair of matching vectors $(0, 3)|(1, 2)$. The periodicity vector \mathbf{d} and the Burgers vector \mathbf{b} are shown. (b-c) Structures of symmetric grain boundaries formed by (b) $\mathbf{b} = (1, 0)$ and (c) $\mathbf{b} = (1, 1)$ dislocations. (d) Degenerate grain boundary ($\theta = 0^\circ$) with the Burgers vector of the constituent dislocations oriented along the grain-boundary line (shown as dashed line).

$$k_{\parallel} \in [0, \pi/d].$$

We consider grain-boundary models constructed as periodic arrays of dislocations following the Read-Shockley model [Read and Shockley, 1950]. Only dislocations formed by pentagons and heptagons are investigated as these structures preserve the three-fold coordination of sp^2 carbon atoms thus ensuring energetically favorable configurations of defects. This construction is consistent with experimental atomic resolution images of grain boundaries in polycrystalline graphene [Huang *et al.*, 2011; Kim *et al.*, 2011]. The relative position of pentagons and heptagons defines the Burgers vectors of the constituent dislocations. The Burgers vectors, their orientation with respect to the grain boundary line, and the distance between dislocation cores define the grain boundary's structural topological invariant, misorientation angle $\theta = \theta_L + \theta_R$, see Section 3.3.3. This relation allows constructing arbitrary grain boundary models. Alternatively, periodic grain boundaries can be defined in terms of a pair of matching vectors $(n_L, m_L)|(n_R, m_R)$, introduced in Ref. [Yazyev and Louie, 2010a], see Fig. 5.1(a). Throughout this section, however, we shall constrain our discussion to the Burgers vectors \mathbf{b}

5.1. Electronic conductance across periodic grain boundaries

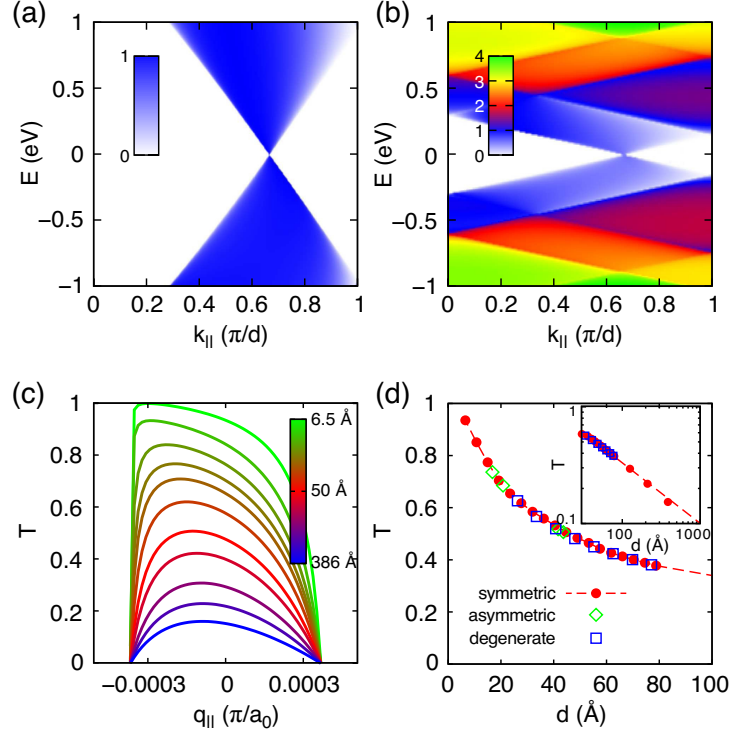


Figure 5.2 – Electronic transport across periodic grain boundaries in graphene formed by the $\mathbf{b} = (1, 0)$ dislocations. (a), (b) Transmission probability as a function of energy E and transverse momentum k_{\parallel} across symmetric grain boundaries characterized by $d = 6.5 \text{ \AA}$ and $d = 36.2 \text{ \AA}$, respectively. (c) Transmission probability close to the Dirac point ($E = 10^{-3} t$) as a function of q_{\parallel} for different values of d . (d) Low-energy transmission of normally-incident charge carriers as a function of inter-dislocation distance d for symmetric, asymmetric and degenerate grain boundaries. The inset shows the same data in logarithmic scale.

and the inter-dislocation distance d in order to simplify the discussion. Figure 5.1(a) shows a generic example of an asymmetric grain boundary formed by $\mathbf{b} = (1, 0)$ dislocations. Figures 5.1(b), (c) depict examples of symmetric ($\theta_L = \theta_R$) periodic grain boundaries formed by $\mathbf{b} = (1, 0)$ and $\mathbf{b} = (1, 1)$ dislocations, respectively. Figure 5.1(d) shows an example of a degenerate grain boundary ($\theta = 0^\circ$) with the Burgers vector of the constituent dislocations oriented along the grain boundary line. In our study, we focus only on those models that do not result in transport gaps due to selection by momentum. Only periodic structures characterized by marching vectors $(n_L, m_L)|(n_R, m_R)$ such that either both $n_L - m_L = 3p$ and $n_R - m_R = 3q$, or both $n_L - m_L \neq 3p$ and $n_R - m_R \neq 3q$ ($p, q \in \mathbb{Z}$) are considered [Yazyev and Louie, 2010a].

5.1.3 Results and discussion

We first focus on symmetric periodic grain boundaries formed by $\mathbf{b} = (1, 0)$ ($b = 2.46 \text{ \AA}$) dislocations. Such grain boundaries are defined by pairs of matching vectors belonging to the $(l, l+1)|(l+1, l)$ series ($l \in \mathbb{N}$). Hence, $d = a_0 \sqrt{3l(l+1) + 1}$, where $a_0 = 2.46 \text{ \AA}$ is the lattice con-

stant of graphene. Figure 5.2(a) shows the transmission probability T as a function of energy E and transverse momentum k_{\parallel} for the first member of this sequence ($l = 1$) characterized by $d = 6.51 \text{ \AA}$ see Fig. 5.1(b). One clearly observes a projected Dirac cone in the irreducible half of the one-dimensional Brillouin zone corresponding to the periodic grain-boundary structure. This model shows $T(k_{\parallel}, E) \lesssim 1$, in agreement with previous calculations [Yazyev and Louie, 2010a]. Figure 5.2(b) shows $T(k_{\parallel}, E)$ for a grain boundary characterized by $l = 8$ and, hence, a larger periodicity $d = 36.2 \text{ \AA}$. The most evident difference between the two is the occurrence of multiple conductance channels as a result of band folding over a smaller Brillouin zone. The striking feature, however, is the clear reduction of transmission (and, consequently, conductance) close to the Dirac point energy $E = 0$. This counter-intuitive decrease of transmission, or equivalently enhancement of scattering upon decreasing the density of dislocations, suggests the topological origin of the discussed transport behavior. Figures 5.2(c-d) further investigate the details of charge-carrier transmission at very low energy ($E = 10^{-3} t$). One clearly observes a monotonic decrease of $T(q_{\parallel})$ (with $q_{\parallel} = k_{\parallel} - (2\pi)/(3d)$ being the transverse momentum relative to the location of the projected Dirac point) as d increases, see Fig. 5.2(c). The transmission probability of normally incident charge carriers ($q_{\parallel} = 0$) exhibits an inverse power scaling law $T \propto d^{-\gamma}$, with an exponent $\gamma \approx 0.5$, see dashed lines in Fig. 5.2(d). Moreover, the observed scaling law is independent of the orientation of the Burgers vectors of dislocations relative to the grain-boundary line. This was explicitly demonstrated using several models of asymmetric and degenerate configurations, see Fig. 5.2(d).

The observed transport anomaly is further investigated by analyzing the local density of states (LDOS) at each site n calculated as

$$\text{LDOS}_n(E) = -\frac{d}{\pi^2} \int_0^{\pi/d} \text{Im}(G_S(E, k_{\parallel}))_{n,n} dk_{\parallel}. \quad (5.5)$$

Figure 5.3(a) shows the density of states (DOS) calculated by summing the LDOS over atoms located in the grain-boundary region of 40 \AA width. One clearly observes the presence of sharp van Hove singularities both in the valence and conduction bands superimposed on the linear contribution of pristine graphene. The peak positions converge to the Dirac point energy as the distance between dislocations d increases, see Fig. 5.3(b). These DOS peaks can be attributed to the emergence of electronic states localized at the dislocations, as indicated by Figure 5.3(c). The presence of localized states results in resonant back-scattering at low energies, similar to dopants and covalent functionalization defects in graphene [Choi *et al.*, 2000; Titov *et al.*, 2010; Wehling *et al.*, 2010; Yuan *et al.*, 2010; Ferreira *et al.*, 2011; Radchenko *et al.*, 2012].

The origin of these localized states is related to the topological nature of defects in polycrystalline graphene. Charge carriers of momentum \mathbf{k} encircling a dislocation with Burgers vector \mathbf{b} gain a phase $\varphi = \mathbf{k} \cdot \mathbf{b}$ [S. V. Iordanskii, 1985]. The aforementioned $\mathbf{b} = (1, 0)$ dislocations thus give rise to $\varphi = +2\pi/3$ and $\varphi = -2\pi/3$ for charge carriers in valleys $\xi = +1$ and $\xi = -1$, respectively. Starting from the Dirac equation for a massless particle the effect of a dislocation

5.1. Electronic conductance across periodic grain boundaries

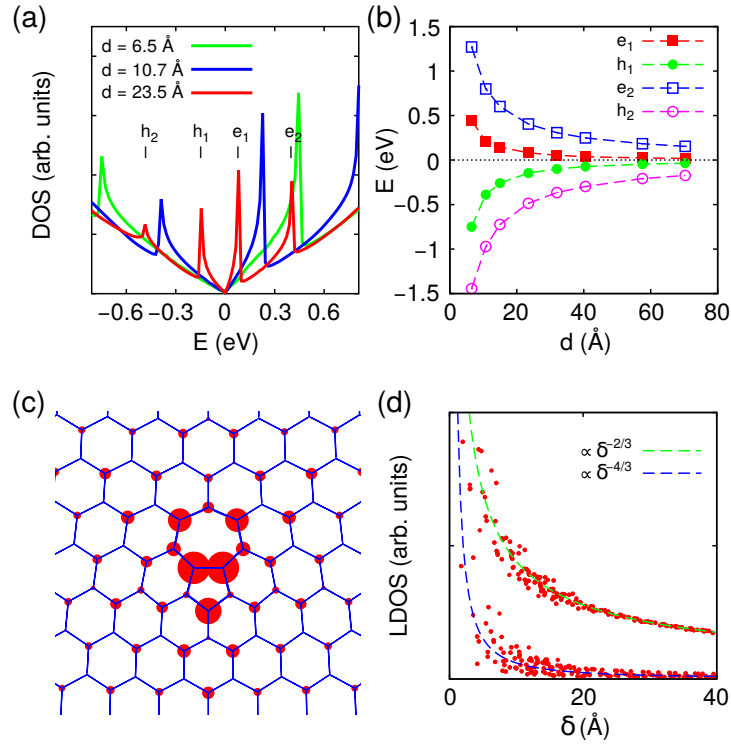


Figure 5.3 – (a) Density of states (DOS) in the interface region computed for the grain boundaries formed by $\mathbf{b} = (1, 0)$ dislocations with different values of d . (b) Positions of the DOS peaks as a function of d . The labels refer to peaks in panel (a) shown for the $d = 23.5$ Å grain boundary. (c) Local density of states (LDOS) at $E = 10^{-3}t$ for the $d = 61.8$ Å grain boundary. Circle areas are proportional to the LDOS. (d) LDOS as a function of distance from the defect core δ calculated at $E = 10^{-3}t$ for the $d = 385$ Å grain boundary. Solid lines indicate two trends consistent with the results of Ref. [Mesaros *et al.*, 2010].

is accounted for by means of a gauge field $\mathbf{A} \propto \mathbf{k} \cdot \mathbf{b}$ [Lammert and Crespi, 2000; Cortijo and Vozmediano, 2007; Mesaros *et al.*, 2009; Vozmediano *et al.*, 2010]:

$$H = (p_x - iA_x)\sigma_x + (p_y - iA_y)\xi\sigma_y, \quad (5.6)$$

Using this continuum model Mesaros *et al.* predicted that an isolated $\mathbf{b} = (1, 0)$ dislocation gives rise to quasi-localized modes at $E = 0$ [Mesaros *et al.*, 2010]. The continuous model for $\mathbf{b} = (1, 0)$ has two low-energy solutions with the LDOS decaying as $\propto \delta^{-2/3}$ and $\propto \delta^{-4/3}$, where δ is the distance from the defect core. These analytic results are confirmed by our numerical calculations on a grain-boundary model with a very large distance between dislocations ($d = 61.8$ Å). In particular, the two solutions coexist on opposite sublattices of the graphene lattice, see Fig. 5.3(d).

In order to gain a qualitative understanding of the dependence of transmission on d , see Figs. 5.2(c-d), one has to appreciate the fact that a finite distance between the dislocations forming a grain boundary is responsible for the hybridization of the localized states. As a

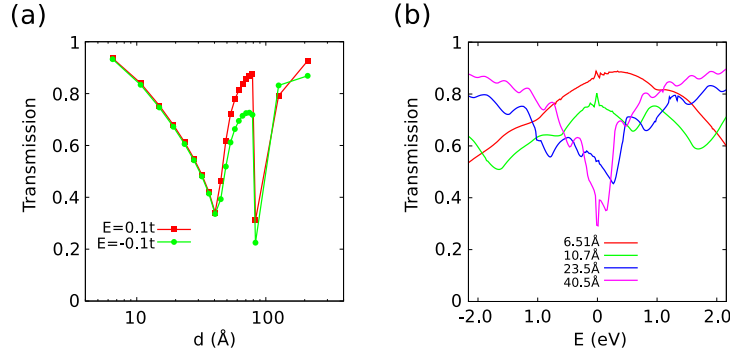


Figure 5.4 – Electronic transport at finite energy across periodic GB composed by $\mathbf{b} = (1, 0)$ dislocations. (a) Transmission probability at $E = \pm 0.1t$, as a function of inter-dislocation distance d . (b) Momentum-averaged transmission as a function of E calculated for different values of d . In this plot, transmission has been renormalized by that of pristine graphene samples.

result, LDOS peaks at positive and negative energies emerge instead of the $E = 0$ peak that is typical of isolated dislocations. As the distance between dislocations d increases, the degree of hybridization diminishes, thus reducing the peak energies, see Figs. 5.3(a-b) and resulting in the progressive decrease of the transmission close to $E = 0$. At finite energies, however, the minimum of transmission is achieved at certain distance between dislocations. Fig. 5.4(a) shows the normal-incidence transmission across $\mathbf{b} = (1, 0)$ grain boundaries as a function of the inter-dislocation distance d at $E = \pm 0.1t$. Upon increase of d , we first observe a decrease of transmission similar to what seen at lower energies, then a first minimum followed by a sudden rise, a second minimum and, finally, an asymptotic approach to $T = 1$. This trend can be understood by tracking the energy position of the LDOS peaks as a function of d . For increasing d , the two LDOS peaks are shifted toward $E = 0$ and the energy value $|E| = 0.1t$ lies, respectively, in the first peak (first minimum of T), between the two peaks (rise of T), into the second peak (second minimum of T), and, finally, beyond the peaks (asymptotic approach to $T = 1$). For higher energies the position of the two minima is expected to move to shorter distances d . Fig. 5.4(b) shows the overall energy behavior of momentum-averaged transmission $T(E)$ defined as

$$T(E) = \frac{d}{\pi} \int_0^{\pi/d} T(E, k_{\parallel}) dk. \quad (5.7)$$

Overall there is a large energy $\simeq [-0.5, 0.5]$ eV window where GBs with large angle (high defect density) are more transparent than small-angle GBs (low defect density). Outside this energy window, small-angle GBs are more transparent, thus recovering the intuitively expected behavior.

It is worth stressing that despite the fact that our conclusions are based on periodic models of dislocations, there is no strict requirement of periodicity, in contrast to the case of suppressed conductivity due to momentum conservation [Yazyev and Louie, 2010a]. This has been explic-

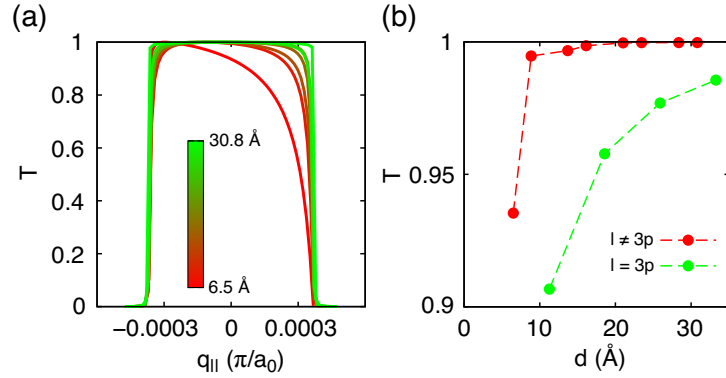


Figure 5.5 – Electronic transport across grain boundaries composed of $\mathbf{b} = (1, 1)$ dislocations. (a) Transmission probability close to the Dirac point ($E = 10^{-3}t$) as a function of $q_{||}$ for the grain boundaries characterized by different values of d within the $l \neq 3p$ family. (b) Low-energy transmission of the normally-incident charge carriers as a function of inter-dislocation distance d . Two families of grain boundaries are distinguished.

itly verified by means of supercell calculations which show that transmission is insensitive to perturbation of the periodic arrangement of dislocations in grain boundaries.

More generally, all dislocations characterized by Burgers vectors $\mathbf{b} = (n, m)$ with $n - m \neq 3q$ ($q \in \mathbb{Z}$) have a similar effect on graphene charge carriers because of equal values of $\mathbf{k} \cdot \mathbf{b}$. However, dislocations with $n - m = 3q$ are expected to behave as ordinary (topologically trivial) scatterers since $\mathbf{k} \cdot \mathbf{b} = 4\pi$. We verify this hypothesis by investigating the transmission through grain boundaries formed by $\mathbf{b} = (1, 1)$ ($b = 4.23$ Å) dislocations, see Fig. 5.1(c). Following the convention defined earlier, these grain boundaries are defined by pairs of matching vectors belonging to $(1, l+1)|(l+1, 1)$ series ($l \in \mathbb{N}$). Figure 5.5(a) shows that already the first members of this family exhibit transmission probabilities close to 1, which further increase as the inter-dislocation distance d increases. Furthermore, one can distinguish two families of grain-boundary structures characterized by $l = 3p$ and $l \neq 3p$ ($p \in \mathbb{N}$), see Fig. 5.5(b). Within both families the effect of dislocations can be described in terms of scattering cross-sections, $\sigma_{l=3p} \approx 0.5$ Å and $\sigma_{l \neq 3p} \approx 0.01$ Å. The first value is significantly larger since both Dirac points correspond to $k_{||} = 0$, thus enabling intervalley scattering upon transmission across the GB. The LDOS calculated for these grain boundary configurations shows no localized states at low energies (not shown here).

5.1.4 Conclusions

The study reported in the present section reveals an intriguing aspect of charge-carrier transport in topologically disordered graphene. We predict anomalous scattering in small-angle grain boundaries ($d \gg |\mathbf{b}|$) composed of dislocations with the minimal Burgers vector $\mathbf{b} = (1, 0)$. These dislocations are dominant in realistic samples due to their reduced elastic response, and may even occur within seemingly single-crystalline domains of graphene [Coraux *et al.*,

2008]. Dilute dislocations act as resonant scattering centers, similarly to covalently bound adatoms, see Section 2.2 [Titov *et al.*, 2010; Wehling *et al.*, 2010; Yuan *et al.*, 2010; Ferreira *et al.*, 2011; Radchenko *et al.*, 2012], but unlike adatoms, dislocations cannot be easily eliminated from the sample due to their topological nature and high diffusion barriers, see Section 3.3.2.

5.1.5 Additional calculations

In order to further validate the choice of the first-neighbor TB Hamiltonian defined in eq. 5.1, which we have employed to obtain all the results reported so far, we repeat some of the important calculations using the third-neighbor TB model defined in Ref. [Lherbier *et al.*, 2011]. In such a model, the second- and third-neighbor hopping term are, respectively, $t' = -0.064t$ and $t'' = 0.052t$.

The comparison between first- and third-neighbor TB model is shown in Fig. 5.6.

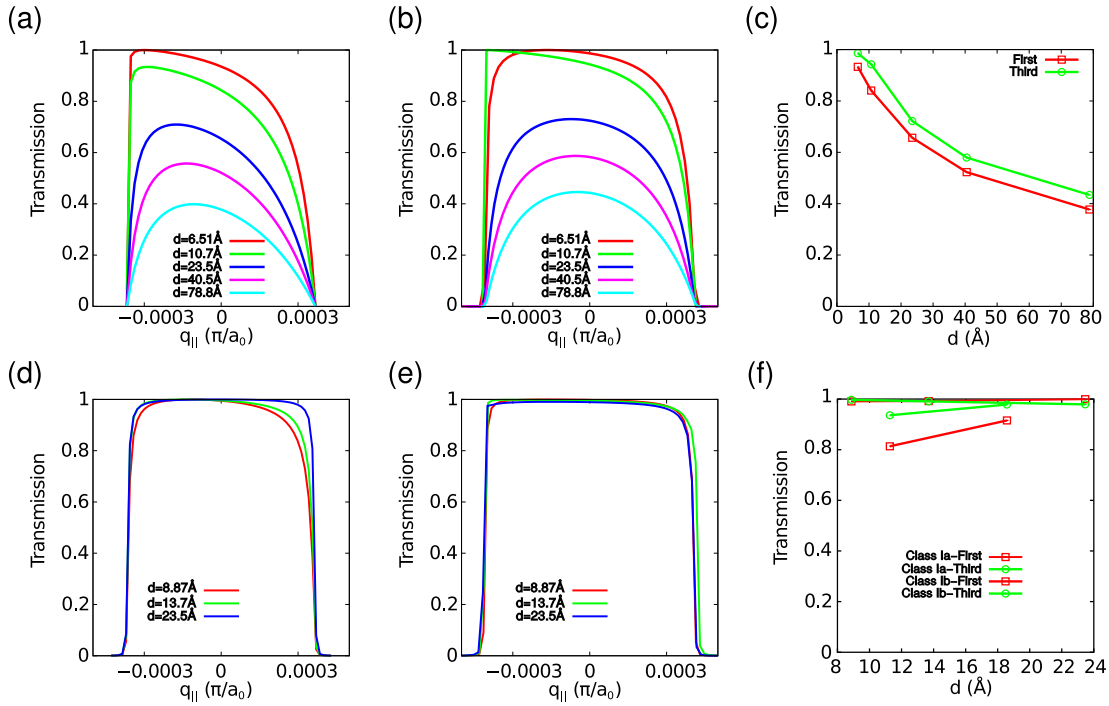


Figure 5.6 – Charge-carrier transmission probability across $\mathbf{b} = (1, 0)$ grain boundaries at low energy ($E = 10^{-3}t$) as a function of $q_{||}$ calculated using (a) the first-neighbor TB model (eq. 5.1) and (b) the third-neighbor TB model proposed in Ref. [Lherbier *et al.*, 2011]. (c) Low-energy transmission of normally-incident charge carriers as a function of d calculated using first- and third-neighbor TB models, labeled NN and 3NN, respectively. Panels (d-f) show the same quantities as (a-c) calculated for $\mathbf{b} = (1, 1)$ grain boundaries.

5.2 Electronic transport across disordered grain boundaries

5.2.1 Introduction

In the previous section, we have studied the effect of periodic GBs on electronic transmission, also accounting for slight perturbation to the periodicity, and predicted anomalous low-energy scattering for small-angle GBs.

In this section, we address the problem of evaluating the conductance of disordered grain boundaries. Having a collection of realistic grain boundaries for a given misorientation angle is propaedeutic to the calculation of any physical observable. We have chosen to employ a Monte Carlo simulation in order to explore the configuration space of the interface between two misaligned domains. This has provided ensembles of defect structures not selected randomly but weighted by their formation energy with respect to the corresponding ordered low-energy configuration. Thereafter, we have sampled several observables to have a complete picture of both the morphology (number of atoms of the rings, atomic coordination, formation energy), and spectral and transport properties (DOS, transmission, conductance). The statistical analysis of the data allowed us to put on a quantitative basis the connection between the average conductance of a single grain boundary and its misorientation angle.

As discussed in Section 3.3.3, it has been shown that the presence of multiple grain boundaries, which is expected in polycrystals, leads to a simple law of direct proportionality between the conductance of the sample and the average linear size of individual grains [Van Tuan *et al.*, 2013]. This can be easily interpreted as the emergence of ohmic behavior induced by the presence of multiple grain boundaries. At this point, our quantitative estimates for the conductance across a single grain boundary combined with the knowledge of the transport regime let us glimpse the opportunity for a multiscale determination of the intrinsic transport properties in large area polycrystalline samples. A very minimal, although meaningful, illustrative example is given at the end of this section.

5.2.2 Description of the work

In Fig. 5.7(a), we illustrate a prototypical initial setup constituted by two domains misaligned by $\theta = \theta_L + \theta_R = 21.2^\circ$ merging at the center, where they form a GB. The rectangular periodic supercell has 10.9 nm width and 5.2 nm height with 2044 atoms in total. The green regions in Fig. 5.7(a) represent regions of pristine graphene that are kept fixed during the simulation.

In order to perform a Monte Carlo simulation two ingredients are necessary: the basic move and the acceptance criterion. We have chosen the Wooten-Winer-Waeire move [Wooten *et al.*, 1985] that consists in the rotation of an atomic bond by 90° , as illustrated in Fig. 5.7(b). The system is therefore relaxed by minimizing the LCBOP classical potential [Los and Fasolino, 2003]. Within a pristine area of graphene, this move results in the creation of the so-called Stone-Wales defect, see Fig. 5.7(b), characterized by a high formation energy of about 5 eV [Li

et al., 2005], see Section 3.2. When the rotation is performed in the vicinity of a dislocation (i.e. a pentagon-heptagon pair), it often represents an energetically low-cost move, see Fig. 5.7(c). In the proximity of a grain boundary, the move can even lead to a structure with a lower energy, thus allowing the exploration of the configuration space. Therefore, our final choice is to rotate bonds that connect at least one atom belonging to the GB. We adopt the Metropolis scheme as an acceptance criteria [Metropolis *et al.*, 1953]. It is important to say that, for our purpose, the MC simulation is not intended as a tool to obtain a thermodynamics ensemble of configurations. In fact, the growth of the grains in a chemical vapor deposition, which leads to the formation of boundaries, takes place in conditions that are out of thermodynamic equilibrium. In our case, the MC simulation rather consists in a tool to collect realistic grain boundary configurations. In this spirit, it must not confuse that the main temperature chosen for the simulation $T = 5000K$ is close to the melting temperature for graphene [Zakharchenko *et al.*, 2011]. In fact, our simulations involve only few degrees of freedom in the boundary region, and the energy equivalent of the simulation temperature ($= 0.43$ eV) divided by the average distance between two carbon atoms (1.42 Å) is comparable to the typical formation energy of a GB ($0.2 - 0.8$ eV/Å). In other words, the temperature has been chosen so that the system has a significant probability to assume distinct configurations along the simulation.

The starting structural models are periodic rectangular supercells containing one GB, as shown in Fig. 5.7(a). The periodicity along the direction parallel to the GB, W , is in the range $[5.2, 6.0]$ nm, except for one asymmetric model with $\theta = 30^\circ$, where $W = 11.0$ nm, whereas the periodicity along the direction orthogonal to the GB, H , is comprised in the range $[8.95, 10.2]$ nm. The total number of atoms lies between 1848 and 2144, except for the asymmetric $\theta = 30^\circ$ model that has 3758 atoms. All the starting configurations can be found in Figs. 5.13.

Initially, all systems have been relaxed in both the atomic and the cell degrees of freedom. After each move, the structure has been relaxed keeping the cell parameters fixed. Relaxations have been achieved by minimizing the total energy calculated by means of the Long-Range Carbon Bond Order Potential (LCBOP) [Los and Fasolino, 2003], as implemented in the open source code LAMMPS [Plimpton, 1995; LAMMPS], see Section 4.3. The LCBOP has been selected among available alternatives after the comparison of the formation energies of several defects (both local and topological) with DFT results.

After each move, the system is relaxed and the minimized energy is employed in the Metropolis scheme, see Section 4.6. For the description of low-energy charge carriers we have adopted a next-neighbor tight-binding Hamiltonian restricted to p_z orbitals in which the hopping term t is set to 2.7 eV, see Sections 1.3 and 5.1.2.

The coherent conductance across the GB is calculated numerically by means of the Landauer-Büttiker theory, see Section 4.5.1. We use a two-terminal device configuration including translationally invariant semi-infinite leads made of ideal graphene. The connection between the leads and the scattering region is ensured by the regions of immobile atoms highlighted in

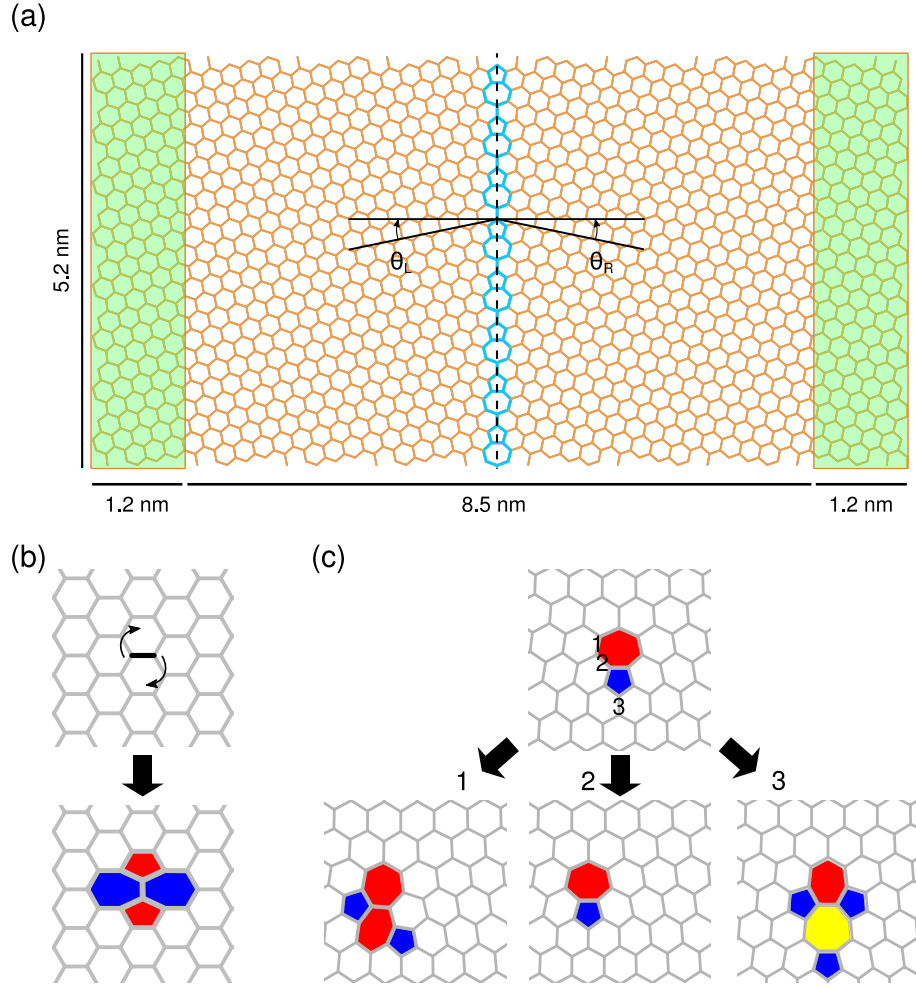


Figure 5.7 – Simulation setup and MC move outcomes. (a) Initial configuration of a two-domain system with misorientation angle $\theta = \theta_L + \theta_R = 21.2^\circ$. The system is periodic in both the directions parallel and orthogonal to the GB. Atoms in green regions are kept fixed along the simulation. (b) Bond rotation in a pristine graphene region resulting in the formation of a Stone-Wales defect. (d) Three relevant outcomes of a bond rotation around a 5-7 pair: (1) creation of an additional 5-7 pair, (2) glide, and (3) a higher energy defect including an eight-membered ring.

green in Fig. 5.7(a). Transmission is a function of transverse momentum k_{\parallel} (defined for the supercell) and energy E , and has been evaluated as $T = \text{Tr}[\Gamma_L G_S^\dagger \Gamma_R G_S]$, where we have omitted explicit dependences on energy and momentum for brevity. The Green's function of the scattering region is defined as $G_S(k_{\parallel}, E) = [E^+ I - H_S(k_{\parallel}, E) - \Sigma_L(k_{\parallel}, E) - \Sigma_R(k_{\parallel}, E)]^{-1}$, the coupling matrices Γ for the left and right lead are given by $\Gamma_{L(R)}(k_{\parallel}, E) = i [\Sigma_{L(R)}(k_{\parallel}, E) - \Sigma_{L(R)}^\dagger(k_{\parallel}, E)]$, $H_S(k_{\parallel}, E)$ is the Hamiltonian of the scattering region Fourier-transformed along direction \parallel , $\Sigma_{L(R)}$ are the self-energies coupling the scattering region to the leads, and $E^+ = E + i\eta$ ($\eta \rightarrow 0^+$). The self-energies, $\Sigma_{L(R)}$, have been calculated by means of the recursion technique described in Ref. [Sanvito *et al.*, 1999]. Given a finite bias $V = V_L - V_R$, where $V_{L(R)}$ is the chemical potential

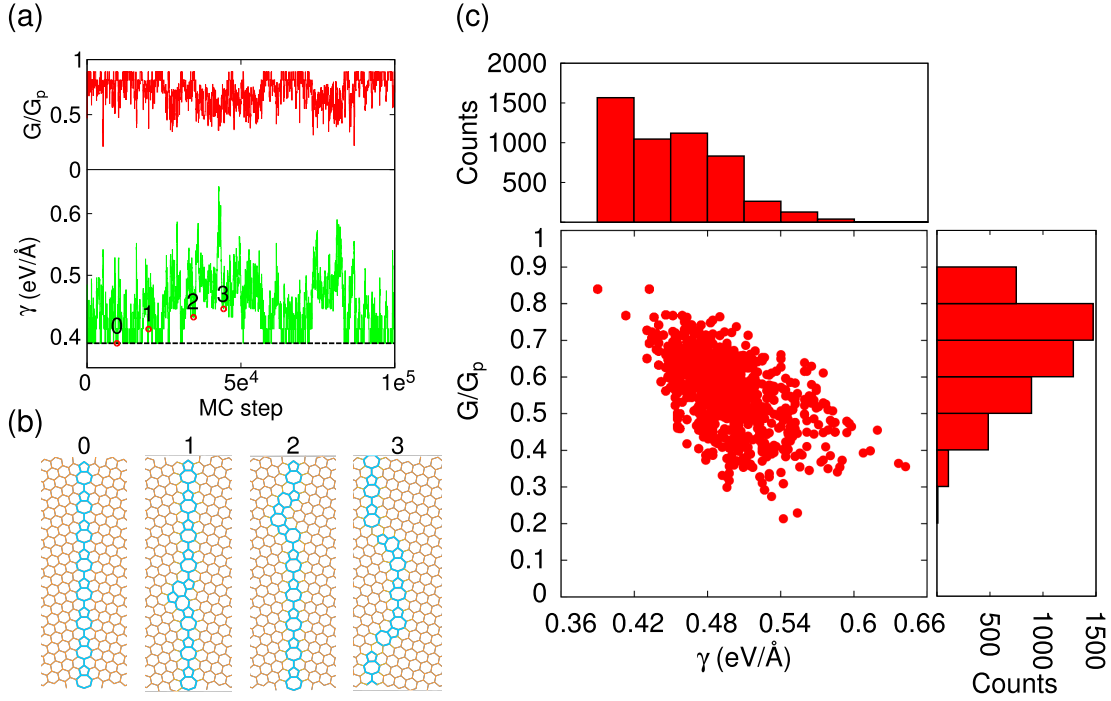


Figure 5.8 – Observables sampled during the simulation of the $\theta = 21.2^\circ$ GB. (a) Evolution of the formation energy and the conductance integrated between -0.5 eV and 0.5 eV. (b) Ground state and three representative low-energy configurations extracted from the simulation. The corresponding energies are indicated in the upper plot by red circles. (c) The main frame contains a scatter plot of conductance *vs.* formation energy. The upper (side) histogram shows the formation energy (transmission) distribution. All conductances are normalized by the value pertaining to a pristine graphene sheet of the same size of the polycrystalline sample.

of the left(right) lead, and assuming that temperature T is such that $k_B T \ll V$, conductance G has been calculated as $G = G_0 \int_{V_L}^{V_R} dE \int_{1BZ} T(k_{\parallel}, E)$. In order to evaluate the latter integral, 11 independent k -points and 48 energy-points have been used, respectively.

The DOS has been calculated as $\text{DOS}(E) = -\frac{W}{\pi^2} \int \text{Im}(G_S(E^+, k_{\parallel})) dk_{\parallel}$ and the integral has been discretized over a 21 k -points grid.

5.2.3 Results and discussion

We have performed simulations starting from 8 symmetric GBs covering a range of misorientation angles $\theta \in [7.3^\circ, 51.5^\circ]$, and one asymmetric GB with $\theta = 30^\circ$. The data collected along a typical simulation are presented in Fig. 5.8. The starting configuration is the left one sketched in Fig. 5.8(b0), consisting in a $\theta = 21.2^\circ$ GB made of 8 pentagon-heptagon pairs.

The evolution of the formation energy, plotted in Fig. 5.8(a) shows that there are several low-energy configuration occurring frequently. Three of these disordered GBs are sketched in Fig. 5.8(b1-3). From a comparison with the initial ordered configuration, it can be seen that

5.2. Electronic transport across disordered grain boundaries

each of them results from a combination of glides, creations or annihilations of pentagon-heptagon pairs. These transformations have been recognized as those responsible for the life cycle of dislocations and for the evolution of grain boundaries [Lehtinen *et al.*, 2013; Kurasch *et al.*, 2012]. Along the simulation, defective rings made of 5 and 7 members represent, respectively, 50.1% and 49.7% of the non-six-membered rings. The remaining 0.2% is given exclusively by 8 membered rings. The absence of rings with less than 5 members and the rare occurrence of 8-membered rings has to be put in connection with the high energy cost of those defects [Liu *et al.*, 2012; Liu and Yakobson, 2010; Yazyev and Louie, 2010b]. A mismatch between the number of pentagons and heptagons of a GB also implies a higher formation energy. As a general fact, in all our simulations, the GBs lying in the low energy region, are formed exclusively by 5- and 7-membered rings in equal number. In addition, along all our simulations, the coordination number of the carbon atoms was identically equal to 3, except for few very high-energy (and rare) configurations in which four-coordinated atoms appeared. Even for high-energy configuration the typical shape of the GBs tended to be meandering but continuous. This is in accordance with what was found in experimental atomic resolution imaging of GBs [Huang *et al.*, 2011; Kim *et al.*, 2011]. Together with formation energy, Fig. 5.8(a) shows the evolution of the conductance calculated for a bias voltage $V = 1$ V. In all our simulations, except two, the lowest-energy was achieved by an ordered periodic configuration, see Figs. 5.13 and 5.14. For the sake of clearness, the conductance of graphene samples containing a grain boundary, G , has been normalized by the conductance of a pristine graphene sample of the same size of the sample employed in the simulation, G_p . Fig. 5.8(c) shows a statistical analysis of the data. The conductance histogram is characterized by a broad distribution, although it shows the persistence of high-transmission configurations. The main panel clearly indicates the existence of some inverse correlation between conductance and energy, meaning that, on average, a higher energy corresponds to a lower conductance. This can be explained by appreciating the fact that configurations with a high formation energy correspond to more disordered GBs with a larger number of non six-membered rings, that is, a larger number of scatterers for the charge carriers.

A movie of the simulation of the $\theta = 21.2^\circ$ GB, performed at $T = 7000$ K in order to accelerate the sampling, is available at this [url](#) (online version).

Fig. 5.9 reports the distribution of G for different misorientation angles. Going through increasing misorientation angles, one sees that the distributions evolve almost continuously with a sudden change registered between 21.8° and 30° , giving an indication for an abrupt transition in the conductance trend. This strong suppression of the conductance cannot be attributed to the asymmetry of the $\theta = 30^\circ$ GBs. In fact, the GBs with the closest misorientation angle $\theta = 32.2^\circ$ have a similar distribution, but are symmetric. This suggests that the misorientation angle θ must be considered as the main parameter which determines the transport across the GBs. It is interesting to notice that, as discussed in Section 3.3.1, the GB formation energy has an analogous trend, showing a minimum around $\theta = 30^\circ$ [Yazyev and Louie, 2010b].

When conductance is evaluated at energy E close to the Fermi energy E_f ($E - E_f = 0.02$ eV), its

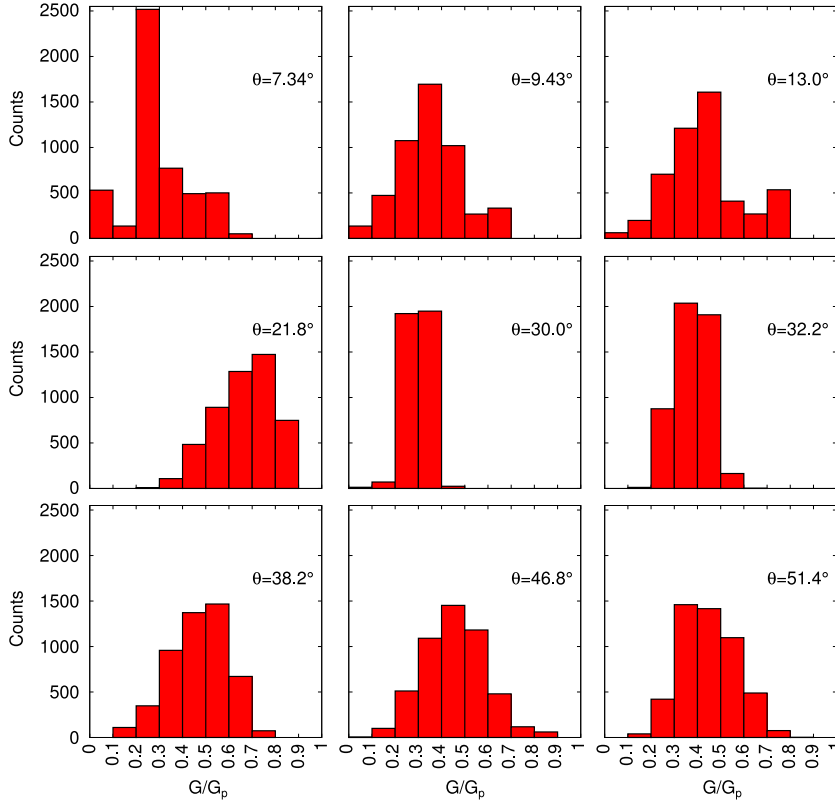


Figure 5.9 – Distributions of the conductance for different systems characterized by the misorientation angle θ , as indicated in the panels. The units adopted for the conductance are the same as in Fig. 5.8

distributions are broader, although the average conductance is slightly higher (not shown here). This instability at the Fermi level is reduced when the conductance is integrated over an finite energy interval. The existence of correlations between formation energy and conductance is also more evident after the integration.

A more detailed picture of the effect of the presence of disorder is obtained by looking at transmission and density of states (DOS) as a function of energy, reported in Fig. 5.10. For systems with $0^\circ < \theta < 30^\circ$, independently of the energy, disorder-averaged transmissions are significantly reduced with respect to those of the ordered GB configuration, namely, the effect of disorder in GBs is to add further charge carrier backscattering. For systems with $0^\circ < \theta < 30^\circ$, where the ordered configurations have already a low transmission compared to pristine graphene, disorder-averaged conductances do not differ significantly. The effect of disorder on the averaged DOS can be summarized in two tendencies. First, the characteristic peaks of the ground-state ordered configurations are smeared out for most misorientation angles. Second, as a result of the disorder average, the DOS shows an increase of the spectral weight around $E = 0$.

The conductance of disordered GBs has a clear, although not trivial, dependence on the mis-

5.2. Electronic transport across disordered grain boundaries

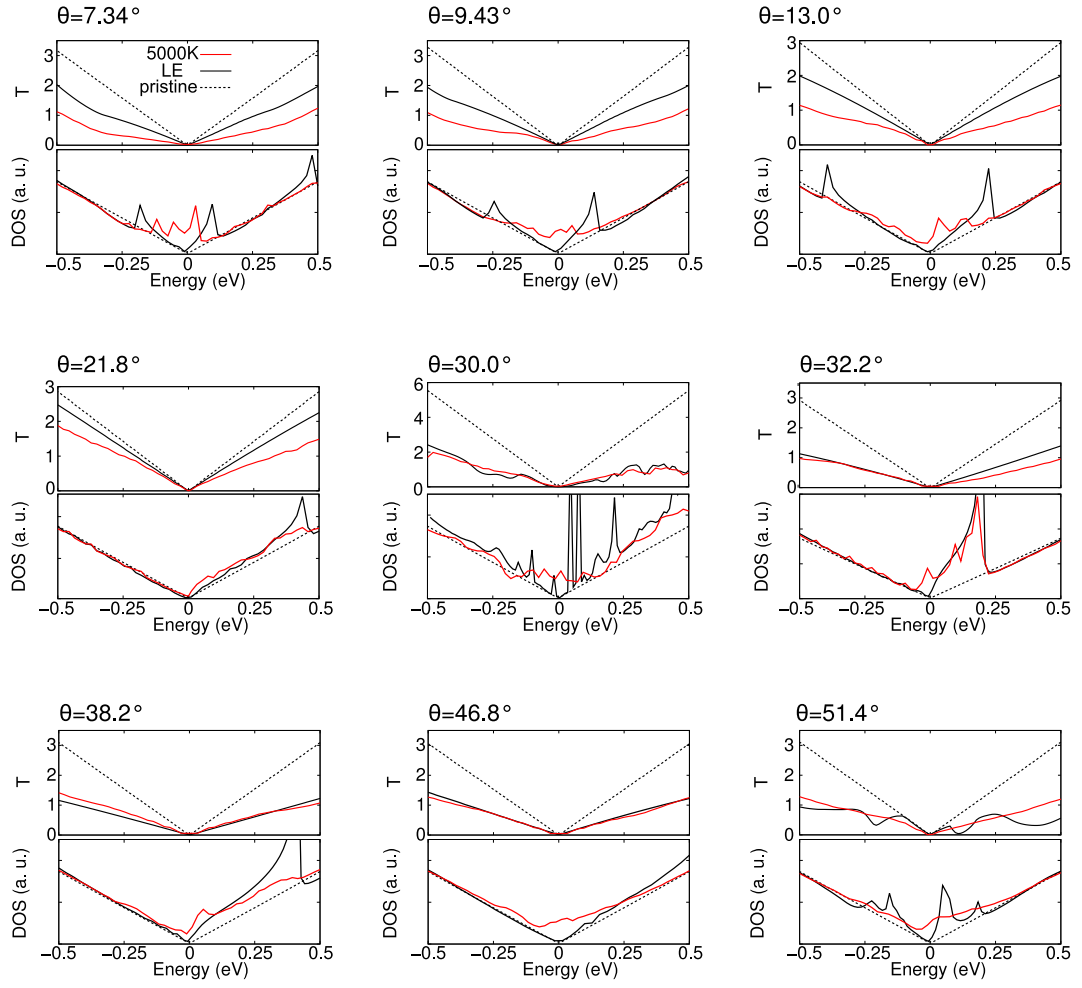


Figure 5.10 – Disorder-average transmission (upper panels) and density of states (lower panels) as a function of energy for all simulations. The dashed lines represent the observables calculated for a pristine graphene sheet of the same size, the black solid lines represent the observables calculated for the lowest-energy configuration found in the simulation, and the red curves are the simulation averages of the observables.

orientation angle θ . This dependence has been put in evidence in Fig. 5.11 for two situations. In panel (a), the average conductance at low energy ($E = 0.02$ eV) is plotted as a function of θ . In order to make a comparison possible with the case of ordered GBs, we have added an analogous curve for the conductance of ordered small-angle GBs (dashed line). As discussed in Section 5.1, the latter is suppressed upon a reduction of the misorientation angle. It is evident that this trend is inherited by the average conductance of disordered GBs, which shows a maximum at $\theta = 21.8^\circ$ and drops for smaller angles. On the other hand, the region $30^\circ < \theta < 60^\circ$ exhibits a less clear trend, as conductance is affected by large relative fluctuations of the order of 20 – 50%. Such a low-energy instability is sensibly improved by calculating conductance in presence of a finite bias $V = 1.0$ V, as shown in Fig. 5.11(b). Although the values of average conductance are now lower for most of the misorientation angle range,

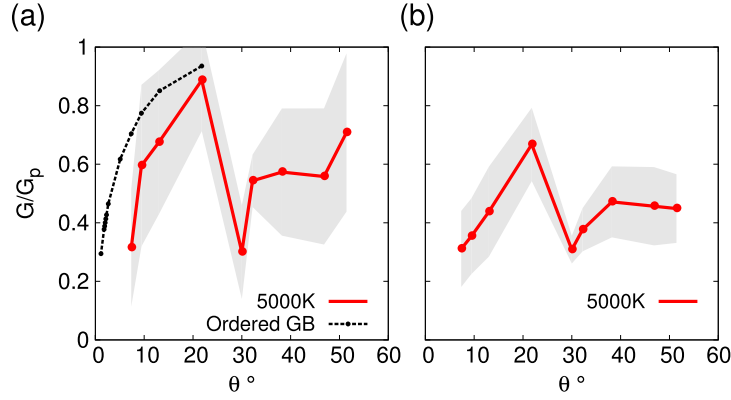


Figure 5.11 – Conductance as a function of misorientation angle θ . Conductance (a) calculated at low energy $E = 2.7$ meV, and (b) integrated between -0.5 eV and 0.5 eV. The red points are the simulation averages. The width of the gray area corresponds to the standard deviation of the distributions. The black dashed lines represent the conductance for the ground-state configurations in the small-angle regime.

fluctuations are reduced by approximately a factor 2 making it possible to identify two well separated trends. Again, starting from the maximum achieved for $\theta = 21.8^\circ$ and going toward small angles, the conductance decreases, reproducing the behavior of ordered GBs. Although computational limitations prevent us from reducing the misorientation angle further, we expect that the average conductance will approach the conductance of the ordered GBs in the limit of zero angle. In this limit, indeed, the ordered low-energy GBs are predominant since they are constituted by largely separated pentagon-heptagon pairs and any deviation from the ordered structure has a high energy cost. As a consequence, the average conductance is dominated by the contribution of the ordered configurations. A different trend characterizes the region $30^\circ < \theta < 60^\circ$. After a minimum for $\theta = 30^\circ$, the conductance increases before stabilizing around $G \approx 0.45G_p$, G_p being the conductance of a pristine sample of the same size. In this region, the overall effect of disordered GBs is to reduce the conductance to about the 40% of the conductance of pristine graphene.

Based on the knowledge of the conductance (or, equivalently, resistance) of a single grain boundary one can calculate the effect on electronic transport of a distribution of grain boundaries typical of a polycrystalline sample. As discussed in Section 3.3.3, the effects of many individual grain boundaries add up incoherently, meaning that quantum interference effects are negligible and the resistance due to individual GBs is additive [Van Tuan *et al.*, 2013]. The resistance of a two-terminal configuration $R = G^{-1}$ can be viewed as arising from two contributions [Datta, 1997]:

$$R = R_P + R_{GB} = G_P^{-1} + G_P^{-1} \left(\frac{G_P - G}{G} \right), \quad (5.8)$$

where R_P is the resistance due to reflectionless contacts (i.e. the resistance of a pristine sample) and R_{GB} is the resistance of the scattering source - the GB in our case. Importantly,

5.2. Electronic transport across disordered grain boundaries

R_{GB} has the property of being additive. Since the resistance is inversely proportional to the transverse width W , it is convenient to introduce a width-independent grain-boundary resistance $\rho_{GB} = R_{GB} * W$ [Tsen *et al.*, 2012]. Our results, recast in terms of ρ_{GB} (see Fig. 5.12), show an even stronger dependence on the misorientation angle. We point out that the values of ρ_{GB} presented in Fig. 5.12 should be considered as lower boundary estimates since they do not account for additional scattering due to potential barriers occurring at the grain boundaries [Tapasztó *et al.*, 2012; Koepke *et al.*, 2013; Ihnatsenka and Zozoulenko, 2013], adsorbates bound to the atoms belonging to GBs (see Section 3.3.2), etc.

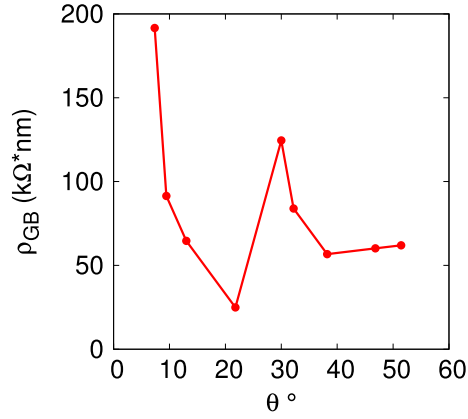


Figure 5.12 – Width-independent resistance ρ_{GB} as a function of the misorientation angle θ calculated for a bias $V = 1$ eV.

Finally, if one introduces an average angle-independent $\langle \rho_{GB} \rangle \simeq 80$ k Ω * nm, a rough estimate for the intrinsic resistance of a polycrystalline sample of width W and length L with a linear density of grain boundaries n is given by

$$R = \frac{nL}{W} \langle \rho_{GB} \rangle \quad (5.9)$$

This formula neglects all details of the angle distribution in realistic GBs. Nevertheless, it provides an order of magnitude for the contribution of the coherent backscattering off GBs to the resistance of polycrystalline graphene. For a square sample with a density $n = 0.1 \text{ nm}^{-1}$, this contribution amounts to $\rho_{GB} \simeq 8 \text{ k}\Omega$.

5.2.4 Conclusions

In the study reported in the present section, we addressed the issue of electronic transport across disordered grain boundaries combining Monte Carlo simulation to obtain grain-boundary configurations, and transport calculations based on the Landauer-Büttiker theory. The disorder-averaged conductance exhibits a clear dependence on the topologically-invariant misorientation angle. We identified a small-angle and a large-angle behavior of conductance, separated by a local minimum at $\theta = 30^\circ$. The small-angle behavior is similar to what found in periodic GBs, namely, conductance drops upon a reduction of θ . In the large-angle behavior, conductance reaches an approximately constant value.

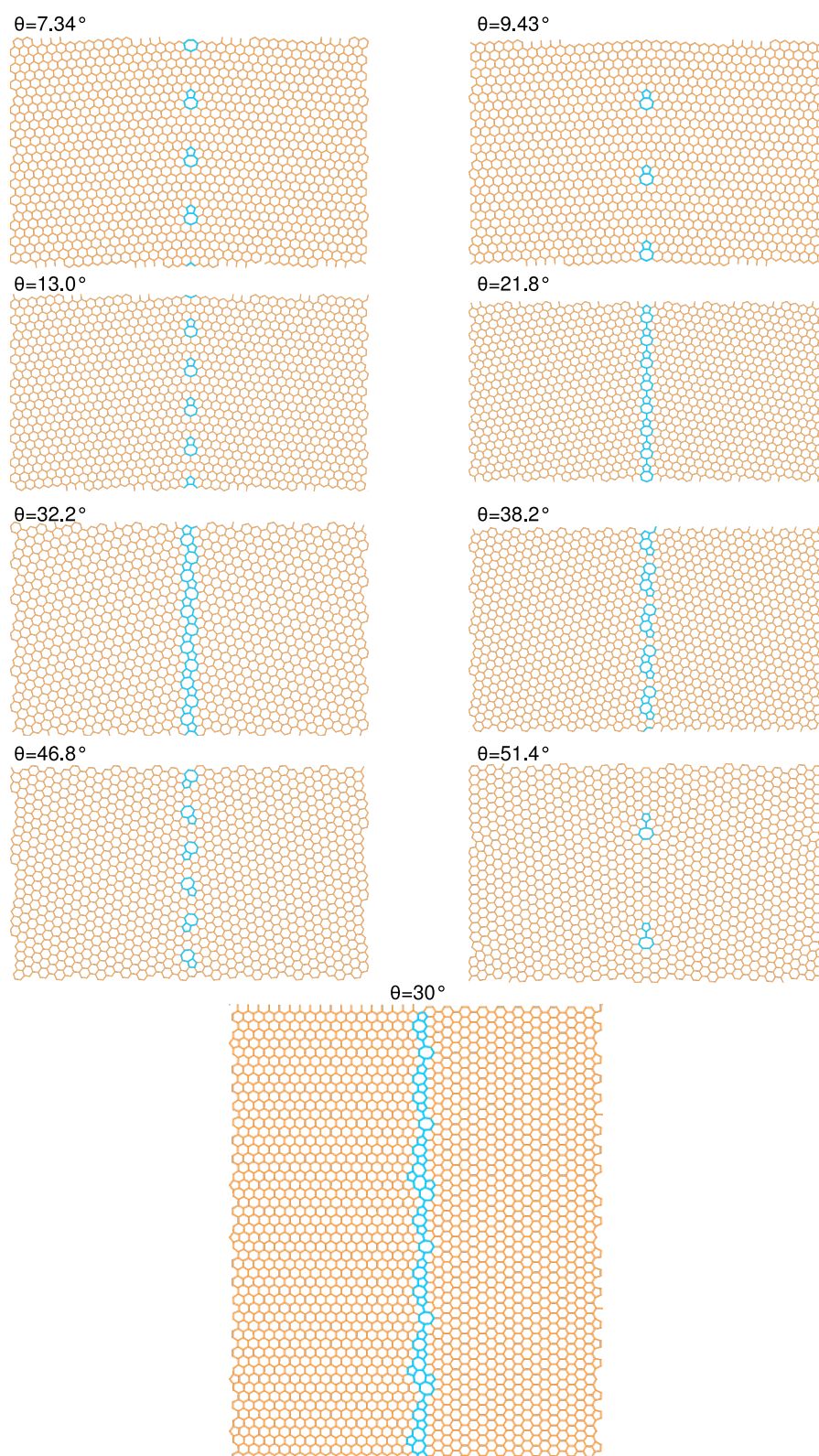


Figure 5.13 – Atomic structures of the starting configurations of the simulations. Notice that for the GBs characterized by $\theta = 30^\circ$ and $\theta = 51.4^\circ$ the starting configuration does not correspond to the lowest energy (see Fig. 5.14).

5.2. Electronic transport across disordered grain boundaries

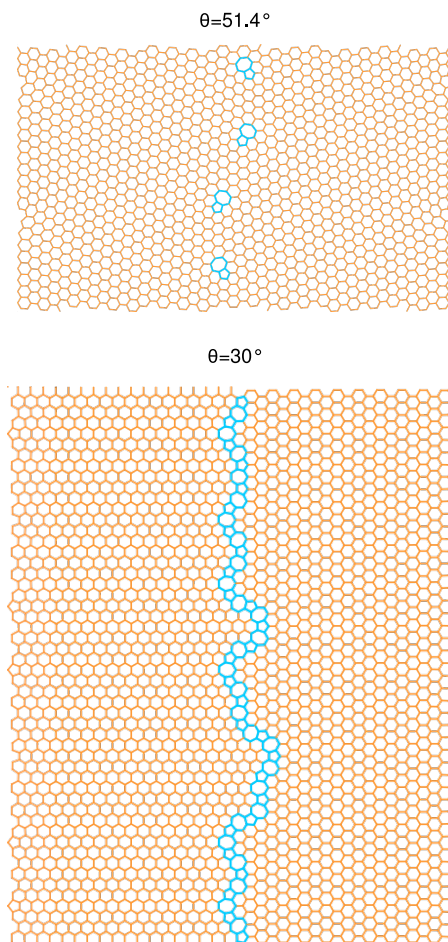


Figure 5.14 – Atomic structures of the lowest-energy configurations achieved in the simulation for $\theta = 51.4^\circ$ and the asymmetric $\theta = 30.0^\circ$ GBs. A comparison with Fig. 5.13 shows that low-energy 51.4° GB is formed by four equidistant pairs of pentagons and heptagons, whereas the asymmetric 30° GB consists in a continuous alternation of adjacent pentagons and heptagons

5.3 Controlled growth of a line defect in graphene with valley filtering properties

*The work presented in this section has been done in collaboration with the group of Prof. Alex Zettl, University of California at Berkeley. The results of our collaboration have been published in Physical Review B***89**, 121407 (2014).

In this section, we report an experimental study that demonstrates the possibility of introducing highly regular line defects in graphene in a controlled manner. These defects are formed by a periodic array of minimal blocks consisting in two pentagons and one octagon (5-5-8 defect). Previous theoretical work suggested that such defect acts as a valley filter for charge carriers in graphene, namely, it selectively transmits the charge carriers of one valley, depending on their incidence angle and energy [Gunlycke and White, 2011].

Fig 5.15(a) shows the Transmission Electron Microscopy (TEM) image of a 5-5-8 line defect originated in proximity of a hole intentionally patterned in the sample. In fact, such line defects nucleate from an isolated pentagon which can be found only at a free edge, as discussed in section 3.3.1. The growth of the defect is induced by a current driven such to traverse the hole. This produces local Joule heating, which leads to the removal of a pair of carbon atoms from the pentagon. The consequent local rearrangement of the atomic structure creates a 5-5-8 block terminated by a new 5-6 block (a pentagon and a hexagon) which acts as a seed for continuing the growth of the defect into the bulk.

With the help of the scheme in Fig. 5.15(b), one can see that the line defect is constituted by

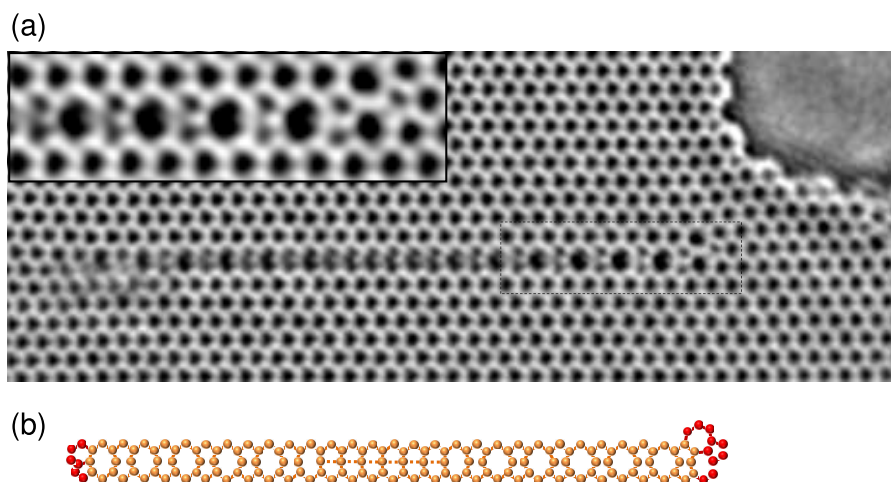


Figure 5.15 – (a) Transmission electron microscopy of a 5-5-8 line defect in graphene. The image was reconstructed from a series of 80 snapshots at different focus. (b) Ball-and-stick model of the atomic structure of the line defect. Adapted with permission from Ref. [Chen *et al.*, 2014], © 2013 American Physical Society.

5.3. Controlled growth of a line defect in graphene with valley filtering properties

identical 5-5-8 blocks and has different terminations at the two ends. The right end terminates with a 7-7-5 block (two heptagons and one pentagon) and does not evolve during the process. Indeed, the growth takes place at the left end that is terminated by a 5-6 block at every step. The 5-6 termination has a rather high formation energy (1.5 eV larger than the 7-7-5 termination) and is unstable under current flow. This instability causes the expulsion of a pair of carbon atoms, thus being the ultimate reason which, under appropriate conditions, determines the growth of the line defect. We remark that this line defect can be considered as a degenerate GB, as it represents the interface between two crystalline domains having the same orientation.

On the base of symmetry arguments, it was argued that a 5-5-8 line defect act as a valley filter, namely, it allows the charge carriers of only one valley to cross the grain boundary, depending on the nature of the charge carries (electrons or holes) and on their angle of incidence θ [Gunlycke and White, 2011]. To have a deeper insight into the valley filtering properties, we performed simulations of the electronic transport within DFT. However, we preliminarily discuss the band structure of a graphene system containing a 5-5-8 line defect, shown in Fig. 5.16(a). We remark the presence of two almost flat bands crossing the Dirac point of the projected band structure of pristine graphene (shaded area), which corresponds to the Fermi energy of the undoped system. These two bands correspond to electronic states localized at the line defect.

Transmission probability was calculated within the Landauer-Büttiker theory coupled to DFT, as implemented in the TRANSIESTA code [Soler *et al.*, 2002]. In our calculations, the transport direction was orthogonal to the line defect and the whole system was assumed to be periodic in the direction parallel to the line defect. Therefore, transmission $T(k_{\parallel}, E)$ is a function of parallel momentum k_{\parallel} as well as energy E . Furthermore, we assumed semi-infinite leads made of pristine graphene. Due to time reversal symmetry, one has $T(k_{\parallel}, E) = T(-k_{\parallel}, E)$, so that we can calculate transmission only for positive value of k_{\parallel} . Fig. 5.16(b) shows that $T(k_{\parallel}, E)$ has a significant suppression at the Dirac point as the charge carriers undergo resonant backscattering off the localized states discussed previously. This low-energy suppression of transmission affects the valley polarization behavior of the defect, which differs from what was predicted in Ref. [Gunlycke and White, 2011]. From a quantitative point of view, the angle-dependent valley polarization is defined as

$$P(\theta, E) = \frac{T_{\xi=1}(\theta, E) - T_{\xi=-1}(\theta, E)}{T_{\xi=1}(\theta, E) + T_{\xi=-1}(\theta, E)}, \quad (5.10)$$

where $\xi = \pm 1$ represents the valley index and $T_{\xi}(\theta, E)$ is the transmission probability of a carrier with energy E and incidence angle θ . Following this definition, positive (negative) values of polarization mean that charge carriers with valley index $\xi = 1$ are transmitted more (less) than those with $\xi = -1$.

Valley polarization for electrons and holes is shown in Figs. 5.16(c-d), respectively. As expected, at low energy $|E| < 0.2$ eV our results radically differ from the functional form $P(\theta, E) = \text{sign}(E) \sin(\theta)$ predicted for low energy particles from symmetry arguments [Gunlycke and

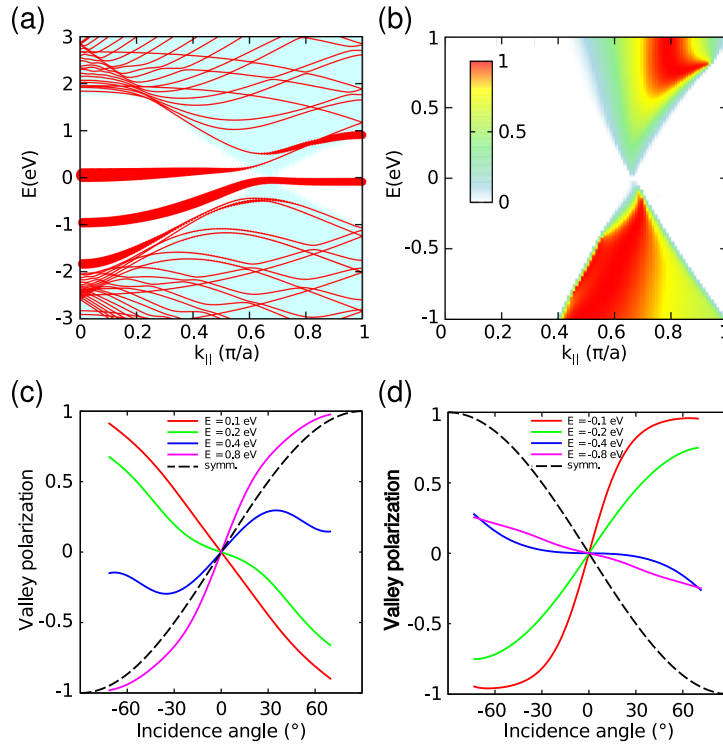


Figure 5.16 – Electronic and transport properties of the periodic 5-5-8 line defect calculated within DFT. (a) Electronic band structure calculated for momenta $\mathbf{k} = (k_{||}, k_{\perp} = 0)$, where $k_{||}$ (k_{\perp}) is the component parallel (orthogonal) to the direction of the line defect. The shaded area represents the projection of the 2D band structure of pristine graphene on the $k_{\perp} = 0$ direction. The zero of the energy has been aligned to the Fermi energy of the system. (b) Transmission probability across the line defect for charge carriers with energy E and momentum $k_{||}$. (c-d) Valley polarization as a function of incidence angle of the charge carriers for (c) electrons and (d) holes at several energies. The dashed lines represents the predictions based on symmetry arguments of Ref. [Gunlycke and White, 2011].

White, 2011]. However, the predicted trend is restored for electrons with sufficiently high energy to overcome the resonances.

These results suggest that the energy dependence can be exploited to control the valley polarization of the charge carriers. This capability is of fundamental importance for valleytronics, that is, the manipulation of the valley degree of freedom of charge carriers. Other valleytronics devices based on graphene and exploiting different physical phenomena have already been proposed [Rycerz *et al.*, 2007; Akhmerov and Beenakker, 2007]. However, differently from previously proposed devices, we suggest a scheme for a valley-valve that is operated by two line defects endowed with electrostatic gates. As shown in Fig. 5.17, the valley valve consists in a graphene sample containing two parallel 5-5-8 line defects and attached to source and drain electrodes. The device is operated by independently setting the Fermi energy at each of the two defects, changing the voltage of the local gates. Once fixed the incidence angle to,

5.4. Periodic grain boundaries in graphene on SiC substrate

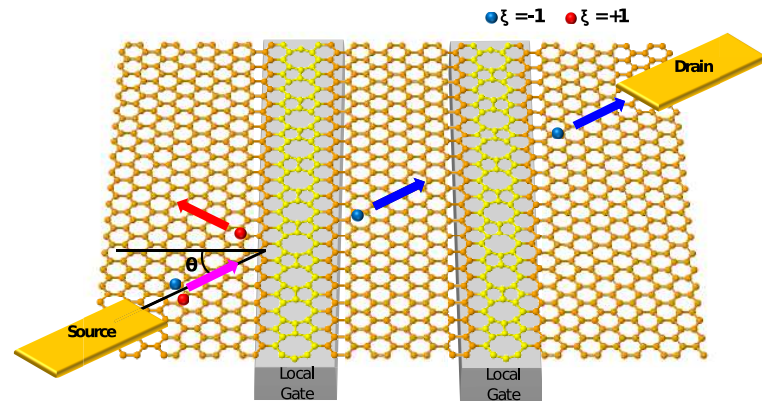


Figure 5.17 – Scheme of a valley valve based on a pair of parallel 5-5-8 line defects endowed with two independent local gates. An unpolarized beam of electrons is injected with a specific incidence angle θ from the source electrode, processed by the defects and collected by the drain electrode. The local voltage of the first defect (filter) determines the valley degree of freedom of the transmitted charge-carriers ($\xi = -1$ in this scheme), whereas the local voltage of the second defect (detector) determines the intensity of the current collected by the drain electrode. reproduced with permission from Ref. [Chen *et al.*, 2014], © 2013 *American Physical Society*.

say, $\theta = 30^\circ$, by changing the energy of the first defect from 0.1 eV to 0.8 eV the polarization of initially unpolarized charge carriers is switched from $P = -0.44$ (i.e. majority of $\xi = -1$ charge carriers) to $P = 0.68$ (i.e. majority of $\xi = 1$ charge carriers). The second line defect acts as a valley polarization detector, switching from a low-resistance state (valley closed) to a high-resistance state (valley open) upon a change of its Fermi energy.

5.4 Periodic grain boundaries in graphene on SiC substrate

The work presented in this section has been done in collaboration with the group of Prof. Vincent Repain, University Paris Diderot. The results of our collaboration have been published in Nano Letters, 14, 6382 (2014).

In this section, we report an experimental and theoretical study of a large-angle grain boundary in graphene showing well-defined periodicity. The investigation of this grain boundary was part of a comprehensive investigation based on scanning tunneling microscopy (STM) and scanning tunneling spectroscopy (STS) of GBs in graphene epitaxially grown on SiC. Simulations of STM pictures based on DFT allowed us to assign the GB to the structure dubbed LAGBII in Ref. [Yazyev and Louie, 2010b].

Fig. 5.18(a) shows a representative topographic STM image of the polycrystalline graphene sample under study, which reveals three single-crystalline domains with different lattice orientation. The grain boundary separating domains B and C has a misorientation angle $\theta = 33.2^\circ$ and shows a high degree of regularity, with an evident periodic and symmetric

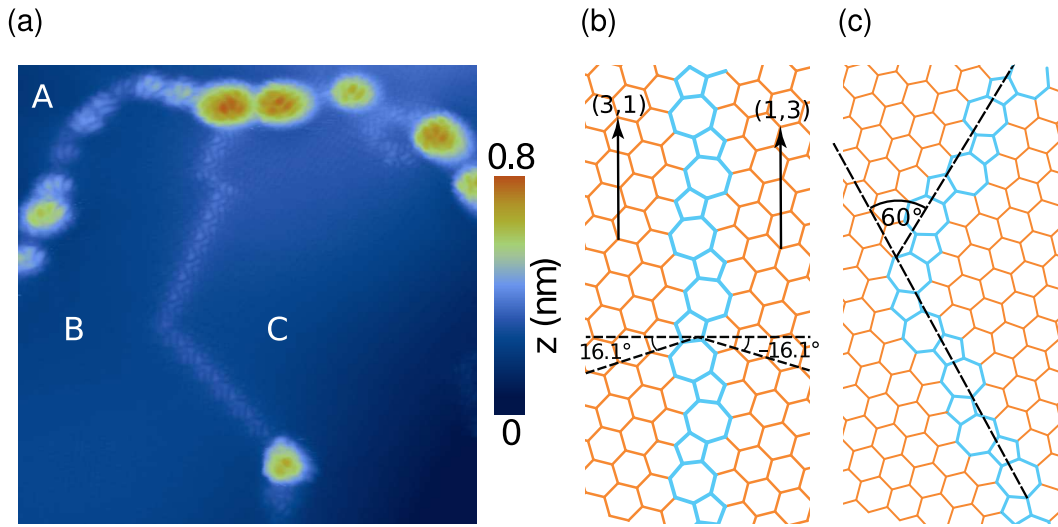


Figure 5.18 – Periodic grain boundary in graphene. (a) STM image of a sample of epitaxial graphene grown on SiC, containing three misoriented crystal domains (labeled A,B, and C). The image has been recorded at positive bias voltage $U = 0.75$ V and constant current $I = 500$ pA. (b-c) Atomic models of the grain boundary separating domains B and C, shown in (a). Both models have misorientation angle $\theta = 32.2^\circ$. The model in (b) is symmetric and periodic over its whole extension with periodicity $d = 8.97 \text{ \AA}$, whereas the model in (c) accommodates a 60° turn. Panel (a) courtesy of Vincent Repain, University Paris Diderot.

pattern. Constant-current STM measurements found a typical height in correspondence of the GB of 0.7 \AA , taking as reference the height measured in the center of a single-crystalline domain, that is, the GB is practically flat. The measured periodicity is $d_{\text{exp}} = 9.1 \text{ nm}$. By searching among symmetric and periodic models of grain boundaries having a misorientation angle compatible with the measured one, we have identified the model shown in Fig 5.18(b) as a candidate to be the GB actually found in the experiments. This model, already proposed in Ref. [Yazyev and Louie, 2010b], is defined by the matching vectors $(3, 1)$ and $(1, 3)$ and has a periodicity $d = 8.97 \text{ \AA}$. It consists in an alternating chain of edge-sharing pentagons and heptagons where all atoms maintain the three-fold coordination typical of sp^2 carbon. Moreover, it naturally accommodates a 60° turn by merging two half-periodic branches, leaving unaltered the misorientation angle, the alternation of non six-membered rings, and the atomic coordination, as shown in Fig. 5.18(c). As several such turns can be seen in the experimental image, this is another element in favor of the proposed model.

A comparison between atomic-resolution experimental images of the GB and the simulated ones provided the final confirmation of our hypothesis. Fig. 5.19(a) shows the dI/dV spectrum measured in different positions of the sample, as indicated in the inset. The spectra measured on the linear segments of the GB shows intense peaks, which are common among GBs in graphene. These features stand out from the spectra measured inside each single-crystalline domain that show a V-shaped curve reminiscent of pristine graphene DOS. The origin of these peaks is due to electronic states localized on the linear segments of the GB. Figs. 5.19(b-d)

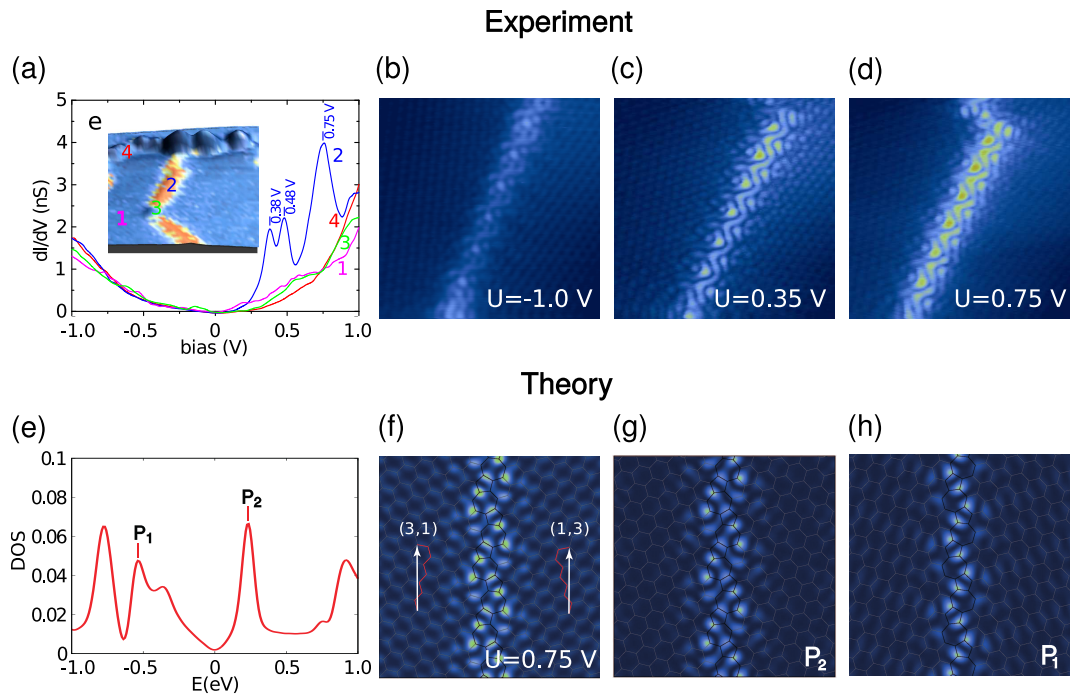


Figure 5.19 – (a) dI/dV spectra measured at the positions indicated in the inset. In particular, the blue curve corresponds to the spectrum measured in the middle of the upper branch of the $\theta = 33.2 \pm 2^\circ$ grain boundary. The inset shows a conductance map recorded at 0.75 V. (b-d) Topographic STM images of the $\theta = 33.2 \pm 2^\circ$ grain boundary recorded at different bias voltages indicated by the labels. (e) Calculated density of states for the $\theta = 32.2^\circ$ model, shown in Fig. 5.18(b). (f) Simulated STM image with positive bias $U = 0.75$ V. (g-h) Simulated dI/dV maps at the energies of the peaks labeled P_1 and P_2 in panel (e). Panels (a-d) courtesy of Vincent Repain, University Paris Diderot.

shows the topographic images obtained at different bias voltages. The positive values of the bias have been chosen to match the energy of the peaks observed in the dI/dV spectrum of the GB. At positive bias the periodic pattern observed on the GB is the same, differently from the motif seen at negative bias. In order to theoretically simulate STM images we employed the Tersoff-Hamann theory, which states that, to first order approximation, the tunnel current recorded in STM is proportional to the local density of states of the sample [Tersoff and Hamann, 1985]. The simulated STM images shown in Figs. 5.19(f-h) have been obtained from the local density of states calculated within DFT for the model proposed in Fig. 5.18(b). The calculations have been performed by means of the code SIESTA [Soler *et al.*, 2002]. Fig. 5.19(f) shows an image simulated assuming a bias $U = 0.75$ V that is in strong qualitative agreement with its experimental counterpart shown in Fig. 5.19(d). In particular, at the GB we note an array of opposed boomerang-shaped areas of intense signal with bright spots inside. From the calculated DOS, shown in Fig. 5.19(e), we observe a pair of van Hove singularities at energies $E = -0.55$ eV (P_1 peak) and $E = 0.25$ eV (P_2 peak). The positions of the peaks do not agree with the dI/dV spectrum shown in Fig. 5.19(a), as the experimental peaks seem to be shifted to higher absolute energies compared to first-principle calculations.

In particular, the experimental counterpart of peak P_1 is likely to be out of scale. We believe that this disagreement is due to multiple reasons: i) tip-induced effects and ii) role of the substrate, which are not accounted for in the simulations, and iii) energy scale compression characteristic of DFT.

Nevertheless, the simulated dI/dV maps shown in Fig. 5.19(g-h) show localized states that are likely to be the main contributions to the features seen in experiments. Notably, the map corresponding to peak P_2 is qualitatively very similar to the STM images measured at positive bias, whereas the map corresponding to peak P_1 shows a narrower profile analogous to what seen in STM image measured at bias $-1.0V$.

For the sake of completeness, we conclude mentioning that the experimental study which imaged the periodic GB discussed in this section [Tison *et al.*, 2014], has also confirmed the previously predicted transition between buckled low-angle GBs to flat large-angle GBs [Yazyev and Louie, 2010b]. In particular, the critical angle for the transition was assigned to $\theta_c = 19 \pm 2^\circ$ and its symmetric counterpart $\theta_c = 41 \pm 2^\circ$, in good agreement with theoretical predictions.

6 Electronic Transport in Graphene with Hydrogen Adatoms

In this chapter, we study the properties of hydrogen adsorbates on graphene. As discussed in Sections 2.2 and 2.4, adatoms bound to graphene act as resonant scattering centers affecting the electronic transport properties and inducing Anderson localization.

In the first section, we show the existence of an effective attractive interaction between hydrogen adatoms on graphene. This interaction, together with the high diffusion mobility of hydrogen on graphene, fully eliminates isolated adatoms and increases the population of adatom aggregates with larger size. We find that such spatial correlation influences the electronic transport properties of partially hydrogenated graphene. Indeed, by performing a scaling analysis, we show that such aggregation of adatoms increases conductance by up to several orders of magnitude and results in significant extension of the Anderson localization lengths. This is due to the non-resonant nature of a large subset of the adatom clusters in the room-temperature equilibrium configurations. Finally, we introduce a simple definition of effective adatom concentration x^ that unifies the description of the transport properties of random and correlated distributions of hydrogen adatoms on graphene across a broad range of concentrations.*

The second section contains an analytic study of the scattering problem of a cluster of vacancies in a honeycomb lattice. Specifically, we investigate under which conditions these defects introduce localized states at the Dirac energy (resonances) by studying the analytic properties of the Green's function of the entire system. We confirm what found numerically in the first section, namely, that cluster with an equal number of adatoms on the two-sublattices are non-resonant, whereas cluster of adatoms with sublattice imbalance are resonant.

6.1 Electronic transport in graphene with aggregated hydrogen adatoms

*The work presented in this section has been done in collaboration with the group of Prof. Tim Wehling, University of Bremen, and has been published in Physical Review Letters **113**, 246601 (2014), whose manuscript was written by Fernando Gargiulo in all of its parts, except those concerning the Kernel Polynomial method (not discussed here). The reader will find a considerable overlap between the article and the present section.*

6.1.1 Introduction

Resonant scattering impurities, such as chemical functionalization defects and topological defects, show the most pronounced effects on charge-carrier transport in graphene, see Sections 2.2 and 5.1). Hydrogen adatoms represent a prototypical resonant scattering impurity, which can be experimentally introduced in a controlled fashion [Ni *et al.*, 2010] and allows for a simple theoretical description [Wehling *et al.*, 2007]. A hydrogen adatom covalently binds to a single carbon atom of graphene resulting in rehybridization into sp^3 state, thus effectively removing that site from the honeycomb network of p_z orbitals. This gives rise to a zero-energy state localized around the defect and results in resonant scattering of charge carriers.

At a fundamental level, the classical scaling theory of Anderson transition predicts complete localization of the electronic spectrum in two dimensions, regardless of the amount of disorder. Although 2D massless Dirac fermions escape Anderson localization when disorder leaves the two valleys decoupled, in the presence of short-range scatterers that enable intervalley coupling, such as vacancies or hydrogen adatoms, Anderson localization is expected to set in also in graphene [Evers and Mirlin, 2008] (see Section 2.4 for a more detailed discussion). However, no unanimous consensus has been reached since experiments on hydrogenated graphene point towards metal-insulator transition, theoretically justified by the presence of electron-hole puddles (2D percolation class) [Bostwick *et al.*, 2009; Song *et al.*, 2011; Jayasingha *et al.*, 2013; Adam *et al.*, 2008]. We also stress that, in 2D systems, localization lengths can be strongly energy-dependent and, possibly, very large.

Early works treating finite concentrations of resonant impurities in graphene assumed that the total scattering cross-section deviates little from the incoherent addition of individual cross-sections, for example, as in the Boltzmann equation framework [Shon and Ando, 1998]. This picture is valid for low defect concentrations, low charge-carrier densities and random adatom distributions. A better description requires including the effect of coherent superposition of wavefunctions scattered by distinct adatoms [Wehling *et al.*, 2010, 2009b; Ferreira *et al.*, 2011; Cresti *et al.*, 2013]. This is particularly important when impurities are in proximity to each other, with the limiting case being the formation of compact clusters in which hydrogen adatoms populate neighboring carbon atoms [Palacios *et al.*, 2008; Leconte *et al.*, 2011; Trambly de Laissardière and Mayou, 2013]. Indeed, the overall short-range attractive interaction between

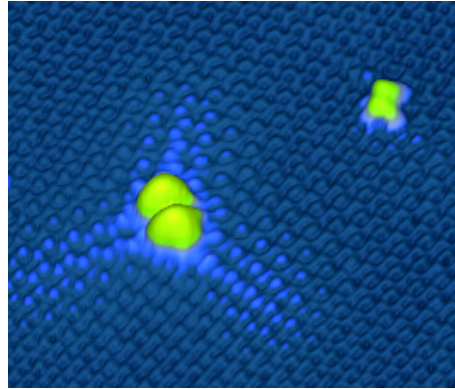


Figure 6.1 – Low-temperature STM image showing hydrogen atoms adsorbed on graphene grown on SiC(000 $\bar{1}$) spontaneously arranging in dimers. Unpublished results, courtesy of Prof. Ivan Brihuega, University of Madrid.

individual hydrogen adatoms on graphene [Boukhvalov *et al.*, 2008; Lin *et al.*, 2008], combined with their relatively high diffusion mobility at room temperature [Yazyev, 2008; Herrero and Ramírez, 2009; Moaied *et al.*, 2015], suggests a high degree of spatial correlation between adatoms. Recent experimental studies using STM to image hydrogenated graphene have revealed a tendency of hydrogen to spontaneously form dimers, as shown in Fig. 6.1. In this section, we address the effects of spatial correlation of resonant impurities on electronic transport in graphene. The equilibrium configurations of hydrogen adatoms are obtained by means of Monte Carlo simulations, and show a strong tendency toward aggregation into small clusters, essentially eliminating isolated adatoms. Landauer-Büttiker calculations show that hydrogen aggregation dramatically increases both the conductivity and the localization length. Finally, we propose a unified framework to account for the effects of spatial correlation of resonant scattering centers on electronic transport in graphene.

6.1.2 DFT study of effective hydrogen interaction

Upon adsorption, a hydrogen adatom covalently binds to a single carbon atom of graphene changing its hybridization state to sp^3 and its coordination sphere to tetrahedral as shown in Fig. 6.2(a) [Yazyev and Helm, 2007]. The covalent binding of a second adatom to the nearest neighbor carbon atom partially releases the elastic energy due to the change of coordination sphere, thus resulting in effective attractive interaction between adatoms [Boukhvalov *et al.*, 2008; Lin *et al.*, 2008]. This suggests that the interaction between adatoms can be accurately described using a short-ranged pair potential. In our study, we expand an Ising-like interaction energy E up to the second nearest-neighbor term

$$E = \gamma_1 \sum_{\langle i,j \rangle} s_i s_j + \gamma_2 \sum_{\langle\langle i,j \rangle\rangle} s_i s_j, \quad (6.1)$$

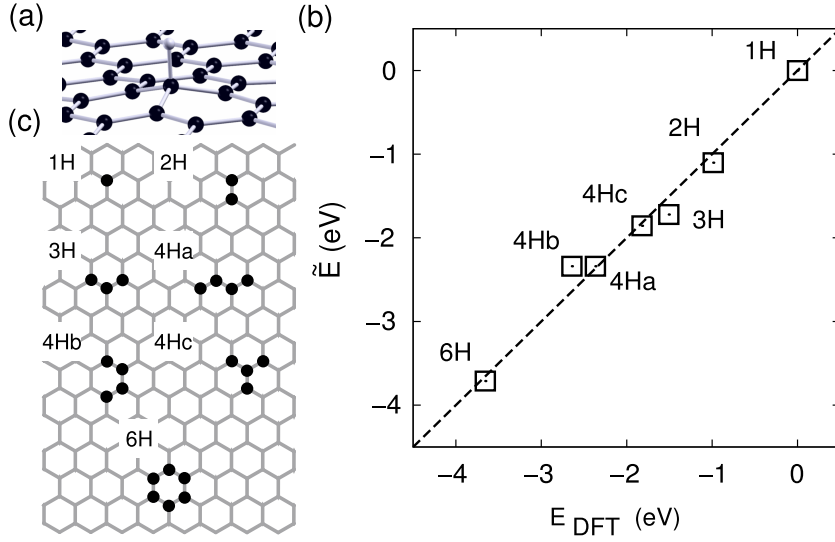


Figure 6.2 – (a) Atomic structure of a hydrogen adatom covalently bound to graphene. (b) Structures of small clusters of hydrogen adatoms used for fitting the pair potential of eq. (6.1) (c) Interaction energy \tilde{E} calculated from eq. 6.1 vs first principle interaction energy E_{DFT} for the set of adatom clusters shown in panel (b).

where γ_1 and γ_2 are the corresponding first and second nearest-neighbor parameters. Here, $s_i = 1$ if a carbon atom i is populated by an adatom, otherwise $s_i = 0$. The optimal values of γ_1 and γ_2 are obtained by fitting the interaction energies calculated from first principles for the set of small adatom aggregates shown in Fig. 6.2(b). Under the assumption of single-side functionalized graphene, the obtained parameters $\gamma_1 = -1.182$ eV and $\gamma_2 = 0.484$ eV signify a considerable first-nearest-neighbor attraction alongside a weaker second-nearest-neighbor repulsion. As seen in Fig. 6.2(c), the excellent agreement between the interaction energy \tilde{E} , estimated using the fitted γ_1 and γ_2 , and the first-principles values E_{DFT} , confirms the applicability of the short-range pair potential form, eq. 6.1, for describing small clusters. Technical details of calculation, together with the results of the fit in the case of hydrogen adsorption on both sides of graphene, are discussed in Section 6.1.7.a.

6.1.3 Equilibrium configuration of adsorbed hydrogen

In order to assess the effect of the interaction between adatoms on their spatial distribution we perform Monte-Carlo simulations (see Section 4.6 for methodological details). We considered models of hydrogenated graphene containing up to $N_C = 10^6$ carbon atoms ($165 \times 165 \text{ nm}^2$) and adatom concentrations $x = N_H/N_C$ ranging from 0.1% to 10%. The starting configuration of hydrogen adatoms was totally random. The trial Monte Carlo move consisted in the displacement of a randomly selected adatom to a random carbon atom not bound to any hydrogen. This move insures the fulfillment of detailed balance. After each move, the interaction energy was recalculated using the pair potential defined in eq. 6.1 and the move was accepted or rejected according to the Metropolis criterion [Metropolis *et al.*, 1953]. The

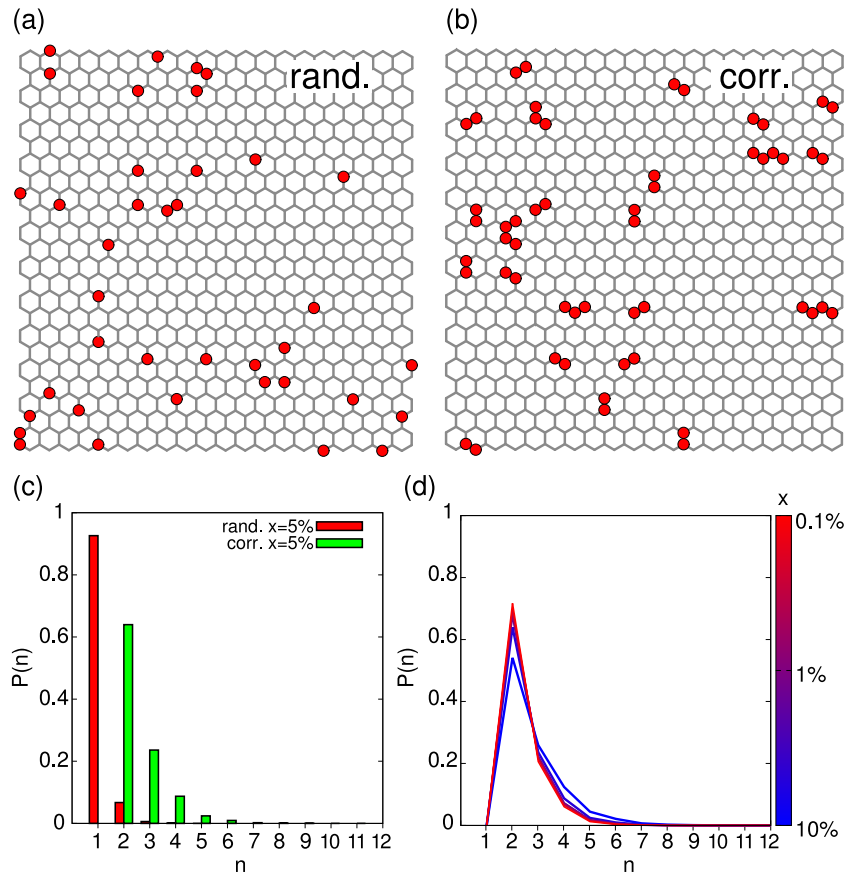


Figure 6.3 – Representative configurations of (a) randomly distributed and (b) correlated hydrogen adatoms on graphene at $x = 5\%$ concentration. (c) Comparison of random and correlated adatoms cluster size distributions $P(n)$ at $x = 5\%$ concentration. (d) Cluster size distributions $P(n)$ of correlated hydrogen adatoms at different concentrations. All correlated configurations are obtained by means of Monte-Carlo simulations carried out at $T = 300$ K.

temperature in all our simulations was $T = 300$ K. At the beginning of each simulation, we performed a number of steps N_{eq} disregarded from Monte Carlo averages in order to let the system reach thermodynamic equilibrium. N_{eq} varied in the range $[10^6, 1.6 \times 10^7]$, depending on the adatom concentration (larger concentrations needed more equilibration steps). The total number of steps in our simulations varied between 10^7 and 3×10^7 . We have checked that $P(n)$ s obtained from Monte-Carlo simulations performed with and without temperature annealing showed negligible differences.

In Figs. 6.3(a-b), a representative configuration of randomly distributed adatoms is compared with a configuration of correlated adatoms issued from a Monte-Carlo simulation at $x = 5\%$. In addition, Fig. 6.3(c) shows the comparison of the cluster size distributions $P(n)$. The cluster size n is determined by assigning adatoms populating neighboring carbon atoms to the same cluster. In the case of a random distribution, most adatoms are isolated ($n = 1$), while the occurrence of clusters ($n > 1$) is merely a probabilistic effect. In contrast, no isolated

adatoms are found in the presence of interactions, with the most abundant species being adatom dimers ($n = 2$). The size distribution for the correlated case shows a longer tail with a significant probability of observing up to $n = 6$ clusters. As shown in Fig. 6.3(d), the dependence of $P(n)$ on the adatom concentration, x , is relatively weak. Finally, in the case of hydrogen absorption on both sides of graphene, the resulting cluster size distributions, however, are very close to those obtained for single-side adsorption, see Section 6.1.7.a.

6.1.4 Electronic spectrum

We now focus on electronic and transport properties calculated using the nearest-neighbor tight-binding Hamiltonian for p_z orbitals

$$H = -t \sum_{\langle i,j \rangle} [c_i^\dagger c_j + \text{h.c.}] \quad (6.2)$$

with the hopping integral constant $t = 2.7$ eV, see Section 1.3. An adsorbed hydrogen atom is modeled by excluding the p_z orbital of the carbon atom to which it is bound as a consequence of sp^3 hybridization, making it similar to a vacancy defect [Pereira *et al.*, 2006; Yazyev and Helm, 2007; Yazyev, 2008]. We stress that adatoms do not introduce coupling between the sites owing to the same sublattice of the bipartite lattice of graphene, thus maintaining electron-hole symmetry of the electronic spectrum. Figures 6.4(a,b) compare the density of states (DOS) of graphene with random and correlated distributions of adatoms at different concentrations. In the case of a random distribution one observes a strong peak at $E = 0$ due to the resonant modes originating from isolated adatoms [Pereira *et al.*, 2006; Wehling *et al.*, 2009b]. The corresponding wave function is localized on the sublattice opposite to that of the carbon atom binding the adatom and decays from the defect position [Pereira *et al.*, 2006; Basko, 2008]. At high adatom concentrations, $x > 1\%$, the $E = 0$ peak is accompanied by flat density regions at higher energies with a noticeable overall renormalization of the DOS, in agreement with previous calculations [Pereira *et al.*, 2006]. In comparison, the DOS calculated for the correlated impurity configurations shows a less intense peak at $E = 0$ and an increased weight for $-0.9t < E < 0.9t$ that is more evident at higher concentrations. This change is a direct consequence of different cluster size distributions. The dominant cluster type in the case of the correlated adatom distribution is the dimer ($n = 2$), which is expected to be non-resonant, meaning that no localized states is added to the continuous spectrum at any energy, see Section 6.2 [Wehling *et al.*, 2007; Trambly de Laissardière and Mayou, 2013]. The local density of states (LDOS) calculated on neighboring atoms of an isolated single adatom shows a singularity at $E = 0$, see Fig. 6.4(c). In contrast, some enhancement of the LDOS in a broad energy region $-t < E < t$, which cannot be considered as an authentic peak, is observed on certain carbon atoms in the vicinity of the adatom dimer, see Fig. 6.4(d). We have checked by means of numerical calculations that only those cluster populating different number of sites in the two sublattices, namely all odd- n aggregates and certain configurations of even- n clusters, lead to resonant modes at $E = 0$ akin to isolated adatoms. Based on these observations and judging on the cluster size distributions shown in Fig. 6.3(d), we conclude that the residual

6.1. Electronic transport in graphene with aggregated hydrogen adatoms

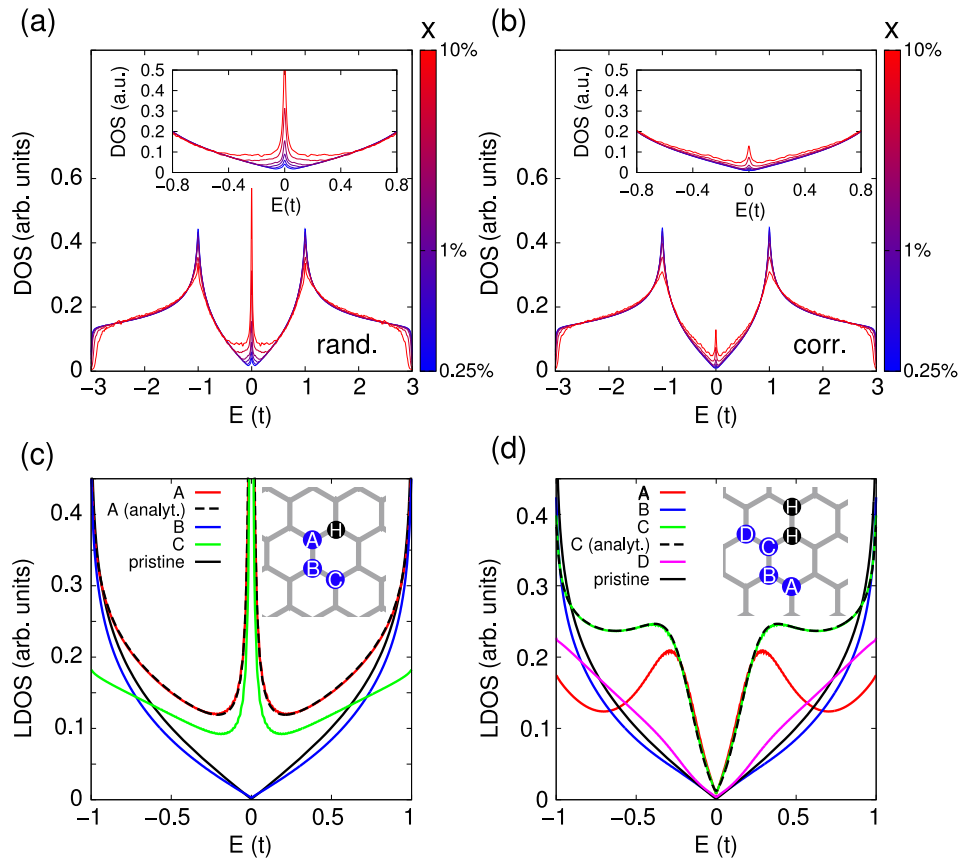


Figure 6.4 – Density of states of graphene in the presence of (a) randomly distributed and (b) correlated hydrogen adatoms at different concentrations. Local density of states (LDOS) on carbon atoms in the vicinity of (c) an isolated hydrogen adatom and (d) a dimer of hydrogen adatoms. In panels (c,d), LDOS referred to as “analyt.” have been obtained using analytic Green’s function calculations illustrated in Section 6.2.

peak at $E = 0$ in the case of correlated distribution is due to $n > 2$ adatom aggregates, with the largest contribution coming from adatom trimers.

6.1.5 Electronic transport

The previous discussions suggest that adatom aggregation has strong effects on the electronic transport properties, because of the reduction of the weight of resonant states. We investigate the electronic transport properties by performing a scaling analysis of conductivity, g , using the Landauer-Büttiker approach [Landauer, 1957; Büttiker *et al.*, 1985], see Section 4.5.1. We assume a two-terminal device configuration with a scattering region of width $W = 40$ nm perpendicular to the current direction, and of variable length $1 \text{ nm} < L < 60 \text{ nm}$. The scattering region is attached to pristine graphene contacts and populated by adatoms according to the statistical distributions discussed above. Further details of our methodology are given in the Section 6.1.7.b.

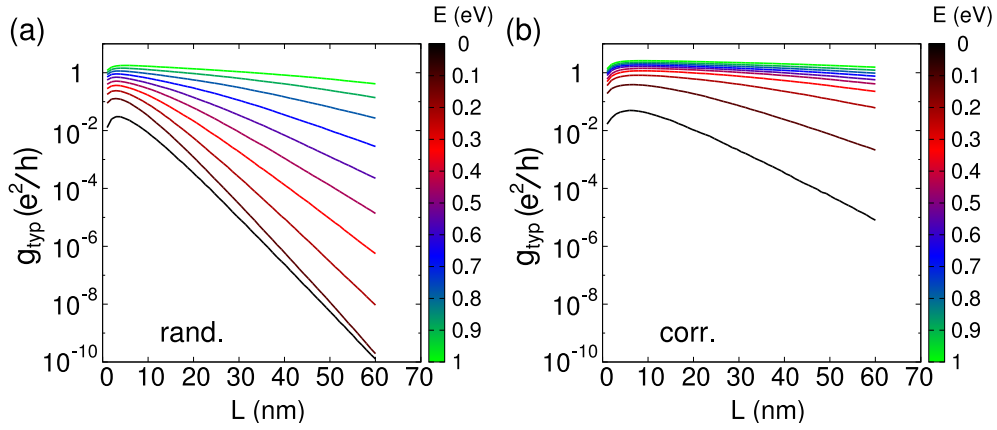


Figure 6.5 – Averaged conductivity g_{typ} for (a) random and (b) correlated adatoms distributions, respectively, as a function of scattering region length L at different energies E and at $x = 5\%$ concentration.

We remind that the characteristic functional laws for the conductivity $g = G \times L/W$ in the ballistic, diffusive and localized transport regimes are, respectively, $g \propto L$, $g = \text{const}$ and $g \propto \exp(-L/\xi_{\text{loc}})$, where ξ_{loc} is the localization length. In the localized regime, $\ln(g)$ follows a broad positively-skewed distribution, which means that g can show strong fluctuations depending on the exact configuration of defects, especially in the presence of strong localization [Choe and Chang, 2012]. An estimate of the mean value for such a distribution is given by the so-called “typical conductivity” $g_{\text{typ}} = \exp\langle \ln(g) \rangle$ [Choe and Chang, 2012; Uppstu *et al.*, 2014]. In our scaling analysis, g_{typ} has been obtained averaging over 9600 disorder realizations. Figure 6.5(a,b) shows g_{typ} as a function of L at different energies for random and correlated impurity distributions, both at $x = 5\%$ concentration. We observe a short transition from ballistic to diffusive and subsequently to localized regime within the first 10 nm. The crossover lengths are expected to be of the order of the elastic mean free path ξ_{el} and localization length ξ_{loc} , respectively. The general trend is that the localized regime is accentuated at low energy, whereas at higher energy the onset of exponential decay occurs at larger L and the absolute slope of the conductance curves is smaller. The scaling of g also depends strongly on the concentration of impurity. For adatom concentrations ($x \lesssim 0.5\%$) the onset of the localized regime is only observable in the vicinity of the Dirac energy (see 6.1.7.b for complete results).

We stress that the conductance curves vary smoothly in the whole range of E and x , never showing singularities which would indicate a phase transition such as the metal-insulator transition (MIT). Thus, we ascribe the non-observance of the localized regime to an insufficient scattering region length of our model, which is shorter than ξ_{loc} for some choices of E and x , as also pointed out in Ref. [Schubert and Fehske, 2012]. From Fig. 6.5(a,b) it follows that the presence of spatial correlation between adatoms enhances the conductance by up to five orders of magnitude in the vicinity of the Dirac point ($E = 2.7$ meV). This is a direct consequence of the suppressed weight of low-energy resonant states, as explained above. A closely related effect is a significant increase of the localization length ξ_{loc} at all energies upon

6.1. Electronic transport in graphene with aggregated hydrogen adatoms

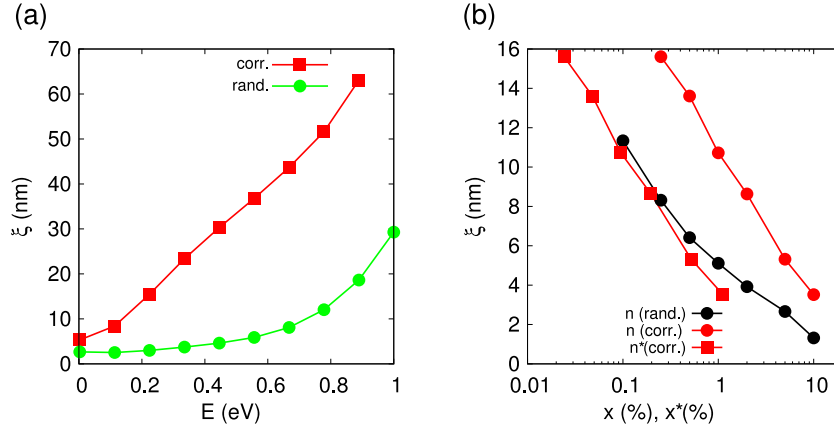


Figure 6.6 – (a) Localization length ξ_{loc} as a function of charge-carrier energy E for the case of random and correlated adatom distribution at $x = 5\%$. (b) Charge-carrier localization length ξ_{loc} at low energy ($E = 10^{-3}t = 2.7$ meV) as a function of real concentration x and effective concentration x^* for random and correlated distributions.

adatom aggregation. ξ_{loc} was obtained by fitting the conductance curves to the expected law $g_{\text{typ}} \propto \exp(-L/\xi_{\text{loc}})$ [Lee and Ramakrishnan, 1985], and is shown in Fig. 6.6(a). At $x = 5\%$, the localization length is well defined for the entire range of investigated energies $-1 \text{ eV} < E < 1 \text{ eV}$, whereas at lower concentrations it is well defined only in proximity of the Dirac point, see Section 6.1.7.b. However, as long as a finite positive ξ_{loc} can be determined, it proves to be up to an order of magnitude larger for the correlated adatom distribution compared to the random case.

On the basis of the identification of resonant adatom clusters we introduce an effective concentration

$$x^* = \frac{1}{N_C} \sum_i N_i |n_i^A - n_i^B|, \quad (6.3)$$

where N_i is the number of instances of the cluster configuration i , and n_i^A (n_i^B) is the number adatoms bound to carbon atoms in sublattice A(B) in this configuration. As discussed above, the main contribution to x^* comes primarily from adatom trimers, the smallest clusters with sublattice imbalance. We assume that the contribution of non-resonant clusters to the total scattering cross-section can be neglected. We stress that this approach is probably the simplest one to account for the diverse scattering effect of different clusters. In order to validate the applicability of the effective concentration x^* , we compare $\xi_{\text{loc}}(x)$ with $\xi_{\text{loc}}(x^*)$ at low charge-carrier energy for the correlated impurity case, see Fig. 6.6(b). One can see that replacing x with the effective concentration x^* brings $\xi_{\text{loc}}(x^*)$ evaluated for correlated impurities in good agreement with $\xi_{\text{loc}}(x)$ calculated for the random impurities. The agreement is particularly good in the low concentration regime where randomly distributed impurities consist almost exclusively of isolated monomers. Deviations at higher adatom concentrations can be ascribed to inter-cluster interference effects, which become important at short average distance between the clusters.

6.1.6 Conclusions

To summarize, spatial correlation between resonant scattering impurities, such as hydrogen adatoms, has pronounced effects on the electronic transport properties of disordered graphene. Hydrogen adsorbed on graphene has a strong tendency toward aggregation, resulting in the formation of small clusters and fully eliminating isolated adatoms. Some of the larger clusters, notably trimers, are responsible for the residual resonant scattering, but the overall conductance and localization length dramatically increase upon aggregation. Within the range of parameters investigated in our work, we find no metal-insulator transition, with the graphene spectrum being fully localized. The predicted effects of adatom aggregation can be investigated experimentally by varying the temperature regime, since the diffusion of hydrogen adatoms occurring at normal conditions can be effectively suppressed at low temperatures. Alternatively, time-resolved transport measurements should evince a rise in conductivity upon formation of adatom clusters.

6.1.7 Methodological details and additional calculations

6.1.7.a First-principles calculations of the energies of hydrogen adatom clusters

First-principles calculations of the interaction energies of hydrogen adatoms on graphene have been performed within the density functional theory (DFT) framework employing the generalized gradient approximation (GGA) to the exchange-correlation functional [Perdew *et al.*, 1996]. Ultrasoft pseudopotentials [Vanderbilt, 1990] for carbon and hydrogen atoms have been used in combination with a plane-wave basis set, using a kinetic energy cutoff of 30 Ry for the wavefunctions and 160 Ry for the density. Models of hydrogen adatom clusters are based on a graphene 6×6 supercell with 15 Å of vacuum separating the periodic replicas. We used a $2 \times 2 \times 1$ Monkhorst-Pack k-point mesh for the Brillouin zone integration [Monkhorst and Pack, 1976]. All hydrogen adatom cluster models were relaxed until a maximum force of 0.15 eV/Å on individual atoms was reached. We verified that the chosen parameters provide sufficiently accurate total energies. All calculations have been performed using the PWSCF code of the QUANTUM ESPRESSO package [Giannozzi *et al.*, 2009].

The interaction energy of a cluster of hydrogen adatoms calculated from first principles E_{DFT} is defined as

$$E_{\text{DFT}} = E_{\text{gr}+n\text{H}} - E_{\text{gr}} - n(E_{\text{gr}+\text{H}} - E_{\text{gr}}), \quad (6.4)$$

where $E_{\text{gr}+n\text{H}}$, E_{gr} and $E_{\text{gr}+\text{H}}$ are the total energies of graphene with a cluster of n hydrogen adatoms, pristine graphene and graphene with a single hydrogen adatom, respectively.

When hydrogen adatoms are deposited on a single side of graphene, the values of the fitted parameters in eq. 6.1 are $\gamma_1 = -1.182$ eV and $\gamma_2 = 0.484$ eV. This scenario is relevant to the case of graphene on a substrate, however, in the situation of suspended graphene, both sides of

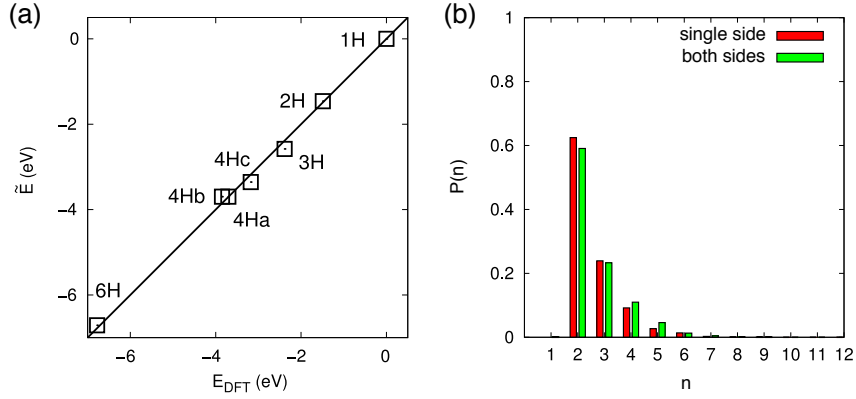


Figure 6.7 – (a) Interaction energy \tilde{E} calculated from eq. 6.1 vs first principle interaction energy E_{DFT} for the set of adatom clusters shown in Fig. 6.2(a) with adatoms alternatively adsorbed on either side of graphene. (b) Comparison of the cluster size distributions $P(n)$ resulting from Monte Carlo simulations in the cases of single-side and both-sides adatom adsorption at $x = 5\%$ concentration and $T = 300$ K.

graphene are available for binding adatoms. We investigated this situation by studying the same set of adatom clusters shown in Fig. 6.2(b) but with adatoms placed on opposite sides of graphene sheet when functionalized carbon atoms belong to different sublattices. The fitted interaction parameters are $\gamma_1 = -1.461$ eV and $\gamma_2 = 0.342$ eV. The excellent agreement between the estimated interaction energies \tilde{E} and the first-principles values E_{DFT} is illustrated in Fig. 6.7(a). This case is characterized by a stronger attractive contribution and a weaker repulsion compared to the single-side adsorption, thus reflecting the known tendency of forming more stable adatom aggregates upon adsorption on both sides [Lin *et al.*, 2008; Boukhvalov *et al.*, 2008]. The cluster size distributions $P(n)$ calculated for single-side and both-sides adsorption at adatom concentration $x = 5\%$ simulated at $T = 300$ K are compared in Fig. 6.7(b). After realizing that the two distributions are qualitatively very similar, nevertheless, one notices that both-sides adsorption exhibits a somewhat stronger tendency to form larger clusters.

6.1.7.b Landauer-Büttiker electronic transport calculations and scaling analysis of conductivity

In order to investigate the transport properties of graphene with resonant scattering impurities we perform Landauer-Büttiker calculations in a two-terminal configuration with a scattering region composed of hydrogenated graphene attached to two semi-infinite leads of pristine graphene, as shown in Fig. 6.8. The overall configuration is periodic along the transverse direction y . For such a setup, the conductance as a function of energy, $G(E)$, is given by

$$G(E) = \frac{W}{2\pi} \int_{-\frac{\pi}{W}}^{\frac{\pi}{W}} T(E, k_{\parallel}) dk_{\parallel}, \quad (6.5)$$

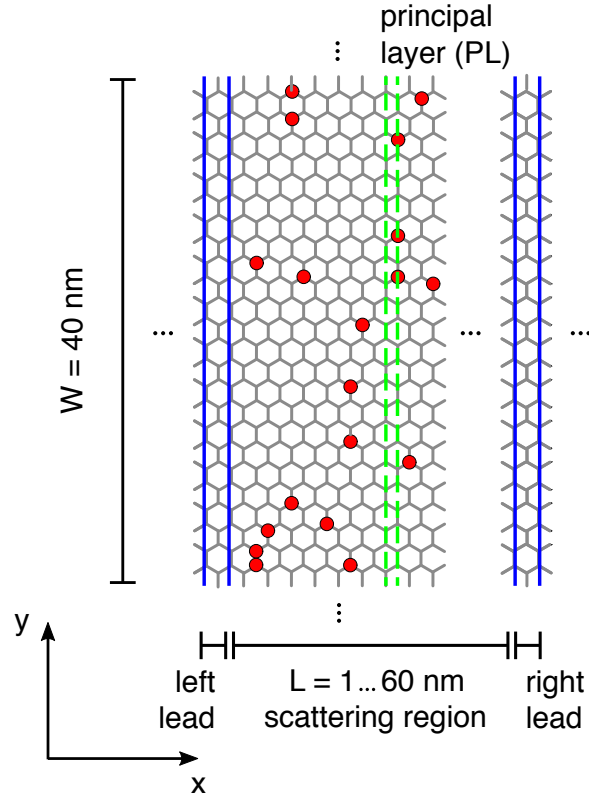


Figure 6.8 – Schematic drawing of the two-terminal configuration employed for investigating the transport properties of graphene with hydrogen adatoms. The transport direction corresponds to the x axis while the system is periodic along the y axis with periodicity $W = 40$ nm. The unit cells of the semi-infinite periodic leads made of pristine graphene are indicated by blue lines. The scattering region is populated by adatoms either randomly or according to the configurations produced by Monte Carlo simulations (in the case of correlated adatom distributions). Green dashed line highlights one of the principal layers (PLs) of the scattering region.

where $T(E, k_{\parallel})$ is the transmission probability and k_{\parallel} is the momentum along y . Due to the large width $W = 40$ nm of the model employed, transmission is only evaluated at $k_{\parallel} = 0$.

In order to calculate $T(E)$ we decompose the scattering region into principal layers (PLs), namely, whose atoms are coupled at farthest to those located in the neighbor layers. Since our tight-binding model is limited to first-nearest-neighbor interactions and the transport direction is oriented along zig-zag direction, see Fig. 6.8, the minimal width of the PL is $d_{\text{PL}} = \frac{\sqrt{3}}{2} d_{\text{CC}}$, where $d_{\text{CC}} = 1.42$ Å is the carbon-carbon bond length. The Hamiltonian restricted to the i -th principal layer is H_i , while t_i is the tight-binding hopping matrix connecting the i -th and $i + 1$ -th principal layers. We introduce an imaginary cleavage plane between the n -th and $n + 1$ -th principal layers dividing the system into two independent parts. We define g_n^{L} and g_{n+1}^{R} as the surface Green's functions of the two decoupled semi-infinite systems located, respectively, at the left and at the right of the cleavage plane. Following Ref. [Mathon and

6.1. Electronic transport in graphene with aggregated hydrogen adatoms

Umerski, 2001], the transmission is given by

$$T(E) = \text{Tr}[T_n \text{Im}(g_n^L) T_n^\dagger \text{Im}(g_{n+1}^R)], \quad (6.6)$$

where T_n is defined as

$$T_n = t_n (1 - g_{n+1}^R t_n^\dagger g_n^L t_n)^{-1}. \quad (6.7)$$

The choice of the position of the cleavage plane is immaterial because of current conservation. Surface Green's functions g_n^L and g_n^R can be related to the preceding (successive) surface Green's functions g_{n-1}^L (g_{n+1}^R) by applying the Dyson equations [Umerski, 1997]

$$g_n^L = (E - H_n - t_{n-1}^\dagger g_{n-1}^L t_{n-1})^{-1} \quad (6.8)$$

and

$$g_n^R = (E - H_n - t_n g_{n+1}^R t_n^\dagger)^{-1}. \quad (6.9)$$

Further iterations of Eqs. 6.8 and 6.9 reduce the problem to the knowledge of the Green's functions at the surfaces separating the scattering region from the left and right leads, g^{LL} and g^{RL} , that we calculated according to the analytic solution described in Ref. [Sanvito *et al.*, 1999]. The time complexity of the Green's function calculation for each lead with respect to the number N_{lead} of orbitals in the lead unit cell is $O(N_{\text{lead}}^3)$ [Umerski, 1997]. On the other hand, as follows from eqs. 6.8 and 6.9, the complexity of repeatedly applying Dyson's equation to reach the cleavage plane is $O(M \times N_{\text{layer}}^3)$, where M and N_{layer} are the number of principal layers and the number of orbitals in each layer, respectively. Consequently, the overall complexity of the method is cubic with respect to the width and linear with respect to the length of the system.

In order to perform our conductance scaling analysis we vary the length of the scattering region in the range [1, 60] nm by steps of 8 PLs, corresponding to $\Delta L \approx 1$ nm. At each step the right lead is moved rightwards whereas the left lead is kept fixed, see Fig. 6.8. The values of conductance $G(E)$ are averaged over an ensemble of $N_{\text{ens}}=9600$ disorder realizations for proper statistical sampling. The conductivity g calculated for the entire investigated range of concentrations is presented in Fig. 6.9(a,b). The overall enhancement of conductivity upon adatom aggregation is a common feature at all the investigated concentrations. This is particularly visible in the strong localization regime, that is, at low energies E and large L . The localization length, ξ_{loc} , can only be determined for the $g(L)$ curves that exhibit a well-defined negative slope in region of high L . This is the case for $\xi_{\text{loc}} < 60$ nm, which is the maximum scattering region length considered in our study. This does not imply that the system does not undergo localization, but rather that a longer scattering region is needed in order to estimate ξ_{loc} correctly. For this reason many values of localization length ξ_{loc} at $x < 5\%$, especially in the case of correlated impurities, are missing in Fig. 6.9(c).

Chapter 6. Electronic Transport in Graphene with Hydrogen Adatoms

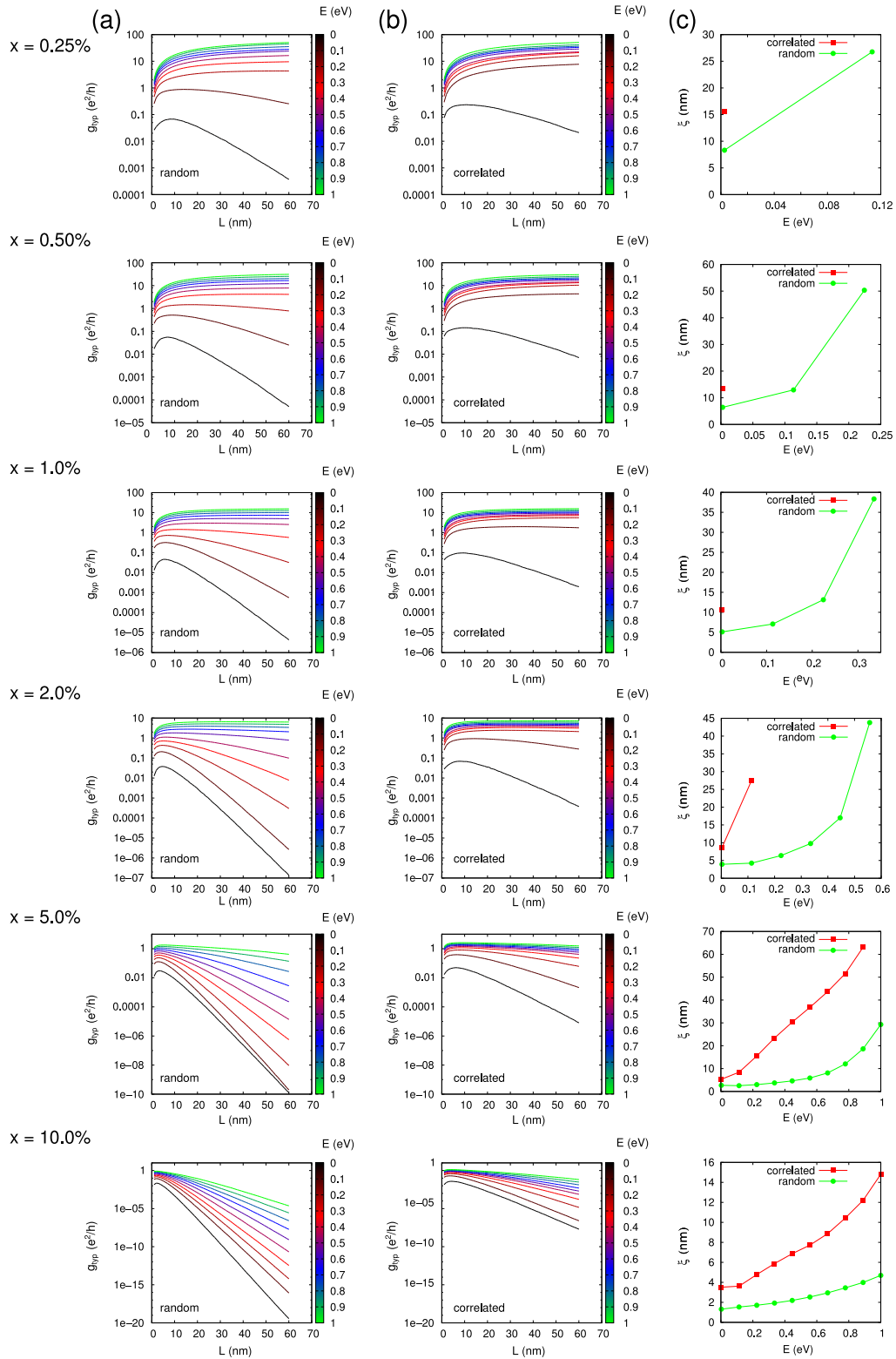


Figure 6.9 – Scaling analysis of conductivity g and localization length ξ_{loc} for concentrations $x = 0.25\% \dots 10\%$. (a,b) Conductivity g as a function of scattering region length L calculated for graphene with random and correlated adatom distributions, respectively, at charge-carrier energies $0 \text{ eV} < E < 1 \text{ eV}$. (c) Localization length ξ_{loc} as a function of charge-carrier energy E .

6.2. Resonant and non-resonant nature of cluster of vacancies in the honeycomb lattice

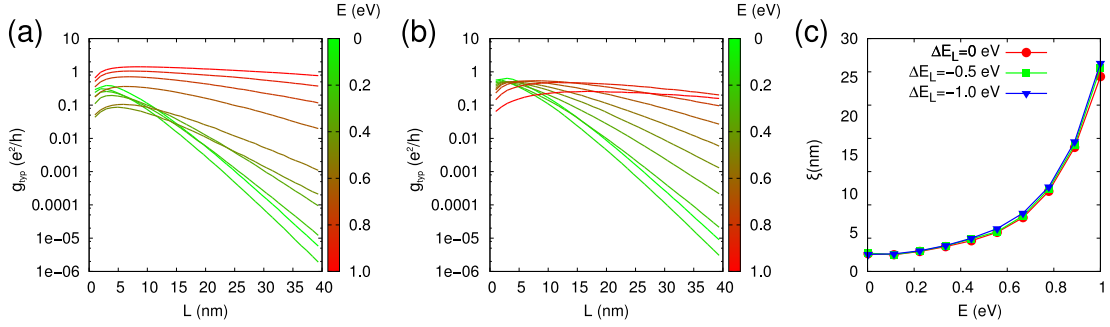


Figure 6.10 – (a,b) Conductivity g as a function of scattering region length L for graphene with randomly distributed adatoms at $x = 5\%$. The charge neutrality point of the leads has been shifted by (a) $\Delta E_L = -0.5$ eV and (b) $\Delta E_L = -1.0$ eV, respectively. (c) Localization length ξ_{loc} as a function of charge-carrier energy E for the two investigated lead doping levels compared to undoped leads $\Delta E_L = 0$ eV.

Figure 6.10(a,b) shows the conductivity curves $g(L)$ for $x = 5\%$ concentration of randomly distributed adatoms obtained by shifting the charge neutrality point of leads by $\Delta E_L = -0.5$ eV and $\Delta E_L = -1.0$ eV, respectively. The effect of the doping of leads is two-fold. First, the DOS of pristine graphene increases away from the charge neutrality point. Hence, upon doping, the number of transport channels increases, which may result in larger values of conductance g . This is particularly important when the scattering region has an enhanced DOS at low energy, such as graphene with resonant impurities. A comparison of Fig. 6.10(a) and Fig. 6.9(a) for $x = 5\%$ shows that conductivity is indeed enhanced at low energies with a crossing of the $g(L)$ curves at $L \approx 10$ nm. Second, doping results in a mismatch between the Fermi wavelength of the leads and that of the scattering region, which has a detrimental effect on conductance g . This effect is expected to be more pronounced at higher doping and high energy, where localization plays a smaller role. Indeed, at higher doping ($\Delta E_L = -1.0$ eV) and high energy ($E = 1.0$ eV) conductivity is reduced, notably at short length $L < 10$ nm, see Fig. 6.10(a,b). On the other hand, at large distances a general increase of the conductance is progressively restored since the conductivity becomes predominantly determined by the localization of the wavefunction and by the increased number of available states. Finally, as shown in Fig. 6.10(c), localization lengths ξ_{loc} are practically unaffected by doping the leads, as it is an intrinsic property of the scattering region.

6.2 Resonant and non-resonant nature of cluster of vacancies in the honeycomb lattice

6.2.1 Preliminary theory

We address the problem of a single hydrogen atom covalently bound on graphene in a Green's function framework. In the following, we use two different systems to label graphene atoms.

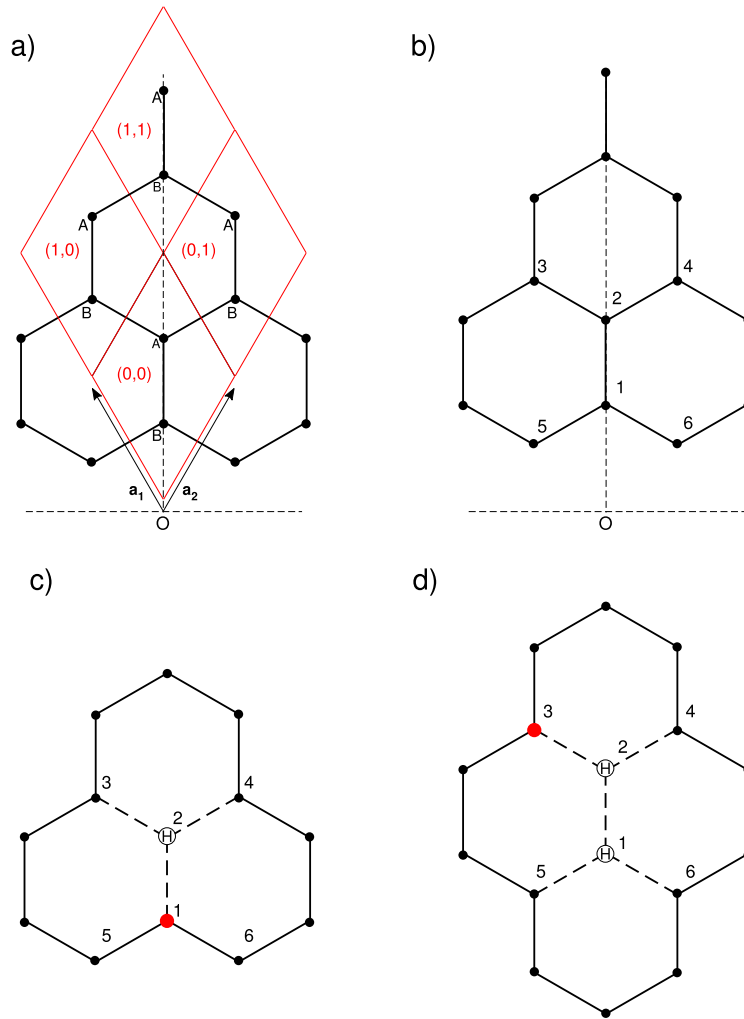


Figure 6.11 – (a) Honeycomb lattice generated by the basis vectors \mathbf{a}_1 and \mathbf{a}_2 . The unit cells with two atoms defining the two sublattices A and B are bounded in red. For each cell the crystal coordinates are indicated. (b) Alternative atoms identification by a single integer. (c-d) Honeycomb lattice with one (two) defect(s) in positions labeled by H. For the atom highlighted in red the LDOS is calculated.

In one system, we specify the coordinates (m, n) defining a cell vector $\mathbf{l} = m\mathbf{a}_1 + n\mathbf{a}_2$ and the sublattice label A, B , see Fig. 6.11(a). In the other system, we employ a single index $1, 2, 3 \dots$ which univocally defines the atom position in the lattice, see Fig. 6.11(b). We choose each time the approach that guarantees the clearest notation. We consider the Hamiltonian:

$$H = H_0 + H_1. \quad (6.10)$$

In this equation, H_0 is the ideal graphene Hamiltonian

$$H_0 = -t \sum_{\langle i,j \rangle} a_i^\dagger b_j + h.c., \quad (6.11)$$

6.2. Resonant and non-resonant nature of cluster of vacancies in the honeycomb lattice

where a_i^\dagger (b_i^\dagger) and a_i (b_i), respectively, create and annihilate a p_z electron on the site \mathbf{i} in the sublattice A (B). H_1 is the perturbation due to the defects. For a single defect, which we assume to be localized on site l , in sublattice A we have

$$H_1 = \varepsilon a_l^\dagger a_l, \quad (6.12)$$

that is, we model the defect by introducing a shift of the on-site energy. This perturbation can arise, for example, by a substitutional impurity. In the case of covalently bound hydrogen we assume $\varepsilon \rightarrow \infty$ such that no electron can be on the defect site due to the absence of p_z orbital. For the case of an hydrogen dimer we consider two defect located in the same cell \mathbf{l} , respectively, on sublattice A and B , see Fig.6.11 (c). The Hamiltonian reads

$$H = H_0 + H_1 + H_2 \quad H_2 = \varepsilon b_l^\dagger b_l. \quad (6.13)$$

The spectral properties are best derived from the Green's function

$$G(z) = (z - H)^{-1} \quad z \in \mathbb{C}. \quad (6.14)$$

The symmetries of the graphene honeycomb lattice are inherited by the free Green's function $G_0(z)$. Translational invariance gives, for any integers (m, n) , $G_0(\mathbf{0}, \mathbf{s}) = G_0(m\mathbf{a}_1 + n\mathbf{a}_2, \mathbf{s} + m\mathbf{a}_1 + n\mathbf{a}_2)$. The equivalence of the two sublattices gives $G_0^{AA}(\mathbf{0}, \mathbf{s}) = G_0^{BB}(\mathbf{0}, \mathbf{s})$ and $G_0^{AB}(\mathbf{0}, \mathbf{s}) = G_0^{BA}(\mathbf{0}, -\mathbf{s})$. The rotational C_6 invariance with respect to the center of any hexagon gives $G_0(\mathbf{r}, \mathbf{s}) = G_0(\mathbf{R}(n\pi/3)\mathbf{r}, \mathbf{R}(n\pi/3)\mathbf{s})$ where n represents any integer and $\mathbf{R}(\alpha)$ is a matrix which represents a rotation by angle α . In the notation shown in Fig. 6.11 (b), we have, for example, $G_0^{12} = G_0^{23} = G_0^{51}$.

By introducing the t-matrix

$$T(z) = H_1(z) + H_1(z)G_0(z)H_1(z) + H_1(z)G_0(z)H_1(z)G_0(z)H_1(z) + \dots, \quad (6.15)$$

the Green's function G can be expressed in terms of the pristine graphene Green's function $G_0(z) = (z - H_0)^{-1}$

$$G(z) = G_0(z) + G_0(z)T(z)G_0(z). \quad (6.16)$$

The exact Green's function for an honeycomb lattice with next-neighbor hopping has been calculated in Ref. [Horiguchi, 1972]. In the following, we will be mostly interested in $G^{AA}(\mathbf{0}, \mathbf{0}; z)$ and $G^{AB}(\mathbf{0}, \mathbf{0}; z)$. For the diagonal matrix element of $G_0(z)$ we have

$$G^{AA}(\mathbf{0}, \mathbf{0}; z) = zG_t((z-3)/2), \quad (6.17)$$

where

$$G_t(s) = \frac{1}{2\pi} g(s) \tilde{K}(k(s)), \quad (6.18)$$

$$g(s) = \frac{8}{[(s+3)^{1/2} - 1]^{3/2} [(s+3)^{1/2} + 3]^{1/2}}, \quad (6.19)$$

$$\tilde{K}(k) = \begin{cases} K(k) & \text{for } \text{Im}z > 0 \text{ and } \text{Im}k < 0 \\ & \text{or } \text{Im}z < 0 \text{ and } \text{Im}k > 0 \\ K(k) + 2iK'(k) & \text{for } \text{Im}z > 0 \text{ and } \text{Im}k < 0 \\ K(k) - 2iK'(k) & \text{for } \text{Im}z < 0 \text{ and } \text{Im}k < 0, \end{cases} \quad (6.20)$$

$$k(s) = 4(s+3)^{1/4} / [(s+3)^{1/2} - 1]^{3/2} [(s+3)^{1/2} + 3]^{1/2}. \quad (6.21)$$

$G_0^{AB}(\mathbf{0}, \mathbf{0}; z)$ can be derived from $G_0^{AA}(\mathbf{0}, \mathbf{0}; z)$. By taking the expectation value of the identity $(z - H_0)G_0(z) = \mathbb{1}$ on the state $|\mathbf{0}, A\rangle$, which represents a p_z state at the site \mathbf{l} on sublattice A , one obtains:

$$\langle \mathbf{0}, A | z | \mathbf{0}, A \rangle \langle \mathbf{0}, A | G_0(z) | \mathbf{0}, A \rangle \quad (6.22)$$

$$- \langle \mathbf{0}, A | H_0 | \mathbf{0}, B \rangle \langle \mathbf{0}, B | G_0(z) | \mathbf{0}, A \rangle \quad (6.23)$$

$$- \langle \mathbf{0}, A | H_0 | \mathbf{a}_1, A \rangle \langle \mathbf{a}_1, A | G_0(z) | \mathbf{0}, A \rangle \quad (6.24)$$

$$- \langle \mathbf{0}, A | H_0 | \mathbf{a}_2, A \rangle \langle \mathbf{a}_2, A | G_0(z) | \mathbf{0}, A \rangle = 1 \quad (6.25)$$

$$zG_0^{AA}(\mathbf{0}, \mathbf{0}; z) + tG_0^{BA}(\mathbf{0}, \mathbf{0}; z) + tG_0^{BA}(\mathbf{a}_1, \mathbf{0}; z) + tG_0^{BA}(\mathbf{a}_2, \mathbf{0}; z) = 1 \quad (6.26)$$

$$G_0^{BA}(\mathbf{0}, \mathbf{0}; z) = \frac{1 - zG_0^{AA}(\mathbf{0}, \mathbf{0}; z)}{3t} \quad (6.27)$$

where in the last step the rotational symmetry has been employed.

6.2.2 Single impurity

By applying eq. 6.15 to the Hamiltonian defined by eq. 6.12, one can derive for the single impurity t -matrix T_1 [Economou, 2006]

$$T_1 = |\mathbf{l}, A\rangle \frac{\varepsilon}{1 - \varepsilon G_0^{AA}(\mathbf{l}, \mathbf{l})} \langle \mathbf{l}, A |, \quad (6.28)$$

where $G_0^{AA}(\mathbf{l}, \mathbf{l}) = \langle \mathbf{l}, A | G_0(z) | \mathbf{l}, A \rangle$ and $|\mathbf{l}, A\rangle$ represents a p_z state at the site \mathbf{l} on sublattice A , that is, the position of the defect.

As a general property, the poles in the complex z -plane of $G(z)$ represent the discrete eigenvalues of H . Since eq. 6.16 holds, the poles of $G(z)$ are given by those of $T(z)$. In the limit $\varepsilon \rightarrow 0$

6.2. Resonant and non-resonant nature of cluster of vacancies in the honeycomb lattice

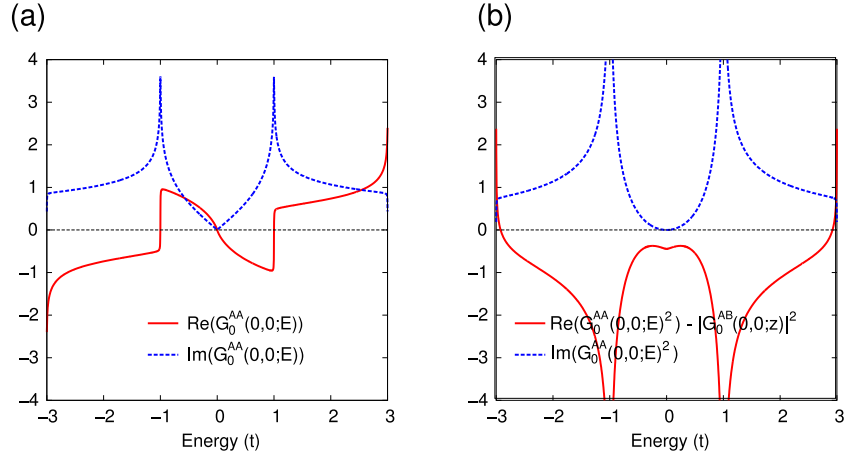


Figure 6.12 – Graphical solution of eqs. (6.29 and 6.36). (a-b) Real (red curve) and imaginary (blue curve) part of (a) eq. 6.29 and (b) eq. 6.36. Simultaneous zeros of real and imaginary part represent discrete states of the overall spectrum. A small negative imaginary part has been added to the energy.

our problem reduces to finding the solution of

$$G_0^{AA}(\mathbf{1}, \mathbf{1}; z) = G_0^{AA}(\mathbf{0}, \mathbf{0}; z) = 0 \quad (6.29)$$

The zeros of $G_{AA}(\mathbf{0}, \mathbf{0}; z)$ are found at $z = 0$ as shown in Fig. 6.12(a). The defect induces a bound state at $E = 0$ which is responsible for a singularity in the DOS.

The Local Density of States at energy E on the site 1, $LDOS(1; E)$ (see Fig. 6.11 (b), atom highlighted in red), is given by

$$LDOS(1; E) = -\frac{1}{\pi} \text{Im}(G^{11}(E)) = -\frac{1}{\pi} \text{Im}(G^{BB}(\mathbf{0}, \mathbf{0}; E)) \quad (6.30)$$

where E is meant to approach the real axis from the upper complex half-plane ($\text{Im}E \rightarrow 0^+$). Taking into account eqs. 6.16 and 6.28, we have

$$LDOS(1; E) = -\frac{1}{\pi} \text{Im}(G^{BB}(\mathbf{0}, \mathbf{0}; E)) = \quad (6.31)$$

$$-\frac{1}{\pi} \text{Im}(G_0^{BB}(\mathbf{0}, \mathbf{0}; E) + \langle \mathbf{0}, B | G_0(E) T(z) G_0(E) | \mathbf{0}, B \rangle) = \quad (6.32)$$

$$-\frac{1}{\pi} \text{Im}(G_0^{BB}(\mathbf{0}, \mathbf{0}; E) - \langle \mathbf{0}, B | G_0(\mathbf{0}, \mathbf{0}; E) \frac{|\mathbf{0}, A\rangle \langle \mathbf{0}, A|}{G_0^{AA}} G_0(E) | \mathbf{0}, B \rangle) = \quad (6.33)$$

$$-\frac{1}{\pi} \text{Im}(G_0^{AA}(\mathbf{0}, \mathbf{0}; E) - \frac{|G_0^{BA}(\mathbf{0}, \mathbf{0}; E)|^2}{G_0^{AA}(\mathbf{0}, \mathbf{0}; E)}). \quad (6.34)$$

The analytic solution for the LDOS has been compared with the numerical result based on a different assumption to model the defect. In the numerical model, indeed, rather than introducing an infinite site energy, a missing p_z orbital in correspondence of the hydrogen is

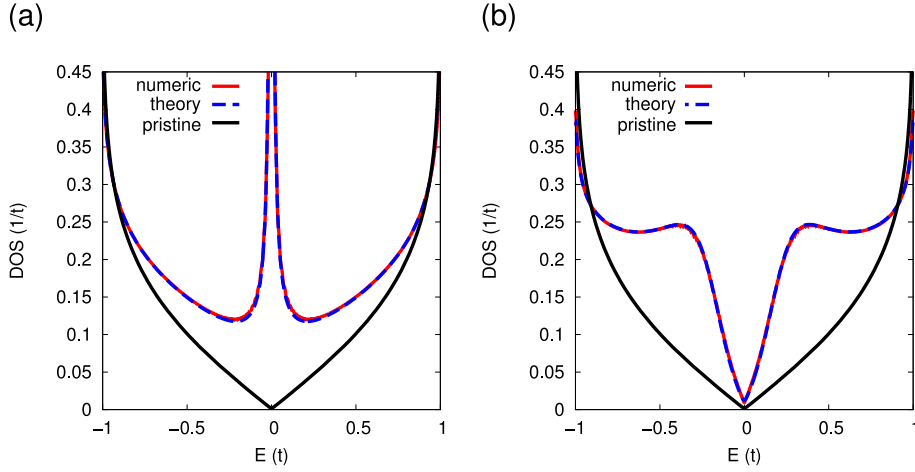


Figure 6.13 – (a-b) LDOS calculated for the atom highlighted in red in Fig. 6.11(b-c). Numerical and theoretical estimate show perfect agreement. The translationally invariant LDOS for a carbon atom of pristine graphene is included as reference.

assumed. Fig. 6.13 (a) shows a perfect agreement between analytic and numerical estimates. This is another confirmation that the two models are equivalent.

6.2.3 Impurity dimer

With reference to the Hamiltonian defined in eq. 6.13, we consider $H_{01} = H_0 + H_1$ as the free Hamiltonian perturbed by H_2 . Similarly to the single impurity we obtain

$$G = G_{01} + G_{01}|\mathbf{l}, B\rangle \frac{\varepsilon}{1 - \varepsilon G_{01}^{BB}(\mathbf{l}, \mathbf{l})} \langle \mathbf{l}, B| G_{01}, \quad (6.35)$$

where $G_{01}(z) = (z - H_{01})^{-1}$. The poles of $T = |\mathbf{l}, B\rangle \frac{\varepsilon}{1 - \varepsilon G_{01}^{BB}(\mathbf{l}, \mathbf{l})} \langle \mathbf{l}, B|$ correspond to additional discrete states induced by the defect. Combining eqs. 6.16, 6.28, and 6.35, in the limit of $\varepsilon \rightarrow 0$, the equation for the poles of the dimer t -matrix becomes

$$G_0^{AA}(\mathbf{0}, \mathbf{0}; z)^2 = |G_0^{AB}(\mathbf{0}, \mathbf{0}; z)|^2. \quad (6.36)$$

Eq. 6.36 can be solved graphically. The equation for the real and imaginary part are $\text{Im}[G_0^{AA}(z)^2] = 0$ and $\text{Re}[G_0^{AA}(z)^2] = |G_0^{AB}(z)|^2$. As shown in Fig. 6.12(b), no solutions are found in the interval $[-3t, 3t]$, meaning that no discrete states are induced by the dimer. The LDOS on site 3 indicated in Fig. 6.11(c) can be calculated taking into account eq. 6.16. We have

$$\text{LDOS}(3; E) = -\frac{1}{\pi} \text{Im} G^{33}(z) = G_{01}^{33} - \frac{G_{01}^{31} G_{01}^{13}}{G_{01}^{11}} \quad (6.37)$$

$$G_{01}^{11} = G_{01}^{33} = G_0^{33} - \frac{G_0^{32} G_0^{23}}{G_0^{22}} \quad (6.38)$$

6.2. Resonant and non-resonant nature of cluster of vacancies in the honeycomb lattice

$$G_{01}^{31} = G_{01}^{13} = G_0^{13} - \frac{G_0^{12}G_0^{23}}{G_0^{22}} \quad (6.39)$$

For the pristine honeycomb GFs we have $G_0^{33} = G_0^{11} = G_0^{22} = G_0^{AA}(\mathbf{0}, \mathbf{0})$ and $G_0^{32} = G_0^{23} = G_0^{12} = G_0^{21} = G_0^{AB}(\mathbf{0}, \mathbf{0})$. In order to calculate G_0^{13} we start from the identity $(z - H)G(z) = \mathbb{1}$ and take the matrix element $\langle 1|(z - H_0)G_0(z)|2\rangle = 0$. One obtains:

$$\langle 1|(z - H_0)G_0|2\rangle = \langle 1|zG_0|2\rangle - \langle 1|H_0G_0|2\rangle = 0 \quad (6.40)$$

$$zG_0^{12} + t(G_0^{22} + G_0^{52} + G_0^{62}) = 0 \quad (6.41)$$

$$zG_0^{BA}(\mathbf{0}, \mathbf{0}) + tG_0^{AA}(\mathbf{0}, \mathbf{0}) + 2tG_0^{31} = 0 \quad (6.42)$$

$$G_0^{31} = -\frac{z}{2t}G_0^{BA}(\mathbf{0}, \mathbf{0}) - \frac{G_0^{AA}(\mathbf{0}, \mathbf{0})}{2} \quad (6.43)$$

$LDOS(3; E)$ obtained both analytically and numerically are plotted in Fig. 6.13(c) showing perfect agreement.

7 Stacking domain boundaries in bilayer graphene

In this chapter, we study defects in the stacking order of bilayer graphene. As already discussed in Section 3.3.4, such defects arise at the interface between domains with different stacking order, thus assuring the overall continuity of covalently bonded crystalline lattice.

In the first section, we investigate one fascinating realization of stacking disorder where triangular domains with well-defined Bernal stacking are delimited by a hexagonal network of strain solitons acting as stacking domain boundaries. First, we show by means of realistic scale simulations that this is nothing but a consequence of a structural transition of the Moiré pattern of twisted bilayer graphene, taking place for small twist angles $\theta < \theta^ \simeq 1.2^\circ$. Next, we investigate the effect of stacking domain boundaries on massive Dirac fermions typical of bilayer graphene. We demonstrate the breakdown of the current low-twist-angle picture consisting in a flat zero-energy band of localized states that, indeed, only holds for rigidly twisted bilayer graphene. In the limit of $\theta \rightarrow 0^\circ$, we rather find an overall almost homogeneous charge density with atomic scale modulations determined by the local stacking.*

The second section reports on a joint experimental and theoretical work on bilayer graphene integrated in a Nanoelectromechanical System (NEMS), namely, a system based on the interplay between mechanical and electrical properties of the constituting materials. NEMS are employed, for instance, to study fundamental phenomena taking place at the nanoscale such as electron-phonon interaction but also in applications such as bandgap engineering or to produce a large variety of sensors. The experiments reported herein measure oscillations in the electrical response of bilayer graphene deformed by an AFM tip. We propose a theoretical model suggesting that these oscillations arise from quantum mechanical interference taking place due to the stacking domain boundaries introduced by the mechanical deformation.

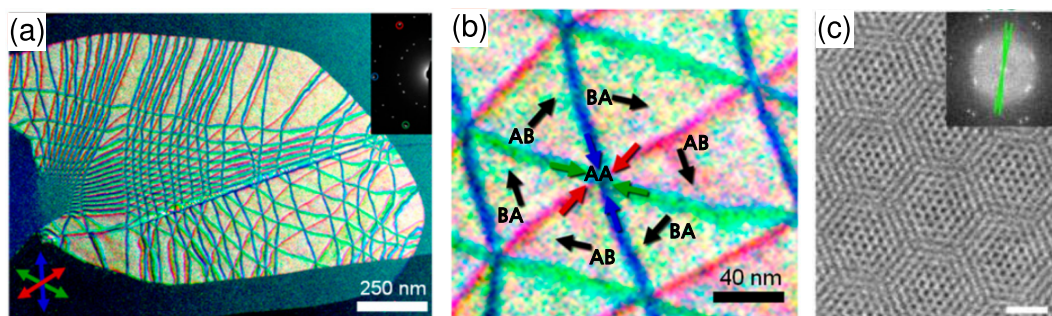


Figure 7.1 – Experimental images of topological defects in bilayer graphene. (a) TEM images of bilayer graphene taken at different diffraction angles (shown in the inset) are overlaid in red, blue, and green, allowing to image individual stacking domain boundaries. Regions with univocally defined Bernal stacking have equal contributions from different colors, thus appearing almost white. (b) Enlarged region taken from panel (a) showing that adjacent stacking domains have inequivalent Bernal stacking AB/BA. (c) TEM of twisted bilayer graphene showing superlattice periodicity. Reproduced with permission from (a-b) Ref. [Alden *et al.*, 2013] © 2013 *National Academy of Science*, (c) Ref. [Lu *et al.*, 2013] © 2013 *American Chemical Society*

7.1 Stacking domain boundaries in twisted bilayer graphene

7.1.1 Introduction

As introduced in Chapters 1 and 2, bilayer graphene differs from monolayer graphene bearing peculiar properties such as the massive nature of its charge carriers [Castro Neto *et al.*, 2009], the possibility of inducing a tunable bandgap by applying a transverse electric field [Ohta *et al.*, 2006], and quantum Hall valley ferromagnetism [Lee *et al.*, 2014]. These properties are essentially due to a weak though finite coupling between the two layers.

With respect to monolayer graphene, an additional degree of freedom is needed to fully characterize the structure of bilayer graphene: the relative position of the two layers, i.e. the stacking order. Not surprisingly, the latter is not immune to disorder which can manifest itself, for example, in a finite rotation between the two layers (twisted bilayer graphene, TBG) [Li *et al.*, 2010; Brown *et al.*, 2012; Beechem *et al.*, 2014] or in boundaries which connect two domains with energetically degenerate but geometrically inequivalent stacking order (stacking domain boundaries), see Section 3.3.4 [Lalmi *et al.*, 2014; Lin *et al.*, 2013; Butz *et al.*, 2014; Gong *et al.*, 2013].

Both these classes of topological defects have been intensively imaged and studied in recent years. Stacking domain boundaries are realized by strain solitons, that is, segments characterized by a typical width where the strain generated by interfacing two inequivalent stacking domains is confined. Solitons are free to move and can be displaced by the action of an STM tip, yet conserving their form due to their topological nature [Yankowitz *et al.*, 2014; Lalmi *et al.*, 2014]. From the theoretical point of view, strain solitons have been described within

7.1. Stacking domain boundaries in twisted bilayer graphene

the 2D Frenkel-Kontorova model predicting a typical width of ≈ 12 nm [Popov *et al.*, 2011]. As shown in Fig. 7.1(b-c), one way solitons manifest themselves in bilayer graphene is by forming a hexagonal network that delimits triangular domains showing alternating AB/BA Bernal stacking [Alden *et al.*, 2013; Lalmi *et al.*, 2014]. Another form of topological defect is the presence of a finite rotation angle between the layers found, for example, in epitaxial graphene on SiC substrate [Hass *et al.*, 2008] or in bilayer graphene obtained by chemical vapor deposition [Lu *et al.*, 2013], see Fig. 7.1(c). Rotational disorder was already documented in the uppermost layers of highly ordered pyrolytic graphite (HOPG) [Pong and Durkan, 2005]. In case of finite twist angle, the stacking order cannot be univocally defined on the whole surface of the sample since the two layers cannot be superimposed by a rigid shift. As shown in Fig 7.2(a), when crossing a Moiré supercell of twisted bilayer graphene the local stacking evolves through the high-symmetry configurations AA, AB, SP, BA and, finally, gets back to AA (see Fig. 7.2(b) for naming conventions). Remarkably, as pointed out in Ref. [Alden *et al.*, 2013], this sequence corresponds to that encountered in the triangular lattice of stacking domains reported in experiments.

In this work, we have simulated Twisted Bilayer Graphene in the limit of small twist angle θ and show that, while for $\theta \gtrsim 1.2^\circ$ the equilibrium structure does not differ sensibly from a rigid twist of the two layers, for angles below $\theta \approx 1.2^\circ$ a structural transition takes place and the samples progressively relax forming a triangular lattice of alternating AB/BA stacking domains separated by shear strain solitons forming a hexagonal network. The electronic structure is profoundly affected by the emergence of this structural phase and exhibits characteristic features determined by the local stacking field. In contrast to the picture valid for low-angle TBG that consists in low-energy states quasi-localized in AA regions, we find that the charge density in AB/BA domains resembles that of pristine AB bilayer graphene. On the other hands, the hexagonal network has a distinct charge density signature which makes it detectable by STM.

7.1.2 Simulation of low-angle Twisted Bilayer Graphene

The underlying physical mechanism responsible for the transition is rooted in the interplay between van der Waals forces, responsible for binding the two graphene layers, and in-plane elasticity forces. As shown in Fig 7.2(b), the binding energy calculated within DFT+vdW is minimal for AB/BA stacking, whereas AA stacking is energetically less favorable by 12.2 meV per atom. In the path connecting AB and BA, one additional high-symmetry stacking SP corresponds to a local energy maximum of about 1.33 meV per atom. This results in finite in-plane forces that drive atoms toward AB-stacking. However, the in-plane atomic rearrangement is hindered by the strain generated by the atomic displacement itself. The ultimate relaxed structures result from the balance between the minimization of the interlayer energy and the reaction of the strain field.

Our simulations consist in relaxing models of twisted bilayer graphene by treating atomic

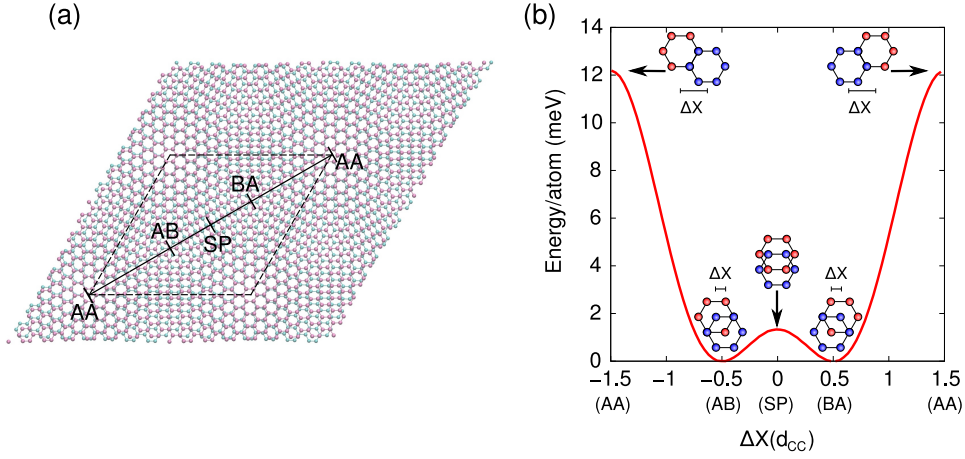


Figure 7.2 – (a) Ball-and-stick representation of twisted bilayer graphene. The Moiré supercell is highlighted by black lines. Along the black line the stacking evolves through AA, AB, SP, BA, AA-stacking configurations defined in (b). (b) Interlayer binding energy of bilayer graphene E_b calculated within DFT+vdW as a function of the interlayer lateral displacement ΔX (see ball-and-stick schemes where atoms with different colors belong to opposite layers). The layer distance is fixed to $\Delta z = 3.417 \text{ \AA}$. The energy axis zero is $E_b(\Delta X = \pm 0.5 d_{CC})$ corresponding to AB/BA stacking.

interactions within a classical potential. Previous DFT studies of TBG have been performed within LDA or GGA functionals, which, unfortunately, disregard dynamical charge correlations responsible for van der Waals interaction [Hass *et al.*, 2008; Uchida *et al.*, 2014; Trambly de Laisardière *et al.*, 2010]. As we aim to treat models with up to $N = 3 \times 10^5$ atoms, an *ab initio* DFT treatment is out of computational capabilities. Currently available implementations of classical potentials for carbon do not reproduce correctly the interlayer energy of layered structures based on sp^2 -hybridized carbon atoms [Spanu *et al.*, 2009; Lebègue *et al.*, 2010; Los and Fasolino, 2003; Brenner *et al.*, 2002; Kolmogorov and Crespi, 2005; Reguzzoni *et al.*, 2012]. For example, AIREBO and LCBOP potentials do reproduce with a good accuracy the formation energy of local and topological defects in monolayer graphene, but lack a correct description of the interlayer energy of graphite as a function of interlayer distance or shift [Brenner *et al.*, 2002; Los and Fasolino, 2003; Reguzzoni *et al.*, 2012]. We define a new potential $V_{LCBOP/KC} = V_{SR} + V_{LR}$ which has a short range contribution V_{SR} inherited from LCBOP [Los and Fasolino, 2003] and a long-range registry-dependent contribution V_{LR} which is a reparametrized version of the Kolmogorov-Crespi potential [Kolmogorov and Crespi, 2005]. The parameters of V_{LR} have been fitted in order to reproduce observables calculated within DFT+vdW. In our DFT calculations, the interlayer distance of graphite is 3.36 \AA and the in-plane bond length is 1.42 \AA . For bilayer graphene we find that the atomic bond-length is $d_{CC} = 1.419 \text{ \AA}$ and the equilibrium interlayer distances of AB, AA, and SP configurations are, respectively, $\Delta z_{AB} = 3.417 \text{ \AA}$, $\Delta z_{AA} = 3.599 \text{ \AA}$, and $\Delta z_{SP} = 3.439 \text{ \AA}$.

Supercells of twisted bilayer graphene are built according to established rules derived by imposing commensurability conditions [Shallcross *et al.*, 2008; Lopes dos Santos *et al.*, 2007].

7.1. Stacking domain boundaries in twisted bilayer graphene

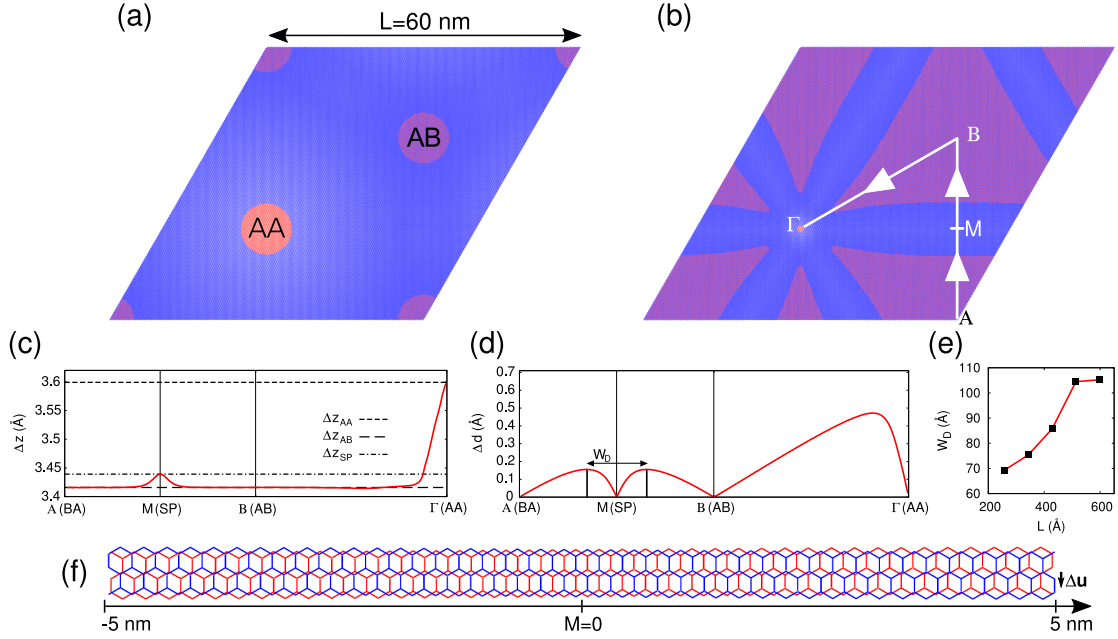


Figure 7.3 – Atomic relaxation of a twisted bilayer graphene commensurate supercell with $\theta = 0.235^\circ$ and $L = |\mathbf{t}_1| = 59.8$ nm ($w = 140$). (a) Representation of the initial model with rigidly rotated layers. Pairs of atoms in opposite layers whose planar projections are closer than $\Delta d = 0.2$ Å are colored in red, otherwise in blue. AA-stacked regions contain only red atoms, whereas atoms in AB-stacked regions are alternatively blue and red. Regions with neither AA nor AB stacking exclusively contain blue atoms. This representation allows to recognize distinct stacking domains at a glance. (b) Representation of the relaxed structure with the same color-coding procedure as in (a). (c) Interlayer distance Δz for the relaxed system along the path AMB Γ defined in (b). (d) Modulus of the displacement that atoms along the path AMB Γ undergo upon relaxation. The distance between the two symmetric maxima with respect to M is referred to as W_D . The dependence of W_D on the L is shown in (e). (f) Shear soliton separating AB and BA domains arising from structural relaxation. $\Delta \mathbf{u}$ represents the shear strain, namely, parallel to the axis of the soliton.

In particular, one class of supercells is defined by an integer w which determines the supercell periodicity vectors $\mathbf{t}_1 = w\mathbf{a}_1 + (w+1)\mathbf{a}_2$ and $\mathbf{t}_2 = -(w+1)\mathbf{a}_1 + (2w+1)\mathbf{a}_2$, with \mathbf{a}_1 and \mathbf{a}_2 ($|\mathbf{a}_{1/2}| = \sqrt{3}d_{CC}$) being the crystal vectors of the graphene honeycomb lattice, and the corresponding twist angle is defined by $\cos\theta = (3w^2 + 3w + 1/2)/(3w^2 + 3w + 1)$ [Lopes dos Santos *et al.*, 2007]. \mathbf{t}_1 and \mathbf{t}_2 form a 60° angle and the Moiré pattern has C_3 symmetry, see Fig. 7.2(a). Notably, in the limit $w \rightarrow \infty$ the twist angle and the supercell linear size are inversely proportional: $\theta^{-1} \propto |\mathbf{t}_1| = L$. The initial interlayer distance is set as $\Delta z_{AB} = 3.417$ Å. We have relaxed models up to $w = 160$ corresponding to $\theta = 0.206^\circ$, $L = 68.4$ nm, and total number of atoms $N = 309124$.

Fig. 7.3(a,b) show the initial and the relaxed structure of a TBG model with $\theta = 0.235^\circ$. The colors of the atomic representation allow to recognize the transformation that the system has undergone. Upon relaxation, AB(BA) regions have extended assuming an approximately triangular shape with a side ≈ 40 nm, AA regions have dramatically reduced their extension now

covering just few atoms. The segments separating AB/BA domains form a hexagonal network whose vertices correspond to AA cores. The atomic in-plane displacement Δd generated by relaxation along a high-symmetry path is shown in Fig. 7.3(d). Departing from the centers A or B toward M , atoms increasingly need to displace to restore the AB/BA favorable stacking. Because of opposite value of Δd along AM and BM strain accumulates in the vicinity of M . When the energy gained by creating a AB/BA domain is compensated by the local strain energy, Δd reaches maxima before abruptly falling to zero. The distance W_D between the two symmetric maxima converges to a constant value $W_D^* = 10.5 \text{ nm}$, upon increasing the cell size L . This explains the emergence of a (shear) strain soliton separating two stacking domains. As shown in Fig. 7.3(f), the amount of shear is $|\Delta \mathbf{u}| = 1.42 \text{ \AA}$. A similar reasoning is valid for the path $B\Gamma$. Additionally, atoms displace in the out-of-plane direction, as shown in Fig. 7.3(c). Out-of-plane relaxation of TBG has been intensively investigated within DFT/LDA for $\theta > 2^\circ$ [Uchida *et al.*, 2014]. It was found that for $\theta < 3^\circ$ the system develops an out-of-plane corrugation described by a sine function. Recently, a work based on classical potential similar to the one employed in the present work investigated TBG in the regime $0.46^\circ < \theta < 2.1^\circ$ [van Wijk *et al.*, 2015]. Similarly to what reported in the latter work, we find that Δz relaxes to Δz_{AB} in correspondence of AB/BA stacking domains giving rise to the plateaus seen in Fig. 7.3(c) and it locally adapts to Δz_{SP} and Δz_{AA} , respectively, at M and Γ , consistently with the local stacking. Therefore, a small corrugation is present in correspondence of the solitons and the AA cores (tilt of the normal vectors $\alpha < 0.2^\circ$).

To get a deeper insight in the Moiré pattern resulting from the relaxation, we have studied the stacking vector field \mathbf{u} , defined as the in-plane component of the minimal shift that must be applied to one layer to make it coincide locally to the opposite layer, see Fig. 7.4(a).

Fig. 7.4(b) allows to appreciate the extension of the triangular domains with almost constant stacking $|\mathbf{u}| = 1.42 \text{ \AA}$ (white regions). By inspecting the local stacking field around A and B (side panels in Fig. 7.4(b)) one can see the confluence of three vector orientations differing by 120° . This discontinuity is immaterial as the vector \mathbf{u} for AB(BA)-stacking has three degenerate representations forming an angle of 120° with each other. However, when going from one stacking domain to its neighbor (e.g. from point A to point B), \mathbf{u} rotates by 60° , that is, the stacking changes from AB to BA or vice versa. The variation $\Delta \mathbf{u} = \mathbf{u}' - \mathbf{u}$ ($|\mathbf{u}| = 1.42 \text{ \AA}$) is orthogonal to the strain soliton and coincides with its shear vector. These stacking domain boundaries are topological defects and $\Delta \mathbf{u}$ is assigned as their topological invariant. In the following, the denominations “strain soliton” and “stacking domain boundary” will be used interchangeably.

As shown in Fig. 7.3(c), along the path AMB $|\mathbf{u}|$ has a minimum at M , corresponding to SP stacking ($|\mathbf{u}| = 1.23 \text{ \AA}$). Upon increasing L , the FWHM W_S of this dip saturates to $W_S^* = 9.5 \text{ nm}$, a value close to $W_D^* = 10.5 \text{ nm}$. We choose to use W_S^* to define the width of the stacking domain boundaries since its determination does not require comparison with the non-relaxed structure. The calculated widths of the solitons are in good accordance with the experiments [Alden *et al.*, 2013; Lin *et al.*, 2013; Butz *et al.*, 2014]. For the sake of comparison $|\mathbf{u}|$ is reported

7.1. Stacking domain boundaries in twisted bilayer graphene

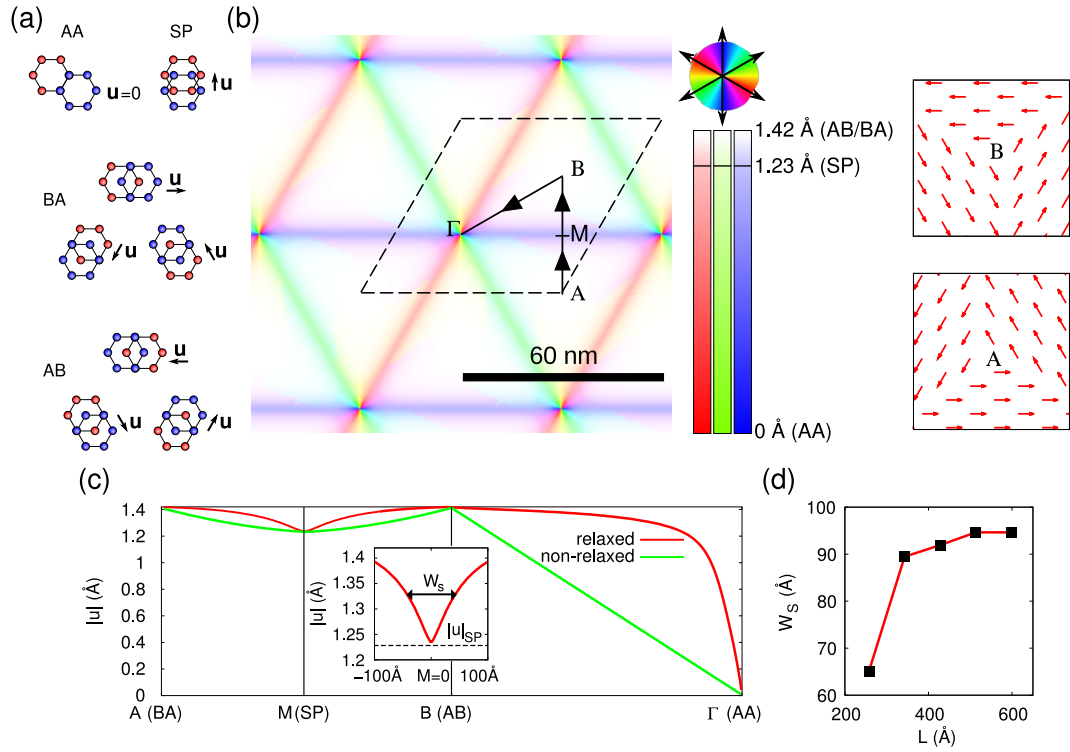


Figure 7.4 – Representation of the stacking vector field \mathbf{u} of relaxed TBG with $\theta = 0.235^\circ$, $L = 59.8\text{nm}$ ($w = 140$). (a) Illustration of \mathbf{u} for high-symmetry stackings. (b) Color coded representation of the field \mathbf{u} . Hue and saturation at each point represent, respectively, the direction and the intensity of the local value of \mathbf{u} . Fully saturated colors correspond to AA ($|\mathbf{u}| = 1.42\text{\AA}$), white regions (vanishing saturation) correspond to AB ($|\mathbf{u}| = 1.42$). The center of the solitons showing SP stacking ($|\mathbf{u}| = 1.23\text{\AA}$) are half-saturated. Hue varies with a period of 180° as shown in the wind rose. Lateral panel show the stacking vector field in the vicinity of B and A. (c) Modulus of \mathbf{u} along the path AMB Γ defined in (b) for relaxed and rigidly (non-relaxed) TBG. The FWHM of the minimum in M is referred to as W_s and used as definition of the soliton width. The dependence of W_s on the system size L is shown in (d).

also for rigidly TBG showing smooth change between AB(BA) and SP stacking along the path AM(BM) as well as linear change between AB and AA stacking along the path B Γ . The vertex of the hexagonal network (Γ) where six stacking domain boundaries merge are topological point defects with $\mathbf{u} = 0$ and non-zero winding number, that is, the field \mathbf{u} rotates by 360° along a closed path that encompasses Γ [Mermin, 1979].

Intuitively, we expect that a transition involving strain soliton generation takes place when the TBG supercell is larger than W_s^* such that strain can be efficiently accommodated. The dependence of several observables on θ (or L) reveals further details of the transition. As shown in Fig. 7.5(a), for $\theta = 21.8^\circ$ the distribution of the interlayer distance Δz has a minimal spread $\Delta z_{\text{MAX}} - \Delta z_{\text{MIN}} = 0.01\text{\AA}$. Upon a reduction of θ , Δz_{MAX} and Δz_{MIN} increasingly differentiate and saturate around $\theta = 2^\circ$ to $\Delta z_{\text{MAX}} = \Delta z_{\text{AA}}$ and $\Delta z_{\text{MIN}} = \Delta z_{\text{AB}}$, consistently with what shown in Fig. 7.3(c). At this stage, out-of-plane relaxation competes with the bending rigidity of graphene

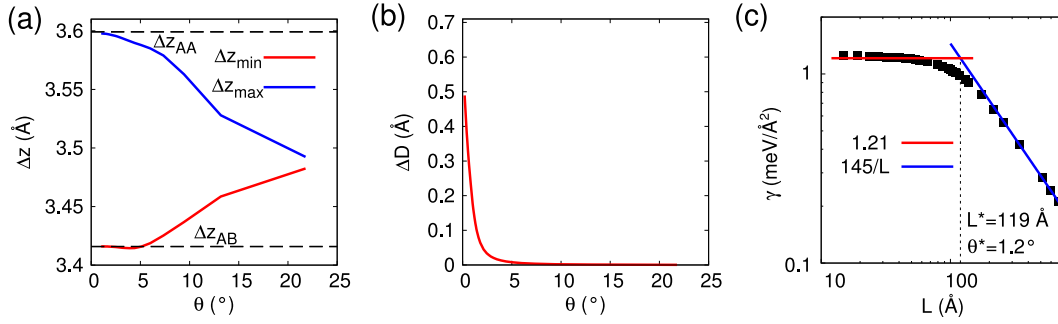


Figure 7.5 – Structural transition of twisted bilayer graphene in the limit of small angle. (a) Largest (lowest) interlayer distance $\Delta z_{MAX(MIN)}$ and (b) maximum atomic displacement as a function of twist angle θ . (c) Density of twist energy γ as a function of supercell size L . The constant and inversely proportional regions are fitted, respectively, by the red and the blue lines (notice the bilogarithmic scale) intersecting at $L^* = 11.9$ nm ($\theta^* = 1.2^\circ$).

whose coefficient is estimated to be $B_M = 1.44$ eV [Wei *et al.*, 2013]. For lower values of θ , in-plane relaxation becomes sizable. Notice that in-plane displacement is upper-bounded by one bond length $d_{CC}/2 = 0.71$ Å since two inequivalent stacking vectors are connected by $|\Delta \mathbf{u}| < d_{CC}$ and the displacement must be equally shared by the two layers. The transition is best revealed by the functional dependence of the twist energy on the cell size $\gamma(L) = (E(L) - E_{AB})/A_S$, where $E(L)$ is the total energy for a supercell of length L , E_{AB} is the energy of a AB bilayer graphene supercell having the same surface area $A_S = L^2 \sqrt{3}/2$, see Fig. 7.5(c). For small supercells the difference $E(L) - E_{AB}$ is proportional to the number of atoms i.e. to the surface of the system and the twist energy equals a constant $\gamma(L) = \gamma_A = 1.2$ meV/Å². On the other hand, for large cells with well-defined stacking domains only the soliton network contributes to $E(L) - E_{AB}$. As the width of the solitons asymptotically approaches the constant value W_S , the twist energy is given by $\gamma = 3\gamma_S L/A_S \propto 1/L$, where γ_S is the energy per soliton unit length and the factor 3 counts the number of solitons in the supercell. We estimate $\gamma_S = 42$ meV/Å. The cross-over length $L^* = \gamma_S/\gamma_A = 11.9$ nm (corresponding to $\theta^* = 1.2^\circ$) is defined as the intersection of the constant line and the curve $\propto 1/L$ fitting the two distinct regimes, as shown in Fig. 7.5(c). Finally, we can pose on a rigorous basis why the transition takes place for large supercells. Regardless the values of γ_S and γ_A , the quadratic “rigid” regime is favorable for $L < L^*$, whereas the linear “solitonic” regime is favorable for $L > L^*$. For this reason the transition is robust to an uncertainty on the effective interatomic potential.

7.1.3 Electronic structure

As known for several years, the low-energy states for TBG with large to intermediate twist angles $3^\circ \lesssim \theta \lesssim 15^\circ$ can be described by a model that treats perturbatively the coupling of the graphene layers [Lopes dos Santos *et al.*, 2007; Bistritzer and MacDonald, 2011; Koshino, 2013]. This model predicts the existence of low-energy massive Dirac fermions with θ -dependent Fermi velocity and a pair of Van Hove singularities slightly asymmetric with respect to the

7.1. Stacking domain boundaries in twisted bilayer graphene

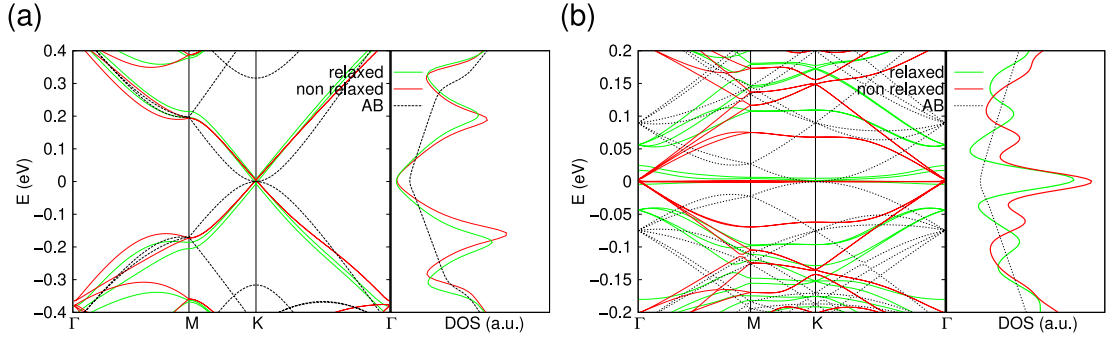


Figure 7.6 – Electronic band structure and density of states (DOS) for rigidly twisted and relaxed TBG. (a) Model with $\theta = 3.8^\circ$ ($L = 3.6$ nm, $w = 8$). (b) Model with $\theta = 1.2^\circ$ ($L = 12.1$ nm, $w = 28$). Band structure and DOS calculated for AB graphene are reported for comparison. The zero of the energy axes represents the Fermi energy.

Dirac point. These predictions have been experimentally confirmed [Li *et al.*, 2010; Luican *et al.*, 2011]. For smaller twist ($1^\circ < \theta < 3^\circ$), the TBG has been predicted to develop a flat band responsible for a zero-energy peak in the DOS [Trambly de Laissardière *et al.*, 2010; Uchida *et al.*, 2014]. This peak is due to states localized in AA regions as a result of the super-periodic potential induced by the Moiré pattern. However, these results cannot be extrapolated to lower θ , since we expect that the prominent structural relaxation sensibly affects the electronic structure.

We investigate the low-energy electronic properties of equilibrium structure of twisted bilayer graphene in the limit $\theta \rightarrow 0^\circ$ by means of a tight-binding model which takes into account $2p_z$ orbitals with hopping parameters depending on the orbital center distance as well as the relative orientation of the orbitals. The latter is achieved by means of Slater-Koster theory, see Section 7.1.5.d. This is particularly important in order to correctly describe the interactions in the soliton region where the relative position of atoms in opposite layers changes continuously. Since the relaxed structures do not show considerable corrugation, in-plane orbital interactions are prevalently of the $pp\pi$ type. For pairs of atoms in opposite layers that are stacked on top of each other, such as those appearing in AA stacking, the orbital interaction is purely of $pp\sigma$ character. However, when atoms are misaligned such as in SP or AB stacking, the interaction is a mixture of $pp\sigma$ and $pp\pi$, see Section 7.1.5.d.

In Fig. 7.6(a), the band structure for a model with $\theta = 3.8^\circ$ shows two degenerate Dirac cones projected on the K point of the supercell BZ, in contrast with the parabolic dispersion of AB graphene [Lopes dos Santos *et al.*, 2007; Shallcross *et al.*, 2008; Hass *et al.*, 2008]. A finite coupling between the states in the two Dirac cones is responsible for flat bands around the M point, whence the appearance of two low-energy van Hove singularities in the DOS [Lopes dos Santos *et al.*, 2007]. We find that the relaxation has negligible effects on the Dirac fermions, except lifting the degeneracy of low-energy bands. As the twist angle decreases, the positions of van Hove singularities become closer to the Dirac energy, eventually merging for $\theta \approx 2^\circ$. In this regime, the Fermi velocity is zero and the low-energy states are localized in AA-stacking

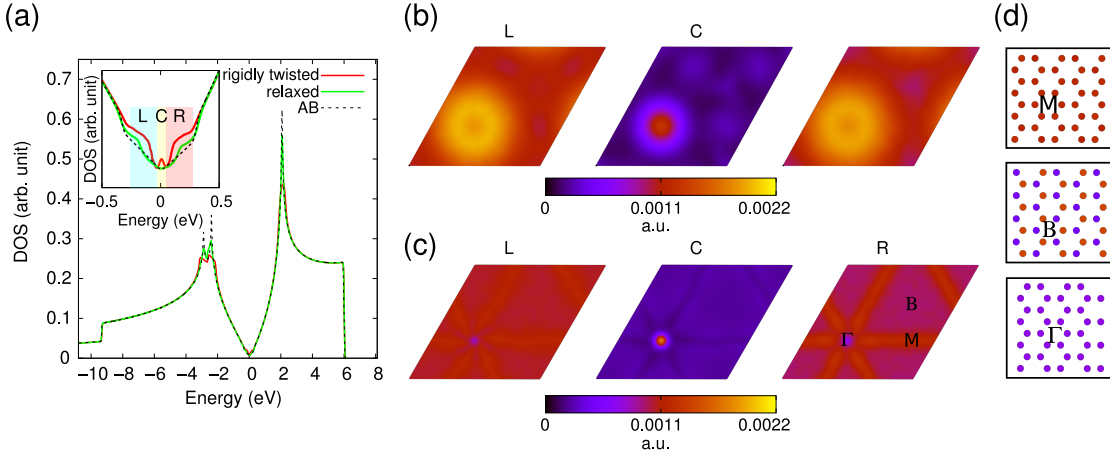


Figure 7.7 – (a) Density of states (DOS) as a function of energy measured from the Fermi energy ($E - E_f$) for twisted bilayer graphene with $\theta = 0.235^\circ$. The DOS for relaxed and rigidly twisted bilayer graphene are compared. As reference, the DOS of AB bilayer graphene ($\theta = 0^\circ$) is shown (dashed line). The inset presents the same data zooming in the interval $[-0.5, 0.5]$ eV. The regions L, C and R individuate, respectively, the energy intervals $[-0.25, -0.038]$ eV, $[-0.038, 0.043]$ eV and $[0.043, 0.26]$ eV. The zero of the energy axes represents the Fermi energy. (b-c) LDOS integrated in the energy intervals L, C, and R for rigidly twisted (b) and relaxed TBG (c). (d) LDOS within 1 nm^2 squares centered around M, B and Γ .

regions. By further reducing θ , the Fermi velocity starts oscillating and vanishes at “magic” angles $\theta_n \approx 1.05^\circ / n$, where n is an integer [Bistritzer and MacDonald, 2011]. However, the Dirac cone is restored only in a very small energy range $\approx 10 \text{ meV}$ [Trambly de Laissardière *et al.*, 2012]. As shown in Fig. 7.6(b), at the transition angle $\theta^* = 1.2^\circ$ the DOS for rigidly TBG shows a trio of low energy peaks ($E \approx -0.06, 0, 0.07 \text{ eV}$) corresponding to the flat low-energy bands observable in the band structure. We find that the relaxation is responsible for lifting the degeneracy of the central band and shifting the side peaks further from the Fermi energy, however, without altering the main electronic features.

Fig. 7.7(a) shows the DOS of a model with $\theta = 0.235^\circ$, that is, well below the transition angle θ^* . The DOS for rigidly TBG still shows a zero-energy peak with two satellite hills, though the reduced computational resolution make them appear quenched. The nature of low-energy states is revealed by the inspection of local density of states (LDOS) integrated in the energy regions around each of the three peaks, see Fig. 7.7(b). In all cases the charge density is localized around AA regions, in accordance with previous predictions, and extends on a fraction of surface $\eta \approx 5\%$ for the central peak and $\eta \approx 25\%$ for satellites, which we have verified to be largely independent of the Moiré periodicity L .

This scenario changes radically upon relaxation. The DOS of relaxed TBG is overall closer to AB bilayer graphene and, in particular, the central peak is suppressed below the computational resolution. Moreover, the nature of the low energy states is reminiscent of the hexagonal network of solitons arising from relaxation. The LDOS in the central energy region C shows a

higher degree of localization on the AA core (Fig. 7.7(c), central map). The absolute real space extension of these states is independent of L , being determined exclusively by the radius of the AA core that converges to a fraction of nm in the limit $L \rightarrow \infty$. The effect of structural relaxation is even more dramatic in the side energy ranges (Fig. 7.7(c), maps L and R) that show a radically different charge density distribution with respect to rigidly TBG. Indeed, charge density is partially depleted on AA cores and AB/BA domains show an overall homogeneous distribution, whereas solitons exhibit a slightly larger charge density. A closer inspection at the center of an AB domain (point B in Fig. 7.7(d)) shows an alternation of bright and dark atoms which is a consequence of broken sublattice symmetry. This is typical of AB-stacked graphene layers as demonstrated by STM images of HOPG [Pong and Durkan, 2005]. The charge at the center of the solitons and at the vertices of the network does not show oscillation on the atomic scale. This is consistent with the sublattice symmetry of the local stacking that in the center of the soliton and in the vertices is, respectively, SP and AA. (Fig. 7.7(d), points M and Γ). This holds true in the whole inspected range of energy $[-0.25, 0.26]$ eV, as it is due to the presence/absence of sublattice symmetry.

7.1.4 Conclusions

We have investigated the equilibrium low-energy structure of twisted bilayer graphene in the limit of vanishing twist angle ($\theta \gtrsim 0.2^\circ$) by means of simulations based on a classical potential capable to describe the dependence of graphene layers' binding energy on the layers' relative position. In-plane atomic rearrangement acts to maximize the extension of energetically favorable AB/BA stacking domains that assume a triangular shape. In-plane strain field is confined in a hexagonal network of shear solitons with a characteristic width $W_S \simeq 9.5$ nm constituting a framework for alternating AB and BA stacking domains. This structural transition takes place for $\theta < \theta^* = 1.2^\circ$ when developing such a hexagonal network becomes energetically favorable for TBG. In the limit $\theta \rightarrow 0^\circ$, the equilibrium geometry of TBG does converge though not uniformly to that of $\theta = 0^\circ$ in the sense that the relative abundance of AB-stacking surface approaches 1, but the soliton network never disappears due to its topological nature. The transition has major consequences on the low-energy charge distribution in the Moiré superlattice. Differently from the range $1.2^\circ < \theta < 2^\circ$ where the DOS of TBG hosts three low-energy peaks due to flat bands of states localized on AA regions, relaxed structures of TBG with $\theta < 1.2^\circ$ show a DOS increasingly closer to that of AB bilayer graphene with a low-energy charge density which can be directly inferred from the local stacking. In AB/BA domains the charge density approaches that of AB bilayer graphene, that is, overall uniform but with a strong unbalance between the two inequivalent sublattices in each layer. The solitons and the network vertices show no atomic fluctuation of the charge as the sublattice symmetry is re-established. Analogously to the stacking, the relative extent of the regions where the charge density differs from AB bilayer graphene asymptotically vanishes for $\theta \rightarrow 0^\circ$. STM/STS experiments are awaited to confirm our predictions.

7.1.5 Methodological details and additional calculations

7.1.5.a DFT study of interlayer interaction in bilayer graphene

All our DFT calculations are based on the non-local rVV10 functional [Vydrov and Voorhis, 2010; Sabatini *et al.*, 2013] implemented in QUANTUM ESPRESSO [Giannozzi *et al.*, 2009] to account for van der Waals interactions. We have employed a pseudopotential generated with revised pw86 functional [Murray *et al.*, 2009]. In fact, at the time the present work started this was the available pseudopotential based on the closest functional to rVV10. However, non-local contribution are expected to not alter significantly the effective potential generated by ions and core electrons. As already found for graphite by the authors of the rVV10 functional, relatively high values of wavefunction and charge-density cutoff are required to accurately describe sp^2 -carbon systems. We have used $E_{\text{wf}} = 80 \text{ Ry}$ and $E_{\rho} = 574 \text{ Ry}$ together with a $16 \times 16 \times 1$ Monkhorst-Pack kpoint grid to obtain converged structural quantities. Periodic replicas of the system are separated by 24 \AA of vacuum to guarantee negligible interaction. The interlayer binding energy E_b is calculated from the total energy E_{tot} , the energy of two isolated layers E_{mono} , and the number of atoms in the unit cell N_c as follows

$$E_b = -\frac{1}{N_c} (E_{\text{tot}} - 2E_{\text{mono}}) \quad (7.1)$$

As reported in Ref. [Sabatini *et al.*, 2013] and confirmed by our calculations, the atomic bond length of graphite is 1.42 \AA and the interlayer distance $\Delta z_{\text{graph}} = 3.36 \text{ \AA}$ in accordance with established value [Bacon, 1951]. Table 7.1 reports the interlayer distance and binding energy for bilayer graphene calculated at fixed bond length $a = 1.42 \text{ \AA}$.

Table 7.1 – Structural quantities calculated within DFT/rVV10 for graphite and bilayer graphene.

	Graphite [Sabatini <i>et al.</i> , 2013]	Bilayer graphene - AB	Bilayer graphene - AA
$\Delta z (\text{\AA})$	3.36	3.41	3.59
$E_b (\text{meV/atom})$	39	30.2	25.7

Interestingly, we have found for AB bilayer graphene an interlayer distance $\Delta z_{\text{AB}} = 3.412 \text{ \AA}$, about 1.5% larger than for graphite. For AA stacking the equilibrium distance is $\Delta z_{\text{AA}} = 3.588 \text{ \AA}$. The dependences of E_b on Δz and on the interlayer shift ΔX are shown in Fig. 7.8(a,b).

7.1.5.b Determination of the classical carbon-carbon potential

The classical pair potential for carbon atoms that we employed in structural relaxations consists in the sum of a short-range contribution V_{SR} and a long-range contribution V_{LR} describing, respectively, covalent bonds and van der Waals interactions between sp^2 -hybridized carbon atoms. V_{SR} is the short-range term of the LCBOP potential defined in Ref. [Los and Fasolino, 2003] imported with no modifications, see Section 4.3.

7.1. Stacking domain boundaries in twisted bilayer graphene

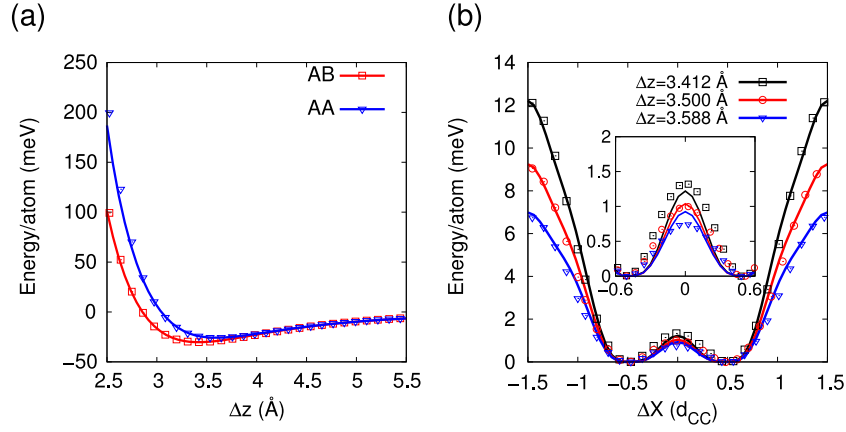


Figure 7.8 – (a) Interlayer binding energy E_b as a function of interlayer distance Δz for AA and AB-stacked bilayer graphene. (b) Binding energy as a function of interlayer shift, ΔX , defined in Fig. 7.2(a). The zero of the energy axis is set at $E_b(\Delta X = \pm 0.5 d_{CC})$ corresponding to AB/BA stacking. Dots correspond to DFT estimates, whereas continuous lines correspond to classical potential estimates.

The long-range term V_{LR} is a reparametrized version of the registry-dependent potential proposed in Ref. [Kolmogorov and Crespi, 2005]. For a pair of atoms at positions \mathbf{r}_i and \mathbf{r}_j , with \mathbf{n}_i (\mathbf{n}_j) being the normal vector to the sp^2 hybridization plane at the position \mathbf{r}_i (\mathbf{r}_j), V_{LR} is defined as

$$\begin{aligned}
 V_{LR}(\mathbf{r}_{ij}, \mathbf{n}_i, \mathbf{n}_j) &= e^{-\lambda(r_{ij}-z_0)} (C + f(\rho_{ij}) + f(\rho_{ji})) - A \left(\frac{r_{ij}}{z_0} \right)^{-6}, \\
 \rho_{ij} &= \left(r_{ij}^2 - (\mathbf{n}_i \cdot \mathbf{r}_{ij}) \right)^{1/2}, \quad \rho_{ji} = \left(r_{ij}^2 - (\mathbf{n}_j \cdot \mathbf{r}_{ij}) \right)^{1/2}, \\
 f(\rho) &= e^{-(\rho/\delta)^2} \sum C_{2n} (\rho/\delta)^{2n} \quad n = 0, 1, 2, \\
 \mathbf{r}_{ij} &= \mathbf{r}_i - \mathbf{r}_j.
 \end{aligned} \tag{7.2}$$

We make the approximation that normal vectors \mathbf{n} are directed along the z axis. Consequently we can simplify $\rho_{ij} = \rho_{ji} = \left((r_{ij}^x)^2 + (r_{ij}^y)^2 \right)^{1/2}$. This assumption is justified by the inspection of the corrugation of the relaxed structures where normal vectors form an angle $\alpha < 0.2^\circ$ with the z axis. Although the original paper of Kolmogorov and Crespi provides a set of parameters for the potential, we have reparametrized it by fitting eq. 7.2 to three data sets calculated within DFT+vdW. The first two datasets are the binding energy E_b as a function of the interlayer distance Δz for AB and AA-stacked bilayer graphene (see dot data series in Fig. 7.8 and the third dataset is E_b as a function of the interlayer shift ΔX (see Fig. 7.2(b) for definition) at fixed interlayer distance $\Delta z = (\Delta z_{AA}^{DFT} + \Delta z_{AB}^{DFT})/2 = 3.50 \text{ \AA}$ (red dots in Fig. 7.8(b)). The fit has been performed employing the non linear optimizer DAKOTA [Adams *et al.*, 2009]. Table 7.2 compares the parameters reported in the original reference and those resulting from our fit.

Fig. 7.8 shows a remarkable accordance between observables calculated within DFT (dotted

Table 7.2 – Parameters for Kolmogorov-Crespi potential.

	C (meV)	C_0 (meV)	C_2 (meV)	C_4 (meV)	z_0 (Å)	δ (Å)	λ (Å ⁻¹)	A (Å)
Ref. [Kolmogorov and Crespi, 2005]	3.030	15.71	12.29	4.933	3.34	0.578	0.578	10.238
This work	7.183	9.806	5.365	4.266	3.516	0.590	3.039	13.17

data series) and KC potential (continuous curves). In particular, the equilibrium distances calculated by means of the reparametrized KC potential are $\Delta z_{AA}^{KC} = 3.599 \text{ \AA}$ and $\Delta z_{AB}^{KC} = 3.416 \text{ \AA}$, and the binding energies for AA and SP stacking calculated at $\Delta z = 3.412 \text{ \AA}$ taking AB energy as reference are, respectively, $E_b^{AA} = 12.2 \text{ meV/atom}$ and $E_b^{SP} = 1.22 \text{ meV/atom}$. Finally, the in-plane bond-length is 1.419 \AA .

7.1.5.c Structural relaxations

The full potential $V = V_{SR} + V_{LR}$ has been implemented in LAMMPS [Plimpton, 1995; LAMMPS]. TBG structures have been initially relaxed by means of conjugate gradient *plus* quadratic line search method and fine minimization was obtained using fast inertia relaxation method, see Section 4.2. The supercell vectors have been kept fixed. At the end of the relaxation the highest force component acting on any atom was weaker than 3 meV/\AA . In Fig. 7.9, the full maps of the interlayer distance and in-plane displacement are shown. With respect to Fig. 7.3(c-d), the full maps allow to appreciate the whole set of symmetries. Δz is almost constantly equal to $\Delta z_{SP}^{KC} = 3.439 \text{ \AA}$ along the soliton axes and to $\Delta z_{AB}^{KC} = 3.416 \text{ \AA}$ in AB/BA domains.

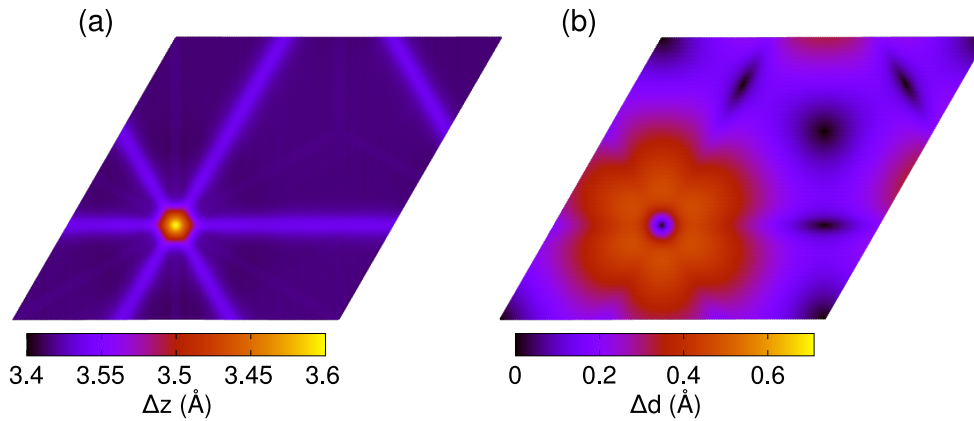


Figure 7.9 – Maps of (a) interlayer distance Δz and (b) modulus of the atomic displacement Δd upon relaxation of TBG with $\theta = 0.235^\circ$ corresponding to $L = 59.8 \text{ nm}$. The upper bound for the displacement modulus is $d_{CC}/2 = 0.71 \text{ \AA}$, as explained in Section 7.1.2.

7.1.5.d Electronic structure calculations

In this section we present details of the electronic structure calculations. The tight-binding model Hamiltonian for bilayer graphene is taken from Ref. [Trambly de Laissardière *et al.*, 2010] (see also Ref. [Trambly de Laissardière *et al.*, 2012] for thorough electronic structure calculations of rigidly twisted bilayer graphene). In this model only p_z -orbitals for carbon atoms are considered:

$$H = \sum_{i \neq j} V a_i^\dagger a_j, \quad (7.3)$$

where the operator $a_i^\dagger(a_i)$ creates (annihilates) an electron in a p_z -orbital of the atom at position \mathbf{R}_i . The off-diagonal matrix elements V are obtained by combining σ and π -type Slater-Koster parameters $V_{pp\sigma}$ and $V_{pp\pi}$ in the approximation that the axes of p_z -orbitals are parallel, akin to the assumption that the normal vectors of the two graphene layers are parallel as well:

$$V = V_{pp\pi} \sin^2(\theta) + V_{pp\sigma} \cos^2(\theta), \quad (7.4)$$

where θ is the angle between the orbital axes and the vector $\mathbf{R}_{ij} = \mathbf{R}_i - \mathbf{R}_j$ that connects the two orbital centers [Slater and Koster, 1954]. For a pair of atoms in the same layer $\theta \simeq 90^\circ$ and $V_{pp\pi}$ dominates. $V_{pp\pi}$ and $V_{pp\sigma}$ depend exponentially on the distance between the two orbital centers r

$$V_{pp\pi}(r) = V_{pp\pi}^0 e^{q_\pi(1-r/a_\pi)}, \quad V_{pp\sigma}(r) = V_{pp\sigma}^0 e^{q_\sigma(1-r/a_\sigma)}. \quad (7.5)$$

Following Ref. [Trambly de Laissardière *et al.*, 2010] we take $V_{pp\pi}^0 = -2.7$ eV, $V_{pp\sigma}^0 = 0.48$ eV, $a_\pi = 1.419$ Å, $q_\pi = 3.1454$. However, in order to be consistent with the interlayer distance for AB stacking calculated in the present work, we take $a_\sigma = 3.417$ Å and $q_\sigma = 8.200$. The long distance cut-offs for $V_{pp\sigma}(r)$ and $V_{pp\pi}(r)$ are fixed, respectively, at $\bar{r}_\sigma = 3.5$ Å and $\bar{r}_\pi = 5$ Å. We have verified that further increasing the cut-offs does not affect sensibly the calculated observables. In all our calculations the neutrality point is located at $E_f = 0.82$ eV.

Density of states is calculated as follows

$$\text{DOS}(E) = \int_{\text{BZ}} d\mathbf{k} \sum_{n_{\mathbf{k}}} \delta(E - E_{n_{\mathbf{k}}}), \quad (7.6)$$

with $n_{\mathbf{k}}$ running over all the eigenvalues at position \mathbf{k} in reciprocal space. For computational needs the δ -function appearing in eq. 7.6 is replaced by a Lorentzian function:

$$\delta(E - E_{n_{\mathbf{k}}}) \rightarrow \frac{1}{\pi} \frac{\eta}{(E - E_{n_{\mathbf{k}}})^2 + \eta^2}, \quad \eta \rightarrow 0^+. \quad (7.7)$$

The local density of states on the i -th atom at position \mathbf{R}_i , integrated in the energy range

$[E_1, E_2]$, is calculated as follows

$$\text{LDOS}(i; E_1, E_2) = \int_{E_1}^{E_2} dE \int_{\text{BZ}} d\mathbf{k} \sum_{n_{\mathbf{k}}} \delta(E - E_{n_{\mathbf{k}}}) |\langle i | n_{\mathbf{k}} \rangle|^2 = \int_{\text{BZ}} d\mathbf{k} \sum_{E_1 < E_{n_{\mathbf{k}}} < E_2} |\langle i | n_{\mathbf{k}} \rangle|^2, \quad (7.8)$$

where $|i\rangle$ represents the p_z orbital of the i -th atom. Spin is not explicitly considered in our calculations.

Integrations over the Brillouin zone are performed introducing a discrete grid. The band structure shown in panels (a) and (b) of Fig. 7.6 has been calculated with a Monkhorst-Pack grid of 25×25 and 5×5 k-points, respectively. The density of states of the largest model shown in Fig. 7.7 has been calculated using the high-symmetry points Γ and M of the hexagonal B.Z., taking advantage of the fact that the Hamiltonian represented in reciprocal space $H(\mathbf{k} = \text{M}, \Gamma)$ is a real matrix.

Matrix diagonalizations are performed employing the Eigenvalue Solvers for Petaflop Applications library (ELPA) [Marek *et al.*, 2014]. This allowed us to diagonalize a $N \times N$ real matrix with $N = 236884$ in about 2.5 hours using 1024 cores.

7.2 Electromechanical Oscillations in Bilayer Graphene

The work presented in this section has been done in collaboration with the group of Prof. Andras Kis, Electrical Engineering Institute, Ecole Polytechnique Fédérale de Lausanne (EPFL), and has been published in Nature Communications 6, 8582 (2015)

In this section, we report an experimental study of the interplay between mechanical and electrical properties of mono- and bilayer graphene, and propose a simple theoretical model to explain the resistance oscillations measured in bilayer graphene devices subjected to the action of the tip of an Atomic Force Microscope (AFM).

The systems investigated in the present study go under the more general class of devices that integrate electrical and mechanical functionalities, called nanoelectromechanical systems (NEMS). The realization of NEMS based on suspended graphene has been already exploited to fabricate nanoresonators [Bunch *et al.*, 2007]. However, to the best of our knowledge, bilayer graphene has not been integrated into NEMS yet. In this study, mono- and bilayer graphene nanoribbons (GNR) have been integrated into a NEMS to investigate the effect of strain on their electronic transport properties. As illustrated in Fig. 7.10, the NEMS devices consisted of field-effect transistors based on suspended mono- and bilayer graphene nanoribbons with widths between 60 nm and 300 nm subjected to the action of an AFM tip. The latter served for both high-resolution imaging and controlled deformation of the GNRs. Electrical conductance of the suspended GNR was measured simultaneously with mechanical deformation of the ribbon. After the GNR was positioned and imaged, the insulating AFM tip was located on top of it. The deformation and successive relaxation of the GNR was induced by moving the stage

7.2. Electromechanical Oscillations in Bilayer Graphene

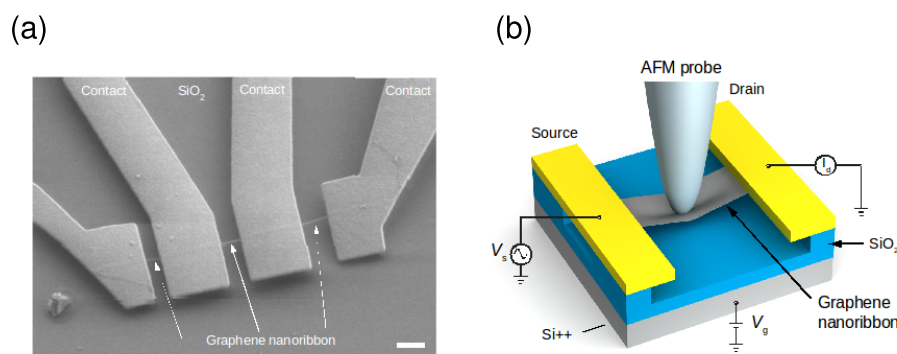


Figure 7.10 – Experiment setup. (a) Scanning electron microscope (SEM) image of a typical device. A graphene nanoribbon is suspended above the SiO_2 substrate and contacted by electrodes. The scale bar is $0.5 \mu\text{m}$. (b) Sketch of the NEMS. Reprinted with permission from Ref. [Benameur *et al.*, 2015], © 2015 Mcmillan Ltd.

upwards against the cantilever of the AFM and downwards far from it. During the deformation cycle, the current I_S and the cantilever deflection $D_{\text{cantilever}}$ as a function of the position of the stage, Z_{piezo} were simultaneously measured. During the experiment, the current flow was assured by an AC bias of 4 meV with a frequency of 8 kHz, while the back-gate voltage was connected to the ground, namely, $V_g = 0 \text{ V}$. Fig. 7.11(a) shows the electromechanical response of a monolayer GNR. It was checked that the electrical and mechanical responses were reproducible for both the extension and the retraction cycles. This proves that: i) GNRs are deformed in the elastic regime, ii) no structural defects are introduced in the GNRs, and iii) the GNRs are tightly anchored to the metallic pads (no slipping).

Let us now focus on the behavior of the current upon mechanical deformation of monolayer graphene. The width of the investigated devices varied in the range [60, 300] nm with resistances in the range [10, 100] k Ω . During the approach cycle and before mechanically contacting the GNRs, the current was constant. The current underwent variations only once the GNR was deformed, thus ensuring that the observed current variations were of electromechanical origin. A linear decrease of the current was observed in samples under strain, and was quantified by the gauge factor $GF = \Delta R/R_0/\epsilon$, where ϵ is the strain. The samples exhibited a positive gauge factor, with the highest value being 3.2. Such strain-induced increase of the resistance agrees with previous reports and is due to the decrease of the Fermi velocity under strain (piezoresistivity) [Smith *et al.*, 2013]. Finally, no opening of a bandgap was observed in the deformation regime.

Let us now turn to bilayer graphene devices. The electromechanical measurements were performed on two nanoribbons with widths of 200 nm and 300 nm, and resistances of 50 k Ω and 40 k Ω , respectively. Similarly to the samples of monolayer graphene, the mechanical response of bilayer devices is reversible, reflecting the mechanical stability of the suspended bilayer GNRs. Fig. 7.11(b-c) shows that the electromechanical response of bilayer GNRs

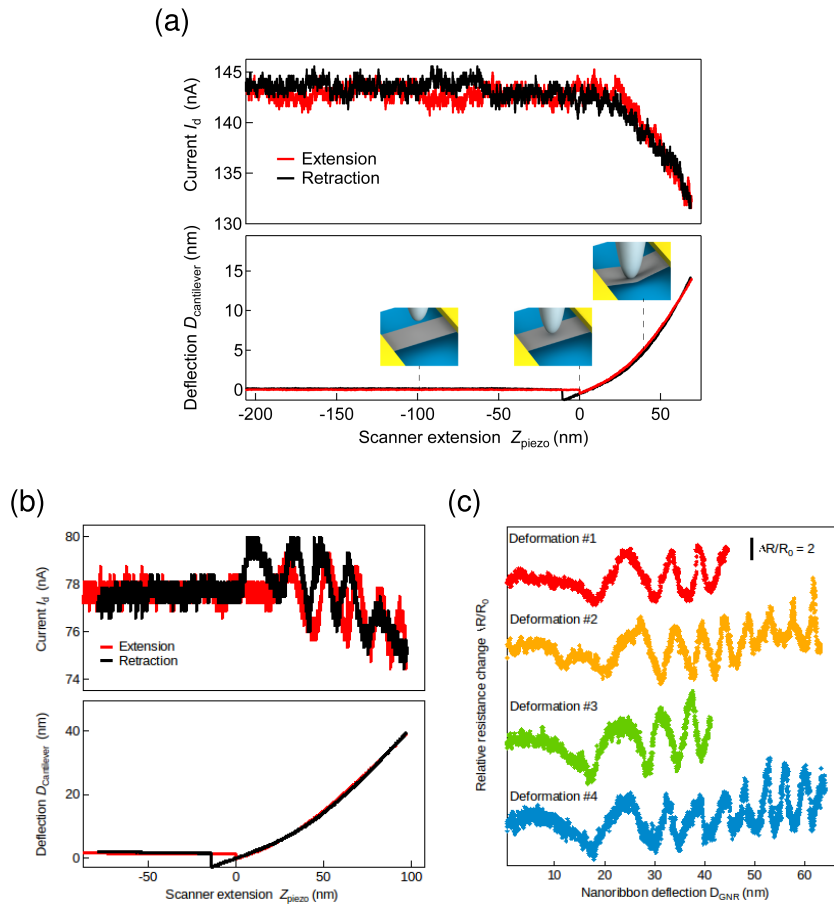


Figure 7.11 – Electromechanical response of monolayer and bilayer graphene. (a) Results of the simultaneous measurements of the current (upper panel) and the cantilever’s deflection (lower panel) as a function of the vertical coordinate of the stage z_{piezo} for a monolayer graphene sample. (b) Analogous results for a bilayer graphene sample. Reprinted with permission from Ref. [Benameur *et al.*, 2015], © 2015 Mcmillan Ltd.

exhibits two main features: i) As in monolayer GNRs, a global linear increase in the resistance is observed. ii) this linear response is convoluted with pronounced oscillations that have the same qualitative behavior in the extension and in the retraction cycles. The amplitude of the oscillations is about 4%. The current before and after deformation remains unchanged, thus confirming that the device has not deteriorated during deformation and proving the electromechanical origin of the observed oscillations. The overall linear increase of resistance can be explained as a piezoresistivity effect, analogously to the case of monolayer devices.

Clearly, interlayer interactions are at the origin of the observed electromechanical oscillations. We propose a simple theoretical model capable of quantitatively reproducing the oscillatory behavior of resistance. Our model assumes that the AFM tip pressure causes finite relative lateral displacement (sliding) of the individual graphene layers. This lateral displacement is expected due to the weak van der Waals force between the two graphene layers [Gong *et al.*,

2013; Brown *et al.*, 2012]. As mentioned in the previous section, there is extensive evidence in the literature that lateral displacement of graphene layers with respect to each other takes place in various types of scanning probe microscopies. In the present experiment, the AFM tip deforms the bilayer GNRs, which leads to an increase in the elastic energy of the system. Therefore, the necessity to lower the energy of the system results in the relative displacement of the layers. The lateral displacement, however, alters the AB-stacking of the two layers which is the energetically preferred configuration of bilayer graphene. As predicted by the Frenkel-Kontorova model, the system then reduces the interlayer binding energy through formation of a “domain wall” transition region separating two AB-stacked domains [Popov *et al.*, 2011]. As mentioned in Sections 3.3.4 and 7.1.1, such boundaries occurring between AB- and BA-stacked regions have recently been observed in multilayer graphene by a number of studies. We assume that the transition region in our system has the shape of a bulge, see Fig. 7.12(a). The width of these transition regions, typically few nanometers according to experimental observations [Alden *et al.*, 2013], is defined by the balance between the total strain energy and the interlayer binding energy [Popov *et al.*, 2011]. The displacement of stacking domain boundaries as well as manipulations and creation of wrinkles in scanning tunneling microscopy (STM) has been also demonstrated [Xu *et al.*, 2009; Yankowitz *et al.*, 2014; Lalmi *et al.*, 2014]. Displacement and removal of wrinkles with an AFM tip was also shown experimentally [Camara *et al.*, 2009]. We note, however, that the effective width of the transition region within the two individual graphene layers is different. Moreover, this effective width difference ΔW will vary as the two graphene layers slide against each other due to the action of the AFM tip. If no transition region was initially present in the sample, ΔW corresponds to the lateral displacement of one graphene layer with respect to another upon indentation. In the transition region, the layers are electronically decoupled either due to their incommensurate stacking for small values of ΔW , or due to enlarged interlayer distance for larger ΔW . We suggest that the observed electromechanical oscillations can be explained from the point of view of quantum interference phenomena due to path difference ΔW of the charge carriers in the decoupled graphene layers. Increasing the strain leads to higher amount of local corrugation and changes ΔW , thus causing constructive or destructive interference.

In order to verify this hypothesis, we perform numerical simulations of electronic transport in a model bilayer graphene device. Our simulations are performed in the assumption of coherent regime because of the few nanometers width of the transition region. The methodology is based on a tight-binding Hamiltonian and Landauer-Büttiker approach, see Section 4.5.1. The Hamiltonian only takes into account the hopping term $t = 2.7$ eV that couples p_z orbitals of first-neighbor atoms within the same layer, and the hopping term $\gamma_1 = 0.15 t$ that couples atoms in opposite layers forming a dimer, see Section 1.5. Without loss of generality, the individual graphene layers are assumed to be fully decoupled ($\gamma_1 = 0$) in the transition region. Our model device is a bilayer graphene with the zigzag direction aligned to the transport direction and is periodic in the perpendicular (armchair) direction [Gong *et al.*, 2013]. We investigated armchair direction of domain boundaries as this orientation was found to be dominant for the case of closely related AB-BA stacking domain boundaries extensively inves-

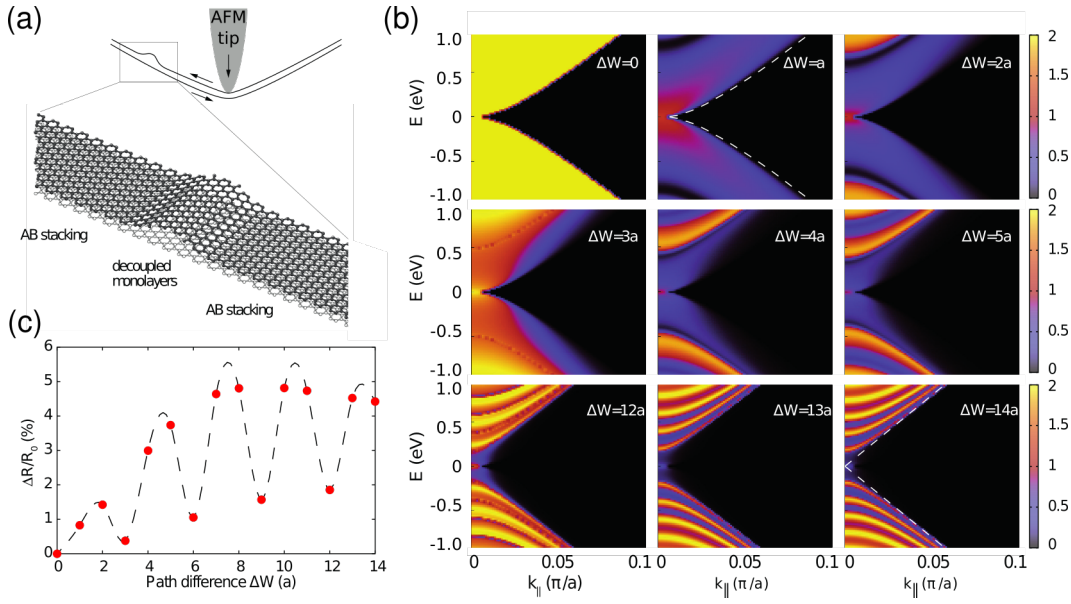


Figure 7.12 – Theoretical calculations of electronic transport properties. (a) Schematic illustration of the reciprocal lateral shift of the graphene layers as a result of the action of the AFM tip. AB-stacked graphene regions are separated by a transition region with different effective width, where individual layers are decoupled either due to the enlarged interlayer distance or due to their incommensurate stacking [Lopes dos Santos *et al.*, 2007]. (b) Transmission probability across a region of decoupled layers as a function of energy E and transverse momentum k_{\parallel} . The maps of the different panels are calculated for different value of the charge-carrier path differences ΔW expressed in lattice units a . The dashed lines in the second and last panel correspond, respectively, to the contour of the quadratic bands of bilayer graphene and linear bands of monolayer graphene. (c) Relative variation of the electrical resistance $\Delta R/R_0$ calculated for a 50 nm wide bilayer GNR subjected to a bias voltage $V_{\text{bias}} = 4$ mV for different charge-carrier path differences, ΔW , expressed in lattice units a . The line is a guide to the eye. Adapted with permission from Ref. [Benameur *et al.*, 2015], © 2015 Mcmillan Ltd.

tigated using transmission electron microscopy. We assume that the sample is large enough that edge effects do not affect significantly transport properties. Furthermore, considering the in-plane isotropic elasticity of graphene, the crystallographic orientation of the transport channel does not affect the electromechanical behavior. Fig. 7.12(b) shows the calculated charge-carrier transmission probabilities as a function of energy E and momentum parallel to the transition region, k_{\parallel} , for various carrier path differences $\Delta W = na$, with $a = 0.246$ nm the lattice constant of graphene and n an integer number. The trivial case of $\Delta W = 0$ (no transition region, i.e. pristine bilayer graphene) reveals the massive character of Dirac fermions in bilayer graphene. Finite path differences ΔW result in significant amount of backscattering developing a clear sub-band sequence resulting from the quantum confinement of massless Dirac fermions in the transition region. Most importantly, configurations characterized by $\Delta W = 3ma$ ($m \in \mathbb{N}$) show enhanced transmission due to constructive interference as the wavenumber of Dirac fermions in graphene $k = 4\pi/3a$. Therefore, one period of oscillations

corresponds to a deformation-induced lateral displacement of $3a = 0.74$ nm.

To gain further insight, we compare the calculated resistance with the experimental observation. A quantitative comparison requires accounting for the role of contacts as well as for the diffusive transport in the rest of device. Both factors, below collected in a single value R_c , act as a “bottleneck” in a realistic device and are responsible for most of its total resistance. We obtained $R_c = 41$ k Ω by fitting both the average value of the calculated resistance and the relative magnitude of the oscillations to the experimental data. In Fig. 7.12(c), oscillations of resistance can be seen clearly with a constant period of $3a$. The amplitude of the calculated oscillations is of the order of 5% in agreement with experiments, except for the fact that calculated resistance for $\Delta W = 0$ corresponds to a minimum of resistance (no backscattering), whereas in experiments the resistance minimum occurs at some finite deformation, see Fig. 7.11(c). This implies that the stacking domain boundary was already present before indentation. In other words, the origin in experimental resistance curves corresponds to a finite value of ΔW in Fig. 7.12(c).

In summary, the electromechanical response of mono- and bilayer graphene nanoribbons has been investigated. Both systems show an overall increase of resistance under strain as a consequence of an effective reduction of the Fermi velocity. In addition, bilayer graphene shows oscillations in resistance superposed on the linear response. These oscillations are explained in the framework of a theoretical model as an interference phenomenon taking place between the two layers.

Outlook

Eleven years after the discovery of graphene, the Physics of two-dimensional materials is one of the “hottest” topics in Condensed Matter Physics, and there is widespread recognition that such materials will represent the basis of many future technologies. However, regarding the research in the fundamental Physics of graphene, it is likely that the main discoveries have been already accomplished and future research will focus increasingly on the applications of graphene in order to harvest the fruits of all the hard work of the first decade of the “2D era”. Possible outlook of the research reported in this thesis should be discussed keeping in mind this perspective. I remind that the main aim of our work has been to address the role of both topological and local disorder on the electronic transport properties of monolayer and bilayer graphene.

Our studies have revealed important topological aspects of the transmission of charge carriers across periodic grain boundaries in monolayer graphene, which are largely retained by disordered grain boundaries. As soon as atomically-resolved imaging of grain boundaries of real graphene samples will be available together with electronic transport measurements, our predictions might receive important confirmations. For an accurate comparison, it will be important to go beyond the tight-binding description of electrons in order to account for electron-electron interaction, which we expect to be sizable due to the charge accumulation in the vicinity of the GBs (self-doping), already reported in experiments. Electron correlation can be included at mean-field level (Hubbard model, Density Functional Theory). Also, the constant progress in the realization of electronic circuits based on graphene might, eventually, unveil the valley-filtering capabilities of grain boundaries.

Moreover, we have investigated the electric conductance of graphene in presence of realistic aggregates of hydrogen adatoms, focusing on Anderson localization aspects that in two-dimensional systems are particularly important. The crucial technique that we used to study Anderson localization, a scaling analysis of the Landauer-Büttiker conductance, can be applied to other classes of defects with the aim of exploring other categories of Anderson-localization universality classes. These include different adsorbates (carbon, alkali metals, transition metals), substitutional impurities, multiple grain boundaries, etc. Despite an incredibly intense study of the electronic transport in graphene, a conclusive experimental characterization of Anderson localization is still lacking. Especially in early experiments, the isolation of samples with a single type of defects was particularly challenging. Nowadays, however, the increasing

availability of ultra-pure graphene samples where defects can be introduced in a controlled manner is creating the ideal playground for studying Anderson localization, and I expect a renovated interest in the investigation of such an elusive phenomenon. The analytic Green's function approach employed to predict the resonant or non-resonant nature of clusters of hydrogen adatoms on graphene can also be extended to other classes of point defects, e.g. substitutional impurities.

Our study of topological defects in bilayer graphene, namely, stacking domain boundaries arising from a twist between the graphene layers and manifesting as shear solitons, relies on a classical potential that we have optimized to describe both covalent bonding and interlayer van der Waals interaction. In the short term, the availability of this potential will allow us to study other type of stacking domain boundaries (tensile solitons) as well as other kinds of topological disorder such as ripples and wrinkles in both mono- and bilayer graphene. The next natural step will be to investigate electronic transport properties across topological defects of bilayer graphene, especially ripples, which are considered the fundamental defects setting the intrinsic mobility of graphene. Finally, another intriguing perspective would be to develop an interatomic classical potential to describe the interaction of carbon atoms with atoms of the neighbor species in the periodic table, boron and nitrogen, in order to study the realistic equilibrium structures of the increasingly popular heterostructures of graphene and two-dimensional boron nitride. One example is represented by the Moiré pattern occurring in graphene deposited on or encapsulated within hexagonal boron nitride layers as a result of the lattice constant mismatch.

Bibliography

- Abrahams, E., Anderson, P. W., Licciardello, D. C., and Ramakrishnan, T. V. *Scaling Theory of Localization: Absence of Quantum Diffusion in Two Dimensions*. Physical Review Letters **42**, 673 (1979).
- Adam, S., Cho, S., Fuhrer, M. S., and Das Sarma, S. *Density inhomogeneity driven percolation metal-insulator transition and dimensional crossover in graphene nanoribbons*. Physical Review Letters **101**, 046404 (2008).
- Adam, S., Hwang, E. H., Galitski, V. M., and Sarma, S. D. *A self-consistent theory for graphene transport*. Proceedings of the National Academy of Sciences **104**, 18392 (2007).
- Adams, B., Bauman, L., Bohnhoff, W., Dalbey, K., Ebeida, M., Eddy, J., Eldred, M., Hough, P., Hu, K., Jakeman, J., Swiler, L.P., and Vigil, D. *DAKOTA, A Multilevel Parallel Object-Oriented Framework for Design Optimization, Parameter Estimation, Uncertainty Quantification, and Sensitivity Analysis: Version 5.4 User's Manual*. Sandia National Laboratories (2009).
- Akhmerov, A. R. and Beenakker, C. W. J. *Detection of Valley Polarization in Graphene by a Superconducting Contact*. Physical Review Letters **98**, 157003 (2007).
- Alden, J. S., Tsen, A. W., Huang, P. Y., Hovden, R., Brown, L., Park, J., Muller, D. A., and McEuen, P. L. *Strain solitons and topological defects in bilayer graphene*. Proceedings of the National Academy of Sciences **110**, 11256 (2013).
- Amelinckx, S. and Delavignette, P. *Dislocation Loops Due to Quenched-in Point Defects in Graphite*. Physical Review Letters **5**, 50 (1960).
- Anderson, P. W. *Absence of Diffusion in Certain Random Lattices*. Physical Review **109**, 1492 (1958).
- Ando, T., Nakanishi, T., and Saito, R. *Berry's Phase and Absence of Back Scattering in Carbon Nanotubes*. Journal of the Physical Society of Japan **67**, 2857 (1998).
- Autès, G. *Transport électronique polarisé en spin dans les contacts atomiques de fer*. Ph.D. thesis Université Pierre et Marie Curie - Paris VI (2008).
- Avouris, P. and Dimitrakopoulos, C. *Graphene: synthesis and applications*. Materials Today **15**, 86 (2012).

Bibliography

- Bacon, G. E. *The interlayer spacing of graphite*. Acta Crystallographica **4**, 558 (1951).
- Balog, R., Jørgensen, B., Nilsson, L., Andersen, M., Rienks, E., Bianchi, M., Fanetti, M., Lægsgaard, E., Baraldi, A., Lizzit, S., Sljivancanin, Z., Besenbacher, F., Hammer, B., Pedersen, T. G., Hofmann, P., and Hornekær, L. *Bandgap opening in graphene induced by patterned hydrogen adsorption*. Nature Materials **9**, 315 (2010).
- Banhart, F. *Irradiation effects in carbon nanostructures*. Reports on Progress in Physics **62**, 1181 (1999).
- Banhart, F., Kotakoski, J., and Krasheninnikov, A. V. *Structural Defects in Graphene*. ACS Nano **5**, 26 (2011).
- Bardarson, J. H., Tworzydło, J., Brouwer, P. W., and Beenakker, C. W. J. *One-Parameter Scaling at the Dirac Point in Graphene*. Physical Review Letters **99**, 106801 (2007).
- Basko, D. M. *Resonant low-energy electron scattering on short-range impurities in graphene*. Physical Review B **78**, 115432 (2008).
- Beechem, T. E., Ohta, T., Diaconescu, B., and Robinson, J. T. *Rotational Disorder in Twisted Bilayer Graphene*. ACS Nano (2014).
- Benameur, M. M., Gargiulo, F., Manzeli, S., Autès, G., Tosun, M., Yazyev, O. V., and Kis, A. *Electromechanical oscillations in bilayer graphene*. Nature Communications **6**, 8582 (2015).
- Berger, C., Song, Z., Li, X., Wu, X., Brown, N., Naud, C., Mayou, D., Li, T., Hass, J., Marchenkov, A., Conrad, E., First, P., and De Heer, W. *Electronic confinement and coherence in patterned epitaxial graphene*. Science **312**, 1191 (2006).
- Bernal, J. D. *The Structure of Graphite*. Proceedings of the Royal Society of London A: Mathematical, Physical and Engineering Sciences **106**, 749 (1924).
- Bistritzer, R. and MacDonald, A. H. *Moiré bands in twisted double-layer graphene*. Proceedings of the National Academy of Sciences **108**, 12233 (2011).
- Bitzek, E., Koskinen, P., Gähler, F., Moseler, M., and Gumbsch, P. *Structural Relaxation Made Simple*. Physical Review Letters **97**, 170201 (2006).
- Bolotin, K. I., Sikes, K. J., Jiang, Z., Klima, M., Fudenberg, G., Hone, J., Kim, P., and Stormer, H. L. *Ultra-high electron mobility in suspended graphene*. Solid State Communications **146**, 351 (2008).
- Bostwick, A., McChesney, J. L., Emtsev, K. V., Seyller, T., Horn, K., Kevan, S. D., and Rotenberg, E. *Quasiparticle transformation during a metal-insulator transition in graphene*. Physical Review Letters **103**, 056404 (2009).
- Boukhvalov, D. W., Katsnelson, M. I., and Lichtenstein, A. I. *Hydrogen on graphene: Electronic structure, total energy, structural distortions and magnetism from first-principles calculations*. Physical Review B **77**, 035427 (2008).

- Brenner, D. W., Shenderova, O. A., Harrison, J. A., Stuart, S. J., Ni, B., and Sinnott, S. B. *A second-generation reactive empirical bond order (REBO) potential energy expression for hydrocarbons*. Journal of Physics: Condensed Matter **14**, 783 (2002).
- Brito, W. H., Kagimura, R., and Miwa, R. H. *Hydrogenated grain boundaries in graphene*. Applied Physics Letters **98**, 213107 (2011).
- Brito, W. H., Kagimura, R., and Miwa, R. H. *B and N doping in graphene ruled by grain boundary defects*. Physical Review B **85** (2012).
- Brown, L., Hovden, R., Huang, P., Wojcik, M., Muller, D. A., and Park, J. *Twinning and Twisting of Tri- and Bilayer Graphene*. Nano Letters **12**, 1609 (2012).
- Bunch, J. S., Zande, A. M. v. d., Verbridge, S. S., Frank, I. W., Tanenbaum, D. M., Parpia, J. M., Craighead, H. G., and McEuen, P. L. *Electromechanical Resonators from Graphene Sheets*. Science **315**, 490 (2007).
- Büttiker, M., Imry, Y., Landauer, R., and Pinhas, S. *Generalized many-channel conductance formula with application to small rings*. Physical Review B **31**, 6207 (1985).
- Butz, B., Dolle, C., Niekietel, E., Weber, K., Waldmann, D., Weber, H. B., Meyer, B., and Spiecker, E. *Dislocations in bilayer graphene*. Nature **505**, 533 (2014).
- Camara, N., Huntzinger, J.-R., Rius, G., Tiberj, A., Mestres, N., Pérez-Murano, F., Godignon, P., and Camassel, J. *Anisotropic growth of long isolated graphene ribbons on the c face of graphite-capped 6H-SiC*. Physical Review B **80**, 125410 (2009).
- Carlsson, J. M., Ghiringhelli, L. M., and Fasolino, A. *Theory and hierarchical calculations of the structure and energetics of [0001] tilt grain boundaries in graphene*. Physical Review B **84**, 165423 (2011).
- Carpio, A., Bonilla, L. L., Juan, F. d., and Vozmediano, M. A. H. *Dislocations in graphene*. New Journal of Physics **10**, 053021 (2008).
- Castro, E. V., Novoselov, K. S., Morozov, S. V., Peres, N. M. R., dos Santos, J. M. B. L., Nilsson, J., Guinea, F., Geim, A. K., and Neto, A. H. C. *Biased Bilayer Graphene: Semiconductor with a Gap Tunable by the Electric Field Effect*. Physical Review Letters **99**, 216802 (2007).
- Castro, E. V., Ochoa, H., Katsnelson, M. I., Gorbachev, R. V., Elias, D. C., Novoselov, K. S., Geim, A. K., and Guinea, F. *Limits on Charge Carrier Mobility in Suspended Graphene due to Flexural Phonons*. Physical Review Letters **105**, 266601 (2010).
- Castro Neto, A. H., Guinea, F., Peres, N. M. R., Novoselov, K. S., and Geim, A. K. *The electronic properties of graphene*. Reviews of Modern Physics. **81**, 109 (2009).
- Ceperley, D. M. and Alder, B. J. *Ground State of the Electron Gas by a Stochastic Method*. Physical Review Letters **45**, 566 (1980).

Bibliography

- Cheianov, V. V. and Fal'ko, V. I. *Selective transmission of Dirac electrons and ballistic magnetoresistance of $n - p$ junctions in graphene*. Physical Review B **74**, 041403 (2006).
- Chen, J.-H., Autès, G., Alem, N., Gargiulo, F., Gautam, A., Linck, M., Kisielowski, C., Yazyev, O. V., Louie, S. G., and Zettl, A. *Controlled growth of a line defect in graphene and implications for gate-tunable valley filtering*. Physical Review B **89**, 121407 (2014).
- Chen, J.-H., Cullen, W. G., Jang, C., Fuhrer, M. S., and Williams, E. D. *Defect Scattering in Graphene*. Physical Review Letters **102**, 236805 (2009).
- Chen, J.-H., Jang, C., Adam, S., Fuhrer, M. S., Williams, E. D., and Ishigami, M. *Charged-impurity scattering in graphene*. Nature Physics **4**, 377 (2008).
- Choe, D.-H. and Chang, K. J. *Effect of dimensionality on the localization behavior in hydrogenated graphene systems*. Nano Letters **12**, 5175 (2012).
- Choi, H. J., Ihm, J., Louie, S. G., and Cohen, M. L. *Defects, quasibound states, and quantum conductance in metallic carbon nanotubes*. Physical Review Letters **84**, 2917 (2000).
- Clark, K. W., Zhang, X.-G., Vlasiouk, I. V., He, G., Feenstra, R. M., and Li, A.-P. *Spatially Resolved Mapping of Electrical Conductivity across Individual Domain (Grain) Boundaries in Graphene*. ACS Nano **7**, 7956 (2013).
- Coraux, J., N'Diaye, A. T., Busse, C., and Michely, T. *Structural Coherency of Graphene on Ir(111)*. Nano Letters **8**, 565 (2008).
- Cortijo, A. and Vozmediano, M. A. H. *Effects of topological defects and local curvature on the electronic properties of planar graphene*. Nuclear Physics B **763**, 293 (2007).
- Couto, N. J. G., Sacépé, B., and Morpurgo, A. F. *Transport through graphene on srtio*. Physical Review Letters **107**, 225501 (2011).
- Cresti, A., Grosso, G., and Parravicini, G. P. *Numerical study of electronic transport in gated graphene ribbons*. Physical Review B **76**, 205433 (2007).
- Cresti, A., Ortmann, F., Louvet, T., Van Tuan, D., and Roche, S. *Broken symmetries, zero-energy modes, and quantum transport in disordered graphene: From supermetallic to insulating regimes*. Physical Review Letters **110**, 196601 (2013).
- Danneau, R., Wu, F., Craciun, M. F., Russo, S., Tomi, M. Y., Salmilehto, J., Morpurgo, A. F., and Hakonen, P. J. *Shot Noise in Ballistic Graphene*. Physical Review Letters **100**, 196802 (2008).
- Das Sarma, S., Adam, S., Hwang, E. H., and Rossi, E. *Electronic transport in two-dimensional graphene*. Reviews of Modern Physics **83**, 407 (2011).
- Datta, S. *Electronic Transport in Mesoscopic Systems*. Cambridge University Press (1997).

- Dennis, J. and Schnabel, R. *Numerical Methods for Unconstrained Optimization and Nonlinear Equations*. Classics in Applied Mathematics. Society for Industrial and Applied Mathematics (1996).
- Dresselhaus, M. S. and Dresselhaus, G. *Intercalation compounds of graphite*. *Advances in Physics* **51**, 1 (2002).
- Duong, D. L., Han, G. H., Lee, S. M., Gunes, F., Kim, E. S., Kim, S. T., Kim, H., Ta, Q. H., So, K. P., Yoon, S. J., Chae, S. J., Jo, Y. W., Park, M. H., Chae, S. H., Lim, S. C., Choi, J. Y., and Lee, Y. H. *Probing graphene grain boundaries with optical microscopy*. *Nature* **490**, 235 (2012).
- Economou, E. N. *Green's Functions in Quantum Physics*. Springer, Berlin (2006).
- Eelbo, T., Waśniowska, M., Thakur, P., Gyamfi, M., Sachs, B., Wehling, T. O., Forti, S., Starke, U., Tieg, C., Lichtenstein, A. I., and Wiesendanger, R. *Adatoms and clusters of 3d transition metals on graphene: Electronic and magnetic configurations*. *Physical Review Letters* **110**, 136804 (2013).
- Evers, F. and Mirlin, A. D. *Anderson transitions*. *Reviews of Modern Physics*. **80**, 1355 (2008).
- Fei, Z., Rodin, A. S., Gannett, W., Dai, S., Regan, W., Wagner, M., Liu, M. K., McLeod, A. S., Dominguez, G., Thiemens, M., Neto, A. H. C., Keilmann, F., Zettl, A., Hillenbrand, R., Fogler, M. M., and Basov, D. N. *Electronic and plasmonic phenomena at graphene grain boundaries*. *Nature Nanotechnology* **8**, 821 (2013).
- Ferrari, A. C., Meyer, J. C., Scardaci, V., Casiraghi, C., Lazzeri, M., Mauri, F., Piscanec, S., Jiang, D., Novoselov, K. S., Roth, S., and Geim, A. K. *Raman Spectrum of Graphene and Graphene Layers*. *Physical Review Letters* **97**, 187401 (2006).
- Ferreira, A., Viana-Gomes, J., Nilsson, J., Mucciolo, E. R., Peres, N. M. R., and Castro Neto, A. H. *Unified description of the dc conductivity of monolayer and bilayer graphene at finite densities based on resonant scatterers*. *Physical Review B* **83**, 165402 (2011).
- Fisher, D. S. and Lee, P. A. *Relation between conductivity and transmission matrix*. *Physical Review B* **23**, 6851 (1981).
- Fletcher, R. *Practical Methods of Optimization*. John Wiley & Sons (2013).
- Fletcher, R. and Reeves, C. M. *Function minimization by conjugate gradients*. *The Computer Journal* **7**, 149 (1964).
- Foa Torres, L., Roche, S., and Charlier, J. C. *Introduction to Graphene-Based Nanomaterials*. Cambridge University Press (2014).
- Frenkel, D. and Smit, B. *Understanding Molecular Simulation: From Algorithms to Applications*. Academic Press (2001).
- Geim, A. K. and Grigorieva, I. V. *Van der Waals heterostructures*. *Nature* **499**, 419 (2013).

Bibliography

- Geim, A. K. and Novoselov, K. S. *The rise of graphene*. Nature Mater. **6**, 183 (2007).
- Ghiringhelli, L. M. *On the nature of phase transitions in covalent liquids*. Ph.D. thesis University of Amsterdam (2006).
- Giannozzi, P., Baroni, S., Bonini, N., Calandra, M., Car, R., Cavazzoni, C., Ceresoli, D., Chiarotti, G. L., Cococcioni, M., Dabo, I., Corso, A. D., Gironcoli, S. d., Fabris, S., Fratesi, G., Gebauer, R., Gerstmann, U., Gougoussis, C., Kokalj, A., Lazzeri, M., Martin-Samos, L., Marzari, N., Mauri, F., Mazzarello, R., Paolini, S., Pasquarello, A., Paulatto, L., Sbraccia, C., Scandolo, S., Sclauzero, G., Seitsonen, A. P., Smogunov, A., Umari, P., and Wentzcovitch, R. M. *Quantum espresso: a modular and open-source software project for quantum simulations of materials*. Journal of Physics: Condensed Matter **21**, 395502 (2009).
- Gong, L., Young, R. J., Kinloch, I. A., Haigh, S. J., Warner, J. H., Hinks, J. A., Xu, Z., Li, L., Ding, F., Riaz, I., Jalil, R., and Novoselov, K. S. *Reversible Loss of Bernal Stacking during the Deformation of Few-Layer Graphene in Nanocomposites*. ACS Nano **7**, 7287 (2013).
- Grüneis, A., Attacalite, C., Wirtz, L., Shiozawa, H., Saito, R., Pichler, T., and Rubio, A. *Tight-binding description of the quasiparticle dispersion of graphite and few-layer graphene*. Physical Review B **78**, 205425 (2008).
- Gunlycke, D. and White, C. T. *Graphene Valley Filter Using a Line Defect*. Physical Review Letters **106**, 136806 (2011).
- Hagstrom, S., Lyon, H. B., and Somorjai, G. A. *Surface structures on the clean platinum (100) surface*. Physical Review Letters **15**, 491 (1965).
- Hamann, D. R., Schlüter, M., and Chiang, C. *Norm-Conserving Pseudopotentials*. Physical Review Letters **43**, 1494 (1979).
- Hashimoto, A., Suenaga, K., Gloter, A., Urita, K., and Iijima, S. *Direct evidence for atomic defects in graphene layers*. Nature **430**, 870 (2004).
- Hass, J., Varchon, F., Millán-Otoya, J. E., Sprinkle, M., Sharma, N., de Heer, W. A., Berger, C., First, P. N., Magaud, L., and Conrad, E. H. *Why multilayer graphene on 4h-sic(0001) behaves like a single sheet of graphene*. Physical Review Letters **100**, 125504 (2008).
- Hellmann, H. *A New Approximation Method in the Problem of Many Electrons*. The Journal of Chemical Physics **3**, 61 (1935).
- Herrero, C. P. and Ramírez, R. *Vibrational properties and diffusion of hydrogen on graphene*. Physical Review B **79**, 115429 (2009).
- Hestenes, M. R. and Stiefel, E. *Methods of conjugate gradients for solving linear systems*. Journal of research of the National Bureau of Standards **49**, 409 (1952).
- Hohenberg, P. and Kohn, W. *Inhomogeneous Electron Gas*. Physical Review **136**, B864 (1964).

- Horiguchi, T. *Lattice green's functions for the triangular and honeycomb lattices*. Journal of Mathematical Physics **13**, 1411 (1972).
- Huang, P. Y., Ruiz-Vargas, C. S., van der Zande, A. M., Whitney, W. S., Levendorf, M. P., Kevek, J. W., Garg, S., Alden, J. S., Hustedt, C. J., Zhu, Y., Park, J., McEuen, P. L., and Muller, D. A. *Grains and grain boundaries in single-layer graphene atomic patchwork quilts*. Nature **469**, 389 (2011).
- Ihnatsenka, S. and Zozoulenko, I. V. *Electron interaction, charging, and screening at grain boundaries in graphene*. Physical Review B **88**, 085436 (2013).
- Jayasingha, R., Sherehiy, A., Wu, S.-Y., and Sumanasekera, G. U. *In situ study of hydrogenation of graphene and new phases of localization between metal–insulator transitions*. Nano Letters **13**, 5098 (2013).
- Katsnelson, M. I. *Zitterbewegung, chirality, and minimal conductivity in graphene*. The European Physical Journal B - Condensed Matter and Complex Systems **51**, 157 (2006).
- Katsnelson, M. I., Novoselov, K. S., and Geim, A. K. *Chiral tunnelling and the klein paradox in graphene*. Nature Physics **2**, 620 (2006).
- Kim, K., Lee, Z., Regan, W., Kisielowski, C., Crommie, M. F., and Zettl, A. *Grain boundary mapping in polycrystalline graphene*. ACS Nano **5**, 2142 (2011).
- Klein, O. *Die Reflexion von Elektronen an einem Potentialsprung nach der relativistischen Dynamik von Dirac*. Zeitschrift für Physik **53**, 157 (1929).
- Koepke, J. C., Wood, J. D., Estrada, D., Ong, Z.-Y., He, K. T., Pop, E., and Lyding, J. W. *Atomic-Scale Evidence for Potential Barriers and Strong Carrier Scattering at Graphene Grain Boundaries: A Scanning Tunneling Microscopy Study*. ACS Nano **7**, 75 (2013).
- Kohn, W. and Sham, L. J. *Quantum Density Oscillations in an Inhomogeneous Electron Gas*. Physical Review **137**, A1697 (1965).
- Kolmogorov, A. N. and Crespi, V. H. *Registry-dependent interlayer potential for graphitic systems*. Physical Review B **71**, 235415 (2005).
- Koshino, M. *Electronic transmission through AB-BA domain boundary in bilayer graphene*. Physical Review B **88** (2013).
- Kotakoski, J., Santos-Cottin, D., and Krasheninnikov, A. V. *Stability of Graphene Edges under Electron Beam: Equilibrium Energetics versus Dynamic Effects*. ACS Nano **6**, 671 (2012).
- Kurasch, S., Kotakoski, J., Lehtinen, O., Skákalová, V., Smet, J., Krill, C. E., Krasheninnikov, A. V., and Kaiser, U. *Atom-by-atom observation of grain boundary migration in graphene*. Nano Letters **12**, 3168 (2012).

Bibliography

- Lahiri, J., Lin, Y., Bozkurt, P., Oleynik, I. I., and Batzill, M. *An extended defect in graphene as a metallic wire*. Nature Nanotechnology **5**, 326 (2010).
- Lalmi, B., Girard, J. C., Pallecchi, E., Silly, M., David, C., Latil, S., Sirotti, E., and Ouerghi, A. *Flower-Shaped Domains and Wrinkles in Trilayer Epitaxial Graphene on Silicon Carbide*. Scientific Reports **4** (2014).
- Lammert, P. E. and Crespi, V. H. *Topological phases in graphitic cones*. Physical Review Letters **85**, 5190 (2000).
- LAMMPS. *Molecular Dynamics Simulator* <http://lammps.sandia.gov/>.
- Landauer, R. *Spatial Variation of Currents and Fields Due to Localized Scatterers in Metallic Conduction*. IBM Journal of Research and Development **1**, 223 (1957).
- Laughlin, R. B. *Quantized Hall conductivity in two dimensions*. Physical Review B **23**, 5632 (1981).
- Lebègue, S., Harl, J., Gould, T., Ángyán, J. G., Kresse, G., and Dobson, J. F. *Cohesive Properties and Asymptotics of the Dispersion Interaction in Graphite by the Random Phase Approximation*. Physical Review Letters **105**, 196401 (2010).
- Leconte, N., Soriano, D., Roche, S., Ordejon, P., Charlier, J.-C., and Palacios, J. J. *Magnetism-dependent transport phenomena in hydrogenated graphene: From spin-splitting to localization effects*. ACS Nano **5**, 3987 (2011).
- Lee, K., Fallahazad, B., Xue, J., Dillen, D., Kim, K., Taniguchi, T., Watanabe, K., and Tutuc, E. *Chemical potential and quantum Hall ferromagnetism in bilayer graphene*. Science **345**, 58 (2014).
- Lee, P. A. and Ramakrishnan, T. V. *Disordered electronic systems*. Reviews of Modern Physics. **57**, 287 (1985).
- Lehtinen, O., Kurasch, S., Krasheninnikov, A. V., and Kaiser, U. *Atomic scale study of the life cycle of a dislocation in graphene from birth to annihilation*. Nature Communications **4**, 2098 (2013).
- Lherbier, A., Dubois, S. M.-M., Declerck, X., Roche, S., Niquet, Y.-M., and Charlier, J.-C. *Two-dimensional graphene with structural defects: Elastic mean free path, minimum conductivity, and anderson transition*. Physical Review Letters **106**, 046803 (2011).
- Li, G., Luican, A., Lopes dos Santos, J. M. B., Castro Neto, A. H., Reina, A., Kong, J., and Andrei, E. Y. *Observation of Van Hove singularities in twisted graphene layers*. Nature Physics **6**, 109 (2010).
- Li, L., Reich, S., and Robertson, J. *Defect energies of graphite: Density-functional calculations*. Physical Review B **72**, 184109 (2005).

- Lifshitz, I. M. *Anomalies of electron characteristic of a metal in the high pressure region*. Soviet Journal of Experimental and Theoretical Physics pp. 1130–1135 (1960).
- Lin, J., Fang, W., Zhou, W., Lupini, A. R., Idrobo, J. C., Kong, J., Pennycook, S. J., and Pantelides, S. T. *AC/AB Stacking Boundaries in Bilayer Graphene*. Nano Letters **13**, 3262 (2013).
- Lin, Y., Ding, F., and Yakobson, B. I. *Hydrogen storage by spillover on graphene as a phase nucleation process*. Physical Review B **78**, 041402 (2008).
- Liu, Y. and Yakobson, B. I. *Cones, pringles, and grain boundary landscapes in graphene topology*. Nano Letters **10**, 2178 (2010).
- Liu, Y., Zou, X., and Yakobson, B. I. *Dislocations and Grain Boundaries in Two-Dimensional Boron Nitride*. ACS Nano **6**, 7053 (2012).
- Lopes dos Santos, J. M. B., Peres, N. M. R., and Castro Neto, A. H. *Graphene bilayer with a twist: Electronic structure*. Physical Review Letters **99**, 256802 (2007).
- Los, J. H. and Fasolino, A. *Intrinsic long-range bond-order potential for carbon: Performance in Monte Carlo simulations of graphitization*. Physical Review B **68**, 024107 (2003).
- Los, J. H., Ghiringhelli, L. M., Meijer, E. J., and Fasolino, A. *Improved long-range reactive bond-order potential for carbon. I. Construction*. Physical Review B **72**, 214102 (2005).
- Lu, C.-C., Lin, Y.-C., Liu, Z., Yeh, C.-H., Suenaga, K., and Chiu, P.-W. *Twisting Bilayer Graphene Superlattices*. ACS Nano **7**, 2587 (2013).
- Luican, A., Li, G., Reina, A., Kong, J., Nair, R. R., Novoselov, K. S., Geim, A. K., and Andrei, E. Y. *Single-Layer Behavior and Its Breakdown in Twisted Graphene Layers*. Physical Review Letters **106**, 126802 (2011).
- Lyon, H. B. and Somorjai, G. A. *Low-energy electron-diffraction study of the clean (100), (111), and (110) faces of platinum*. The Journal of Chemical Physics **46**, 2539 (1967).
- Ma, C., Sun, H., Zhao, Y., Li, B., Li, Q., Zhao, A., Wang, X., Luo, Y., Yang, J., Wang, B., and Hou, J. G. *Evidence of van Hove Singularities in Ordered Grain Boundaries of Graphene*. Physical Review Letters **112**, 226802 (2014).
- Marek, A., Blum, V., Johanni, R., Havu, V., Lang, B., Auckenthaler, T., Heinecke, A., Bungartz, H.-J., and Lederer, H. *The ELPA library: scalable parallel eigenvalue solutions for electronic structure theory and computational science*. Journal of Physics: Condensed Matter **26**, 213201 (2014).
- Markoš, P. and Schweitzer, L. *Critical regime of two-dimensional Ando model: relation between critical conductance and fractal dimension of electronic eigenstates*. Journal of Physics A: Mathematical and General **39**, 3221 (2006).

Bibliography

- Massimiliano Di Ventra. *Electrical Transport in Nanoscale Systems*. Cambridge University Press (2008).
- Mathon, J. and Umerski, A. *Theory of tunneling magnetoresistance of an epitaxial Fe/MgO/Fe(001) junction*. Physical Review B **63**, 220403 (2001).
- May, J. W. *Platinum surface LEED rings*. Surface Science **17**, 267 (1969).
- Mayorov, A. S., Gorbachev, R. V., Morozov, S. V., Britnell, L., Jalil, R., Ponomarenko, L. A., Blake, P., Novoselov, K. S., Watanabe, K., Taniguchi, T., and Geim, A. K. *Micrometer-Scale Ballistic Transport in Encapsulated Graphene at Room Temperature*. Nano Letters **11**, 2396 (2011).
- McCann, E. *Asymmetry gap in the electronic band structure of bilayer graphene*. Physical Review B **74**, 161403 (2006).
- McCann, E. and Fal'ko, V. I. *Landau-Level Degeneracy and Quantum Hall Effect in a Graphite Bilayer*. Physical Review Letters **96**, 086805 (2006).
- McCann, E. and Koshino, M. *The electronic properties of bilayer graphene*. Reports on Progress in Physics **76**, 056503 (2013).
- McClure, J. W. *Diamagnetism of Graphite*. Physical Review **104**, 666 (1956).
- McClure, J. W. *Band Structure of Graphite and de Haas-van Alphen Effect*. Physical Review **108**, 612 (1957).
- McClure, J. W. *Theory of Diamagnetism of Graphite*. Physical Review **119**, 606 (1960).
- Mermin, N. D. *The topological theory of defects in ordered media*. Reviews of Modern Physics **51**, 591 (1979).
- Mesaros, A., Papanikolaou, S., Flipse, C. F. J., Sadri, D., and Zaanen, J. *Electronic states of graphene grain boundaries*. Physical Review B **82**, 205119 (2010).
- Mesaros, A., Sadri, D., and Zaanen, J. *Berry phase of dislocations in graphene and valley conserving decoherence*. Physical Review B **79**, 155111 (2009).
- Metropolis, N., Rosenbluth, A. W., Rosenbluth, M. N., Teller, A. H., and Teller, E. *Equation of state calculations by fast computing machines*. Journal of Chemical Physics **21**, 1087 (1953).
- Meyer, J. C., Kisielowski, C., Erni, R., Rossell, M. D., Crommie, M. F., and Zettl, A. *Direct Imaging of Lattice Atoms and Topological Defects in Graphene Membranes*. Nano Letters **8**, 3582 (2008).
- Miao, F., Wijeratne, S., Zhang, Y., Coskun, U. C., Bao, W., and Lau, C. N. *Phase-Coherent Transport in Graphene Quantum Billiards*. Science **317**, 1530 (2007).
- Moaied, M., Moreno, J. A., Caturla, M. J., Ynduráin, F., and Palacios, J. J. *Theoretical study of the dynamics of atomic hydrogen adsorbed on graphene multilayers*. Physical Review B **91**, 155419 (2015).

- Monkhorst, H. J. and Pack, J. D. *Special points for brillouin-zone integrations*. Physical Review B **13**, 5188 (1976).
- Morgan, A. E. and Somorjai, G. A. *Low energy electron diffraction studies of gas adsorption on the platinum (100) single crystal surface*. Surface Science **12**, 405 (1968).
- Morozov, S. V., Novoselov, K. S., Katsnelson, M. I., Schedin, F., Elias, D. C., Jaszczak, J. A., and Geim, A. K. *Giant Intrinsic Carrier Mobilities in Graphene and Its Bilayer*. Physical Review Letters **100**, 016602 (2008).
- Moser, J., Barreiro, A., and Bachtold, A. *Current-induced cleaning of graphene*. Applied Physics Letters **91**, 163513 (2007).
- Mounet, N. and Marzari, N. *First-principles determination of the structural, vibrational and thermodynamic properties of diamond, graphite, and derivatives*. Physical Review B **71**, 205214 (2005).
- Murray, É. D., Lee, K., and Langreth, D. C. *Investigation of Exchange Energy Density Functional Accuracy for Interacting Molecules*. Journal of Chemical Theory and Computation **5**, 2754 (2009).
- Nair, R. R., Tsai, I.-L., Sepioni, M., Lehtinen, O., Keinonen, J., Krasheninnikov, A. V., Castro Neto, A. H., Katsnelson, M. I., Geim, A. K., and Grigorieva, I. V. *Dual origin of defect magnetism in graphene and its reversible switching by molecular doping*. Nature Communications **4** (2013).
- Ni, Z. H., Ponomarenko, L. A., Nair, R. R., Yang, R., Anissimova, S., Grigorieva, I. V., Schedin, F., Blake, P., Shen, Z. X., Hill, E. H., Novoselov, K. S., and Geim, A. K. *On resonant scatterers as a factor limiting carrier mobility in graphene*. Nano Letters **10**, 3868 (2010).
- Nomura, K. and MacDonald, A. H. *Quantum Transport of Massless Dirac Fermions*. Physical Review Letters **98**, 076602 (2007).
- Novoselov, K. S. *Nobel Lecture: Graphene: Materials in the Flatland*. Reviews of Modern Physics **83**, 837 (2011).
- Novoselov, K. S., Fal'ko, V. I., Colombo, L., Gellert, P. R., Schwab, M. G., and Kim, K. *A roadmap for graphene*. Nature **490**, 192 (2012).
- Novoselov, K. S., Geim, A. K., Morozov, S. V., Jiang, D., Katsnelson, M. I., Grigorieva, I. V., Dubonos, S. V., and Firsov, A. A. *Two-dimensional gas of massless dirac fermions in graphene*. Nature **438**, 197 (2005).
- Novoselov, K. S., Geim, A. K., Morozov, S. V., Jiang, D., Zhang, Y., Dubonos, S. V., Grigorieva, I. V., and Firsov, A. A. *Electric field effect in atomically thin carbon films*. Science **306**, 666 (2004).

Bibliography

- Novoselov, K. S., Jiang, Z., Zhang, Y., Morozov, S. V., Stormer, H. L., Zeitler, U., Maan, J. C., Boebinger, G. S., Kim, P., and Geim, A. K. *Room-Temperature Quantum Hall Effect in Graphene*. *Science* **315**, 1379 (2007).
- Novoselov, K. S., McCann, E., Morozov, S. V., Fal'ko, V. I., Katsnelson, M. I., Zeitler, U., Jiang, D., Schedin, F., and Geim, A. K. *Unconventional quantum hall effect and berry's phase of 2π in bilayer graphene*. *Nature Physics* **2**, 177 (2006).
- Ochoa, H., Castro, E. V., Katsnelson, M. I., and Guinea, F. *Temperature-dependent resistivity in bilayer graphene due to flexural phonons*. *Physical Review B* **83**, 235416 (2011).
- Ohta, T., Bostwick, A., Seyller, T., Horn, K., and Rotenberg, E. *Controlling the Electronic Structure of Bilayer Graphene*. *Science* **313**, 951 (2006).
- Oshima, C. and Nagashima, A. *Ultra-thin epitaxial films of graphite and hexagonal boron nitride on solid surfaces*. *Journal of Physics: Condensed Matter* **9**, 1 (1997).
- Palacios, J. J., Fernández-Rossier, J., and Brey, L. *Vacancy-induced magnetism in graphene and graphene ribbons*. *Physical Review B* **77**, 195428 (2008).
- Perdew, J. P., Burke, K., and Ernzerhof, M. *Generalized gradient approximation made simple*. *Physical Review Letters* **77**, 3865 (1996).
- Pereira, V. M., Guinea, F., Lopes dos Santos, J. M. B., Peres, N. M. R., and Castro Neto, A. H. *Disorder Induced Localized States in Graphene*. *Physical Review Letters* **96**, 036801 (2006).
- Pisanty, A. *The electronic structure of graphite: A chemist's introduction to band theory*. *Journal of Chemical Education* **68**, 804 (1991).
- Plimpton, S. *Fast Parallel Algorithms for Short-Range Molecular Dynamics*. *Journal of Computational Physics* **117**, 1 (1995).
- Polak, E. and Ribière, G. *Note sur la convergence de méthodes de directions conjuguées*. *Revue française d'automatique informatique, recherche opérationnelle* **16**, 35 (1969).
- Pong, W.-T. and Durkan, C. *A review and outlook for an anomaly of scanning tunnelling microscopy (STM): superlattices on graphite*. *Journal of Physics D: Applied Physics* **38**, R329 (2005).
- Ponomarenko, L. A., Yang, R., Mohiuddin, T. M., Katsnelson, M. I., Novoselov, K. S., Morozov, S. V., Zhukov, A. A., Schedin, F., Hill, E. W., and Geim, A. K. *Effect of a high- κ environment on charge carrier mobility in graphene*. *Physical Review Letters* **102**, 206603 (2009).
- Popov, A. M., Lebedeva, I. V., Knizhnik, A. A., Lozovik, Y. E., and Potapkin, B. V. *Commensurate-incommensurate phase transition in bilayer graphene*. *Physical Review B* **84**, 045404 (2011).
- Radchenko, T. M., Shylau, A. A., and Zozoulenko, I. V. *Influence of correlated impurities on conductivity of graphene sheets: Time-dependent real-space kubo approach*. *Physical Review B* **86**, 035418 (2012).

- Read, W. T. and Shockley, W. *Dislocation Models of Crystal Grain Boundaries*. Physical Review **78**, 275 (1950).
- Reguzzoni, M., Fasolino, A., Molinari, E., and Righi, M. C. *Potential energy surface for graphene on graphene: Ab initio derivation, analytical description, and microscopic interpretation*. Physical Review B **86**, 245434 (2012).
- Reich, S., Maultzsch, J., Thomsen, C., and Ordejón, P. *Tight-binding description of graphene*. Physical Review B **66**, 035412 (2002).
- Richard M. Martin. *Electronic Structure, basic theory and practical methods*. Cambridge University Press (2013).
- Roscoe, C. and Thomas, J. M. *The revelation of small-angle boundaries and forest dislocations in graphite monocrystals*. Carbon **4**, 383 (1966).
- Rycerz, A., Tworzydło, J., and Beenakker, C. W. J. *Valley filter and valley valve in graphene*. Nature Physics **3**, 172 (2007).
- S. V. Iordanskii, A. E. K. *Interaction of excitations with dislocations in a crystal*. Journal of Experimental and Theoretical Physics **63**, 820 (1985).
- Sabatini, R., Gorni, T., and de Gironcoli, S. *Nonlocal van der Waals density functional made simple and efficient*. Physical Review B **87**, 041108 (2013).
- Sancho, M. P. L., Sancho, J. M. L., and Rubio, J. *Quick iterative scheme for the calculation of transfer matrices: application to Mo (100)*. Journal of Physics F: Metal Physics **14**, 1205 (1984).
- Sanvito, S., Lambert, C. J., Jefferson, J. H., and Bratkovsky, A. M. *General green's-function formalism for transport calculations with spd hamiltonians and giant magnetoresistance in co- and ni-based magnetic multilayers*. Physical Review B **59**, 11936 (1999).
- Schubert, G. and Fehske, H. *Metal-to-insulator transition and electron-hole puddle formation in disordered graphene nanoribbons*. Physical Review Letters **108**, 066402 (2012).
- Semenoff, G. W. *Condensed-Matter Simulation of a Three-Dimensional Anomaly*. Physical Review Letters **53**, 2449 (1984).
- Shallcross, S., Sharma, S., and Pankratov, O. A. *Quantum Interference at the Twist Boundary in Graphene*. Physical Review Letters **101**, 056803 (2008).
- Shon, N. H. and Ando, T. *Quantum transport in two-dimensional graphite system*. Journal of the Physical Society of Japan **67**, 2421 (1998).
- Slater, J. C. and Koster, G. F. *Simplified LCAO Method for the Periodic Potential Problem*. Physical Review **94**, 1498 (1954).
- Slonczewski, J. C. and Weiss, P. R. *Band Structure of Graphite*. Physical Review **109**, 272 (1958).

Bibliography

- Smith, A. D., Niklaus, F., Paussa, A., Vaziri, S., Fischer, A. C., Sterner, M., Forsberg, F., Delin, A., Esseni, D., Palestri, P., Östling, M., and Lemme, M. C. *Electromechanical Piezoresistive Sensing in Suspended Graphene Membranes*. Nano Letters **13**, 3237 (2013).
- Soler, J. M., Artacho, E., Gale, J. D., García, A., Junquera, J., Ordejón, P., and Sánchez-Portal, D. *The SIESTA method for ab initio order-N materials simulation*. Journal of Physics: Condensed Matter **14**, 2745 (2002).
- Song, H. S., Li, S. L., Miyazaki, H., Sato, S., Hayashi, K., Yamada, A., Yokoyama, N., and Tsukagoshi, K. *Origin of the relatively low transport mobility of graphene grown through chemical vapor deposition*. Scientific Reports **2** (2012).
- Song, Y., Song, H., and Feng, S. *The effects of disorder and interactions on the anderson transition in doped graphene*. Journal of Physics: Condensed Matter **23**, 205501 (2011).
- Spanu, L., Sorella, S., and Galli, G. *Nature and Strength of Interlayer Binding in Graphite*. Physical Review Letters **103**, 196401 (2009).
- Stander, N., Huard, B., and Goldhaber-Gordon, D. *Evidence for Klein Tunneling in Graphene p-n Junctions*. Physical Review Letters **102**, 026807 (2009).
- Stauber, T., Peres, N. M. R., and Guinea, F. *Electronic transport in graphene: A semiclassical approach including midgap states*. Physical Review B **76**, 205423 (2007).
- Stone, A. and Wales, D. J. *Theoretical studies of icosahedral C₆₀ and some related species*. Chemical Physics Letters **128**, 501 (1986).
- Suzuura, H. and Ando, T. *Crossover from Symplectic to Orthogonal Class in a Two-Dimensional Honeycomb Lattice*. Physical Review Letters **89**, 266603 (2002).
- Tan, Y.-W., Zhang, Y., Bolotin, K., Zhao, Y., Adam, S., Hwang, E. H., Das Sarma, S., Stormer, H. L., and Kim, P. *Measurement of Scattering Rate and Minimum Conductivity in Graphene*. Physical Review Letters **99**, 246803 (2007).
- Tapasztó, L., Nemes-Incze, P., Dobrik, G., Jae Yoo, K., Hwang, C., and Biró, L. P. *Mapping the electronic properties of individual graphene grain boundaries*. Applied Physics Letters **100**, 053114 (2012).
- Tersoff, J. and Hamann, D. R. *Theory of the scanning tunneling microscope*. Physical Review B **31**, 805 (1985).
- Tison, Y., Lagoute, J., Repain, V., Chacon, C., Girard, Y., Joucken, F., Sporcken, R., Gargiulo, F., Yazyev, O. V., and Rousset, S. *Grain Boundaries in Graphene on SiC(000 $\bar{1}$) substrate*. Nano Letters (2014).
- Titov, M., Ostrovsky, P. M., Gornyi, I. V., Schuessler, A., and Mirlin, A. D. *Charge transport in graphene with resonant scatterers*. Physical Review Letters **104**, 076802 (2010).

- Trambly de Laissardière, G. and Mayou, D. *Conductivity of graphene with resonant and nonresonant adsorbates*. Physical Review Letters **111**, 146601 (2013).
- Trambly de Laissardière, G., Mayou, D., and Magaud, L. *Localization of Dirac Electrons in Rotated Graphene Bilayers*. Nano Letters **10**, 804 (2010).
- Trambly de Laissardière, G., Mayou, D., and Magaud, L. *Numerical studies of confined states in rotated bilayers of graphene*. Physical Review B **86**, 125413 (2012).
- Tsen, A. W., Brown, L., Levendorf, M. P., Ghahari, F., Huang, P. Y., Havener, R. W., Ruiz-Vargas, C. S., Muller, D. A., Kim, P., and Park, J. *Tailoring Electrical Transport Across Grain Boundaries in Polycrystalline Graphene*. Science **336**, 1143 (2012).
- Tworzydło, J., Groth, C. W., and Beenakker, C. W. J. *Finite difference method for transport properties of massless Dirac fermions*. Physical Review B **78**, 235438 (2008).
- Tworzydło, J., Trauzettel, B., Titov, M., Rycerz, A., and Beenakker, C. W. J. *Quantum-limited shot noise in graphene*. arXiv:cond-mat/0603315v3 (2006a).
- Tworzydło, J., Trauzettel, B., Titov, M., Rycerz, A., and Beenakker, C. W. J. *Sub-poissonian shot noise in graphene*. Physical Review Letters **96**, 246802 (2006b).
- Uchida, K., Furuya, S., Iwata, J.-I., and Oshiyama, A. *Atomic corrugation and electron localization due to Moiré patterns in twisted bilayer graphenes*. Physical Review B **90**, 155451 (2014).
- Ugeda, M. M., Brihuega, I., Guinea, F., and Gómez-Rodríguez, J. M. *Missing Atom as a Source of Carbon Magnetism*. Physical Review Letters **104**, 096804 (2010).
- Umerski, A. *Closed-form solutions to surface green's functions*. Physical Review B **55**, 5266 (1997).
- Uppstu, A., Fan, Z., and Harju, A. *Obtaining localization properties efficiently using the kubo-greenwood formalism*. Physical Review B **89**, 075420 (2014).
- Van Tuan, D., Kotakoski, J., Louvet, T., Ortmann, F., Meyer, J. C., and Roche, S. *Scaling Properties of Charge Transport in Polycrystalline Graphene*. Nano Letters **13**, 1730 (2013).
- van Wees, B. J., van Houten, H., Beenakker, C. W. J., Williamson, J. G., Kouwenhoven, L. P., van der Marel, D., and Foxon, C. T. *Quantized conductance of point contacts in a two-dimensional electron gas*. Physical Review Letters **60**, 848 (1988).
- van Wijk, M. M., Schuring, A., Katsnelson, M. I., and Fasolino, A. *Relaxation of moiré patterns for slightly misaligned identical lattices: graphene on graphite*. arXiv:1503.02540 [cond-mat] (2015).
- Vanderbilt, D. *Soft self-consistent pseudopotentials in a generalized eigenvalue formalism*. Physical Review B **41**, 7892 (1990).

Bibliography

- Varlet, A., Bischoff, D., Simonet, P., Watanabe, K., Taniguchi, T., Ihn, T., Ensslin, K., Mucha-Kruczyński, M., and Fal'ko, V. I. *Anomalous Sequence of Quantum Hall Liquids Revealing a Tunable Lifshitz Transition in Bilayer Graphene*. *Physical Review Letters* **113**, 116602 (2014).
- Vozmediano, M., Katsnelson, M., and Guinea, F. *Gauge fields in graphene*. *Physics Reports* **496**, 109 (2010).
- Vydrov, O. A. and Voorhis, T. V. *Nonlocal van der Waals density functional: The simpler the better*. *The Journal of Chemical Physics* **133**, 244103 (2010).
- Wallace, P. R. *The Band Theory of Graphite*. *Physical Review* **71**, 622 (1947).
- Wang, L., Meric, I., Huang, P., Gao, Q., Gao, Y., Tran, H., Taniguchi, T., Watanabe, K., Campos, L., Muller, D., Guo, J., Kim, P., Hone, J., Shepard, K., and Dean, C. *One-dimensional electrical contact to a two-dimensional material*. *Science* **342**, 614 (2013).
- Wehling, T. O., Balatsky, A. V., Katsnelson, M. I., Lichtenstein, A. I., Scharnberg, K., and Wiesendanger, R. *Local electronic signatures of impurity states in graphene*. *Physical Review B* **75**, 125425 (2007).
- Wehling, T. O., Katsnelson, M., and Lichtenstein, A. *Adsorbates on graphene: Impurity states and electron scattering*. *Chemical Physics Letters* **476**, 125 (2009a).
- Wehling, T. O., Katsnelson, M. I., and Lichtenstein, A. I. *Impurities on graphene: Midgap states and migration barriers*. *Physical Review B* **80**, 085428 (2009b).
- Wehling, T. O., Yuan, S., Lichtenstein, A. I., Geim, A. K., and Katsnelson, M. I. *Resonant scattering by realistic impurities in graphene*. *Physical Review Letters* **105**, 056802 (2010).
- Wei, Y., Wang, B., Wu, J., Yang, R., and Dunn, M. L. *Bending Rigidity and Gaussian Bending Stiffness of Single-Layered Graphene*. *Nano Letters* **13**, 26 (2013).
- Williams, J. R., DiCarlo, L., and Marcus, C. M. *Quantum Hall Effect in a Gate-Controlled p-n Junction of Graphene*. *Science* **317**, 638 (2007).
- Wooten, F., Winer, K., and Weaire, D. *Computer generation of structural models of amorphous si and ge*. *Physical Review Letters* **54**, 1392 (1985).
- Xia, J., Chen, E., Li, J., and Tao, N. *Measurement of the quantum capacitance of graphene*. *Nature Nanotechnology* **4**, 505 (2009).
- Xu, K., Cao, P., and Heath, J. R. *Scanning Tunneling Microscopy Characterization of the Electrical Properties of Wrinkles in Exfoliated Graphene Monolayers*. *Nano Letters* **9**, 4446 (2009).
- Yan, Z., Peng, Z., and Tour, J. M. *Chemical Vapor Deposition of Graphene Single Crystals*. *Accounts of Chemical Research* **47**, 1327 (2014).

- Yang, B., Xu, H., Lu, J., and Loh, K. P. *Periodic Grain Boundaries Formed by Thermal Reconstruction of Polycrystalline Graphene Film*. *Journal of the American Chemical Society* **136**, 12041 (2014).
- Yankowitz, M., Wang, J. I.-J., Birdwell, A. G., Chen, Y.-A., Watanabe, K., Taniguchi, T., Jacquod, P., San-Jose, P., Jarillo-Herrero, P., and LeRoy, B. J. *Electric field control of soliton motion and stacking in trilayer graphene*. *Nature Materials* **13**, 786 (2014).
- Yazyev, O. V. *Magnetism in disordered graphene and irradiated graphite*. *Physical Review Letters* **101**, 037203 (2008).
- Yazyev, O. V. *Emergence of magnetism in graphene materials and nanostructures*. *Reports on Progress in Physics* **73**, 056501 (2010).
- Yazyev, O. V. and Chen, Y. P. *Polycrystalline graphene and other two-dimensional materials*. *Nature Nanotechnology* **9**, 755 (2014).
- Yazyev, O. V. and Helm, L. *Defect-induced magnetism in graphene*. *Physical Review B* **75**, 125408 (2007).
- Yazyev, O. V. and Louie, S. G. *Electronic transport in polycrystalline graphene*. *Nature Mater.* **9**, 806 (2010a).
- Yazyev, O. V. and Louie, S. G. *Topological defects in graphene: Dislocations and grain boundaries*. *Physical Review B* **81**, 195420 (2010b).
- Yazyev, O. V., Tavernelli, I., Rothlisberger, U., and Helm, L. *Early stages of radiation damage in graphite and carbon nanostructures: A first-principles molecular dynamics study*. *Physical Review B* **75**, 115418 (2007).
- Young, A. F. and Kim, P. *Quantum interference and Klein tunnelling in graphene heterojunctions*. *Nature Physics* **5**, 222 (2009).
- Yu, L., Lee, Y.-H., Ling, X., Santos, E. J. G., Shin, Y. C., Lin, Y., Dubey, M., Kaxiras, E., Kong, J., Wang, H., and Palacios, T. *Graphene/MoS₂ Hybrid Technology for Large-Scale Two-Dimensional Electronics*. *Nano Letters* **14**, 3055 (2014).
- Yu, Q., Jauregui, L. A., Wu, W., Colby, R., Tian, J., Su, Z., Cao, H., Liu, Z., Pandey, D., Wei, D., Chung, T. F., Peng, P., Guisinger, N. P., Stach, E. A., Bao, J., Pei, S.-S., and Chen, Y. P. *Control and characterization of individual grains and grain boundaries in graphene grown by chemical vapour deposition*. *Nature Materials* **10**, 443 (2011).
- Yuan, S., De Raedt, H., and Katsnelson, M. I. *Modeling electronic structure and transport properties of graphene with resonant scattering centers*. *Physical Review B* **82**, 115448 (2010).
- Zakharchenko, K. V., Fasolino, A., Los, J. H., and Katsnelson, M. I. *Melting of graphene: from two to one dimension*. *Journal of Physics: Condensed Matter* **23**, 202202 (2011).

Bibliography

Zakharchenko, K. V., Roldán, R., Fasolino, A., and Katsnelson, M. I. *Self-consistent screening approximation for flexible membranes: Application to graphene*. Physical Review B **82**, 125435 (2010).

Zhang, Y., Tan, Y.-W., Stormer, H. L., and Kim, P. *Experimental observation of the quantum hall effect and berry's phase in graphene*. Nature **438**, 201 (2005).



Fernando Gargiulo

Physicist, Expert in System Modeling and Simulations
Curriculum Vitæ

*"Surprisingly, most of what you will read here is the pure truth."
(Anonymous)*

Personal Details

Birth: Naples (Italy), September 15, 1986

Nationality: Italian

Experience

2011–present **Ph.D. in Theoretical Physics**, ECOLE POLYTECHNIQUE FÉDÉRALE DE LAUSANNE, (EPFL), Lausanne, Switzerland, graduation obtained in September 2015.

○ Detailed duties:

- Research in Condensed Matter Physics: Theory and Computation
- Development of software for Physics modeling and simulation of Complex Systems
- Teaching assistant for Master Courses in Physics - Master student supervisor

○ Achievements:

- 8 research papers (6 as first author) published or submitted to prestigious international journals (e.g. Physical Review Letters, Nature Communications)
- Member of the organizing team of an international Summer School funded by ETH Zurich upon acceptance of our proposal <http://school-molecules.epfl.ch/>

2011 **Research assistant**, UNIVERSITY "FEDERICO II", Naples, Italy.

○ Detailed duties: Research in Computational Condensed Matter Physics and software development.

○ Achievements: 1 research paper as first author and 1 review paper as second author.

Education

2008–2010 **Master in theoretical Physics**, University "Federico II", Naples, Italy, 110/110 cum laude.

2004–2008 **Bachelor in Physics**, University "Federico II", Naples, Italy, 110/110 cum laude.

6, Rue de la Tour – Lausanne, CH-1004

☎ (+41)764323962 • ☎ (+41)215466840

✉ fernandogargiulo@gmail.com

🌐 <http://people.epfl.ch/fernando.gargiulo>

Skype name: fernandogargiulo1986

Computer skills

Advanced MATLAB, C/C++, Linux, OpenOffice, Vectorial Graphics, L^AT_EX
Intermediate FORTRAN, PYTHON, Microsoft Windows, Photo Editing

Languages

Italian **Mother tongue**
English **Proficient** TOEFL score 106/120 (2011)
French **Proficient** DALF C1 (2015)
Spanish **Fluent**

Awards

2014 Best Ph.D. presentation, Graphene Conference, Toulouse
2013 Special Prize for teaching engagement awarded by EPFL

Miscellaneous

2010–2011 Co-founder of my hometown's "Youth Forum" (institution to promote participation of young people to local political life)

Interests

- Singing	- Guitar
- Literature	- Theater
- Nature	- History

List of Publications

- [1] **Gargiulo, F.**, Perroni, C. A., Ramaglia, V. M. and Cataudella, V. “Electronic transport within a quasi-two-dimensional model for rubrene single-crystal field effect transistors”. *Physical Review B* **84**, 245204 (2011).
- [2] **Gargiulo, F.** and Yazyev, O. V. “Topological Aspects of Charge-Carrier Transmission across Grain Boundaries in Graphene”. *Nano Letters* **14**, 250 (2014).
- [3] **Gargiulo, F.**, Autès, G., Virk, N., Barthel, S., Rösner, M., Toller, L. R. M., Wehling, T. O., Yazyev, O. V. “Electronic Transport in Graphene with Aggregated Hydrogen Adatoms”. *Physical Review Letters* **113**, 246601 (2014).
- [4] Chen, J.-H., Autès, G., Alem, N., **Gargiulo, F.**, Gautam, A., Linck, M., Kisielowski, C., Yazyev, O. V., Louie, S. G., Zettl, A. “Controlled growth of a line defect in graphene and implications for gate-tunable valley filtering”. *Physical Review B* **89**, 121407 (2014).
- [5] Tison, Y., Lagoute, J., Repain, V., Chacon, C., Girard, Y., Joucken, F., Sporcken, R., **Gargiulo, F.**, Yazyev, O. V., Rousset, S. “Grain Boundaries in Graphene on SiC(000 $\bar{1}$) Substrate”. *Nano Letters* **14**, 6382 (2014).
- [6] Perroni, C. A., **Gargiulo, F.**, Nocera, A., Ramaglia, V. M., Cataudella, V. “The Effects of Different Electron-Phonon Couplings on the Spectral and Transport Properties of Small Molecule Single-Crystal Organic Semiconductors”. *Electronics* **3**, 165 (2014).
- [7] Benameur M. M.*, **Gargiulo, F.***, Manzeli S.*, Autès, G., Tosun M., Yazyev O. V., Kis A. “Electromechanical Oscillations in Bilayer Graphene”, *Nature Communications* **6**, 8582 (2015).
- [8] **Gargiulo, F.**, Autès, G., Yazyev, O. V. “Electronic transport across realistic grain boundaries in graphene”, to be submitted.
- [9] **Gargiulo, F.**, Autès, G., Yazyev, O. V. “Resonant and non-resonant cluster of hydrogen adatoms in graphene”, to be submitted.
- [10] **Gargiulo, F.**, Yazyev, O. V. “Electronic signatures of stacking domain boundaries in twisted bilayer graphene”, to be submitted.

*These authors contributed equally

List of presentations

Oral presentations

- [1] “Electronic transport properties of grain boundaries in graphene”, given at CCMX Summer School “Multiscale Modelling of Materials”, August 29-31, 2012, Lausanne, Switzerland.
- [2] “Electronic transport in polycrystalline graphene”, given at “HP2C/PASC Materials Simulation Junior Retreat”, July 9-12, 2013, Mannedorf, Switzerland.
- [3] “Electronic transport in graphene with aggregated hydrogen adatoms”, given at “Graphene Conference”, May 6-9, 2014, Toulouse, France.
- [4] **Invited contribution:** “Graphene and 2D-materials: The revolution of the flat”, given in occasion of “Conversación abierta con el colegio de ingenieros de Chile”, January 9, 2015, Santiago de Chile, Chile.
- [5] “Electronic signatures of stacking domain boundaries in twisted bilayer graphene”, given at “APS March Meeting 2015”, March 2-6, 2015, San Antonio, USA.

Posters

- [1] “Electronic transport properties of grain boundaries in graphene”, CECAM workshop “Chemical and topological functionalization of graphitic surfaces”, 23-25 April, 2012, Lausanne, Switzerland.
- [2] “Electronic transport properties of grain boundaries in graphene”, presented at Summer School “Nanosciences Ile de France 2012”, June 24-29, 2012, Domaine du Tremblay, France.
- [3] “Electronic transport properties of grain boundaries in graphene”, presented at CECAM workshop “Graphene: from band structure to many-body physics”, September 3-7, 2012, Bremen, Germany.
- [4] “Electronic transport properties of grain boundaries in graphene”, presented at CECAM workshop “Total Energy and Force Methods”, January 10-12, 2013, Trieste, Italy.
- [5] “Electronic transport properties of grain boundaries in graphene”, presented at CECAM workshop “Total Energy and Force Methods”, January 9-11, 2014, Lausanne.
- [6] “Electronic transport in graphene with aggregated hydrogen adatoms”, presented at CECAM workshop “High performance models of charge transport in large scale systems”, October 6-10, 2014, Bremen (Germany).
- [7] “Electronic signatures of stacking domain boundaries in twisted bilayer graphene”, presented at “Nothing is perfect: The Quantum Mechanics of Defects”, April 26-29, 2015, Ascona (Switzerland).

Teaching

- 2012 Assistant for “Statistical Physics 4”, given by Prof. Vincenzo Savona
2013-2015 Assistant for the course “Physique Numérique 3”, given by Prof. Oleg V. Yazyev
2012-2015 Tutor for “Travaux Pratique”, MSc in Physics

6, Rue de la Tour – Lausanne, CH-1004

☎ (+41)764323962 • ☎ (+41)215466840

✉ fernandogargiulo@gmail.com

🌐 <http://people.epfl.ch/fernando.gargiulo>

Skype name: *fernandogargiulo1986*